



The Panoramic Deep Fields

Michael J.I. Brown

Submitted in total fulfilment of the requirements
of the degree of Doctor of Philosophy

June 2001

Supervisors: Dr. R.L. Webster & Dr. B.J. Boyle

School of Physics
University of Melbourne

Produced on acid-free paper

Abstract

The Panoramic Deep Fields are a deep multicolour survey of two $\sim 25^\circ$ fields at high galactic latitude. The survey images have been constructed by digitally stacking scans of UK Schmidt plates. Deep images ($B_J \sim 23.5$) with low contamination have been obtained by subtracting the background from the individual plates scans and using bad pixel rejection during the stacking. The size and depth of the fields allow the accurate statistical measurement of the environments and evolution of galaxies and AGN.

The clustering of galaxies and galaxy clusters has been measured from $z \sim 0.4$ until the current epoch. The clustering properties of galaxies are strongly correlated with colour and blue $U - B_J$ selected galaxies exhibit weaker clustering than any morphologically selected sample. The weak clustering ($r_0 \lesssim 3h^{-1}\text{Mpc}$) of blue galaxies implies galaxy colour and stellar population are more strongly correlated with environment than galaxy morphology. Despite the large fields-of-view, the clustering of red galaxies and clusters varies significantly between the two fields and the distribution of clusters is consistent with this being due to large-scale-structure at $z \sim 0.4$.

The evolution and environments of AGN have been measured at intermediate redshifts with the Panoramic Deep Fields. Photometric redshifts, colour selection and the NVSS have been used to compile a catalogue of ~ 180 $0.10 < z < 0.55$ radio galaxies. The evolution of the radio galaxy luminosity function is consistent with luminosity evolution parameterised by $L(z) \sim L(0)(1+z)^{3.4}$. The environments of UBR selected AGN and radio galaxies have been measured at $z \sim 0.5$ using the Panoramic Deep Field galaxy catalogue. By applying photometric redshifts and colour selection criteria to the galaxy catalogue, it has been possible to increase the signal-to-noise of the angular correlation function and measure the cross-correlation with specific galaxy types. Most AGN host environments are comparable to the environments of galaxies with the same morphology. However, $\sim 6\%$ of UBR selected AGN are in significantly richer environments. No significant correlation between AGN luminosity and environment was detected in the Panoramic Deep Fields. The richness of AGN environments is not strongly correlated with redshift and the rapid evolution of the AGN luminosity function is not caused by evolution of AGN host environments.

This is to certify that

- (i) the thesis comprises only my original work,
- (ii) due acknowledgement has been made in the text to all other material used,
- (iii) the thesis is less than 100,000 words in length, exclusive of tables, figures, bibliographies, appendices and footnotes.

Michael Brown

Acknowledgements

First and foremost, my sincere gratitude to Rachel and Brian for their supervision. They gave me considerable independence while I pursued my research and provided suggestions which have significantly improved the thesis.

I'm indebted to Nigel Hambly and Harvey MacGillivray for scanning the plates and answering numerous questions about SuperCOSMOS. I would also like to thank Nigel and Bryn Jones for productive discussions concerning the stacking and calibration of plate scans.

During the course of this work I have received financial support via an Australian Postgraduate Award and travel scholarships from the University of Melbourne and the Astronomical Society of Australia. Without this financial support, much of the thesis would not have been possible.

I would like to thank past and present members of the University of Melbourne Astrophysics Group for their advice, comments and good humour. Finally, I would like to thank family and friends who have been tremendously supportive throughout the PhD.

Contents

| | | |
|----------|--|-----------|
| 1 | Introduction | 1 |
| 1.1 | Wide Field Surveys | 1 |
| 1.2 | Digital stacking of Photographic Material | 2 |
| 1.3 | Galaxy Clustering | 2 |
| 1.4 | AGN Evolution and Environments | 6 |
| 1.5 | Overview of thesis | 7 |
| 2 | Digital Stacking | 8 |
| 2.1 | Plate material | 8 |
| 2.2 | SuperCOSMOS scans | 10 |
| 2.3 | Data Reduction | 11 |
| 2.3.1 | Background Subtraction | 11 |
| 2.3.2 | Drilling | 13 |
| 2.3.3 | Intensity Scaling | 13 |
| 2.3.4 | Coaddition | 13 |
| 2.4 | Source Extraction | 21 |
| 2.4.1 | Astrometry | 22 |
| 2.4.2 | Object Classification | 23 |
| 2.5 | Summary | 29 |
| 3 | Photometric Calibration | 31 |
| 3.1 | CCD photometry | 31 |
| 3.2 | Colour Equations | 33 |
| 3.3 | Photometric Calibration of Panoramic Deep Fields | 36 |
| 3.4 | Comparison of Galaxy Number Counts and Colours | 43 |
| 3.5 | Comparison with Other Photometry | 49 |
| 3.6 | Summary | 51 |

| | | |
|----------|--|------------|
| 4 | The Clustering of Colour Selected Galaxies | 56 |
| 4.1 | Introduction | 56 |
| 4.2 | Estimation of the Angular Correlation Function | 57 |
| 4.3 | Modelling the Spatial Correlation Function | 59 |
| 4.4 | The Angular Correlation Function at Large Angular Scales | 62 |
| 4.5 | The Correlation Function as a Function of Limiting Magnitude . . | 62 |
| 4.6 | The Correlation Function of Colour Selected Galaxies | 71 |
| 4.7 | Summary | 80 |
| 5 | A Survey for Distant Clusters | 82 |
| 5.1 | Introduction | 82 |
| 5.2 | Methods for Identifying Clusters | 83 |
| 5.3 | The Adaptive Matched Filter | 85 |
| 5.4 | Photometric Redshifts | 88 |
| 5.5 | Implementing the AMF | 92 |
| 5.6 | Redshift Accuracy | 96 |
| 5.7 | Detection Limits | 98 |
| 5.8 | B_J , R and I Cluster Properties | 98 |
| 5.9 | Comparison with the Low z Catalogues | 101 |
| 5.10 | Comoving Density of Clusters | 105 |
| 5.11 | The Cluster Correlation Function | 109 |
| 5.12 | Comparison of the SGP and F855 fields | 110 |
| 5.13 | Summary | 112 |
| 6 | The Clustering of AGN and Galaxies | 118 |
| 6.1 | Introduction | 118 |
| 6.2 | Multicolour imaging and photometric redshifts | 119 |
| 6.3 | The Clustering of Faint Galaxies | 121 |
| 6.4 | The AGN Sample | 132 |
| 6.5 | AGN-Galaxy Clustering | 134 |
| 6.6 | Summary | 152 |
| 7 | The Evolution of Radio Galaxies | 153 |
| 7.1 | Introduction | 153 |
| 7.2 | Selection of Radio Galaxies | 154 |
| 7.3 | Redshift Distribution | 159 |
| 7.4 | Colour Distribution | 160 |

| | | |
|----------|---|------------|
| 7.5 | The 1.4 GHz Luminosity Function | 166 |
| 7.6 | The Environment of Radio Galaxies | 169 |
| 7.7 | Summary | 180 |
| 8 | Conclusions and Future Prospects | 182 |
| 8.1 | The Panoramic Deep Fields | 182 |
| 8.2 | Galaxy and Cluster Environments | 183 |
| 8.3 | AGN Evolution and Environments | 184 |
| A | References | 187 |
| B | Cluster Candidates | 194 |
| C | Radio Galaxies | 210 |

List of Tables

| | | |
|-----|---|-----|
| 1.1 | Wide Field Optical Surveys | 3 |
| 1.2 | Stacks of Scanned Plates/Films | 4 |
| 2.1 | Panoramic Deep Field plate catalogue | 9 |
| 2.2 | Filters and Emulsions | 10 |
| 2.3 | Stacking Methods | 16 |
| 2.4 | Stellar FWHM estimates | 20 |
| 2.5 | Limiting Magnitudes | 20 |
| 2.6 | Comparison of SExtractor classifications with published data . . . | 30 |
| 3.1 | Summary of MSSSO 40-inch observations. | 32 |
| 3.2 | Photographic R colour equations | 36 |
| 3.3 | Galaxy Median Colour | 48 |
| 4.1 | Galaxy number counts and the parameters for $\omega(\theta)$ | 65 |
| 4.2 | Measured parameters for $\omega(\theta)$ without $z = 0.11$ clusters | 67 |
| 4.3 | Measured parameters for $\omega(\theta)$ for the red and blue subsamples . . | 75 |
| 5.1 | A Sample of Cluster Surveys and Methods | 84 |
| 5.2 | Filter Parameters | 93 |
| 5.3 | Identifications of Clusters from Couch <i>et al.</i> (1991) | 100 |
| 6.1 | A sample of studies of the AGN environment | 120 |
| 6.2 | The Early Subsample Angular Correlation Function | 126 |
| 6.3 | The Late Subsample Angular Correlation Function | 127 |
| 6.4 | The Early-Late Angular Cross-Correlation Function | 128 |
| 6.5 | The cross-correlation function of AGN and galaxies | 136 |
| 6.6 | The AGN-early cross-correlation function with photometric z constraints | 140 |
| 6.7 | AGN with an excess of AGN-galaxy pairs | 144 |

| | | |
|------|--|-----|
| 6.8 | AGN within $20''$ of NVSS sources | 148 |
| 7.1 | The Radio Galaxy Luminosity Function | 168 |
| 7.2 | The Radio Galaxy Luminosity Function Parameters | 170 |
| 7.3 | The cross-correlation function of radio galaxies with other galaxies | 173 |
| 7.4 | The cross-correlation function of $B_J < 23.5$ radio galaxies with early subsample galaxies | 174 |
| B.1 | Cluster Candidate Catalogue | 195 |
| B.2 | Cluster Candidate Catalogue | 196 |
| B.3 | Cluster Candidate Catalogue | 197 |
| B.4 | Cluster Candidate Catalogue | 198 |
| B.5 | Cluster Candidate Catalogue | 199 |
| B.6 | Cluster Candidate Catalogue | 200 |
| B.7 | Cluster Candidate Catalogue | 201 |
| B.8 | Cluster Candidate Catalogue | 202 |
| B.9 | Cluster Candidate Catalogue | 203 |
| B.10 | Cluster Candidate Catalogue | 204 |
| B.11 | Cluster Candidate Catalogue | 205 |
| B.12 | Cluster Candidate Catalogue | 206 |
| B.13 | Cluster Candidate Catalogue | 207 |
| B.14 | Cluster Candidate Catalogue | 208 |
| B.15 | Cluster Candidate Catalogue | 209 |
| C.1 | Radio Galaxy Catalogue | 211 |
| C.2 | Radio Galaxy Catalogue | 212 |
| C.3 | Radio Galaxy Catalogue | 213 |
| C.4 | Radio Galaxy Catalogue | 214 |
| C.5 | Radio Galaxy Catalogue | 215 |
| C.6 | Radio Galaxy Catalogue | 216 |
| C.7 | Radio Galaxy Catalogue | 217 |

List of Figures

| | | |
|------|---|----|
| 2.1 | Coadded stack with poor sky subtraction | 12 |
| 2.2 | Single plate noise distribution | 15 |
| 2.3 | Comparison of single plate scan and stack | 17 |
| 2.4 | Stack with sky background subtraction and min-max rejection . . | 18 |
| 2.5 | Noise distribution of stacked data | 19 |
| 2.6 | Catalogue completeness as a function of magnitude | 22 |
| 2.7 | Comparison of Tycho-2 & Panoramic Deep Field astrometry . . . | 24 |
| 2.8 | Comparison of APM and Panoramic Deep Field astrometry . . . | 25 |
| 2.9 | Comparison of FIRST and Panoramic Deep Field astrometry . . . | 26 |
| 2.10 | Comparison of NVSS and Panoramic Deep Field astrometry . . . | 26 |
| 2.11 | SExtractor image classifications | 27 |
| 2.12 | B_J and R images with SExtractor classifications | 28 |
| 3.1 | Comparison of stellar colours | 34 |
| 3.2 | Comparison of photographic and CCD estimates of B_J | 35 |
| 3.3 | Difference between photographic and Cousins R | 37 |
| 3.4 | Difference between photographic and CCD U and I estimates . . | 38 |
| 3.5 | Photometric calibration of the SGP | 40 |
| 3.6 | Photometric calibration of F855 | 41 |
| 3.7 | Vignetting correction | 42 |
| 3.8 | Plot of dust extinction as a function of declination | 43 |
| 3.9 | Galaxy number counts | 44 |
| 3.10 | Galaxy counts as a function of radius | 46 |
| 3.11 | Galaxy colour-colour diagrams | 47 |
| 3.12 | Comparison of CCD and Panoramic Deep Field photometry . . . | 50 |
| 3.13 | Stellar locus as a function of limiting magnitude | 52 |
| 3.14 | Stellar locus in the SGP field | 53 |
| 3.15 | Comparison of F855 CCD and Panoramic Deep Field photometry | 54 |

| | | |
|------|---|----|
| 3.16 | Comparison of photometry at the centre and edge of the SGP . . . | 55 |
| 4.1 | Flux weighted map of $R < 22$ galaxies in the SGP | 57 |
| 4.2 | Median redshift as a function of survey depth | 61 |
| 4.3 | The $B_J < 23.5$ angular correlation function | 63 |
| 4.4 | The $R < 22$ angular correlation function | 64 |
| 4.5 | The I band correlation function amplitude | 68 |
| 4.6 | The R band correlation function amplitude | 69 |
| 4.7 | The B_J band correlation function amplitude | 69 |
| 4.8 | The U band correlation function amplitude | 70 |
| 4.9 | The colours of RC3 catalogue galaxies by morphological type . . . | 71 |
| 4.10 | The colour selection criteria for the red and blue subsamples . . . | 72 |
| 4.11 | Galaxy colour-colour diagrams for the SGP | 72 |
| 4.12 | A plot of the red and blue subsample number counts for the SGP and F855. | 73 |
| 4.13 | Colour-colour diagram of $B_J < 21.5$ galaxies in the SGP and F855 with spectroscopic observations by Colless <i>et al.</i> (1990) | 74 |
| 4.14 | The angular correlation function for the red and blue subsamples | 76 |
| 4.15 | Median redshift as a function of magnitude for the red subsample | 77 |
| 4.16 | Median redshift as a function of magnitude for the blue subsample | 78 |
| 4.17 | The amplitude of the clustering of the red subsamples as a function of magnitude | 78 |
| 4.18 | The amplitude of the clustering for the blue subsamples as a func- tion of magnitude | 79 |
| 5.1 | The colours of galaxies with known redshifts in the Panoramic Deep Fields. | 89 |
| 5.2 | The colours and photometric redshifts of galaxies in the SGP field. | 89 |
| 5.3 | Comparison of photometric and spectroscopic redshifts for galaxies with 3 or more colours | 90 |
| 5.4 | Comparison of photometric and spectroscopic redshifts for galaxies with B_J and R photometry | 91 |
| 5.5 | The $z = 0.1$ \mathcal{L}_{coarse} map of the SGP field | 95 |
| 5.6 | Comparison of the estimated redshifts of clusters and spectroscopic redshifts | 97 |

| | | |
|------|--|-----|
| 5.7 | The estimated detection limits for clusters in B_J , R and I for the AMF. | 99 |
| 5.8 | Plots of the comparing the B_J , R and I band redshift estimates. . | 100 |
| 5.9 | A comparison of the richness estimates of clusters derived from the B_J , R and I bands. | 101 |
| 5.10 | Redshift distributions for the Abell and APM catalogues | 102 |
| 5.11 | The estimated redshift distribution of Panoramic Deep Field clusters | 103 |
| 5.12 | The richness distribution of clusters with $z < 0.2$ | 104 |
| 5.13 | Estimated cluster number density as a function of redshift | 106 |
| 5.14 | Correlation between richness and redshift estimates | 107 |
| 5.15 | Estimated $\Lambda > 40$ cluster number density as a function of redshift | 108 |
| 5.16 | The R band $\Lambda > 35$ cluster correlation function | 111 |
| 5.17 | The B_J $\Lambda > 35$ cluster correlation function | 112 |
| 5.18 | The B_J $z = 0.4$ \mathcal{L}_{coarse} map for the SGP | 113 |
| 5.19 | The R $z = 0.4$ \mathcal{L}_{coarse} map for the SGP | 114 |
| 5.20 | The B_J $z = 0.4$ \mathcal{L}_{coarse} map for the F855 field | 115 |
| 5.21 | The R $z = 0.4$ \mathcal{L}_{coarse} map for the F855 field | 116 |
| 6.1 | Comparison of photometric and spectroscopic redshifts of red galaxies | 122 |
| 6.2 | The colours and photometric redshifts of galaxies with morphological classifications | 123 |
| 6.3 | The early subsample autocorrelation function | 125 |
| 6.4 | The late subsample autocorrelation function | 125 |
| 6.5 | The early-late cross-correlation function | 128 |
| 6.6 | Comparison of observed and model redshift distributions | 129 |
| 6.7 | Estimated redshift distribution of early subsample galaxies | 130 |
| 6.8 | Estimated redshift distribution of late subsample galaxies | 130 |
| 6.9 | The amplitude of the autocorrelation function of the early subsample | 131 |
| 6.10 | The amplitude of the autocorrelation function of the late subsample | 132 |
| 6.11 | The amplitude of the early-late cross-correlation function | 133 |
| 6.12 | The distribution of the UBR -selected AGN sample | 133 |
| 6.13 | Absolute magnitudes of the UBR -selected AGN sample | 134 |
| 6.14 | The AGN-early subsample angular cross-correlation function | 137 |
| 6.15 | The AGN-late subsample angular cross-correlation function | 137 |
| 6.16 | The cross-correlation of AGN with all galaxies | 138 |
| 6.17 | The amplitude of the AGN-early angular cross-correlation function | 138 |

| | | |
|------|--|-----|
| 6.18 | The amplitude of the AGN-late cross-correlation function | 139 |
| 6.19 | The AGN-early angular cross-correlation function with photometric z constraints | 141 |
| 6.20 | Comparison of AGN-early cross-correlation with and without photometric z constraints | 141 |
| 6.21 | The amplitude of the AGN-early cross-correlation function with photometric redshift constraints applied | 142 |
| 6.22 | The distribution of AGN-early pairs with separations less than $56''$ | 143 |
| 6.23 | B_J -band images of AGN with excess AGN-galaxy pairs | 145 |
| 6.24 | R -band images of AGN with excess AGN-galaxy pairs | 146 |
| 6.25 | The amplitude of the AGN-early cross-correlation without the 4 AGN from Table 6.7 | 147 |
| 6.26 | R band images of AGN within $20''$ of NVSS sources | 149 |
| 6.27 | The amplitude of the Seyfert 1 and QSO cross-correlation functions | 150 |
| 6.28 | The amplitude of the AGN-early cross-correlation function for $0.3 < z < 0.5$ and $0.5 < z < 0.7$ AGN | 151 |
| 6.29 | The median absolute magnitude of early subsample galaxies which satisfy the photometric redshift constraints with the $0.3 < z < 0.7$ AGN sample | 151 |
| 7.1 | Estimated errors of NVSS positions as a function of flux | 155 |
| 7.2 | FIRST and R band images of radio galaxy candidates | 156 |
| 7.3 | Distribution of projected distances between optical and radio sources | 157 |
| 7.4 | The distribution of radio galaxies | 158 |
| 7.5 | Comparison of photometric and spectroscopic redshifts of galaxies matched to the NVSS | 159 |
| 7.6 | Hubble diagrams of $B_J < 23.5$ radio-galaxies in the Panoramic Deep Fields | 161 |
| 7.7 | Hubble diagrams of control objects | 161 |
| 7.8 | Redshift distributions of radio galaxies and control objects | 162 |
| 7.9 | Colours of radio galaxies as a function of photometric redshift | 163 |
| 7.10 | The colours of the control sample as a function of photometric redshift | 163 |
| 7.11 | The colours of Dunlop <i>et al.</i> (1989) radio galaxies as a function of redshift | 164 |

| | | |
|------|--|-----|
| 7.12 | The distribution of the difference of the $B_J - R$ colours of the radio galaxy sample and the colour selection criteria. | 164 |
| 7.13 | The restframe $B_J - R$ colours of the radio galaxy sample | 165 |
| 7.14 | The restframe colours of Govoni <i>et al.</i> (1989) radio galaxies | 165 |
| 7.15 | The luminosity function of radio galaxies detected in the Panoramic Deep Fields | 167 |
| 7.16 | The luminosity function of radio galaxies at the current epoch | 170 |
| 7.17 | The distribution of radio galaxy-galaxy pairs with separations less than $56''$ | 172 |
| 7.18 | The angular cross-correlation function of radio galaxies with the early subsample. | 175 |
| 7.19 | The cross-correlation function of $B_J < 23.5$ radio galaxies and late type galaxies | 175 |
| 7.20 | The angular cross-correlation function of $B_J < 23.5$ radio galaxies with all galaxies. | 176 |
| 7.21 | The amplitude of the angular cross-correlation function of radio galaxies with early subsample galaxies | 177 |
| 7.22 | The amplitude of the angular cross-correlation function of radio galaxies with the late subsample | 177 |
| 7.23 | The amplitude of the angular cross-correlation function of radio galaxies and all galaxies | 178 |
| 7.24 | The amplitude of the angular cross-correlation function of $0.10 \leq z < 0.30$ radio galaxies and early subsample galaxies. | 179 |
| 7.25 | The amplitude of the angular cross-correlation function of $0.30 \leq z < 0.55$ radio galaxies and early subsample galaxies. | 179 |
| 7.26 | The amplitude of the angular cross-correlation function of $P(0) > 10^{24.0} \text{WHz}^{-1}$ radio galaxies and early subsample galaxies. | 181 |
| 7.27 | The amplitude of the angular cross-correlation function of $P(0) < 10^{24.0} \text{WHz}^{-1}$ radio galaxies and early subsample galaxies. | 181 |

Chapter 1

Introduction

1.1 Wide Field Surveys

Wide field surveys are an extremely powerful tool for determining the large-scale structure and evolution of the universe. The ability of these surveys to compile large catalogues of objects ($\sim 10^6$) allows the accurate measurement of astronomical phenomena with high statistical certainty. This is not possible with narrow “pencil-beam” surveys (field-of-view $\lesssim 10'$) which contain small numbers of objects and may be biased by individual structures such as galaxy clusters.

Historically, most wide field surveys have been based on photographic plates taken with Schmidt Telescopes (e.g. POSS-I). The results of these surveys have often been determined by visual searches for objects (e.g. The Abell Catalogue, Abell 1958) which can result in biases. Machine measurements of photographic plates (Kibblewhite *et al.* 1984, MacGillivray & Stobie 1984) can remove errors associated with visual searches of plates and be used to uniformly select objects over wide survey areas. However, single photographic plates have a non-linear response to photon counts, background variations, limited depth ($B_J \sim 22$) and cosmetic flaws.

CCD cameras provide a solution to many of the problems encountered with photographic plates. They have high quantum efficiency, linear response to photon counts and their cosmetic flaws are comparatively easy to remove from the data. While several wide field CCD surveys are in progress (SDSS, ESO Imaging Survey, Millennium Galaxy Catalogue), they have smaller survey areas than photographic surveys or are several years from completion. This is due to the $\lesssim 1^\circ$ field-of-view of current CCD mosaics which is considerably smaller than the $6^\circ \times 6^\circ$ field-of-view of photographic plates from the UK or Palomar Schmidt Telescopes.

Optimally, for wide field surveys one would want a field-of-view comparable to a Schmidt plate with a linear detector.

The coaddition of scans of photographic plates can be used to obtain deep imaging of wide fields with many of the characteristics normally associated with CCD imaging. For sky-limited plates, the response to intensity is approximately linear near the sky background (Bland-Hawthorn, Shopbell & Malin 1993, Knox *et al.* 1998). It is therefore possible to coadd scans of photographic plates to obtain deeper images. Since the same techniques can be used to coadd CCD images and plate scans (Schwartzberg, Phillipps & Parker 1996, Chapter 2), it is possible to apply bad-pixel rejection algorithms to remove cosmetic flaws which are typically found in individual plate scans.

1.2 Digital stacking of Photographic Material

It has only been practical to stack digitised photographic scans since the 1980s when computing power and disk space made it practical to process images larger than 1Gb. Most stacks documented in the literature are summarised in Table 1.2. All have used photographic material (plates or films) from the UK Schmidt Telescope. While the field-of-view of individual scans is $6^\circ \times 6^\circ$, most stacks have used smaller areas due to limits imposed by disk space or software used to process the data.

Most stacks in Table 1.2 have been used to study low surface brightness objects or to select stellar and quasi-stellar objects using colour selection criteria. This takes advantage of the improved signal-to-noise and wide field-of-view of stacked plates while not being compromised by the low resolution ($\geq 2.5''$) of photographic material. While faint $z > 0.1$ galaxies dominate stacked Schmidt plates, only McNally, Peacock & Hawkins (1995) have attempted to measure galaxy angular correlation function using the Hawkins (1994, 1995) B_J stack. The capability of stacked plates to compile large, deep, multicolour galaxy catalogues has not been explored by previous work.

1.3 Galaxy Clustering

Correlations between galaxy properties and clustering are well established (Davis & Geller 1976, Loveday *et al.* 1995) but the physical processes responsible for

Table 1.1: A Sample of Recent Wide Field Optical Surveys

| Survey | Magnitude Limits | Area (\square°) | Telescope Aperture | Material |
|--|-------------------------------------|-----------------------------|-----------------------|----------------|
| Couch <i>et. al</i> (1990) | $B_J \simeq 24.4, R_F \simeq 22.9$ | ~ 80 | 3.9m | Plates |
| DSS 1 | $B_J \sim 20.5$ | All Sky | 1.2m | Scanned Plates |
| DSS 2 | $R \sim 21.5$ | All Sky | 1.2m | Scanned Plates |
| EIS Wide | $I \simeq 23.0$ | 24 | 3.6m | CCD |
| Gunn, Hoessel & Oke (1986) | Various | 154.7 | 1.2-5m | Plates |
| Maddox <i>et al.</i> (1990) | $B_J \sim 22$ | 4300 | 1.2m | Scanned Plates |
| Millennium Galaxy Catalogue [†] | $B \sim 24$ | 30 | 2.5m | CCD |
| Postman <i>et. al</i> (1998) | $I \simeq 24$ | 16 | 4m | CCD |
| SDSS [†] | $g \sim 22.5, r \sim 22.3, u, i, z$ | 10000 | 2.5m | CCD Drift Scan |
| SDSS (Southern Strip) [†] | $g = 25.3, r = 25.1, u, i, z$ | 225 | 2.5m | CCD Drift Scan |
| Zaritsky <i>et. al</i> (1997) | $I \simeq 22.5?$ | 140 | 1.5m | CCD Drift Scan |
| † In progress | | | | |

Table 1.2: Stacks of Scanned Plates/Films

| Reference | Magnitude Limits | Area (\square°) | Number of Plates | Pixel Scale |
|---|---------------------|-----------------------------|---------------------|----------------|
| Hawkins (1994, 1995) | $B_J \geq 24.0$ | 25 | 65 | $1.1''$ |
| Hawkins (1994, 1995) | $R \geq 22.5$ | 25 | 65 | $1.1''$ |
| Hawkins (1994, 1995) | $I \geq 20.5$ | 25 | 30 | $1.1''$ |
| Hawkins (1994, 1995) | $U \geq 22.5$ | 25 | 7 | $1.1''$ |
| Hawkins (1994, 1995) | $V \geq 21.0$ | 25 | 3 | $1.1''$ |
| Katsiyannis <i>et al.</i> (1998) | $R \sim 22.5$ | 38 | 13 | $2.0''$ |
| Kemp & Meaburn (1995) | $B_J \sim 23.5?$ | 16 | 8 | $2.0''$ |
| Knox <i>et al.</i> (1998) | $B_J \leq 23.5$ | 0.06 | ≤ 16 | $0.7''$ |
| Knox, Hawkins & Hambly (1999) | $B_J \sim 22.5$ | 38 | 4×4 | $0.7''$ |
| Knox, Hawkins & Hambly (1999) | $R \sim 21.2$ | 38 | 4×4 | $0.7''$ |
| La Franca <i>et al.</i> (1999) | $U \sim 22.0$ | 38 | 3 | $1.1''$ |
| La Franca <i>et al.</i> (1999) | $B_J \sim 23.0$ | 38 | 5 | $1.1''$ |
| La Franca <i>et al.</i> (1999) | $R \sim 21.5$ | 38 | 5 | $1.1''$ |
| Marston (1988) | $B_J \sim 23.5?$ | 1 | 8 | $1.7''$ |
| Schwartzzenberg, Philipps & Parker (1996) | $R \sim 22.5$ | 2 | 6 | $0.7''$ |
| Panoramic Deep Fields | $U \sim 22$ | ~ 50 | 2 & 5 | $0.7''$ |
| Panoramic Deep Fields | $B_J \sim 23.5$ | ~ 50 | 9 & 13 | $0.7''$ |
| Panoramic Deep Fields | $R \sim 22$ | ~ 50 | 8 & 24 | $0.7''$ |
| Panoramic Deep Fields | $I \sim 20$ | ~ 50 | 5 & 10 | $0.7''$ |

the correlations are poorly understood. At low redshift, the correlation between galaxy clustering and morphology has been known for several decades (Davis & Geller 1976). The strong clustering of red early-type galaxies is not unexpected as they are typically more massive than field galaxies but it is also plausible that rich environments change the colours and morphologies of galaxies (Barger *et al.* 1996, Baugh, Cole & Frenk 1996, Poggianti *et al.* 1999). As colour and morphology both depend on the galaxy evolution, it is useful to measure galaxy environments as a function of these properties to constrain models of galaxy formation and evolution. Colour provides information on stellar populations and dust extinction which are related to the history of star formation within a galaxy (Tinsley 1978, Barger *et al.* 1996). Morphology, generally a classification derived from the projected distribution of observed optical emission from a galaxy, does provide information on the evolution of galaxies (Ellis 1998). However, the physical processes which produce the observed galaxy morphological types are not well determined (Ellis 1998). Previous studies have not determined whether galaxy stellar population or morphology is the property primarily correlated with galaxy environment.

The evolution of galaxy clustering is strongly influenced by the process of galaxy formation (Frenk *et al.* 1990, Baugh *et al.* 1999). For this reason, there have been numerous studies of $z \gtrsim 0.1$ galaxies which attempt to measure the evolution of the clustering (e.g. Maddox, Efstathiou & Sutherland 1996, Brunner, Szalay, & Connolly 2000). Most galaxy catalogues have been selected with flux limits in a single band, so morphology and colour information are not available. The estimates of the clustering at $z \gtrsim 0.2$ are strongly dependent on the selection criteria used and I band selected catalogues measure significantly stronger clustering than B band selected catalogues. As early-type galaxies have large k -corrections, deep B band images are dominated by late-type galaxies which are weakly clustered at $z \sim 0$. However, the observed clustering of $B > 22$ galaxies is weaker than the clustering of any morphologically selected population of galaxies at low redshift (Efstathiou *et al.* 1991, Brown, Webster & Boyle 2000).

The process of galaxy formation and evolution is often studied in the cluster environment as clusters are readily identified and observed over a large range of redshifts. Also, unlike field galaxies, redshifts are not required for each cluster member to estimate its distance and therefore its intrinsic properties. While this has allowed the detailed study of small samples of $0.3 \lesssim z \lesssim 1.0$ clusters (Postman, Lubin & Oke 1998, Poggianti *et al.* 1999), the space density and clustering

properties of $z > 0.1$ clusters are not well determined. The space density and clustering properties are predicted by models of galaxy and cluster formation (Kaiser 1986, Jenkins *et al.* 1998) but it has been difficult to constrain these properties as deep wide fields are required to obtain suitable cluster catalogues.

1.4 AGN Evolution and Environments

Evolution of the radio-loud AGN is required to explain the observed sky-density and redshift distribution of radio sources (Condon 1984, Peacock 1985). The evolution of the radio galaxy luminosity function is comparable to the evolution of optically selected AGN (Dunlop & Peacock 1990, Rowan-Robinson *et al.* 1993) and it is plausible the same physical processes are responsible for the evolution of the optical and radio AGN luminosity function. However, measurements of the space density of radio galaxies have generally relied on small samples of objects or redshifts derived from K band photometry so constraints on the evolution are poor.

The environments of Active Galactic Nuclei (AGN) have been studied for several decades to determine whether AGN occur in particular galaxy environments (Bahcall, Schmidt & Gunn 1969). Several studies of AGN have detected environments richer than the field (e.g. Yee & Green 1987). Radio-loud AGN in particular appear to be found in rich environments similar to galaxy clusters (Yee & Green 1987, Prestage & Peacock 1988). However, as radio galaxies and many $M_B \sim -22$ radio-quiet AGN hosts have early-type morphologies (Matthews, Morgan & Schmidt 1964, McLure *et al.* 1999, Schade, Boyle & Letawsky 2000, Urry *et al.* 2000), it is not unexpected that AGN occur in environments richer than the field. At present, it is not clear if AGN hosts have the same clustering properties as other galaxies with similar morphologies or if they occur in unusually rich environments.

If there is a correlation between AGN luminosity and environment, then the rapid evolution of the AGN luminosity function may be caused by rapid evolution of the AGN environment. Several studies of radio-loud AGN find AGN occur in increasingly rich environments with redshift (Yee & Green 1987, Hill & Lilly *et al.* 1991, Wurtz *et al.* 1997) but the statistical detection of evolution often relies on the signal from $\lesssim 5$ AGN.

While there have been several studies of the environments of radio-quiet AGN

at intermediate redshifts (e.g. Ellingson, Yee & Green 1991, Smith, Boyle & Maddox 2000), there is little consistency between estimates of the AGN environment at $z > 0.3$. This is due to the small numbers of AGN used to study the $z \gtrsim 0.3$ AGN environment and the estimates of the angular cross-correlation function being dominated by unassociated galaxies along the line-of-sight. In addition, studies of the AGN environment suffer the same problems as studies of the galaxy environment. In particular, deep images are often dominated by weakly clustered late-type galaxies so a small signal (and signal-to-noise) is not unexpected.

1.5 Overview of thesis

This thesis describes the construction, calibration and application of a deep wide-field multicolour catalogue, the Panoramic Deep Fields. Chapters 2 and 3 describe the construction and calibration of the Panoramic Deep Fields. Comparisons of object classifications, astrometry and photometry with published catalogues are also discussed in Chapters 2 and 3.

Chapters 4 and 5 present estimates of the galaxy and cluster environment from $z \sim 0.4$ until the current epoch. In Chapter 4, the clustering of galaxies is measured as a function of colour and selection criteria are used to measure the same population of galaxies as a function of redshift. In Chapter 5, a catalogue of distant clusters is constructed to measure the space density and distribution of clusters.

The environments of *UBR* selected AGN and radio galaxies at $z \sim 0.5$ are measured in Chapters 6 and 7. Chapter 7 also describes the construction of a deep catalogue of uniformly selected radio galaxies which are used to measure the evolution of radio galaxies. Photometric redshifts and colour selection criteria are used to improve the signal-to-noise of estimates of the AGN environment. The colour selection criteria are also used to measure the cross-correlation with particular galaxy types and to measure the evolution of AGN environments.

Chapter 2

Digital Stacking

The digitisation of photographic material offers clear advantages for quantitative analysis of images. It allows accurate calibration and parameterisation of survey data and individual scans can be added for faint object searches (Marston 1988, Schwartzenberg 1996, Hawkins *et al.* 1998). Image detection and classification can also be automated, removing many of the biases of manually selected catalogues. This has already been achieved with CCD imaging, but digital stacking is still a relatively new technique with photographic plates. Digital stacking of plate scans offers 2 clear advantages over deep CCD imaging: efficient use of telescope time for wide field imaging (Bland-Hawthorn, Shopbell & Malin 1993) and the use of archival material (Hawkins *et al.* 1998, Knox *et al.* 1998).

A serious disadvantage of photographic material is that its response to light is non-linear. However, over a limited dynamic range the response of the photographic material is approximately linear (Bland-Hawthorn *et al.* 1993, Knox *et al.* 1998). For sky limited plates the linear regime includes the sky background and faint images, allowing the stacking of digital scans to achieve deep limiting magnitudes.

2.1 Plate material

The plates used to produce the Panoramic Deep Fields have been taken for a range of projects since the late 1970s. All exposures were approximately centred on B1950.0 $00^h53' -28^{\circ}03'$ (the SGP) or $10^h40' 00^{\circ}00'$ (F855). Exposures were sky-limited and have exposure times between 60 and 100 minutes. Lists of the plates used for the digital stacking are provided in Table 2.1. The filter and emulsion combinations used for each of the bands are listed in Table 2.1.

Table 2.1: UKST plates used for the Panoramic Deep Fields. Details of the plate quality and exposure times can be found at the online UKST Plate Catalogue (www.aao.gov.au).

| Field | Band | Plates |
|-------|-------|--|
| SGP | U | U6326, U6380 |
| SGP | B_J | J3497, J3554, J9764, J9765, J9766, J9770, J9771, J13857, J14605 |
| SGP | R_F | R4676, OR9563, R9594, OR9595, OR9671, R9672, R11336, OR16297 |
| SGP | I | I4338, I6523, I10545, I10604, I10615 |
| F855 | U | UX7709, UX7714, UX9173, UX16600, UX16932 |
| F855 | B_J | J6800, J6954, J7743, J9241, J9309, J16076, J17417, J17477, J17916, J17917, J17921, J17929 |
| F855 | R_F | OR10854, OR12420, OR12489, OR13020, OR14220, OR15308, OR15323, OR15330, OR15357, OR17061, OR17089, OR17412, OR17429, OR17561, OR17863, OR17874, OR17501, OR17504, OR17506, OR17507, OR17536, OR17550, OR17879, OR17911 |
| F855 | I | I6910, I17448, I17460, I17478, I17518, I17521, I17521, I17523, I17528, I17541 |

Table 2.2: Filter and Emulsion combinations used in the Panoramic Deep Fields

| Plate Prefix | Band | Emulsion | Filter | Fields |
|--------------|-------|---------------|--------|------------|
| U | U | IIIaJ | UG 1 | SGP |
| UX | U | IIIaJ or 4415 | UG 1 | SGP & F855 |
| J | B_J | IIIaJ | GG 395 | SGP & F855 |
| OR | R | IIIaF | OG 590 | SGP & F855 |
| R | R | IIIaF | RG 630 | SGP |
| I | I | IVN | RG 715 | SGP & F855 |

2.2 SuperCOSMOS scans

The SuperCOSMOS machine at Royal Observatory Edinburgh is a plate scanning machine capable of scanning an entire UKST plate in 2 hours, producing 2.1 Gb of data. The SuperCOSMOS scans have $15\mu\text{m}$ resolution with $10\mu\text{m}$ pixels (Hambly & Miller 1997) with the corresponding pixel scale for UKST plates being $0.67''$. As stellar images from the UKST have FWHM of $\geq 2.5''$, the data is adequately sampled. More detailed discussions of the SuperCOSMOS plate scanning machine are provided by Miller *et al.* (1992) and Hambly (1998).

The pixel data for each plate was provided in 16 subregions (before 1999) or in large 2.1 Gb files. The data has been converted from the SuperCOSMOS “lane” format into FITS files by Nigel Hambly’s `mm2fits` fortran code. This code also converts the data from measured plate scan transmissions into approximate arbitrary intensities using the equation

$$\text{Log}_{10}i = \gamma \text{Log}_{10} \left(\frac{t_c - t_b}{t - t_b} + c \right), \quad (2.1)$$

where i and t are the intensity and transmission. The transmission constants t_c and t_b correspond to the maximum and minimum possible transmissions while c and γ are parameters which describe the nonlinear response of transmission to intensity. The resulting values of i have a linear response to intensity near the

sky background. The data has also been regridded with respect to a “master” plate so images on each plate are accurately aligned.

2.3 Data Reduction

2.3.1 Background Subtraction

Before coaddition of the data, background subtraction must be performed. Unless this is done, the local sky background for each image on each plate will differ, resulting in suboptimal performance of bad pixel rejection and coaddition algorithms. While vignetting introduces the largest variation of background, the most problematic variations of the background are introduced by plate fogging and plate flaws. If background subtraction is not performed, the flaws may not be rejected by the bad pixel rejection algorithm as the difference between the sky background on each plate may be larger than the pixel values of the plate flaws. An example of a serious flaw in a coadded image produced with bad pixel rejection but with poor background subtraction is shown in Figure 2.1.

The most obvious method of mapping the background is to use a large scale median filter. This method is accurate for regions without bright stars but it is extremely CPU intensive. Producing a 256×256 pixel median filter of a 6800×6800 pixel image uses approximately 7 hours of CPU time on a SparcUltra 5 (Bryn Jones private communication). As a scan of a single UKST plate is 32256×32256 pixels, the time required to produce a median map would be several days.

A method of speeding up the background mapping using a median filter is to only calculate a value for small regions rather than for every pixel. The approximate median can also be calculated from only a fraction of the pixels within the large scale filter rather than every pixel. This method reduces the CPU time required by more than an order of magnitude. Calculating the background for 32×32 pixel regions using a median filter sampling every 4th pixel reduces the CPU time required by almost 2 orders of magnitude. This allows the background map (with a 160×160 filter) of an entire UKST plate to be produced in less than 2 hours. The filter will degrade the images of objects comparable to or larger than the filter size. However, almost all the object images larger than the filter size are brighter than $B_J \sim 16$ and are not included in the galaxy samples used in Chapters 4 to 7. Another minor flaw with this method is that it does not handle

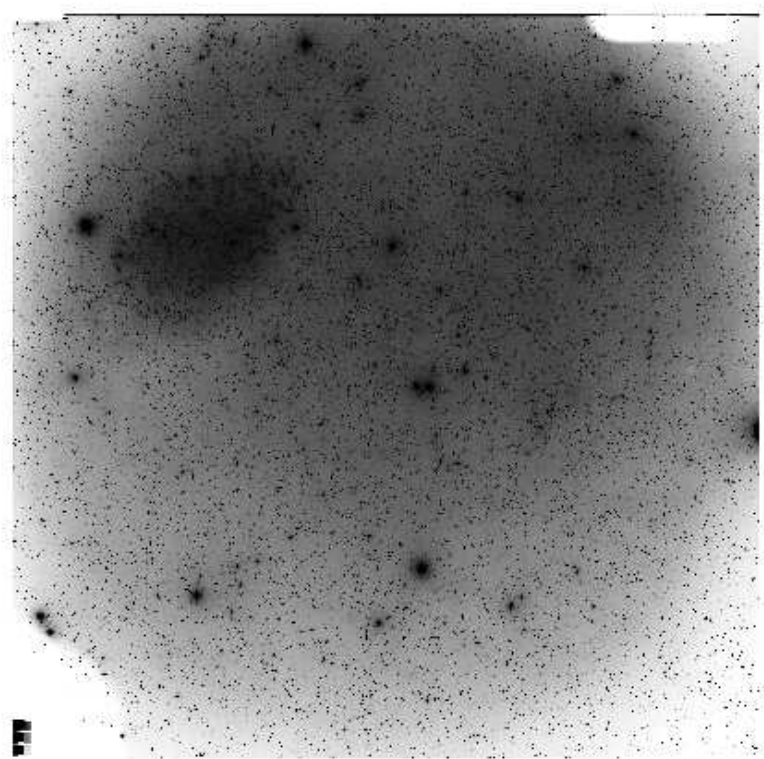


Figure 2.1: A coadded stack where proper sky subtraction has not been applied. The vignetting at the edges of the plate is obvious. A large flaw can also be seen towards the top left of the image.

steep gradients which are found near bright stars. However, these regions of the plate are typically of low quality and would not be used even with a more robust background subtraction. Once the background map has been determined, it is subtracted from the original image.

2.3.2 Drilling

A small number of large ($\geq 100 \times 100$ pixel) plate flaws are rescaled by the background subtraction resulting in poor bad pixel rejection and artifacts in the stacked data. To prevent this occurring, these regions are removed manually (drilled) with IRAF's¹ `imreplace` task to replace flawed regions with pixel values of -10000 . This is well below the pixel values of good data and the flawed regions can be rejected during the stacking by setting the low threshold option of IRAF's `imcombine` task to $\gg -10000$ and $\ll 0$. With stacks of more than 5 plates the increase in background noise in the effected regions is less than $\sim 10\%$.

2.3.3 Intensity Scaling

Before coaddition can take place, the images must be scaled such that the measured intensities of the objects in each plate are approximately equal. To do this a multiplicative scaling is applied to the images once the background has been subtracted. To determine the rescaling required, the fluxes of objects within a central 2000×2000 pixel region are determined using SExtractor (Bertin & Arnouts 1996). Only objects with signal-to-noise ratios between 10 and 30 are used for the scaling to prevent noise and saturated objects biasing the scaling factor. The flux ratios between each object and the same object on a master plate are then determined. The multiplicative scalings are then determined from the median of flux ratios.

2.3.4 Coaddition

Several coadditions of the SGP and F855 plate data have been performed by the SuperCOSMOS group which are deeper than single plate scans but do suffer significant flaws. The original stack of the SGP used an unweighted average

¹IRAF is distributed by the National Optical Astronomy Observatories, which are operated by the Association of Universities for Research in Astronomy, Inc., under cooperative agreement with the National Science Foundation.

of data in transmission space which results in increased depth but does not reject plate flaws, satellite trails and other features which appear in single plates. This is a particular problem for automated measurements of galaxy clustering where small errors may significantly effect measurements of two-point correlation function. Flaws overlapping object detections can alter magnitudes, colours and classifications resulting in increased contamination of catalogues.

Knox *et al.* (1998) describe several techniques for the coaddition of SuperCOSMOS scans of UKST plates. They use a 300×300 pixel region of 16 plate scans to test the techniques and find a weighted average with average sigma clipping results in high signal-to-noise and good bad-pixel rejection for a stack of 16 plate scans. However, only the F855 field has more than 16 scans in a single band (R) and average sigma clipping is poor at rejecting noise for small number of plates. Also, the use of a small region allows a single value for the background to be used for each scan rather than having to produce a larger background map for the entire field. If single values of the background are used for large regions, the residual variations of the background are comparable to the pixel values of plate flaws.

A stack by the SuperCOSMOS group of the F855 field using the methods of Knox *et al.* (1998) and single sky background values for 32256×1280 pixel regions (corresponding to SuperCOSMOS scan “lanes”) is shown in Figure 2.1. A large plate flaw is clearly visible at the top left despite the use of bad-pixel rejection algorithms. The flaw is broken up into multiple objects as the rejection algorithm works when the flaw has large pixel values and fails for smaller values. If bad-pixel rejection algorithms are to be successfully applied to stacks of plate scans, effective background subtraction is required.

SuperCOSMOS scans of TechPan films have been stacked by Schwartzberg (1996) with the aim of detecting low surface brightness galaxies. He used a 256×256 pixel median filter to subtract the background on each plate with the median stacking in “intensity” space to produce the final image. The “intensity” space described in Schwartzberg (1996) is actually equal to the density subtracted from the background. This is a very close approximation to intensity space near the sky background and the intensities of low surface brightness galaxies. Schwartzberg used median stacking as the depth achieved is similar to average stacking but with more robust bad pixel rejection than sigma-clipping for the small number of plates used.

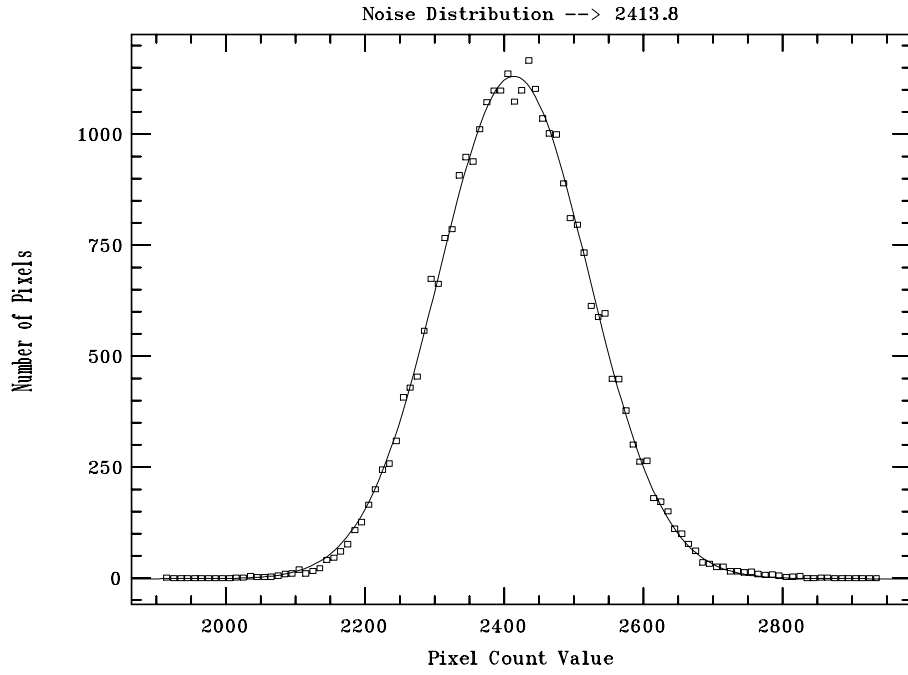


Figure 2.2: Noise distribution of a region of plate I17448 without obvious sources. A Gaussian fit to the distribution is shown by the line. The plot was generated using IRAF's `imhist` and `fgauss` routines.

Table 2.3: Stacking Methods

| Method | Noise (pixel values) | Bad pixel Rejection | Cosmetics (e.g. satellite trails) |
|-----------------|-------------------------|------------------------------|--------------------------------------|
| SuperCOSMOS | 134.7 | Av. Sigma Clip (3σ) | Yes |
| Weighted mean | 145.1 | min-max (3,3) | No |
| Weighted mean | 144.5 | Sigma Clip (2σ) | No |
| Unweighted mean | 150.1 | min-max (2,2) | No |
| Weighted mean | 135.5 | none | Yes |
| Median | 163.6 | none | No |

Several methods for stacking SuperCOSMOS scans were compared to evaluate their effectiveness. The sample of data used was the F855 B_J band data which consists of 12 plate scans. The results are summarised in Table 2.3. All stacking methods have had intensity scaling performed to the original data. The weighted mean minimises the noise in a stack of n scans by weighting the i -th scan by

$$\omega_i = \frac{1/\sigma_i^2}{\sum_{j=1}^n 1/\sigma_j^2}, \quad (2.2)$$

where σ_i is the background noise. The ability of each stacking method to remove plate flaws and other spurious objects was determined by manually comparing single plate scans and the stacked data (see Figure 2.3). The weighted mean with min-max rejection and sigma clipping provides good signal to noise and robust bad pixel rejection. The min-max rejection was chosen for the Panoramic Deep Field stacks as it is effective for small numbers of plates. The F855 B_J stack with sky subtraction and min-max rejection, shown in Figure 2.4, is a significant improvement on the original stack shown in Figure 2.1.

Bland-Hawthorn, Shopbell & Malin (1993) and Knox *et al.* (1998) state that the noise distribution in intensity space may not be Poissonian due to the non-linear relationship between photographic density and intensity. To determine if

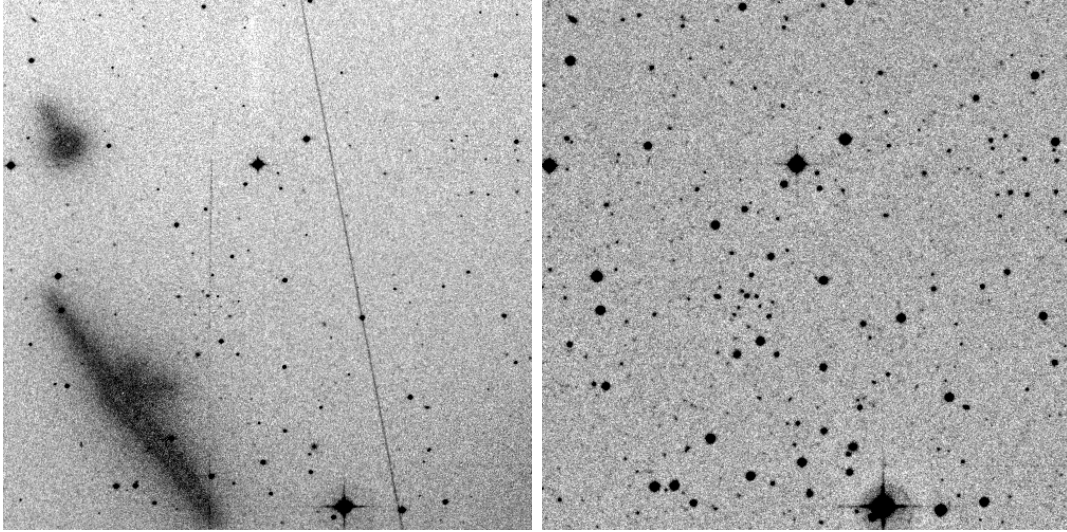


Figure 2.3: A comparison of a single plate scan (J6954) and a stack of the same 1000×1000 pixel region. The stack uses a weighted average with min-max rejection. The single plate scans shows a significant gradient in the sky background, plate flaws and a satellite trail. The stacked data is considerably deeper and no contamination from J6954 is in the stacked data set.

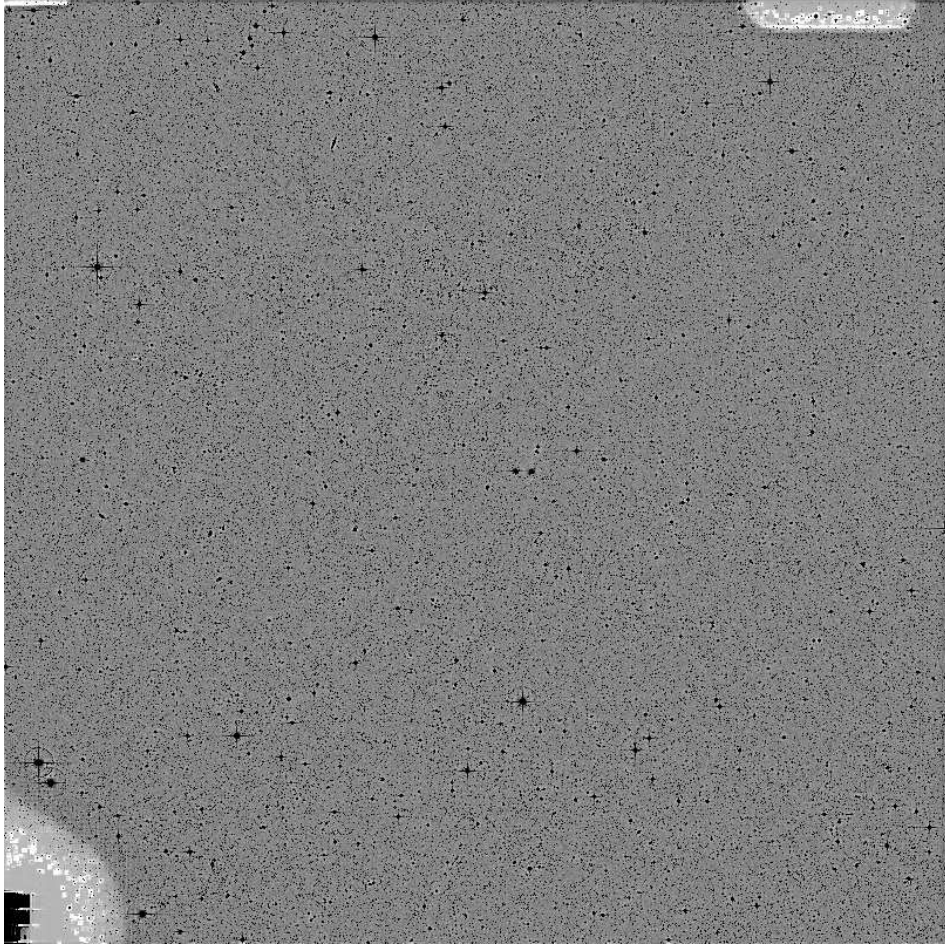


Figure 2.4: A coadded stack where sky background subtraction and min-max bad pixel rejection have been applied. The stack uses the same set of plates as Figure 2.1. The image has been scaled so black and white are $\geq 2\sigma$ above and below the sky background. While the image scaling will make plate flaws more obvious than in Figure 2.1, there are no plate flaws and the sky background is constant over most of the field-of-view.

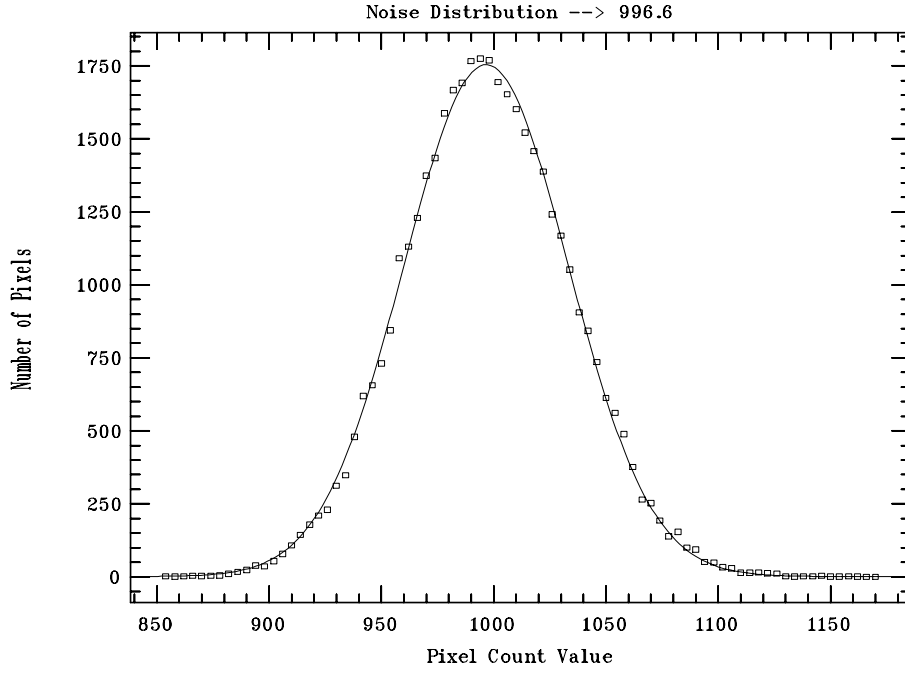


Figure 2.5: Noise distribution of a region of the *I* band stack using a weighted mean with min-max rejection. The line is a Gaussian fit to the distribution. The location of the peak is slightly less than 1000 due to the background subtraction overestimating the background on all the original plates.

this is the case, the noise distribution of single plates was measured and then fitted with a Gaussian, as shown in Figure 2.2. It can be clearly seen that the noise distribution is fitted extremely well by a Gaussian implying that the noise distribution in intensity space is accurately modelled by a normal distribution. Therefore, stacking in intensity space should not result in a large systematic errors.

To determine if any significant bias has been introduced stacking of the scans in intensity space, the noise distribution has been plotted in Figure 2.5. To prevent a spike in the noise distribution caused by `imcombine` converting floats to integers by rounding towards zero, the subtracted background of each scan was increased from 0 to 1000 before stacking. The noise distribution is fitted well by a Gaussian though the peak of the function is slightly offset from 1000. This is seen in all the images and the offset is $\lesssim 5\%$ of the background noise of the stacked scans. The overestimate of the background is not unexpected as the estimate of

Table 2.4: Stellar FWHM estimates determined with unsaturated stellar objects

| Field | Stellar FWHM | | | |
|-------|--------------|-------|-------|-------|
| | U | B_J | R | I |
| SGP | 2.9'' | 3.1'' | 2.9'' | 2.9'' |
| F855 | 2.8'' | 3.0'' | 2.7'' | 2.7'' |

Table 2.5: Limiting magnitudes estimated with 5σ detections within a 2.8'' radius aperture.

| Field | Detection thresholds | | | |
|-------|----------------------|-------|------|------|
| | U | B_J | R | I |
| SGP | 22.7 | 23.9 | 22.7 | 20.4 |
| F855 | 22.6 | 23.7 | 22.9 | 20.8 |

the background is derived from the data which includes stars and galaxies. As the overestimate of the background depends on the sky surface density of sources, the overestimate is the same for all scans of the same region in the same band. Therefore, the overestimate of the background does not cause a significant error in the stacking of the data.

Tables 2.4 and 2.5 summarise the stellar FWHM and limiting magnitudes of the stacked scans. Calibration of the photometry used to determine the limiting magnitudes is discussed in Chapter 3. The seeing in all the stacks is $\sim 2.8''$ which is comparable to the seeing in the single plate scans. The depth of the data has been significantly improved by stacking the scans and the limiting magnitudes are $\gtrsim 1$ magnitude deeper than single scans.

2.4 Source Extraction

Source extraction was performed using SExtractor (Bertin & Arnouts 1996) version 2.1.16. SExtractor has several advantages over other source extraction codes as it is easy to install, runs reasonably quickly, has reliable image classification (Smith 1998) and documentation. SExtractor is also frequently used for analysis of survey data (Brunner *et al.* 1997, Prandoni *et al.* 1999) and is being regularly upgraded so it is relatively bug free.

Source extraction parameters were set to at least 5 connected pixels with the pixel threshold set to 1.8σ above the local background level. The choice of these parameters provides a deep catalogue without serious contamination, provided there has been effective bad pixel rejection. The choice of pixel connection algorithm has a significant effect on the level of contamination (Irwin 1985). A pixel connection algorithm which connects pixels horizontally, vertically and diagonally results in significantly more contamination than an algorithm which connects pixels horizontally and vertically.

SExtractor connects horizontally and vertically which improves on the COSMOS and SuperCOSMOS image detection software (Beard, MacGillivray & Thanish 1990) which connects diagonally aligned pixels (Hambly private communication). The SuperCOSMOS pixel connection algorithm resulted in the signal-to-noise cutoff being set to a high level ($\sim 8\sigma$) to prevent contamination by spurious objects. The detection of faint spurious objects by COSMOS has been previously noted by Couch *et al.* (1990). The use of a high signal-to-noise threshold is reasonable when detecting sources in SuperCOSMOS scans of single plates where large quantities of signal-to-noise ~ 4 spurious images exist. These images are not present in robustly coadded data and a lower signal-to-noise threshold is therefore appropriate.

The completeness of the SExtractor catalogues as a function of limiting magnitude is shown in Figure 2.6. The completeness was estimated by adding artificial stellar objects to subsets of the data with IRAF's `mkobject` task. SExtractor was then used to compile object catalogue and the fraction of artificial objects detected by SExtractor was measured. The 80% completeness limits of the catalogues are slightly brighter than the limiting magnitudes in Table 2.5 as the estimates in Table 2.5 do not take into account seeing or confusion.

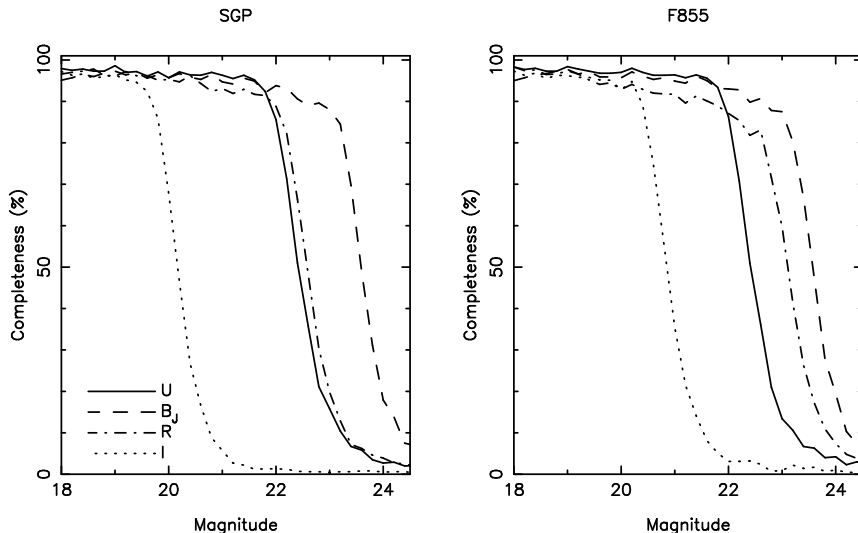


Figure 2.6: The completeness of the SExtractor catalogues as a function of magnitude. The completeness was estimated with stellar objects generated with IRAF’s `mkobject` task.

2.4.1 Astrometry

Accurate astrometry is extremely important if spectroscopic candidates are to be observed by automated instruments such as 2dF. Internal astrometric accuracy of $< 0.5''$ is required for 2dF (Bailey & Glazebrook 1999) if no significant light loss is to occur.

The original SuperCOSMOS image format data contains astrometry for all the objects detected by the SuperCOSMOS software. The stated accuracy of the SuperCOSMOS astrometric solution is $< 0.3''$ (Hambly *et al.* 1998) though larger ($> 1''$) systematic errors have been observed in COSMOS and SuperCOSMOS scans (Savage & Cannon 1995, Hunstead private communication). Systematic errors may originate from the use of bright ($B < 10$) stars from the Hipparcos/Tycho catalogue (ESA 1997) as the basis of the astrometry solution. These stars have diffraction spikes and halos which are detected by the source extraction software resulting in reduced accuracy for image positions. Also, on UKST plates, the halos are only centred on bright stars when they are near the plate centre. This introduces a systematic error as a function of distance from the plate centre. For these reasons, it was decided that a new astrometric solution would be determined.

The astrometric solution is determined with Tycho-2 catalogue stars (Høg *et*

al. 2000) and the **astrom** package. To reduce errors which could be introduced by bright stars and large proper motions, only $B > 12.5$ stars moving less than $0.05''$ per yr are used to determine the solution. The average of the residuals $\sim 0.5''$ though a plot of the residuals as a function of plate position (Figure 2.7) shows the residuals are typically $\lesssim 0.3''$ near the centre of the field.

To determine if there are any significant systematic errors in the astrometric solution, Panoramic Deep Field astrometry has been compared with the APM, FIRST (White *et al.* 1997) and NVSS (Condon *et al.* 1998). Plots of the residuals as a function of position are shown in Figures 2.8 and Figures 2.9. There is good agreement between the APM and Panoramic Deep Field astrometry with residuals typically less than $\sim 0.05''$. The small size of the residuals is not unexpected as the APM derived astrometry is from scans of UK Schmidt plates calibrated with Tycho catalogue stars. Comparison with the FIRST catalogue shows larger residuals and evidence for Panoramic Deep Field astrometry being offset $0.22'' \pm 0.05$ west and $0.07'' \pm 0.05$ south of the FIRST astrometric solution. Comparison of Panoramic Deep Field positions with NVSS sources in Figure 2.10 also shows evidence for small systematic offsets though their significance is $< 3\sigma$. While individual radio sources are often offset from their optical counterparts, it is improbable that there is an alignment of radio sources over the entire field. Systematic errors between optical and radio astrometry are not uncommon (Savage & Cannon 1995) and the offsets presented here are equivalent to a fraction of a pixel in the FIRST, NVSS and Panoramic Deep Field images.

2.4.2 Object Classification

SExtractor uses a neural network for star-galaxy separation which, though somewhat experimental, has been found to be robust (Smith 1998). A detailed description of the neural network scheme used is provided by Bertin & Arnouts (1995). The neural network consists of an input layer, a hidden layer and an output layer. Each layer consists of nodes which are linked to nodes in the other layers by weighted synapses. The input and hidden layers consist of as many nodes as there are input parameters while the output layer consists of a single node which produces the classification output.

The input parameters are 8 isophotal areas, the maximum intensity and the seeing. The weights of each of the synapses was determined by training the network with $\sim 10^6$ artificial stars and galaxies with seeing between $0.025''$ and

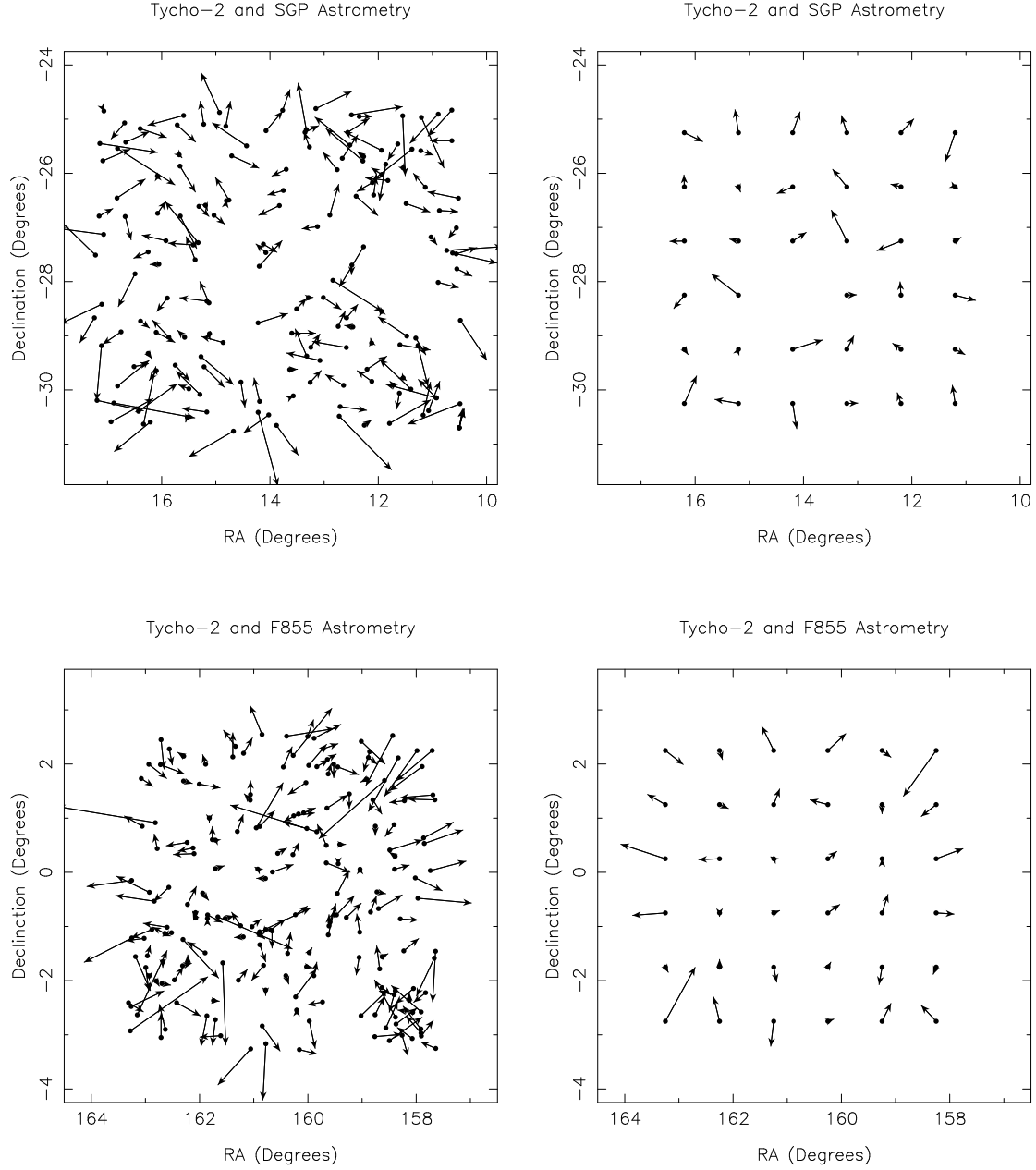


Figure 2.7: Plots of the residuals between the Tycho-2 and Panoramic Deep Field astrometry. The residuals have been multiplied by 3600 for clarity. The left-hand panels show the residuals for individual stars while the right-hand panels show the median of the residuals determined in 1° regions.

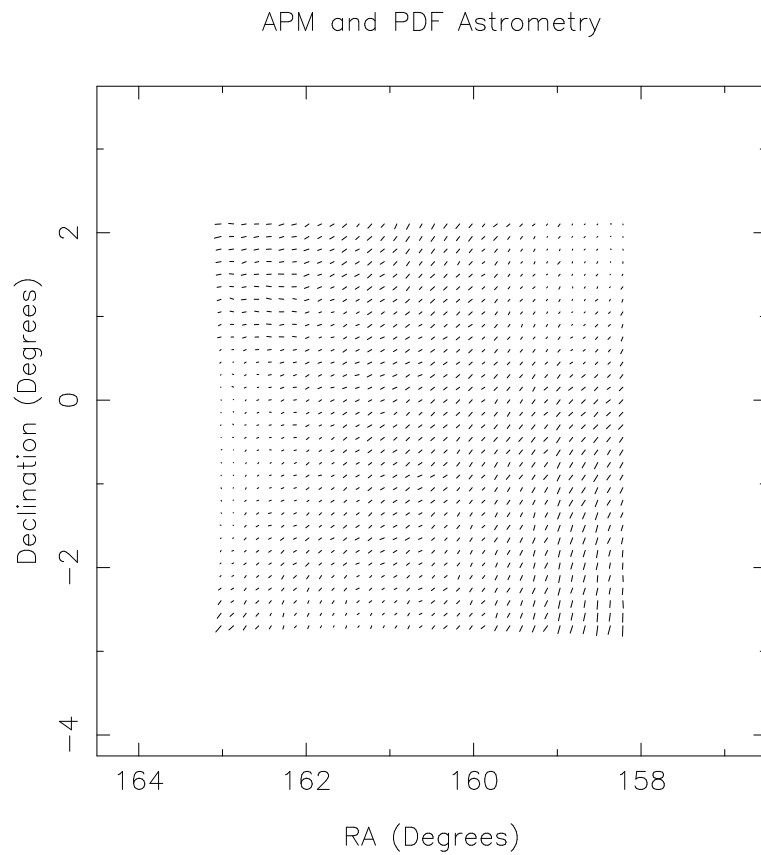


Figure 2.8: The median of the residuals between APM and Panoramic Deep Field astrometry for $10''$ regions. The residuals have been multiplied by 3600 for clarity. There are some systematics as a function of plate position but the residuals are typically $\sim 0.05''$.

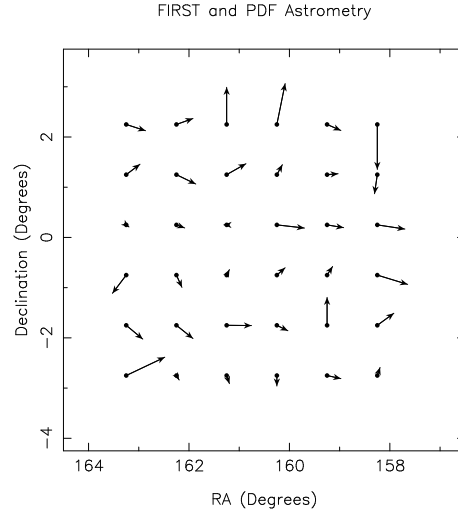


Figure 2.9: The median of the residuals between FIRST and F855 astrometry determined with 1° regions. The residuals have been multiplied by 3600 for clarity. While individual FIRST positions are only accurate to $\sim 1''$, the reference frame used to derive the FIRST positions is accurate to $0.05''$ (White *et al.* 1997).

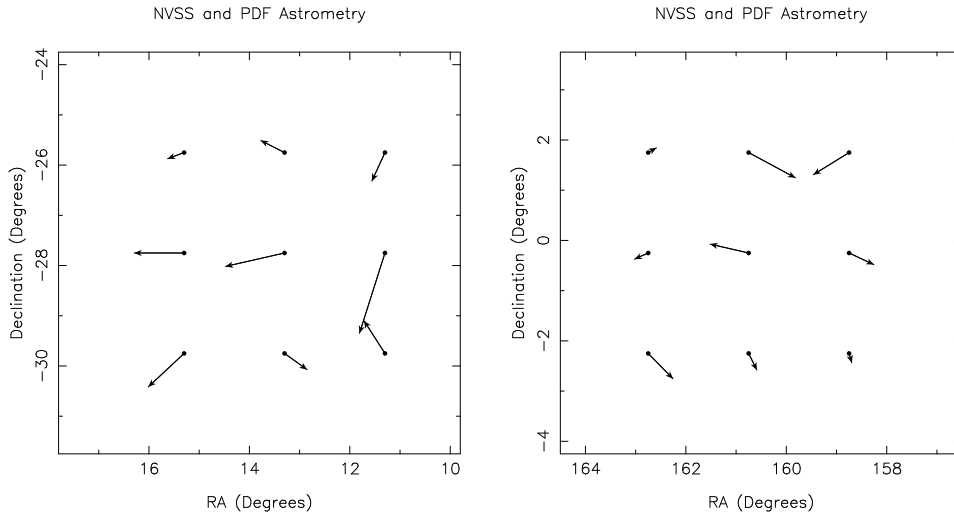


Figure 2.10: The median of the residuals between NVSS and Panoramic Deep Field astrometry with 2° regions. The residuals have been multiplied by 3600 for clarity. Only NVSS point sources with estimated position errors less than $1''$ have been included. The Panoramic Deep Field astrometry is offset from the NVSS by 0.33 ± 0.16 east and 0.42 ± 0.14 south in the SGP and 0.16 ± 0.14 west and 0.39 ± 10.4 south in F855.

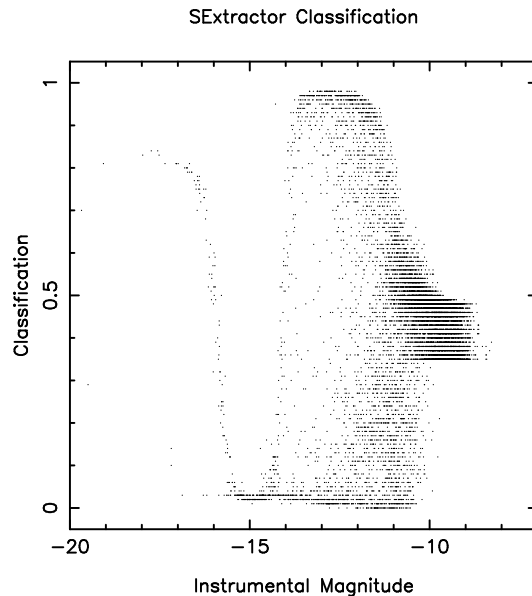


Figure 2.11: SExtractor image classifications as a function of Instrumental magnitude. The dip at instrumental magnitude -15 is due to SExtractor being unable to classify stars outside the linear regime of the plate response. At faint magnitudes the classification scheme breaks down as faint objects have low signal to noise.

$5.5''$. For the sets of artificial objects, the network is run forwards producing a set of outputs. The weights of the synapses are then adjusted layer by layer backward to adjust the outputs towards the correct values. This process is run up to $\sim 10^6$ times until the network is stable. The synapse weights were then saved as it is assumed that the training set of images were representative of galaxies and stars observed by any astronomical telescope with a linear detector.

The star-galaxy classifier was trained on equal numbers of stars and galaxies so the classification can not be directly interpreted as the probability of an object being stellar or non-stellar. The cut-off value must be determined using a comparison with expected number counts, CCD images and faint spectroscopic samples. The reliability of the star-galaxy classification is significantly improved by using classifications in multiple bands. Objects with SExtractor classification scores greater than 0.7 in 3 bands, 0.80 in 2 bands or 0.90 in a single band are classified as stellar objects.

While SExtractor can perform object classification on data near the plate limit where the pixel value scales linearly with intensity, for saturated objects

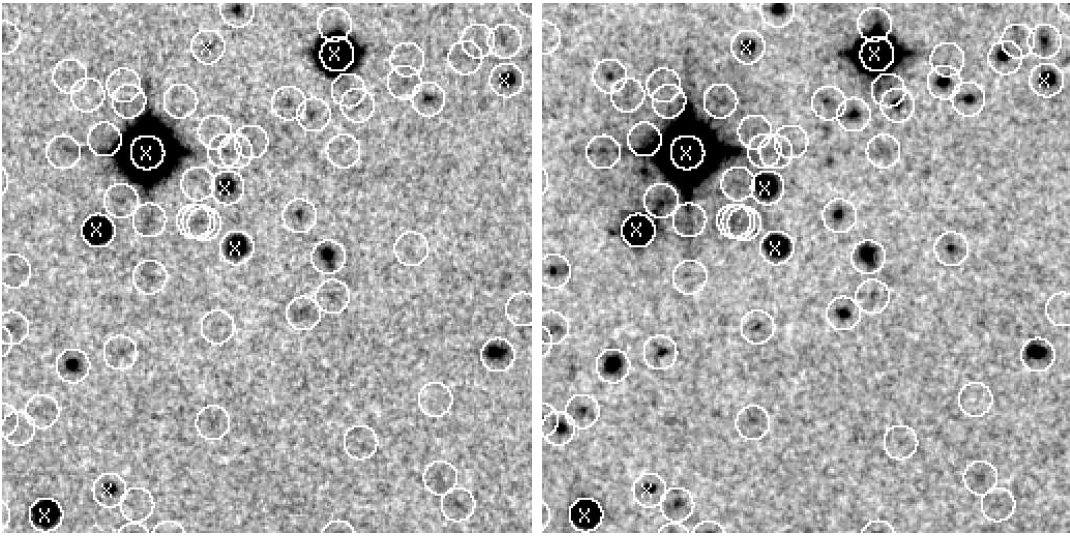


Figure 2.12: B_J and R images of a small region of the F855 field. All objects brighter than the U , B_J , R or I magnitude limits are circled. Objects classified as stellar are labelled with crosses. Spurious objects generated by the diffraction spikes and halo of the bright star can be seen.

($R \lesssim 18$) the object classification starts to break down (see Figure 2.11). To prevent contamination of the galaxy catalogue, bright objects are reclassified as stellar if they are within the stellar locus in peak intensity versus instrumental magnitude space and area versus instrumental magnitude space. Figure 2.12, a region of the F855 field with image classifications overlaid, shows that most bright stars are correctly classified by the classification scheme.

To determine the reliability of the classification scheme, object classifications were compared with deep imaging and spectroscopic samples. The results of the classification comparisons are summarised in Table 2.6. The reliability of the classification scheme derived from COSMOS scans and spectroscopic identifications by Colless *et al.* (1990) differ significantly despite the samples being the same set of $21 < B_J < 22.5$ objects. This is due to errors in the star-galaxy separation by COSMOS with AAT plates obtained in $< 2''$ seeing. As similar errors could be in other samples of ground-based imaging, the discussion of the reliability of classification scheme is restricted to spectroscopic samples and HST imaging.

Approximately 90% of stellar objects with spectroscopic identifications are correctly classified in the Panoramic Deep Fields. This improves to $\gtrsim 95\%$ for

$B_J < 20$ QSOs from the Veron-Cetty & Veron (2000) catalogue. The reliability of classifications derived from HST data (Abraham *et al.* 1996, Smail *et al.* 1997) are poorer but suffer from small number statistics. Approximately 85% of $20 < B_J < 23.5$ galaxies in the Panoramic Deep Fields with spectroscopic identifications from Colless *et al.* (1990) and Glazebrook *et al.* (1995) are correctly classified. The reliability of the classifier is somewhat better for objects from the NED database as it contains many $B_J < 20$ objects from the Las Campanas (Schectman *et al.* 1996) and APM (Loveday *et al.* 1992) redshift surveys.

2.5 Summary

A deep wide-field multicolour survey of two fields has been compiled by coadding SuperCOSMOS scans of UK Schmidt photographic plates. By subtracting the background before coaddition of the scans, it has been possible to apply bad pixel rejection algorithms to the data so clean object catalogues can be obtained. Several algorithms for coadding the scans were tested and a weighted average with min-max rejection was found to provide high signal-to-noise with robust bad pixel rejection. As faint objects are in the linear regime of the plate response, it has been possible to use SExtractor to detect and classify objects in the survey. By combining image classifications from multiple bands, it has been possible to reliably classify $B_J \lesssim 22.5$ objects imaged in $\sim 3''$ seeing.

Table 2.6: Comparison of Panoramic Deep Field classification with published object classifications. COSMOS AAT and HST data use classifications derived from imaging data while all the other datasets use spectroscopic identifications.

| Sample | Published Stellar Classification | | Published Extended Classification | |
|---|----------------------------------|-----------------------------------|-----------------------------------|----------------------------------|
| | PDF Stellar classification | PDF Extended classification | PDF Extended classification | PDF Stellar classification |
| Colless <i>et al.</i> (1990) | 17 | 0 | 39 | 6 |
| COSMOS AAT [†] | 18 | 6 | 33 | 5 |
| Glazebrook <i>et al.</i> (1995) | 6 | 1 | 33 | 2 |
| HST | 2 | 2 | 41 | 0 |
| NED | - | - | 620 | 32 |
| Veron-Cetty & Veron (2000) | 507 | 10 | - | - |
| [†] COSMOS classifier reliability $\sim 85\%$ (Colless <i>et al.</i> 1990) | | | | |

Chapter 3

Photometric Calibration

3.1 CCD photometry

Accurate photometric calibration is critical in a survey where colour criteria are applied to the selection of objects. This is particularly important for the clustering of colour selected galaxies and photometric redshifts. In order to calibrate the Panoramic Deep Fields, deep CCD sequences of the two fields have been obtained.

Photometric calibration data of the SGP consists of *BVRI* CCD images obtained by Bruce Peterson with the Mount Stromlo and Siding Spring Observatories' (MSSSO) 40-inch telescope and *U* band photometry from Croom *et al.* (1999). The 40-inch detector was a 2048×2048 thinned Tek CCD with $\sim 75\%$ quantum efficiency in *R* band dropping to $\sim 60\%$ in *B* band. The pixel scale of $0.6''$ resulted in a $\sim 20'' \times 20''$ field of view in coadded frames. This allowed accurate photometry of $\gtrsim 100$ stars and galaxies in each band in the field.

Photometric calibration data for the F855 field consists of *I* band data obtained by the author with the MSSSO 40-inch and *UBVR'* photometry from Osmer *et al.* (1998). Other photometry is available for the F855 field (Glazebrook *et al.* 1994, Glazebrook *et al.* 1995, Bryn Jones private communication) but the Osmer *et al.* data has a wider field-of-view resulting in a better calibration of $16 \lesssim B_J \lesssim 20$ stars. The availability of *V* band photometry also allows a colour correction to be applied to the calibration of the *B_J* data.

CCD images were reduced and coadded using IRAF routines `ccdproc`, `imalign` and `imcombine`. Flatfield images were produced by combining unshifted images to produce high signal-to-noise flatfield images. However, the SGP *I* band flatfield produced from the data had halos near the locations of bright stars while a flatfield produced from sky flats did not have any of the fringing patterns ob-

Table 3.1: Summary of MSSSO 40-inch observations.

| Field | Band | Integration Time (secs) | RMS of fit to standards | Seeing | Mag Limit |
|-------|----------|----------------------------|----------------------------|---------|--------------|
| SGP | <i>B</i> | 29×900 | 0.017 | $2.3''$ | ~ 23.5 |
| SGP | <i>V</i> | 10×900 | 0.013 | $2.3''$ | ~ 22.0 |
| SGP | <i>R</i> | 9×900 | 0.012 | $2.3''$ | ~ 22.5 |
| F855 | <i>I</i> | 20×600 | 0.038 | $2.1''$ | ~ 21.7 |

served in the images taken during darktime. As the *I* band photometry was of unknown quality, *I* band photometry from Caldwell & Schechter (1996) was used to calibrate the SGP *I* band data.

To correct for atmospheric extinction, offsets were determined by comparing instrumental magnitudes determined with SExtractor of $\gtrsim 100$ objects in each image. The fluxes (with errors) and positions of objects in the combined images were also determined with SExtractor. As the seeing in most of the CCD images is comparable to the Panoramic Deep Fields, object classifications from the CCD data were not used for the photometric calibration. An astrometric solution for the CCD data was determined using faint stellar objects from the APM catalogue and **astrom** package.

Magnitude zero-points, extinction and colour terms (where possible) relating instrumental magnitudes for the 40-inch photometry were obtained by multiple observations of Graham (1982) E-Region and Landolt (1992) standard stars. Instrumental magnitudes for standard stars observed with the 40-inch were obtained with the MAG_BEST option of SExtractor (Bertin & Arnouts 1996). As shown in Table 3.1, the fits to the standard star magnitudes had RMS errors for between 0.01 and 0.04 magnitudes.

The *R'* filter of Osmer *et al.* (1998) has a similar effective wavelength (6615Å) to *R* (6625Å) but has a shorter red tail. The difference between *R* and *R'* photometry has been found by Martini & Osmer (1998) to be small for “all but the reddest objects”. To determine if this statement is correct, the relationship

between $B - R$ and $B - V$ colours for stars from Landolt (1992), the MSSSO 40-inch, Croom *et al.* (1999) and the DMS (Osmer *et al.* 1998) have been plotted in Figure 3.1. The MSSSO 40-inch and DMS photometry have similar colours which is consistent with R' magnitudes being similar to R for most objects. All three sets of CCD photometry have stellar loci which are redder than Landolt (1992). Unless there is a systematic error in all 3 sets of CCD photometry, this is indicative of the BVR stellar locus being redder for faint ($R > 16$) stars than $R \lesssim 15$ Landolt standards.

3.2 Colour Equations

Photographic plates do not have an ideal response to intensity and photographic magnitudes are not necessarily the same as Johnson-Cousins magnitudes. To calibrate photographic plates with Johnson-Cousins photometry, a correction is required which is usually a function of object colour. As the median colour of a sample is a function of limiting magnitude, an incorrect colour equation can result in a zero-point error which changes with magnitude.

To calibrate the Panoramic Deep Fields in the B_J band, estimates of the B_J magnitudes were determined using the colour equation

$$B_J = B - 0.28(B - V) \quad -0.1 \leq B - V \leq 1.6 \quad (3.1)$$

(Blair & Gilmore 1982). A comparison of B_J magnitudes determined with the CCD data and the calibrated Panoramic Deep Fields is shown in Figure 3.2. For most objects the agreement between the datasets is good and there is no evidence of a significant systematic offset between the CCD data and the photographic data. However, to prevent variable stars and AGN from possibly skewing the calibration of the Panoramic Deep Fields, $B_J - R < 0.4$ objects were excluded from the calibrating data.

For photographic R band data there are several different colour equations available in the literature which are summarised in Table 3.2. To determine if a colour equation is required for the Panoramic Deep Fields, the difference between calibrated photographic R and Cousins R has been plotted as a function of photographic $B_J - R$ in Figure 3.3. It is clear from the plot that the photographic and Cousins R band photometry are similar for $B_J - R < 1.6$ but photographic R is larger than Cousins R for very red objects. The colour equation of Couch & Newell (1980) is a poor fit to the data over the observed magnitude range. As

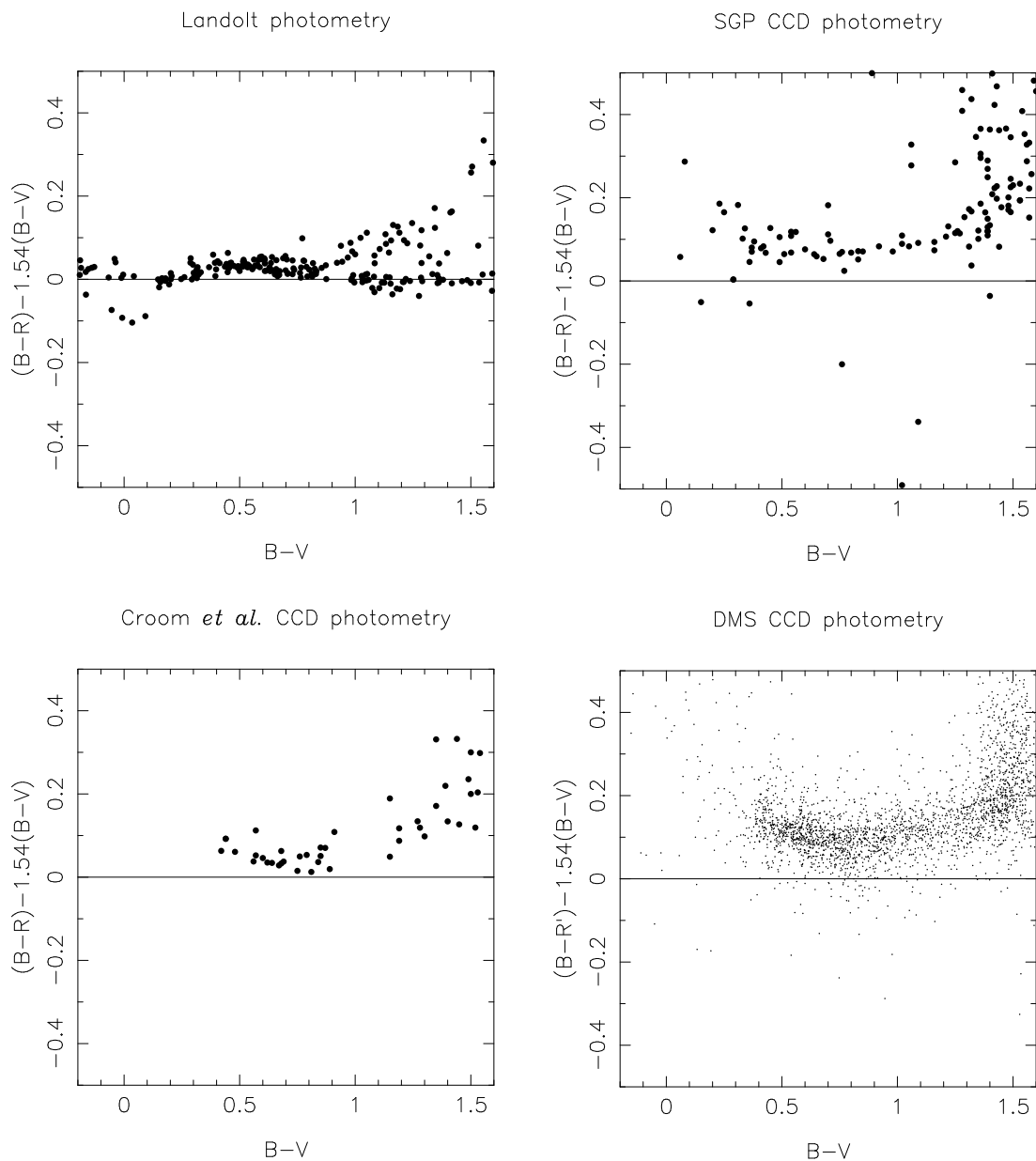


Figure 3.1: Comparison of $B - R$, $B - R'$ and $B - V$ colours of $R < 20$ stellar objects for different sets of photometry. The approximate colours of main-sequence stars are given by $B - R = 1.54(B - V)$ (Metcalf *et al.* 1991, Croom 1997) and this has been subtracted from the $B - R$ or $B - R'$ values. The relationship between the colours differs significantly between the CCD photometry and the photoelectric standards of Landolt (1992).

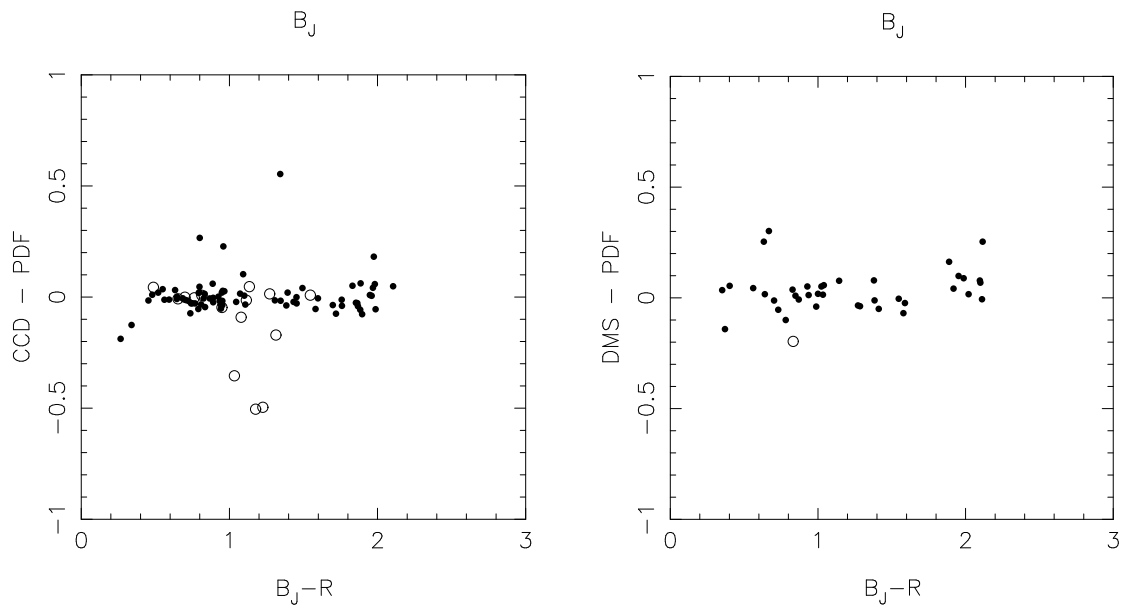


Figure 3.2: The difference between B_J magnitude estimates from CCD data (MSSSO 40-inch and Osmer *et al.* 1998) and the Panoramic Deep Fields. Solid symbols are stellar objects and open circles are galaxies. The values of the $B_J - R$ colour have been determined with the Panoramic Deep Field data. The difference between the B_J estimates is small for both fields and there is no evidence for a large systematic error in the data.

Table 3.2: Photographic R colour equations. The value of δR is Cousins R minus photographic R .

| Emulsion & Filter | Colour Equation | Notes & Reference |
|----------------------------|---|-----------------------------|
| <i>III-aF</i> +RG630 | $\delta R = (0.00 \pm 0.05) \times (R - I)$ | Blair & Gilmore (1982) |
| <i>4415</i> +OG590 | $\delta R = (-0.033 \pm 0.01) \times (R - I)$ | Morgan & Parker (1997) |
| <i>III-aF</i> +RG630 | $\delta R = 0.0058 \times (B - R) + 0.008$ | Couch & Newell (1980) |
| <i>III-aF</i> +OG590/RG630 | $\delta R = (0.00 \pm 0.01) \times (B_J - R)$ | $B_J - R < 1.6$, This work |

photographic and Cousins R are very similar for most objects in the survey, R will be used to describe photographic R for this work.

The colour equations for U and I determined by Blair & Gilmore (1982) have colour terms ~ 0 . Figure 3.4 shows plots of the difference between CCD and photographic photometry in the U and I bands as a function of colour. There is no evidence for a measurable colour term for the I band data though U band shows discrepancies for very blue and red objects. This could be due to the transmission curve of the photographic U differing from Johnson-Cousins U and the variability of blue AGN. To prevent very red and blue objects from skewing the calibration of the U band photometry, only $0.0 < U - B_J < 1.6$ objects have been used to calibrate the Panoramic Deep Fields.

3.3 Photometric Calibration of Panoramic Deep Fields

Photometric calibration of the Panoramic Deep Fields was determined with the CCD data and published photometry described in the previous section. The calibration of objects in the linear regime of the plate response can be determined with a zero-point. This was determined by finding the median value of the offsets between the calibrated and instrumental magnitudes for unsaturated stars.

The instrumental magnitudes of saturated stars are outside the linear regime

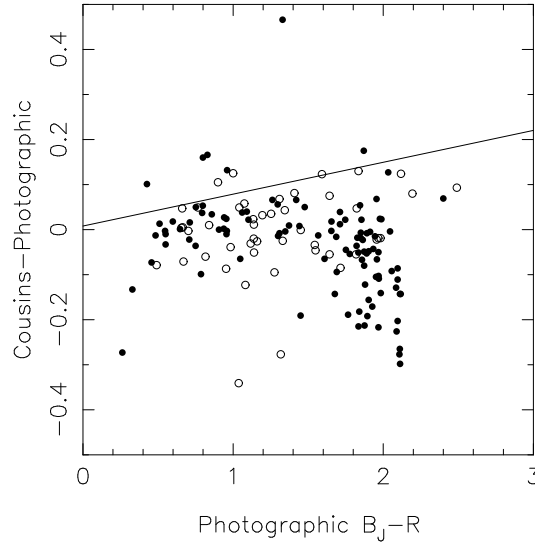


Figure 3.3: The difference between photographic and Cousins R as a function of photographic $B_J - R$ colour for $16 < R < 20$ objects. Solid symbols are stellar objects and open circles are galaxies. The line is the colour equation of Couch & Newell (1980) with $B_J - R = 0.82(B - R)$.

and a more complex function must be fitted. Photometric calibration of saturated stars was determined by fitting a polynomial to the relation between the Panoramic Deep Field instrumental magnitude and the calibrated magnitude for objects classified as stellar in the Panoramic Deep Fields. The CCD photometry contains few bright stars so bright stars from Landolt (1992) and the General Catalogue of Photometric Data (Mermilliod, Mermilliod & Hauck 1997) were used to constrain the fits at $B_J < 15$. While this is considerably brighter than any objects studied in this work, the inclusion of bright stars constrains the fit and prevents bright objects from having spuriously faint magnitude estimates. Saturated and unsaturated stars were used to better constrain the polynomial fit at faint magnitudes and the intercept between the polynomial fit and the zero-point is used to estimate the brightest magnitude where stars are in the linear regime of the plate response.

After the calibration of the data has been performed, the plots of the fit between the instrumental and calibrated magnitudes are visually inspected. It is not unusual for outliers to skew the fit, especially at bright magnitudes where relatively small numbers of objects are available. If a star is observed to be

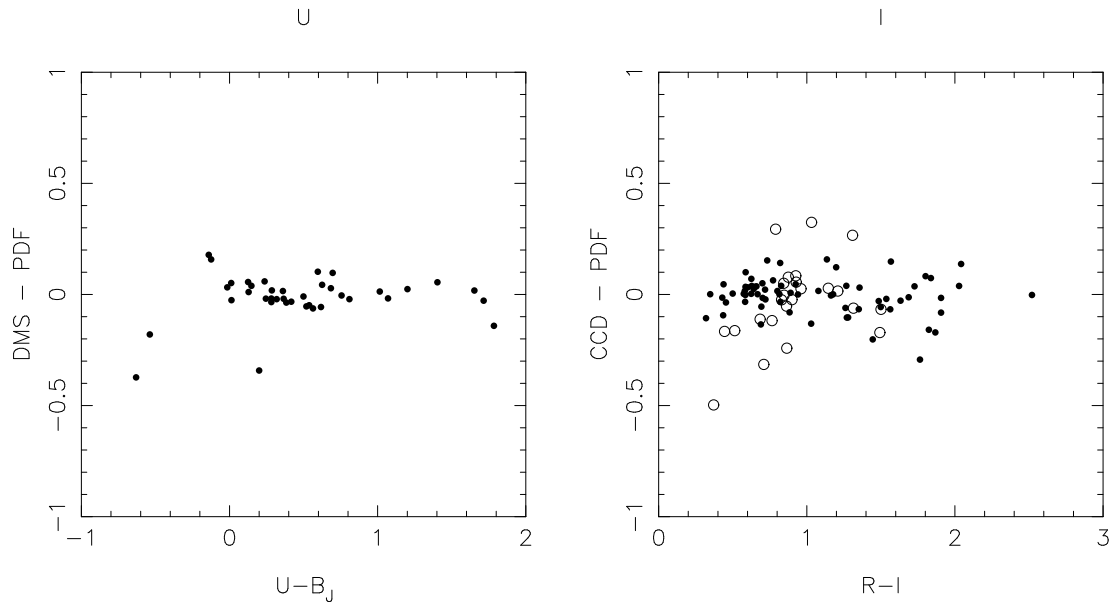


Figure 3.4: The difference between U and I band photometry from CCD imaging and photography as a function of colour. Dots are stellar objects while open circles are galaxies. The U band CCD data is from Osmer *et al.* (1998) and the I band data is 40-inch imaging of the F855 field. There are significant differences between the U band photometry estimates for very blue objects. The I band data does not show evidence for a large colour term though the galaxy photometry has significantly larger errors than the photometry of stars.

$\gg 3\sigma$ from locus of stars used to calibrate the photometry, it is removed from the calibrating data set and the calibration is rerun. The final calibration curves for the SGP and F855 fields are shown in Figures 3.5 and 3.6.

In addition to the calibration determined with CCD photometry, 2 corrections need to be applied to calibrate data. The first is a correction to the magnitudes to compensate for vignetting at the edges of the field. As sky subtraction was used during the coaddition of the scans, it is not possible to use the intensity of the sky background to estimate the vignetting correction (Hambly 1998b). Vignetting estimates for the UKST are available from Tritton (1983) and Dawe & Metcalfe (1982) but neither contain a table of estimated values. Several vignetting corrections were determined with polynomial fits to data read from graphs. The availability of Dawe & Metcalfe (1982) on ADS allowed the use of the DEXTER Java applet to read data, increasing the accuracy of the fit.

The vignetting correction is only accurate for unsaturated objects as the saturation level of plates (relative to the background) and the resulting instrumental magnitudes of bright stars is a function of radius from the plate centre. Unfortunately, comparing photometry of faint objects isn't possible as there are no large accurate catalogues of faint galaxy photometry at various radii from the field centres. However, the galaxy correlation function can be used to evaluate vignetting correction as the vignetting results in an apparent excess of galaxies in the plate centre and an excess of clustering at large angular scales. If the incorrect vignetting correction is applied, the value of γ of the angular correlation function will rapidly decrease with magnitude due to an excess of galaxy pairs at large angular scales. Of the vignetting functions tested, the vignetting for unhypered plates including geometric effects and backscattering from the emulsion from Dawe & Metcalfe (1982) resulted in the smallest variations of γ with magnitude. The polynomial fit for the vignetting correction is given by

$$\delta m \times 10^{10} = 35180r + 30777r^2 - 565r^3 + 3.97r^4 - 0.00574r^5 \quad (3.2)$$

where r is the radius from the plate centre in millimetres. At large radii there are large differences between the published vignetting estimates and, as shown in Figure 3.7, the vignetting increases rapidly. It is therefore probable that there are large systematic errors in the vignetting correction beyond 160mm (3.0°) from the plate centre. For this reason, only objects with vignetting corrections less than 0.06 were used to calibrate the Panoramic Deep Field photometry.

Galaxy magnitude estimates are corrected for dust extinction using the dust

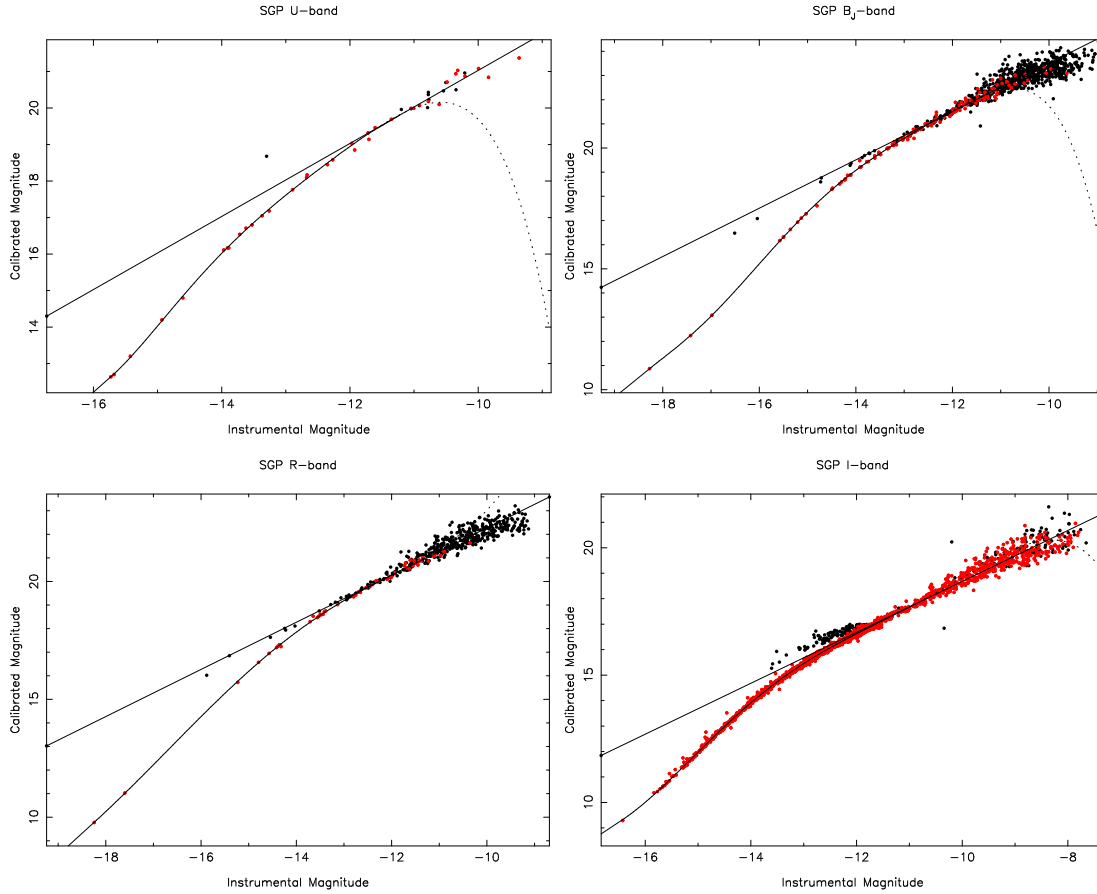


Figure 3.5: Photometric calibration of the SGP. Grey points are stellar objects and dark points are galaxies. The straight line (with gradient fixed to 1) is a fit for the calibration of galaxies and faint objects while the curved line is for the calibration of bright stars. The group of galaxies above the calibration line in the *I* band data are objects misclassified as stars by Caldwell & Schechter (1996) resulting in overestimates of their magnitudes.

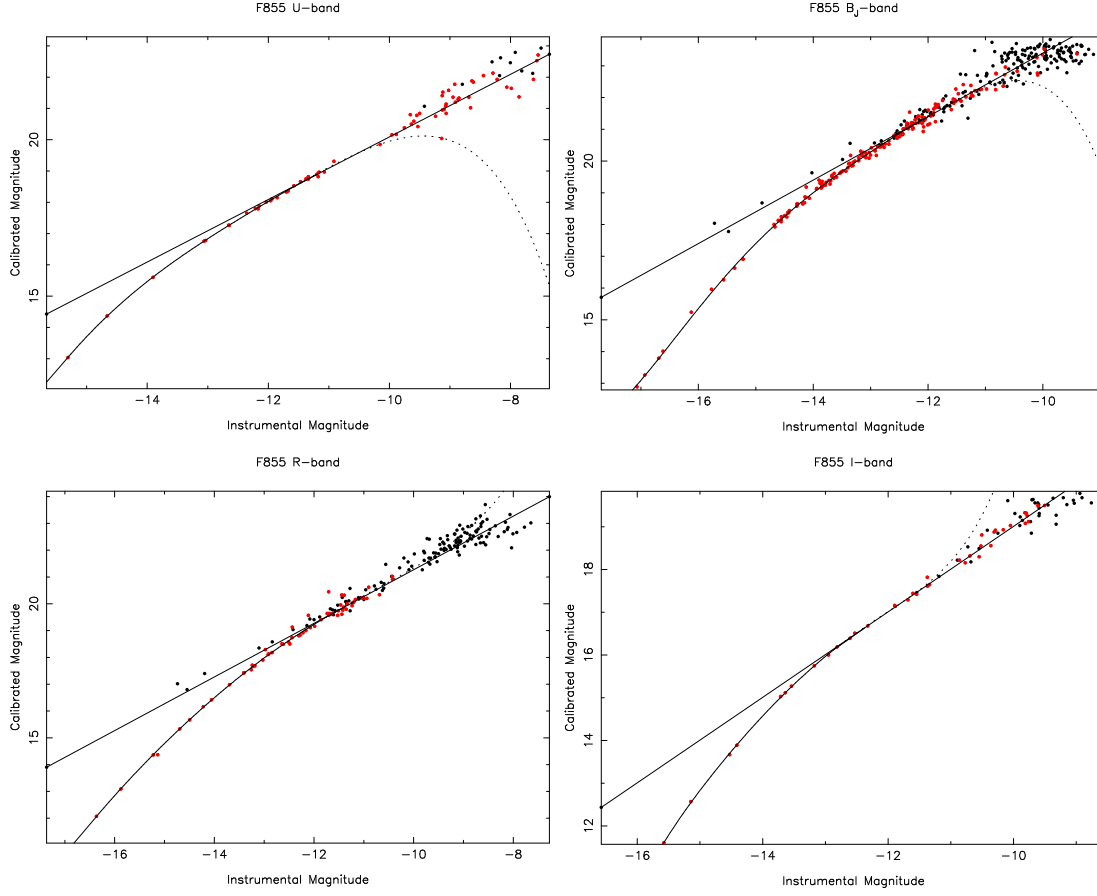


Figure 3.6: Photometric calibration of F855. Grey points are stellar objects and dark points are galaxies. The straight line is a fit for the calibration of galaxies and faint objects while the curved line is for the calibration of bright stars.

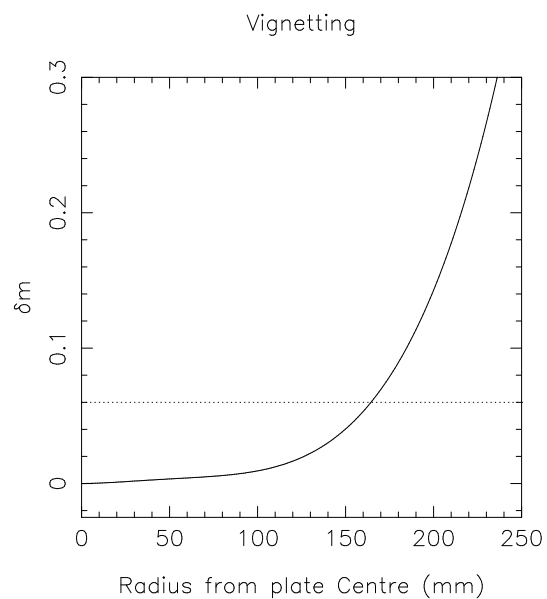


Figure 3.7: The correction for the vignetting as a function of radius from the plate centre. The line is a fit to a plot from Dawe & Metcalfe (1982) for unhypered plates including geometric effects and backscattering from the emulsion. The dotted line at 0.06 magnitudes is the maximum vignetting correction allowed for objects used to calibrate the photometry.

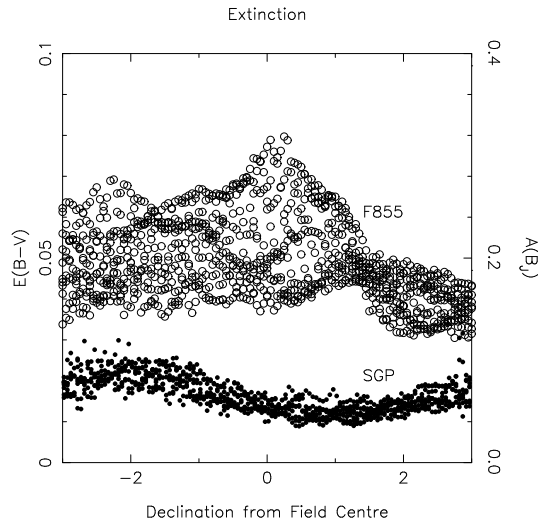


Figure 3.8: A plot of the dust extinction across the SGP and F855 fields using $E(B - V)$ estimates from Schlegel, Finkbeiner & Davis (1998). The dust extinction in F855 ($l \sim 45^\circ$) is significantly larger and shows more structure than the SGP. The extinction in F855, if left uncorrected, would introduce spurious structure on large angular scales.

maps of Schlegel, Finkbeiner & Davis (1998). Figure 3.8 shows that there are significant variations in the dust extinction in F855 which could introduce spurious large-scale structure into the catalogue. In contrast, the dust extinction in the SGP is restricted to the range $0.01 < E(B - V) < 0.03$ which is comparable to the estimated errors of the $E(B - V)$ estimates (0.028). The dust map estimates of the extinction are therefore only applied to the F855 field while a constant value of $E(B - V) = 0.015$ is used to correct for dust extinction in the SGP.

3.4 Comparison of Galaxy Number Counts and Colours

A systematic error in the photometry in one of the fields should produce a noticeable difference in the number counts compared with the other field and previous work. Figure 3.9 shows a comparison of number counts in the two fields and with previous wide-field photographic surveys. The number counts for the two fields are in good agreement with each other in all 4 bands. However, at $B_J < 19$ and $B_J > 21$ the number counts are slightly higher than those measured by Mad-

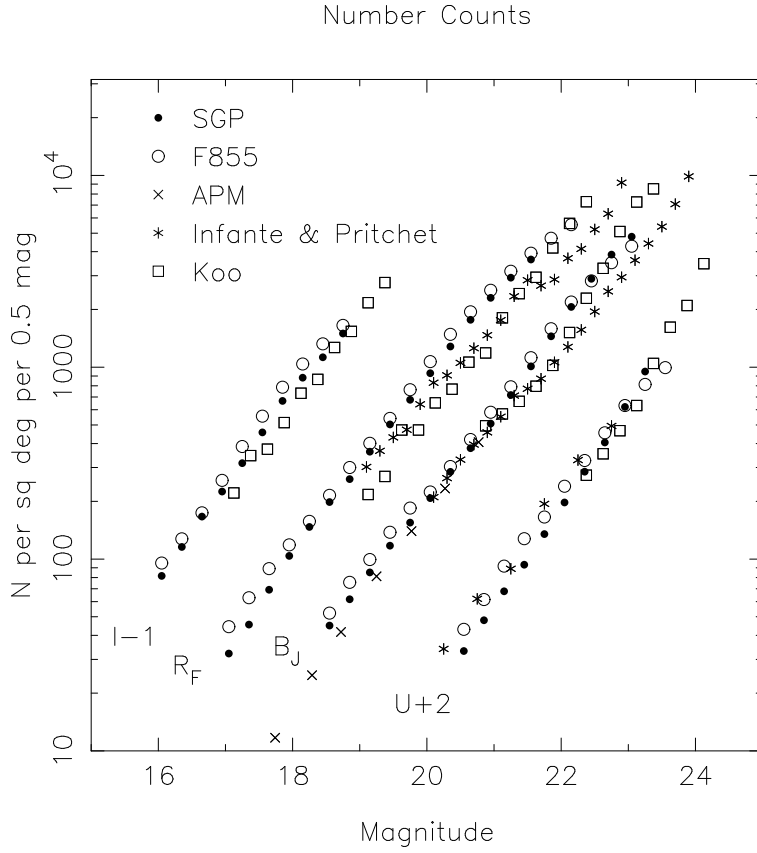


Figure 3.9: A plot of the galaxy number counts as a function of magnitude (after correction for dust extinction). Data from both fields is compared with number counts from the APM survey (Maddox *et al.* 1990), Koo (1988) and Infante & Pritchett (1992). *I* band counts have been moved 1 magnitude to the left and *U* band counts have been moved 2 magnitudes to the right for clarity. Error bars are not shown as their size would be comparable to or smaller than the data points.

dox *et al.* (1990) and Infante & Pritchett (1992). It is plausible that systematic errors could be altering the number counts at bright magnitudes. However, as bright galaxies will be entering the non-linear regime of the plate response, the photometry of bright galaxies should be systematically overestimated resulting in underestimates of the number counts of bright galaxies. Near the magnitude limits of the data, there is good agreement with Koo (1988) and it is therefore plausible that there is a systematic error in the number counts of Infante & Pritchett (1992). This conclusion is supported by *B* band number counts by Metcalfe *et al.* (2001) which are significantly higher than those of Infante & Pritchett (1992).

An error in the vignetting correction would introduce a systematic error which would be a function of radius from the plate centre. This error would be observed as a changing density of galaxies as a function of radius from the plate centre. To see if such an error exists in the data, the angular cross-correlation of the plate centre and galaxies has been determined and plotted in Figure 3.10. There is no consistent error as a function of plate radius for either field. There are also significant differences between angular cross-correlation determined with $20.5 < B_J < 21.5$ and $22.5 < B_J < 23.5$ galaxies. As an error in the vignetting correction should produce the same error for all magnitudes, it is reasonable to assume that errors in the vignetting correction are not significant in the Panoramic Deep Fields. However, as a precaution, estimates of the angular correlation function are only determined with galaxies where the vignetting correction is less than 0.1 magnitudes.

If there is a systematic offset of the photometry in a single band in one of the fields, it should be possible to observe this in colour-colour diagrams of galaxies. Inspection of the the diagrams showed an $R - I$ offset of 0.1 magnitudes between the SGP and F855 fields. As there is no apparent offset in the $B_J - R$ colours of galaxies in the two fields, the error is presumably in I band. Caldwell & Schechter (1996) compared their photometry with other I band data in the SGP and find good agreement between their photometry and other published data. For this reason, it was decided to change the zero-point of the I band photometry in the F855 field by -0.1 magnitudes so galaxy colours are consistent in both fields. Figure 3.11 shows plots of the galaxy colours in the two fields after corrections for dust extinction and the F855 I band zero-point have been applied. The position of the loci in the 2 sets of diagrams are consistent with there being no large errors in the determination of the zero-points for the two fields.

A further check of the photometry is the median colour of galaxies as a function of magnitude. Table 3.3 lists the median colour of galaxies in each field for a series of magnitude slices. The median colours of galaxies differ by $\lesssim 0.1$ at bright magnitudes and $\lesssim 0.05$ at faint magnitudes except for $U - B_J$. The discrepancy in $U - B_J$ disappears if the median colour is only determined with weakly clustered blue galaxies. It is therefore possible that the differences in median $U - B_J$ colour of all galaxies are caused by red galaxies associated with large-scale-structure.

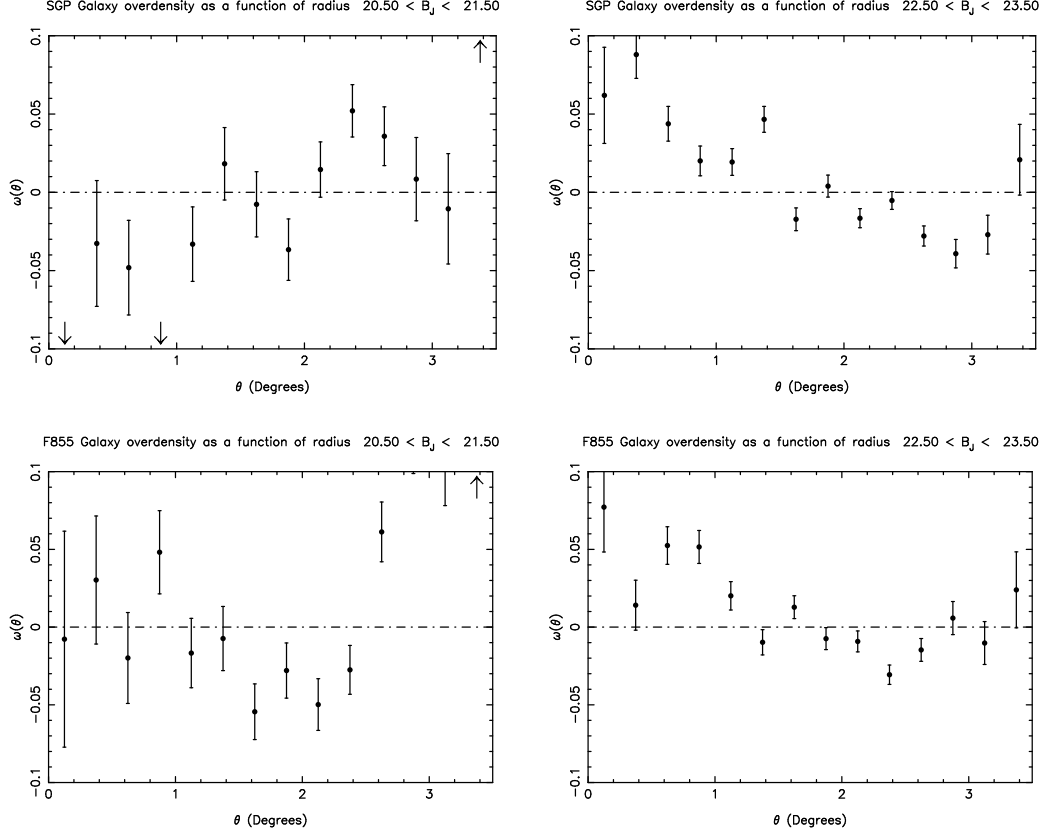


Figure 3.10: The angular cross-correlation of galaxies with the centre of each field. If the vignetting correction was producing a significant error, the values of the cross-correlation would be comparable for bright and faint galaxies. The low values of the cross-correlation are consistent with the errors of the vignetting correction being small.

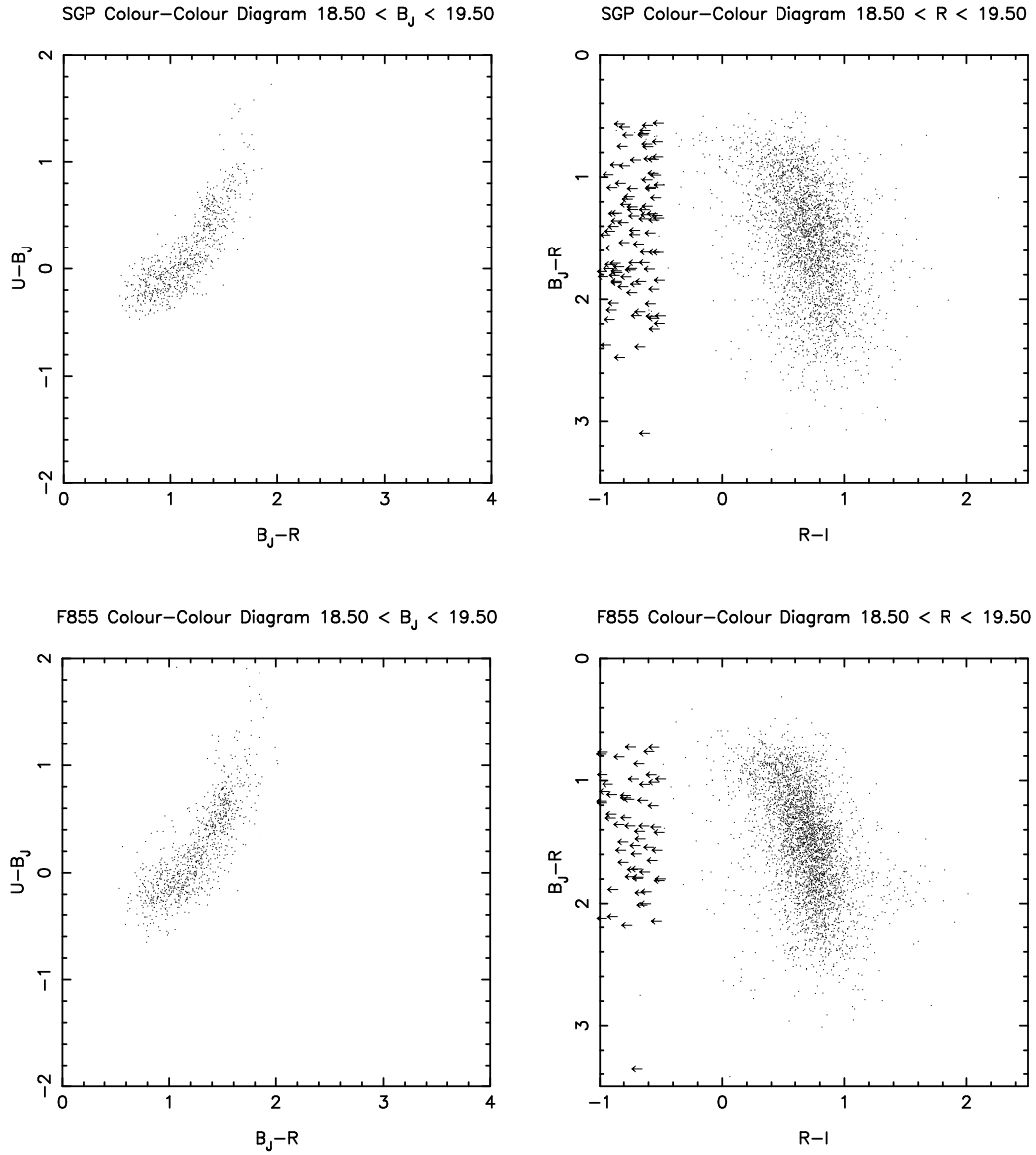


Figure 3.11: Galaxy colour-colour diagrams for the SGP and F855 fields. Galaxy magnitudes and colours have been corrected for dust extinction and a possible error in the F855 I band zero-point.

Table 3.3: Galaxy Median Colour

| Magnitude Range | Colour | Colour Range | Median Value | |
|--------------------|-----------|-----------------|--------------|-------|
| | | | SGP | F855 |
| $17 < B_J < 18$ | $U - B_J$ | All | 0.07 | 0.01 |
| $18 < B_J < 19$ | $U - B_J$ | All | 0.05 | 0.14 |
| $19 < B_J < 20$ | $U - B_J$ | All | 0.05 | 0.13 |
| $16 < R < 17$ | $B_J - R$ | All | 1.25 | 1.36 |
| $17 < R < 18$ | $B_J - R$ | All | 1.31 | 1.41 |
| $18 < R < 19$ | $B_J - R$ | All | 1.42 | 1.47 |
| $19 < R < 20$ | $B_J - R$ | All | 1.53 | 1.52 |
| $15 < I < 16$ | $R - I$ | All | 0.90 | 0.89 |
| $16 < I < 17$ | $R - I$ | All | 0.84 | 0.81 |
| $17 < I < 18$ | $R - I$ | All | 0.79 | 0.76 |
| $18 < I < 19$ | $R - I$ | All | 0.83 | 0.81 |
| $19 < I < 20$ | $R - I$ | All | 0.87 | 0.88 |
| $17 < B_J < 18$ | $U - B_J$ | < 0.4 | -0.03 | -0.06 |
| $18 < B_J < 19$ | $U - B_J$ | < 0.4 | -0.04 | -0.03 |
| $19 < B_J < 20$ | $U - B_J$ | < 0.4 | -0.03 | -0.02 |

3.5 Comparison with Other Photometry

Panoramic Deep Field photometry was compared with photometry from Caldwell & Schechter (1996), Croom *et al.* (1999), Prandoni *et al.* (1999) and Smith & Boyle (in preparation) to determine if there were any significant zero-point errors in either field. Comparisons of the UB_JRI photometry in the SGP with Croom *et al.* (1999) and Prandoni *et al.* (1999) are shown Figure 3.12. Offsets between the Panoramic Deep Field photometry and the CCD photometry are $\lesssim 0.05$ magnitudes. There is evidence of the offset changing as a function of magnitude in the sets of photometry. For the Prandoni *et al.* (1999) data this is limited to the very brightest stars in the sample but for the other bands it appears over a much larger range of magnitudes.

A systematic error in the photometry as a function of magnitude should produce a significant gradient in the stellar locus as a function of magnitude. Figure 3.13 shows colour-magnitude diagrams for $U - B_J$ and $u - g$ photometry from Croom *et al.* (1999), Newberg *et al.* (1999), Osmer *et al.* (1998), Smith & Boyle (in preparation). The colour of the stellar locus is a function of magnitude in all 4 diagrams though the gradient of the locus varies from diagram to diagram. It is difficult to compare Newberg *et al.* (1999) with the other diagrams as the filters are different from the other diagrams. However, it is clear that the DMS has a shallower slope than Croom *et al.* (1999) and Smith & Boyle (in preparation). It is unclear from the diagrams which gradient is correct and it is also probable that the shape of the locus is a function of galactic latitude and longitude (Newberg *et al.* 1999, Croom private communication). For comparison with the CCD data, the stellar locus of the SGP field is plotted in Figure 3.14. The colour of the locus does change with magnitude but has a slightly shallower slope than Croom *et al.* (1999).

Panoramic Deep Field photometry for the F855 field is compared with photometry from Smith & Boyle (in preparation) and DENIS (Epchtein *et al.* 1994) in Figure 3.15. There is an offset between the DENIS and Panoramic Deep Field photometry which is approximately equal to the correction applied zero-point of the F855 I band CCD data. It is plausible that the error is in the SGP I band data though this would require ~ 0.1 magnitude errors in multiple sets of photometry. The Panoramic Deep Field and Smith & Boyle photometry are in good agreement for U and R though there is a ~ 0.08 offset in B_J .

The survey of Caldwell & Schechter (1996) imaged a $\sim 20^\circ$ area of the

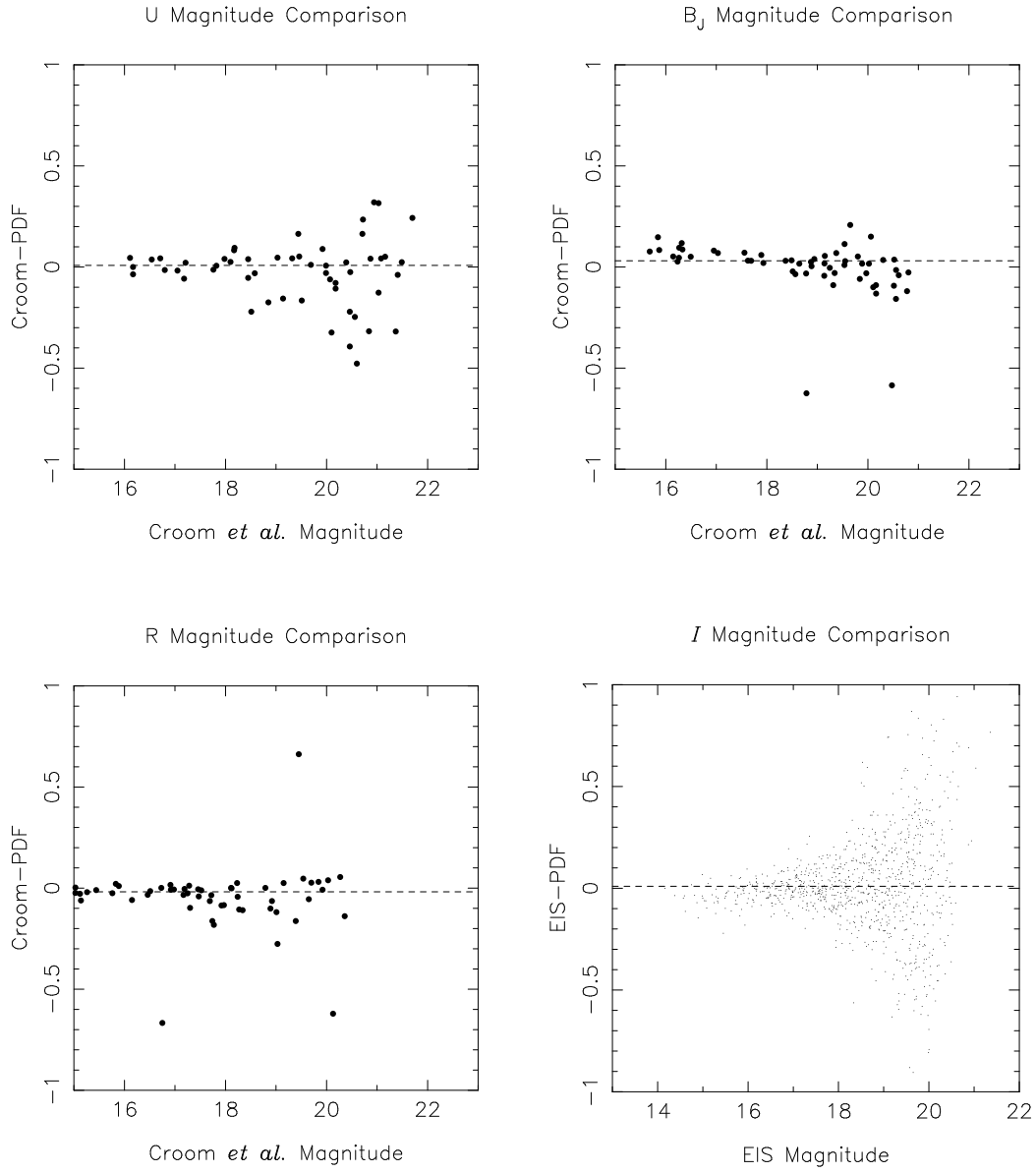


Figure 3.12: Comparison of SGP Panoramic Deep Field photometry with CCD photometry from Croom *et al.* (1999) and Prandoni *et al.* (1999). The dashed line is the median offset between the sets of photometry.

SGP and allows comparison of the photometry near the centre and edge of the field. The two panels of Figure 3.16 show a comparison of photometry near the centre and edge of the field. The photometry near the edge of the field has vignetting > 0.1 magnitudes. The median offset between the Panoramic Deep Field and Caldwell & Schechter photometry at the edge of the SGP field is ~ 0.02 magnitudes. This is consistent with there being no large systematic errors in the photometry as a function of radius from the field centre. However, the magnitude range studied here is limited and large systematic errors have been observed for $R < 15$ stars near the edges of scans of single plates (Hambly 1998b).

3.6 Summary

The Panoramic Deep Fields have been calibrated with *UBVRI* CCD imaging. Colour equations have been applied to the data and the magnitude estimates are equivalent to U , B_J , V and I for most objects. The only exceptions are objects with very red or blue colours where errors of several tenths of a magnitude are detected. Comparisons of the galaxy number counts and colours are consistent with there being no large systematic offset of the photometry between the two fields. Finally, comparisons of the Panoramic Deep Field photometry with several catalogues of CCD photometry show no evidence for errors larger than ~ 0.1 magnitudes in the estimated zero-points of the *UB_JRI* photometry.

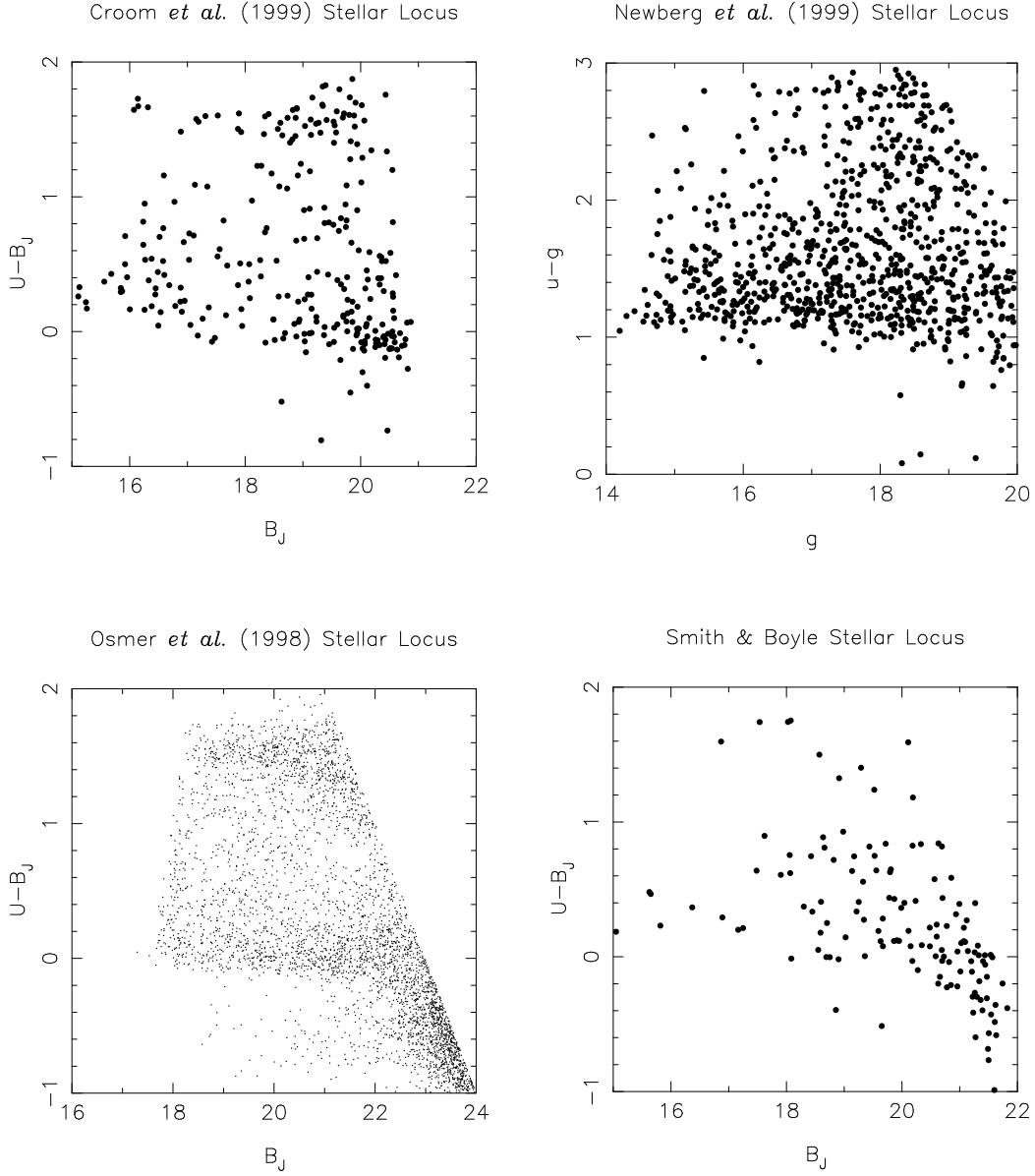


Figure 3.13: The $U - B_J$ or $u - g$ colours of stars as a function of limiting magnitude from Croom *et al.* (1999), Newberg *et al.* (1999), Osmer *et al.* (1998) and Smith & Boyle (in preparation).

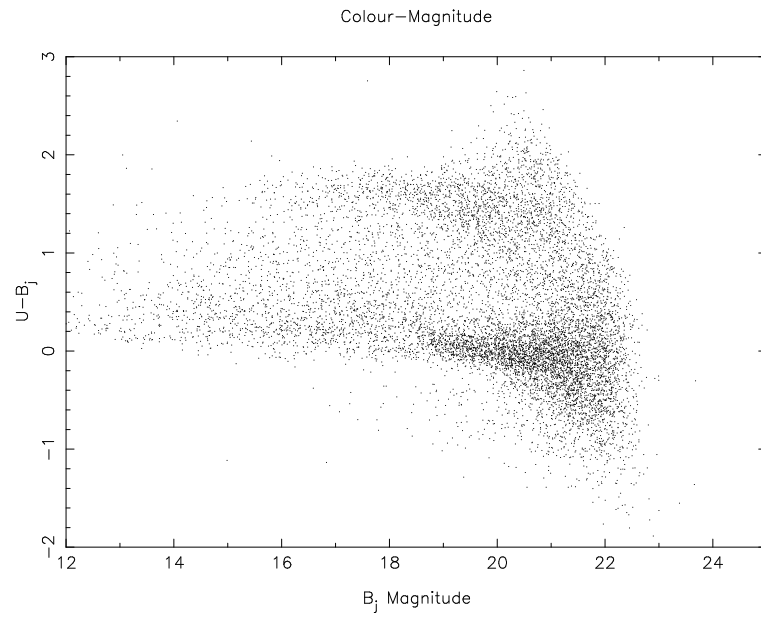


Figure 3.14: The $U - B_J$ colours of stars as a function of magnitude for the SGP field.

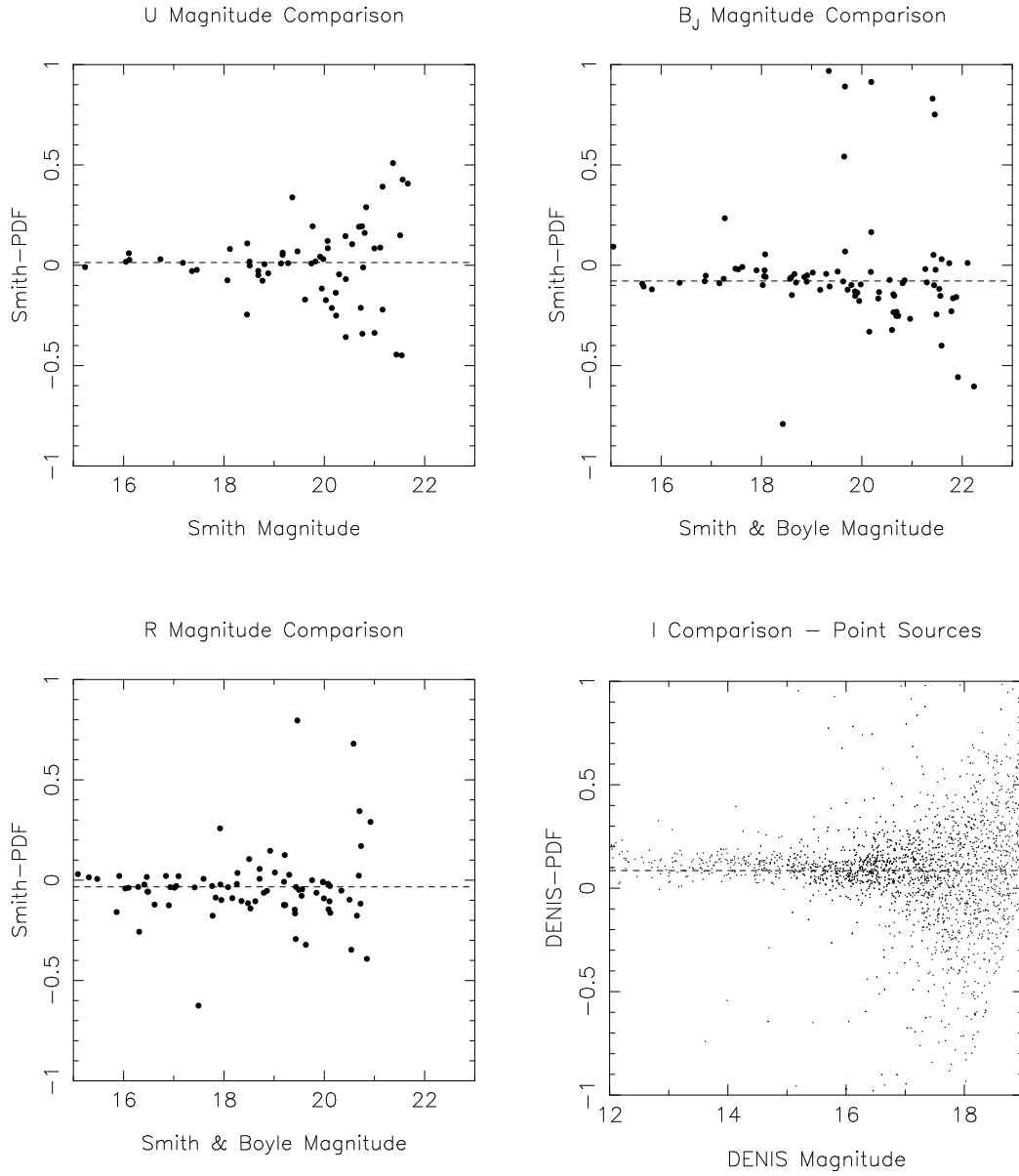


Figure 3.15: Comparison of F855 Panoptic Deep Field photometry with CCD photometry from Smith & Boyle (in preparation) and the DENIS survey (Epchtein *et al.* 1994).

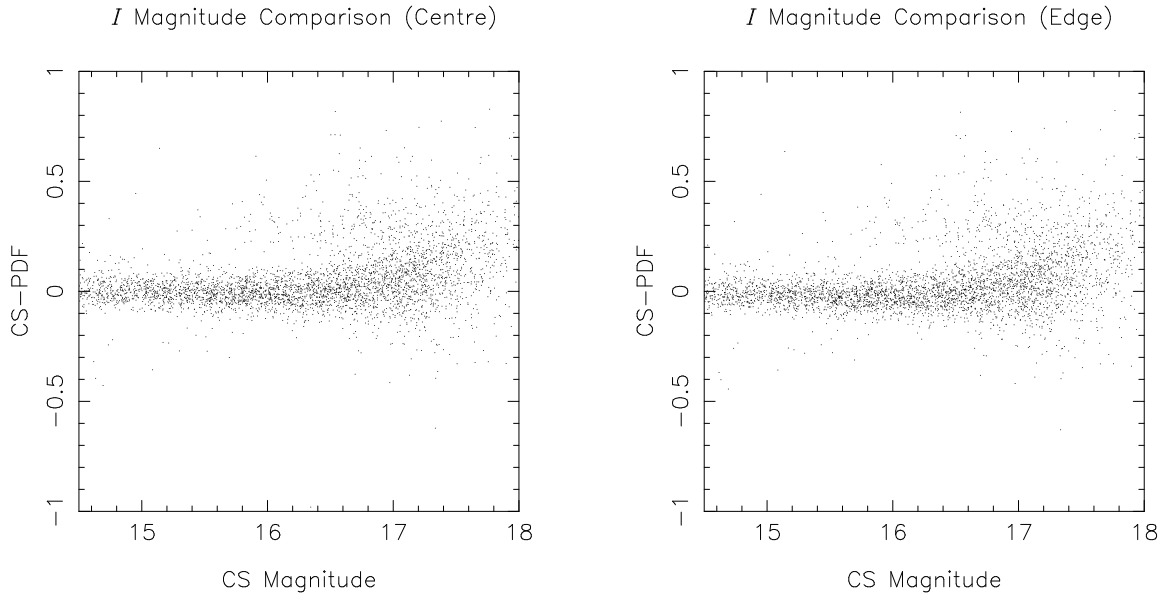


Figure 3.16: A comparison of photometry in the SGP field with Caldwell & Schechter (1996). The left and right panels show photometry of objects where vignetting is less than and more than 0.1 magnitudes respectively. The offset between the Panoramic Deep Field and Caldwell & Schechter magnitudes is ~ 0.02 magnitudes at the edge of the field.

Chapter 4

The Clustering of Colour Selected Galaxies

4.1 Introduction

The galaxy two-point correlation function is commonly used to measure the structure of the galaxy environment from high redshift until the present epoch. The clustering properties of galaxies in the local Universe are well measured by large representative surveys of the galaxy population (Maddox, Efstathiou & Sutherland 1996). Catalogues of galaxies selected by morphology show large variations of the galaxy correlation function with late type galaxies having considerably weaker clustering than early type galaxies (Davis & Geller 1976, Loveday *et al.* 1995).

The results from studies of galaxies with fainter apparent magnitudes and higher redshifts are less conclusive. Pencil-beam surveys with CCDs and photographic plates from 4m telescopes have measured the amplitude of the $B > 22$ correlation function; however, estimates vary by $\gtrsim 100\%$ (Infante & Pritchet 1995). Also, while $B > 22$ surveys show evidence for a rapid decline of the amplitude of the correlation function (Efstathiou *et al.* 1991, Infante & Pritchet 1995, Roche *et al.* 1996), I band imaging surveys to similar depths show no evidence for a rapid decrease of the correlation function amplitude (Postman *et al.* 1998).

The small areas of previous studies of the faint galaxy correlation function are a possible source of the discrepancy. Large individual structures and voids in the Universe could bias estimates of the correlation function if the field-of-view of the survey is small. The use of single band data to select catalogues of galaxies could

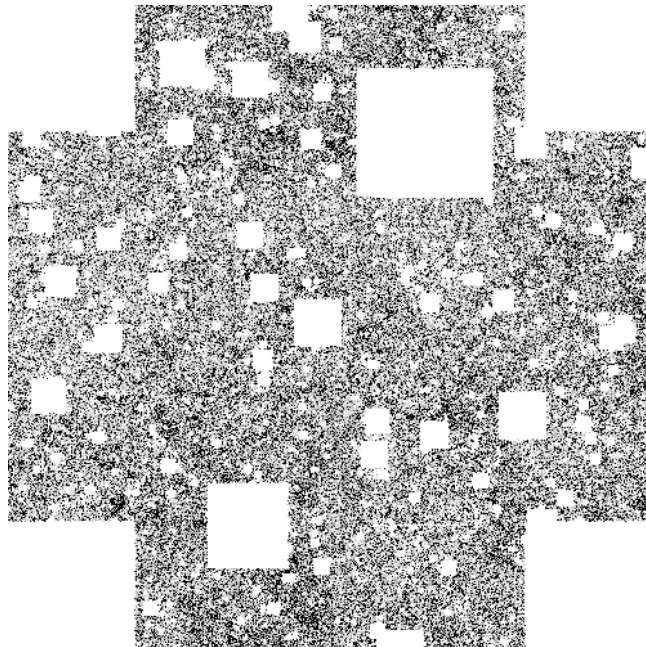


Figure 4.1: A flux weighted map of $R < 22$ galaxies in the SGP. The dark blocks are regions which have been removed from the catalogue. The corners of both fields have been removed to prevent objects with significant vignetting entering the catalogue. Some of the Abell clusters in the field can be seen as overdense regions.

suffer from biases as the morphological mix of galaxies will change as a function of limiting magnitude. It is probable that the differing amplitudes of the B and I band correlation functions are due to faint B band data being dominated by weakly clustered blue galaxies (Efsthathiou *et al.* 1991) while the I band data has a larger fraction of early type galaxies.

4.2 Estimation of the Angular Correlation Function

The galaxy two-point correlation function, $\omega(\theta)$, measures the mean excess surface density of pairs at angular separation θ compared with the expected number of pairs if galaxies were randomly distributed. The most commonly used estimator of the angular correlation function is

$$\hat{\omega}(\theta) = \frac{DD}{DR} - 1 \quad (4.1)$$

where DD and DR are the number of galaxy-galaxy and galaxy-random object pairs at angular separations $\theta \pm \delta\theta$. The random objects are typically copies of real objects distributed randomly across the field-of-view. To reduce errors, multiple random copies of each object can be made and the estimate of DR renormalised. However, the DD/DR estimator is subject to first-order errors in the galaxy density contrast (Hamilton 1993) making it unsuitable for measuring weak clustering at large angular scales. An estimator with lower variance than DD/DR is required, the estimator

$$\hat{\omega}(\theta) = \frac{DD - 2DR + RR}{RR} \quad (4.2)$$

(Landy & Szalay 1993) where RR is the number of random-random object pairs at angular separations $\theta \pm \delta\theta$. The value of $\hat{\omega}(\theta)$ is determined for different angular scale bins with the values of DD , DR and RR being determined with pairs of individual objects at small angular scales and weighted pairs of cells containing multiple objects at large angular scales. The use of cells to determine the angular correlation function reduces the computational time required to several hours and does not introduce significant errors.

The estimator of the angular correlation function satisfies the integral constraint,

$$\int \int \hat{\omega}(\theta) \delta\Omega_1 \delta\Omega_2 \simeq 0 \quad (4.3)$$

(Groth and Peebles 1977), resulting in an underestimate of the angular correlation function. To remove this bias from the correlation function, the term

$$\omega(\theta)_\Omega = \frac{1}{\Omega^2} \int \int \omega(\theta) \delta\Omega_1 \delta\Omega_2 \quad (4.4)$$

is added to the estimate of the correlation function. The term, $\omega(\theta)_\Omega$ does require an assumption of the form of the correlation function to correctly estimate the value of correlation function. However, previous work with smaller fields of view and at brighter limiting magnitudes shows that the angular correlation is well approximated by a power law at angular scales less than 1° (Maddox, Efstathiou & Sutherland 1996).

A further source of bias in estimates of the correlation function is contamination of the catalogue by randomly distributed objects such as stars. If the fraction of the catalogue contaminated by stars is f , the estimate of the correlation function is reduced by a factor of $(1 - f)^2$ at all angular separations. As mentioned previously, comparison with spectroscopic samples indicates the

star galaxy separations if $\gtrsim 85\%$ reliable at magnitude brighter than $B_J < 22$. At fainter magnitudes, the contamination of the catalogue by stars is negligible as galaxies consist more than $\gtrsim 80\%$ of the object number counts at $B_J \geq 23$ (Glazebrook *et al.* 1995).

4.3 Modelling the Spatial Correlation Function

For this work, the spatial correlation function is assumed to be a power law of the form,

$$\xi(r, z) = \left(\frac{r}{r_0}\right)^{-\gamma} (1+z)^{-(3+\epsilon)}, \quad (4.5)$$

(Efstathiou *et al.* 1991) where r is the spatial separation in physical coordinates, z is the redshift and r_0 , γ and ϵ are constants. If $\epsilon = 0$ the clustering is fixed in physical coordinates while if $\epsilon = \gamma - 3$ the clustering is fixed in comoving coordinates. This parameterisation of the evolution of the spatial correlation function is not valid at all redshifts but is a good approximation at $z < 1$ (Baugh *et al.* 1999). For galaxies selected with images in a single broadband, typical values of the parameters of $\xi(r, z)$ are $r_0 \sim 5h^{-1}\text{Mpc}$, $\gamma \sim 1.7$ (Maddox, Efstathiou & Sutherland 1996) and $\epsilon \sim -1$.

For a power law spatial correlation function, the resulting angular correlation function is a power law with

$$\omega(\theta) = \sqrt{\pi} \frac{\Gamma[(\gamma-1)/2]}{\Gamma(\gamma/2)} B r_0^\gamma \theta^{(1-\gamma)} \quad (4.6)$$

(Baugh & Efstathiou 1993) where B is a constant. The value of B is given by

$$B = \int_0^\infty g(z) \left(\frac{dN(z)}{dz}\right)^2 dz \bigg/ \left[\int_0^\infty \frac{dN(z)}{dz} dz \right]^2 \quad (4.7)$$

where

$$g(z) = \frac{dz}{dx} x^{1-\gamma} F(x) (1+z)^{-(3+\epsilon-\gamma)}, \quad (4.8)$$

x is the coordinate distance at redshift z , dN/dz is the number of galaxies per unit redshift detected by the survey and

$$F(x)^2 = 1 + \Omega_k (H_0 x/c)^2. \quad (4.9)$$

The value of x is given by

$$x = \frac{c}{H_0} \int_0^z \frac{dz}{E(z)} \quad (4.10)$$

where

$$E(z) \equiv \sqrt{\Omega_M(1+z)^3 + \Omega_k(1+z)^2 + \Omega_\Lambda}. \quad (4.11)$$

For values of $z < 0.5$, the value of B is more strongly dependent on r_0 , γ and the galaxy redshift distribution than the cosmological model. This is not unexpected as the value of x for $z = 0.4$ varies by less than 10% between $\Omega_M = 1$ and $\Omega_M = 0.2$ models of the Universe. As B does not strongly depend on cosmology at $z < 0.5$, only a single cosmological model is used with $H_0 = 75 \text{ km s}^{-1} \text{ Mpc}^{-1}$, $\Omega_M = 0.2$ and $\Omega_\Lambda = 0$.

There are two approaches to modelling the galaxy redshift distribution which are often used in the literature. The first approach uses an accurate description of the local luminosity function of different galaxy types, plus models of galaxy evolution and k -corrections for each type, and attempts to model the observed number counts and redshift distribution where data is available (i.e. Roche *et al.* 1996). This model includes the physics of galaxy evolution, however, it contains large numbers of free parameters and different models can readily reproduce the observed number counts. The second approach, which is applied to our single band imaging data, assumes a functional form for the redshift distribution and uses the observed number counts and redshift surveys to constrain the model (Baugh & Efstathiou 1993). This approach produces a good model of the redshift distribution but contains no physics of galaxy evolution and is limited by the depth of redshift surveys.

For a complete sample of galaxies brighter than magnitude m , the number of galaxies detected per unit redshift is given by

$$\frac{dN(z)}{dz} = A(m)z^2 \exp \left(- \left[\frac{z}{1.412z_m(m)} \right]^{3/2} \right) \quad (4.12)$$

where

$$A(m) = \frac{1.062N(m)\Omega}{z_m(m)} \quad (4.13)$$

(Baugh & Efstathiou 1993), $N(m)$ is the galaxy number counts, Ω is the survey area and z_m is the median redshift of the galaxy sample. As the value of B depends on the galaxy redshift distribution and not the galaxy number counts, the most important free parameter is z_m which is a function of band and limiting magnitude.

The median redshift as a function of limiting magnitude is obtained from a polynomial fit to median redshifts derived from galaxy redshift surveys. At low

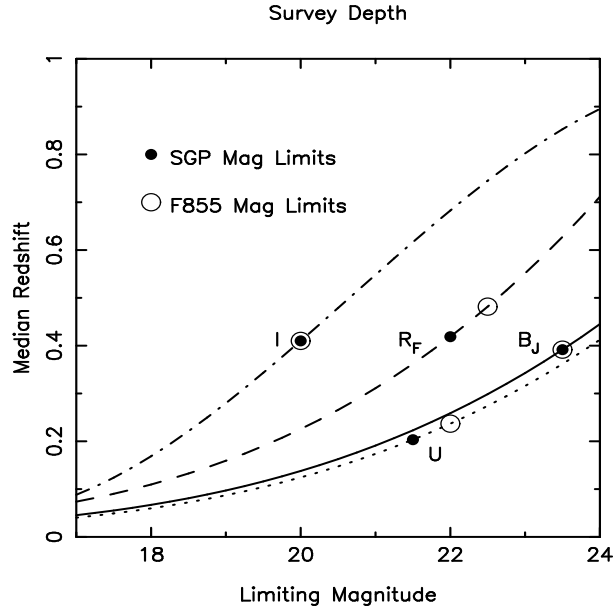


Figure 4.2: A plot of the model median redshift as a function of survey depth for U , B_J , R and I bands. The median redshift for the U band is derived using a median galaxy colour of $U - B_J \sim 0.3$. Magnitude limits for the SGP and F855 are shown with the large filled and open circles respectively.

redshift this is derived from the local galaxy luminosity function while at higher redshifts the median redshifts determined directly from the survey data are used. Local luminosity functions are assumed to be Schechter functions with $\alpha = -1.00$,

$$M_{B_J}^* = -19.5 - 5\log h \quad (4.14)$$

Loveday *et al.* (1992) and

$$M_R^* = -20.5 - 5\log h. \quad (4.15)$$

Changing the value of α to -1.3 reduces the estimate of the median redshift by $\sim 15\%$ resulting in a similar decrease of the estimate of r_0 . Galaxy k -corrections are approximated by $k_B(z) = 2z$ and $k_R(z) = 0.5z$. At $z \gtrsim 0.2$, median redshifts as a function of survey depth are derived from the redshift surveys of Colless *et al.* (1990), Glazebrook *et al.* (1995), Lin *et al.* (1999) and Munn *et al.* (1997). I band median redshifts are the same as Postman *et al.* (1998) which were derived from the CFHT redshift survey (Lilly *et al.* 1995). The median redshift of the U band data is determined with the B_J model and by assuming a median colour of $U - B_J \sim 0.2$. The functions for median redshift as a function of limiting magnitude are shown in Figure 4.2.

4.4 The Angular Correlation Function at Large Angular Scales

The $5^\circ \times 5^\circ$ field-of-view of each field allows the measurement of the faint galaxy correlation function at large angular scales. At $B_J \sim 23.5$ and $R \sim 22$, the median redshift of the data is $z \sim 0.4$ and a break in the spatial correlation function at $\sim 15h^{-1}\text{Mpc}$ in comoving coordinates (Maddox, Efstathiou & Sutherland 1996) corresponds to an angular scale of $\sim 1^\circ$.

It is possible to measure the angular correlation for each field to $\sim 5^\circ$ but at large angular scales the estimate of the correlation function will be dominated by individual structures. To determine the range of angular scales where the correlation function is representative, the estimates of the angular correlation functions for the SGP and F855 fields are compared. This provides a more reliable estimate than subsamples of the data as each subsample would have smaller field-of-view than the original data, resulting in overestimates of the errors at large angular scales.

The $B_J < 23.5$ and $R < 22$ correlation functions for each field are shown in Figures 4.3 and 4.4. As the integral constraint depends of γ , the data has been fitted with power laws with fixed γ to allow comparison of the 2 fields estimates of $\omega(\theta)$. For both fields the integral constraint is less than the amplitude of the correlation function at 1° . A power law matches the data well and there is no evidence of a break from a power law on all angular scales. However, on angular scales $\gtrsim 2^\circ$, the estimates of $\omega(\theta)$ for both fields are within 2σ of 0. It is therefore possible that the break in the correlation function is present at $15h^{-1}\text{Mpc}$ in comoving coordinates but can not be detected with this dataset.

4.5 The Correlation Function as a Function of Limiting Magnitude

The large fields-of-view used for this study reduce the errors associated with large structures along the line-of-sight. Also, the input catalogue of up to 2.5×10^5 galaxies results in small random errors in estimates of $\omega(\theta)$. Previous measures of the correlation function in U , B_J and R have been restricted to fields-of-view less than $\sim 2^\circ \times 2^\circ$ (Infante & Pritchett 1995). At the present time, only the I band survey by Postman *et al.* (1998) has a comparable field-of-view with greater

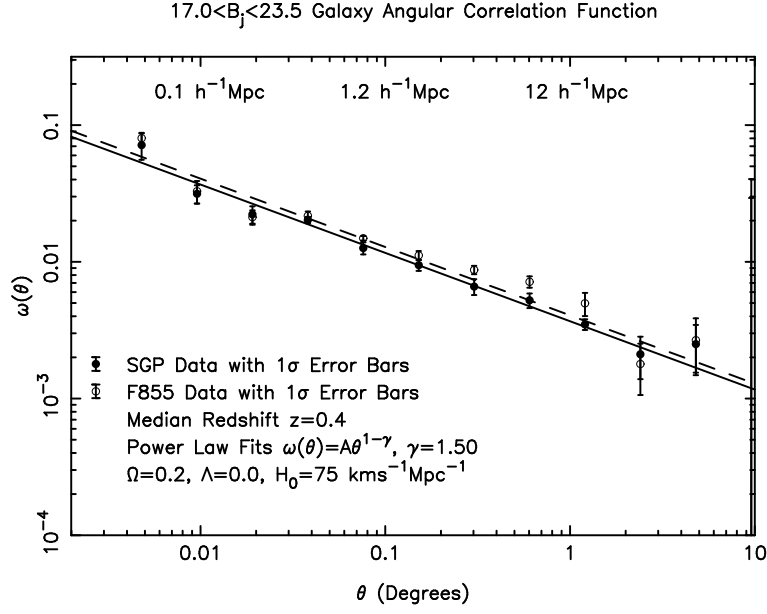


Figure 4.3: The $B_J < 23.5$ angular correlation function for the SGP and F855 fields. Power law fits to the SGP and F855 data are shown with solid and dashed lines respectively. The data in each field is fitted well by a power law and most data points are within 2σ of each other. There is no evidence of a break in the correlation function on any of the scales measured though $\omega(\theta)$ at $> 1^\circ$ is only $\sim 2\sigma$ more than 0. It is also possible both correlation functions could be biased by large structures on scales $> 1^\circ$.

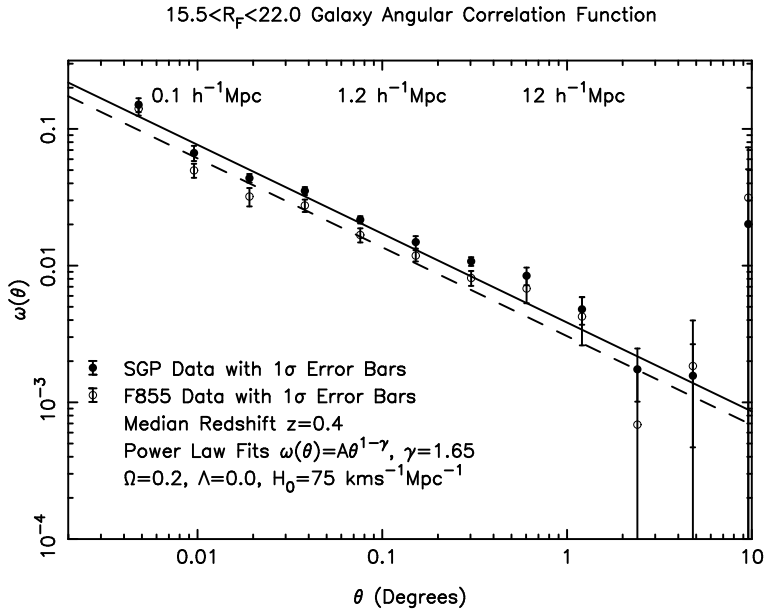


Figure 4.4: The $R < 22$ angular correlation function for the SGP and F855 fields. Power law fits to the SGP and F855 data are shown with solid and dashed lines respectively. The data for each field is fitted well by a power law and there is no evidence of a break in the correlation function on scales less than $\sim 2^\circ$. However, unlike the $B_J < 23.5$ data, there is an offset between the data in the two fields.

depth than this work.

Previous measurements of γ indicate that it may vary with band and survey depth (Infante & Pritchet 1995, Postman *et al.* 1998) though most values in the literature are between 1.6 and 1.8. The consistent data reduction method used for this work should allow the accurate comparison of γ as a function of band and survey depth.

Estimates of the value of $\omega(1')$ and γ derived from power law fits to the data are shown in Table 4.1. The amplitude of the correlation function is determined at $1'$ rather than 1° as the amplitude and γ are not independent and estimates of $\omega(1^\circ)$ depend strongly on γ . The values of γ show a weak trend towards smaller values with magnitude and bluer survey bands. As there is a correlation between galaxy colour and morphology (see Figure 4.9) and late type galaxies have shallower values of γ than early type galaxies, this trend is not unexpected.

While the value of γ does not differ by more than $\sim 2\sigma$ between the two fields, the amplitude of the correlation function varies by $\sim 100\%$ at bright magnitudes. While variations of amplitude could be caused by zero point errors, the error required is approximately 0.4 magnitudes in all bands at bright magnitudes with it decreasing to ~ 0 at $B_J \sim 23$. This is inconsistent with the photometric calibra-

Table 4.1: Galaxy number counts and the parameters for $\omega(\theta)$ determined with power law fits to data between $10''$ and 0.3° .

| Field (Area) | SGP (15.64°) | | | F855 (13.58°) | | |
|---------------------------|-----------------------|-----------------|--------------------------|------------------------|-----------------|--------------------------|
| Magnitude Range | N_{gal} | γ | $\omega(1') \times 10^3$ | N_{gal} | γ | $\omega(1') \times 10^3$ |
| $18.0 \leq U \leq 20.0$ | 4309 | 1.39 ± 0.18 | 418 ± 151 | 4913 | 1.53 ± 0.27 | 239 ± 52 |
| $18.0 \leq U \leq 21.0$ | 16379 | 1.65 ± 0.10 | 196 ± 16 | 16695 | 1.84 ± 0.10 | 125 ± 16 |
| $18.0 \leq U \leq 22.0$ | 80502 | 1.47 ± 0.10 | 63 ± 4 | 82965 | 1.47 ± 0.15 | 37 ± 5 |
| $18.0 \leq B_J \leq 20.0$ | 5267 | 1.58 ± 0.15 | 530 ± 85 | 5486 | 1.76 ± 0.17 | 335 ± 62 |
| $18.0 \leq B_J \leq 21.0$ | 15372 | 1.60 ± 0.12 | 280 ± 32 | 15149 | 1.72 ± 0.12 | 196 ± 27 |
| $18.0 \leq B_J \leq 22.0$ | 45519 | 1.53 ± 0.07 | 122 ± 7 | 43743 | 1.66 ± 0.11 | 90 ± 8 |
| $18.0 \leq B_J \leq 22.5$ | 82919 | 1.48 ± 0.09 | 72 ± 5 | 76149 | 1.60 ± 0.07 | 56 ± 4 |
| $18.0 \leq B_J \leq 23.0$ | 144577 | 1.53 ± 0.07 | 45 ± 2 | 123325 | 1.47 ± 0.08 | 38 ± 2 |
| $18.0 \leq B_J \leq 23.5$ | 230024 | 1.46 ± 0.07 | 28 ± 1 | 184717 | 1.49 ± 0.05 | 31 ± 2 |
| $16.5 \leq R \leq 18.5$ | 4330 | 1.68 ± 0.10 | 586 ± 80 | 4294 | 1.82 ± 0.17 | 397 ± 82 |
| $16.5 \leq R \leq 19.5$ | 13752 | 1.72 ± 0.07 | 346 ± 50 | 12841 | 1.81 ± 0.13 | 232 ± 32 |
| $16.5 \leq R \leq 20.5$ | 39748 | 1.70 ± 0.03 | 179 ± 9 | 37069 | 1.80 ± 0.08 | 130 ± 12 |
| $16.5 \leq R \leq 21.5$ | 112919 | 1.58 ± 0.05 | 72 ± 3 | 102373 | 1.70 ± 0.07 | 61 ± 4 |
| $16.5 \leq R \leq 22.0$ | 174385 | 1.57 ± 0.05 | 54 ± 2 | 173295 | 1.60 ± 0.05 | 43 ± 2 |
| $16.5 \leq R \leq 22.5$ | - | - | - | 234957 | 1.65 ± 0.07 | 32 ± 2 |
| $16.5 \leq I \leq 18.5$ | 9812 | 1.73 ± 0.07 | 322 ± 26 | 8913 | 1.82 ± 0.15 | 254 ± 41 |
| $16.5 \leq I \leq 19.5$ | 32178 | 1.67 ± 0.06 | 156 ± 11 | 28365 | 1.79 ± 0.12 | 115 ± 14 |
| $16.5 \leq I \leq 20.0$ | 54737 | 1.71 ± 0.05 | 108 ± 8 | 48743 | 1.80 ± 0.08 | 93 ± 8 |

tion, the galaxy number counts in Figure 3.9 and the colour-colour diagrams. A systematic error could be present in the data but it seems unlikely that it could effect $\omega(1')$ without causing large variations of γ .

If the values of $\omega(1')$ do not have significant systematic errors, a possible cause of the variations is that the two fields measure different populations of galaxies with different clustering properties. The SGP, which has stronger clustering than F855, contains “sheets” perpendicular to the line-of-sight (Broadhurst *et al.* 1990) and smaller structures including 11 Abell clusters (Abell, Corwin & Olowin 1989). Of these clusters, 8 appear to be associated with a structure at $z \sim 0.11$ identified by Broadhurst *et al.* (1990). $M_{B_J} \sim -19.5$ (M^*) galaxies at $z \sim 0.11$ have an apparent magnitude of $B_J \sim 18$ and this population of galaxies is too small to significantly bias estimates of the $B_J > 20$ correlation function. However, it is possible that the cluster population of $M_{B_J} \gtrsim -16$ galaxies could bias estimates of the correlation function if they are a significant fraction of the observed galaxy number counts.

To test if the $z = 0.11$ clusters do significantly effect the correlation function, the correlation function has been determined with $2^\circ \times 2^\circ$ ($\sim 10h^{-1}\text{Mpc} \times 10h^{-1}\text{Mpc}$) regions surrounding the clusters removed from the data. As the clusters are not uniformly distributed across the field-of-view, the size of the catalogue is reduced by $\sim 60\%$. Table 4.2 lists the amplitude of the B_J and R band correlation functions for the SGP field without the clusters and F855 for comparison. The amplitude of the correlation function has decreased significantly compared with the original estimates for the SGP. While most noticeable at bright magnitudes, the effect is also significant at fainter magnitudes where the contribution from nearby clusters might be expected to be small. This is consistent with $M_{B_J} \gtrsim -16$ galaxies within the clusters significantly effecting estimates of the faint galaxy correlation function. However, details of the relationship between clusters and the observed clustering will be explored in Chapter 5.

For the following discussion of the amplitude as a function of limiting magnitude, the estimates of the SGP correlation function including the $z = 0.11$ clusters are used. While it is probable relatively nearby clusters do effect estimates of the correlation function, there is no clear justification for excluding them. Also, excluding the regions surrounding the clusters significantly reduces the number of galaxy pairs used to determine the correlation function, significantly increasing random errors.

Table 4.2: Measured parameters for $\omega(\theta)$ determined from power law fits to data between $10''$ and 0.3° . Clusters at $z \sim 0.11$ have been removed from the SGP sample to reduce the effect dwarf galaxies may have on the estimate of the correlation function.

| Field | SGP (no $z = 0.11$ clusters) | | | F855 | | |
|---------------------------|------------------------------|-----------------|--------------------------|-----------|-----------------|--------------------------|
| Magnitude Range | N_{gal} | γ | $\omega(1') \times 10^3$ | N_{gal} | γ | $\omega(1') \times 10^3$ |
| $18.0 \leq B_J \leq 20.0$ | 1742 | 1.95 ± 0.35 | 530 ± 85 | 5486 | 1.76 ± 0.17 | 335 ± 62 |
| $18.0 \leq B_J \leq 21.0$ | 5487 | 1.76 ± 0.20 | 200 ± 44 | 15149 | 1.72 ± 0.12 | 196 ± 27 |
| $18.0 \leq B_J \leq 22.0$ | 16679 | 1.72 ± 0.12 | 108 ± 11 | 43743 | 1.66 ± 0.11 | 90 ± 8 |
| $18.0 \leq B_J \leq 22.5$ | 30886 | 1.61 ± 0.17 | 60 ± 8 | 76149 | 1.60 ± 0.07 | 56 ± 4 |
| $18.0 \leq B_J \leq 23.0$ | 54549 | 1.54 ± 0.15 | 36 ± 4 | 123325 | 1.47 ± 0.08 | 38 ± 2 |
| $18.0 \leq B_J \leq 23.5$ | 87453 | 1.56 ± 0.16 | 22 ± 3 | 184717 | 1.49 ± 0.05 | 31 ± 2 |
| $16.5 \leq R \leq 18.5$ | 1460 | 2.16 ± 0.14 | 339 ± 170 | 4294 | 1.82 ± 0.17 | 397 ± 82 |
| $16.5 \leq R \leq 19.5$ | 4974 | 1.84 ± 0.18 | 223 ± 30 | 12841 | 1.81 ± 0.13 | 232 ± 32 |
| $16.5 \leq R \leq 20.5$ | 14481 | 1.76 ± 0.13 | 144 ± 12 | 37069 | 1.80 ± 0.08 | 130 ± 12 |
| $16.5 \leq R \leq 21.5$ | 41767 | 1.67 ± 0.11 | 65 ± 6 | 102373 | 1.70 ± 0.07 | 61 ± 4 |
| $16.5 \leq R \leq 22.0$ | 65168 | 1.71 ± 0.10 | 49 ± 2 | 173295 | 1.60 ± 0.05 | 43 ± 2 |

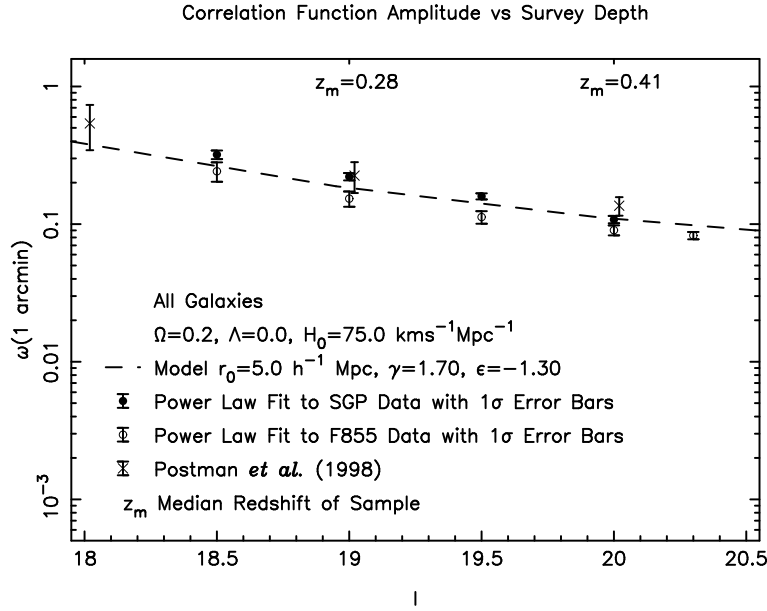


Figure 4.5: The I band correlation function amplitude. The measurements of the amplitude are consistent with the data of Postman *et al.* (1998) which is shown with crosses. The data from Postman *et al.* (1998) has been corrected for the assumption that $\gamma = 1.7$.

Figures 4.5 to 4.8 plot the I , R , B_J and U band angular correlation function amplitudes as a function of limiting magnitude. The amplitude of the correlation function has been determined with fixed values of γ to reduce the dependence of the amplitude on γ . As the values of the angular correlation function differ significantly between each field, no attempt has been made to fit the data. Instead, a model has been plotted with clustering fixed in comoving coordinates and $r_0 = 5h^{-1}\text{Mpc}$. The value of r_0 is similar to values derived by Maddox, Efstathiou & Sutherland (1996) and Postman *et al.* (1998).

Figure 4.5 shows the measured amplitude of the I band correlation function for the SGP, F855 and Postman *et al.* (1998). The measured clustering in the SGP is in good agreement with Postman *et al.* (1998), while F855 measures slightly weaker clustering. The model of the clustering is also a reasonable estimate of the observed clustering across the magnitude range observed. Figures 4.6 to 4.8 show the R , B_J and U band clustering to be significantly weaker than the I band clustering for galaxies with a similar range of redshifts. Comparison with the results of Infante & Pritchett (1995) show the SGP has similar clustering in B_J and weaker clustering in R . Infante & Pritchett (1995) may measure stronger clustering than F855 as their field is located in the NGP which has similar large scale structures as the SGP (Broadhurst *et al.* 1990).

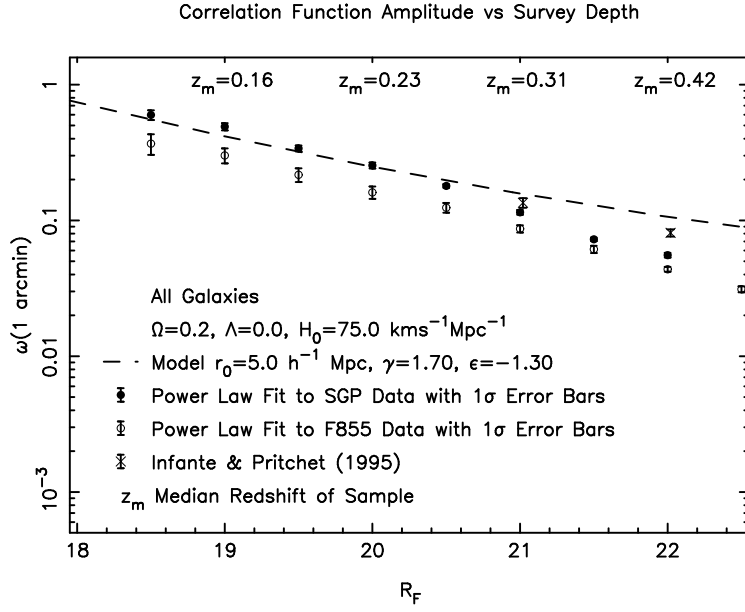


Figure 4.6: The R band correlation function amplitude. While the redshift range is similar to the I band data, the galaxy clustering is significantly weaker.

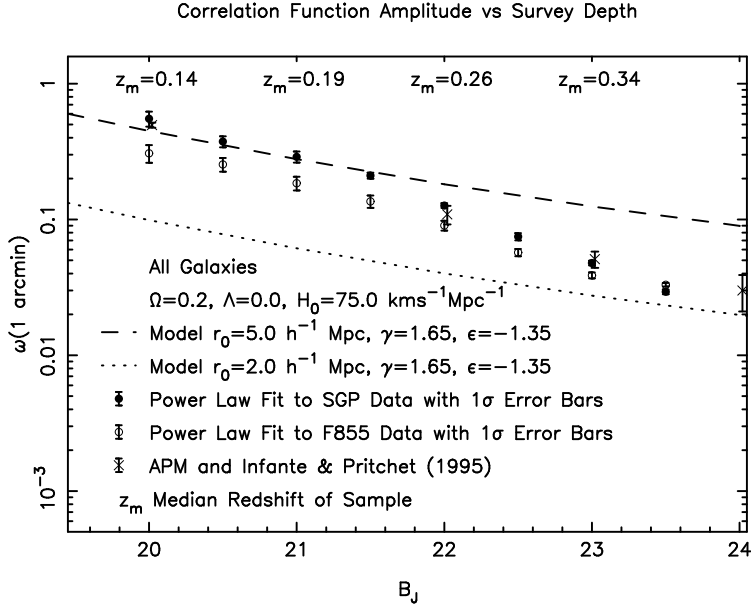


Figure 4.7: The B_J band correlation function amplitude. As with the R band data, the amplitude of the correlation function is significantly weaker than the I band correlation function. At magnitudes fainter than $B_J \sim 22$, the correlation function rapidly decreases with limiting magnitude. There is also a decrease in the discrepancy between the SGP and F855 measurements with increasing limiting magnitude.

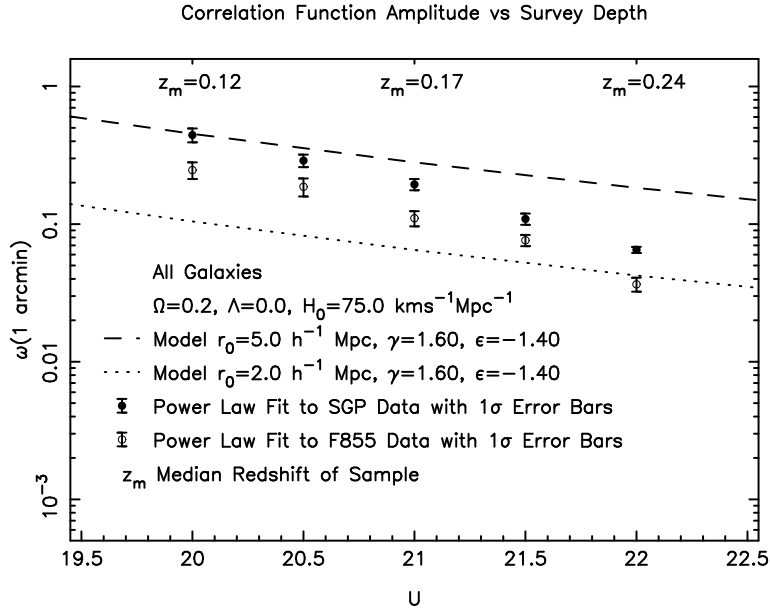


Figure 4.8: The U band correlation function amplitude. The amplitude of the correlation function is consistently weaker than the fit to the I band data shown with the dashed line.

While the $r_0 = 5.0 h^{-1} \text{ Mpc}$ model is a good fit to the SGP $R < 20$ and $B_J < 21$ data, at fainter magnitudes a rapid decline in the amplitude of the correlation function is observed. The rapid decline of the faint correlation function has been observed previously by Efstathiou *et al.* (1991), Infante & Pritchet (1995) and Roche *et al.* (1996). Obviously, the R and B_J band data are sampling a different population of galaxies to the I band sample. To be consistent with galaxy redshift surveys, the $B_J \sim 23$ galaxies must be dominated by a population of weakly ($r_0 \sim 2.0 h^{-1} \text{ Mpc}$) clustered galaxies at $z \sim 0.4$ (Efstathiou *et al.* 1991, Efstathiou 1995).

For a no-evolution model for the galaxy population, the blue bands will sample galaxies with bluer colours due to the large k -corrections of early-type galaxies (Coleman, Wu & Weedman 1980). As shown in Figure 4.9, the local population of blue ($U - B_J \lesssim 0$) galaxies is dominated by late-type galaxies. Measurements of the galaxy clustering in the local universe with morphology-selected catalogues show the clustering of late-type galaxies is considerably weaker than early-type galaxies (Davis & Geller 1976, Loveday *et al.* 1995). If the colours and clustering of $z \sim 0.4$ late and early type galaxies are similar to $z \sim 0$ galaxies, the decrease in the amplitude of the B_J angular correlation function could be a selection effect. While it is impossible to determine the morphologies of the $B_J > 21$ galaxies with this catalogue, it should be possible to use colour selection to select early and late

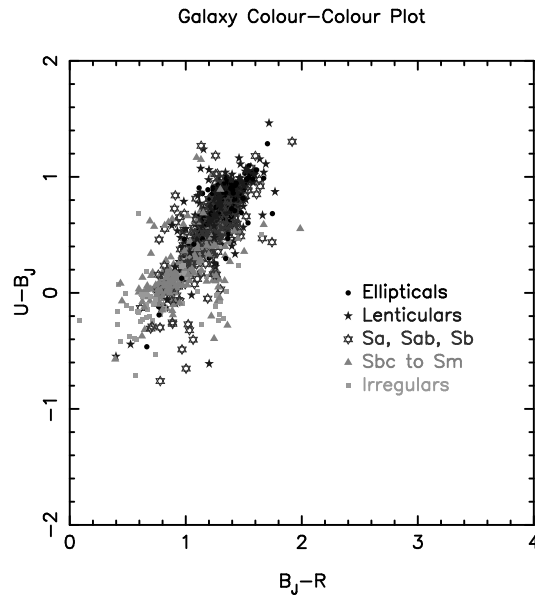


Figure 4.9: The colours of RC3 catalogue (de Vaucouleurs *et al.* 1991) galaxies by morphological type. Photometry is from Prugniel & Heraudeau (1998) while morphological classification of galaxies is from de Vaucouleurs *et al.* (1991). The correlation between morphology and colour can be clearly seen with late type galaxies generally having bluer colours than early types.

type galaxies over a range of redshifts.

4.6 The Correlation Function of Colour Selected Galaxies

The obvious colour selection criteria for galaxies is a single colour cut in the deepest bands available (B_J and R). However, as shown in Figure 4.10, the colour of individual galaxy types varies with redshift. Even with a single colour cut, the blue subsample will generally select later type galaxies than the red subsample and blue subsamples generally show weak clustering (Infante & Pritchett 1995, Roche *et al.* 1996). A $B_J - R$ cut that varies with magnitude may select the same population over a range of redshifts but the selection criteria would depend on the cosmological parameters used. Also, colour selection of a fraction of galaxies (i.e. the reddest 20% of the catalogue) may not be effective due to the changing morphological mix of galaxies with magnitude.

Selection of galaxies with two or more colour criteria should allow the selection of galaxy types over a large range of redshifts without strong dependence on

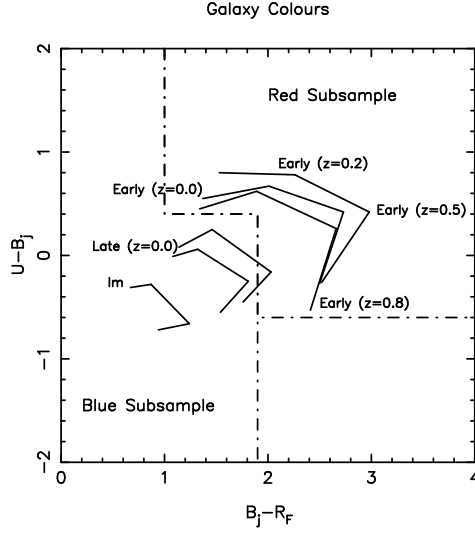


Figure 4.10: The colour selection criteria for the red and blue subsamples. Colours of early, late and irregular type galaxies at $z = 0$, $z = 0.2$, $z = 0.5$ and $z = 0.8$ from Fukugita, Shimasaku & Ichikawa (1995) are shown. The colour selection criteria for each subsample are shown with the dot-dash line. The blue subsample consists of galaxies below and to the left of the line while the red subsample consists of galaxies above and to the right of the line. The blue subsample is dominated by late and irregular type galaxies while the red subsample selects early type galaxies.

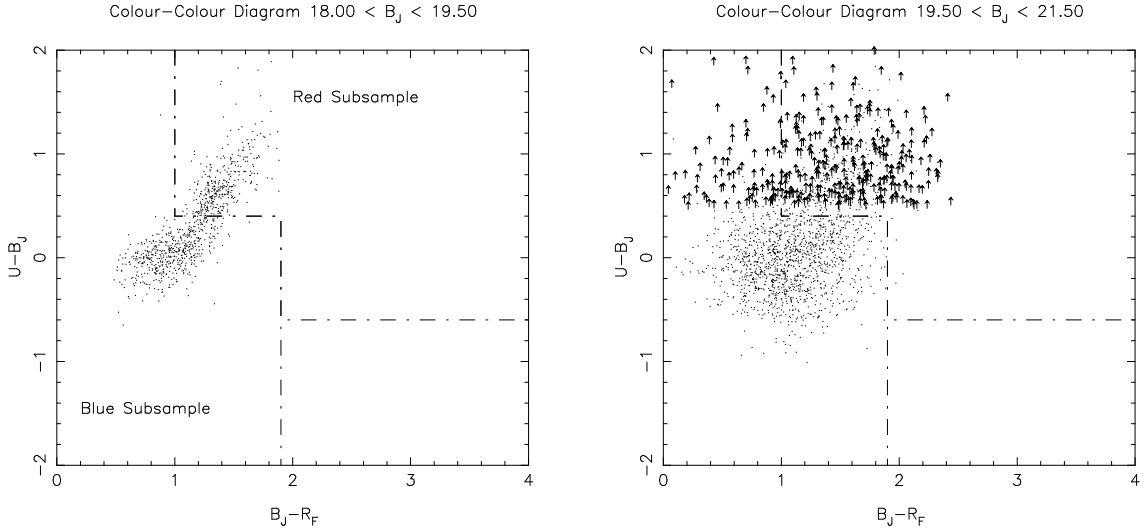


Figure 4.11: Galaxy colour-colour diagrams for the SGP shown with the selection criteria for the two subsamples.

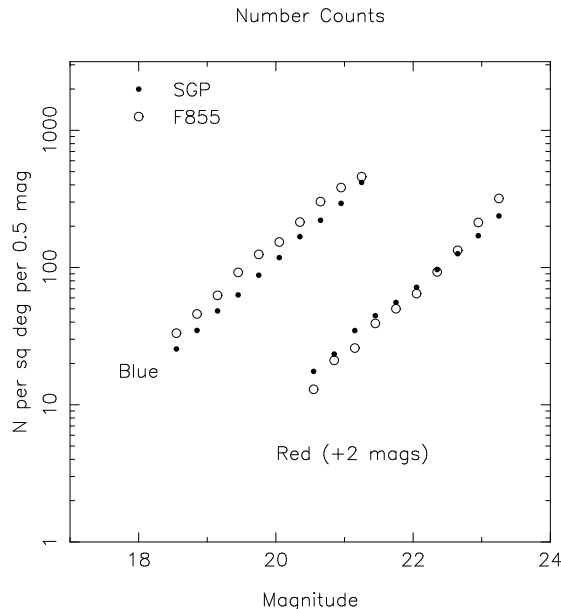


Figure 4.12: A plot of the red and blue subsample number counts for the SGP and F855.

cosmological parameters. Figure 4.10 shows the predicted colours of early, late and irregular type $0 \leq z \leq 0.8$ galaxies from Fukugita, Shimasaku & Ichikawa (1995). Colour selection criteria for a red and blue subsample are also shown. The samples are limited to $B_J < 21.6$ due to the $U = 22$ magnitude limit of the catalogues and the $U - B_J > 0.4$ selection criteria. As most $B_J < 21.6$ galaxies are at redshifts $z \leq 0.3$, most galaxies in the subsamples are selected with the $U - B_J$ selection criteria. Galaxies with $U - B_J$ lower limits and $B_J - R$ upper limits have been included in the subsamples to prevent incompleteness. Figure 4.11 shows the colours of galaxies in the SGP with the subsample selection criteria. The location of the $B_J < 19.5$ galaxy locus is similar to that for RC3 catalogue galaxies in Figure 4.9 though at $B_J > 19.5$ there is an increasing fraction of very blue galaxies. Galaxy number counts for the 2 subsamples are shown in Figure 4.12. While the SGP does include significantly more clusters than F855 at low redshift, there is good agreement between the number counts across the magnitude range observed.

While the selection criteria are relatively simple, it can be clearly seen that the red and blue subsample should select early and late type galaxies respectively. The blue subsample should also contain most of the galaxies with significant star formation rates while the red subsample should contain more passive galaxies. As shown in Figure 4.13, comparison with the spectroscopic catalogue of Colless *et al.* (1990) shows that most of the [OII] 3727Å emitters detected in the SGP

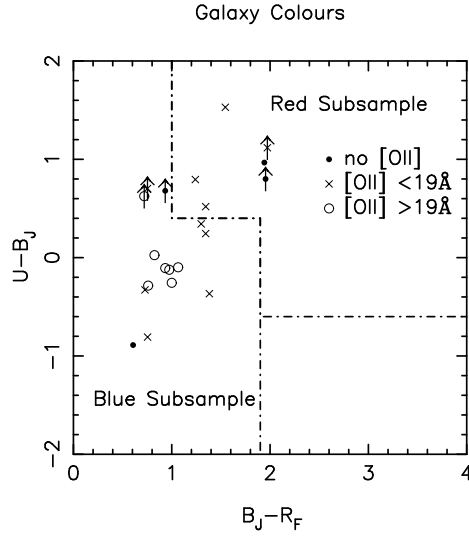


Figure 4.13: A colour-colour diagram of $B_J < 21.5$ galaxies in the SGP and F855 with spectroscopic observations by Colless *et al.* (1990). Lower limits in $U - B_J$ are shown with arrows. A trend towards bluer colours with $[\text{OII}] 3727\text{\AA}$ emission can be observed with strong $[\text{OII}] 3727\text{\AA}$ emitters restricted to the blue subsample.

and F855 are included in the blue subsample. To measure the clustering of star-forming galaxies Cole *et al.* (1994) selected galaxies with $[\text{OII}] 3727\text{\AA}$ equivalent widths greater than 19\AA ; all galaxies matching this selection criteria would be included in the blue subsample for both fields. Interestingly, the galaxies without $[\text{OII}] 3727\text{\AA}$ emission do not show such an obvious trend with similar numbers in both subsamples. However, the small number of galaxies without $[\text{OII}] 3727\text{\AA}$ emission results in these galaxies comprising less than 15% of the total of blue galaxies.

The $B_J < 21.5$ angular correlation functions of the blue and red subsamples of F855 are shown in Figure 4.14. Visual inspection shows the significant difference in clustering strength and the value of γ for the two subsamples with the red subsample being strongly clustered and having a higher value of γ . This trend is consistent with measurements of the angular correlation functions of morphology selected catalogues where $\gamma \sim 1.8$ for early-type galaxies and $\gamma \sim 1.5$ for late-type galaxies (Loveday *et al.* 1995).

Estimates of γ and $\omega(1')$ as a function of limiting magnitude are listed in Table 4.3. The $z \sim 0.11$ clusters in the SGP have been retained in the data as there is no obvious justification for rejecting them from the sample. While γ differs significantly between the two subsamples, the values of γ are within 1σ

Table 4.3: Measured parameters for $\omega(\theta)$ for the red and blue subsamples determined from power law fits to data between $10''$ and 0.3° .

| Field | | | SGP | | | F855 | |
|--------|---------------------------|-----------|-----------------|--------------------------|-----------|-----------------|--------------------------|
| Sample | Magnitude Range | N_{gal} | γ | $\omega(1') \times 10^3$ | N_{gal} | γ | $\omega(1') \times 10^3$ |
| Blue | $18.0 \leq B_J \leq 20.0$ | 2963 | 1.45 ± 0.51 | 212 ± 3200 | 3354 | 1.41 ± 0.58 | 170 ± 2710 |
| Blue | $18.0 \leq B_J \leq 21.0$ | 9079 | 1.49 ± 0.18 | 138 ± 27 | 9228 | 1.61 ± 0.38 | 110 ± 39 |
| Blue | $18.0 \leq B_J \leq 21.5$ | 15579 | 1.57 ± 0.20 | 86 ± 19 | 14329 | 1.51 ± 0.32 | 75 ± 32 |
| Red | $18.0 \leq B_J \leq 20.0$ | 1993 | 1.65 ± 0.22 | 1339 ± 278 | 1851 | 2.09 ± 0.17 | 954 ± 210 |
| Red | $18.0 \leq B_J \leq 21.0$ | 5552 | 1.69 ± 0.12 | 782 ± 73 | 5424 | 1.89 ± 0.13 | 480 ± 82 |
| Red | $18.0 \leq B_J \leq 21.5$ | 9317 | 1.72 ± 0.08 | 616 ± 51 | 9922 | 1.83 ± 0.14 | 319 ± 44 |

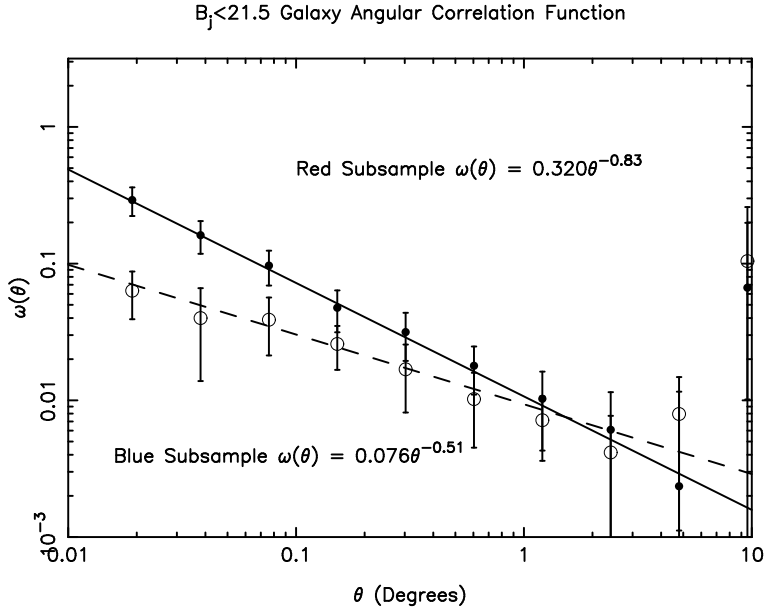


Figure 4.14: The $B_J < 21.5$ angular correlation function for the red and blue subsamples of F855. The red subsample shows stronger clustering and a higher value of γ , consistent with the strong clustering of elliptical and early type galaxies in the local universe.

of being constant as a function of limiting magnitude. The values of $\omega(1')$ for the blue subsamples are remarkably similar for the SGP and F855. However, the red subsamples show large differences with the amplitude of the clustering in the SGP being $\sim 100\%$ larger than F855.

To model the spatial correlation function, a model of the redshift distribution for the red and blue subsamples is required. Luminosity functions for galaxies selected by morphology are available but it is not clear if luminosity is more or less strongly correlated with colour than morphology. The $U - B_J < 0.2$ and $U - B_J > 0.2$ galaxy luminosity functions of Metcalfe *et al.* (1998) are therefore used. Approximate k -corrections of $k(z) = 3z$ and $k(z) = z$ are used for the red and blue subsample respectively. The Metcalfe *et al.* (1998) luminosity functions are used rather than the redshift distribution model as the steep slope of faint end of the luminosity functions results in skewed redshift distributions.

Plots of the estimated median redshift for the red and blue luminosity functions are shown in Figures 4.15 and 4.16. The SGP and/or F855 overlap the B_J magnitude limited redshift surveys of Colless *et al.* (1990) and Ratcliffe *et al.* (1998) which have been used to measure the median redshifts of the red and blue subsamples as a function of magnitude. In addition, ~ 700 galaxy redshifts are available from the NASA/IPAC Extragalactic Database (NED) and these have

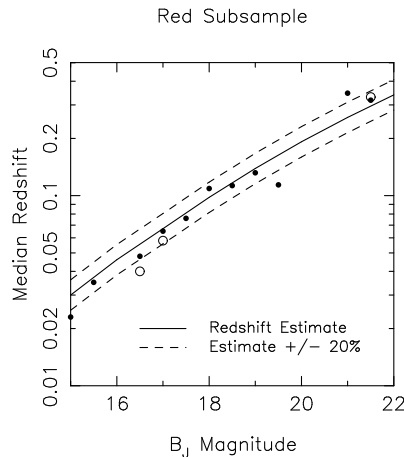


Figure 4.15: The median redshift as a function of magnitude for the red subsample. Data points from B_J band magnitude limited surveys are shown with circles while data using NED redshifts is shown with dots. The median redshift estimate and data points have been determined using 0.5 magnitude wide bins. As the estimates of the correlation function use wider magnitude bins, the estimates of the median redshift in this plot are higher than in Figure 4.17.

been used to show the *approximate* median redshift as a function of magnitude. For both subsamples, the model is a reasonable estimate of the redshift with few data points being more than 20% from the model redshift estimate.

Figure 4.17 shows the amplitude of the SGP and F855 red subsamples as a function of limiting magnitude with γ fixed at 1.8. A model of the early type galaxy correlation function with $r_0 = 5.9h^{-1}\text{Mpc}$ (Loveday *et al.* 1995) and clustering fixed in physical coordinates ($\epsilon = 0$) is also shown. Clustering fixed in physical coordinates would be applicable to galaxies in gravitationally bound clusters. The model, shown with the dashed line, does not fit either set of data but this is not unexpected as the SGP and F855 fields exhibit significantly different clustering amplitudes. However, the clustering in both fields is consistently stronger than the clustering of all B_J galaxies in F855. This is consistent with the red subsample being dominated by strongly clustered early type galaxies.

Figure 4.18 plots the amplitude of the blue subsample correlation function derived from power law fits with γ fixed to 1.5. Unlike the red subsample, the amplitudes derived from the SGP and F855 data agree at all magnitudes. If dwarf galaxies are increasing the amplitude of the SGP correlation function, this implies that they are red galaxies such as dwarf ellipticals within the clusters. A model with extremely weak clustering ($r_0 = 2h^{-1}\text{Mpc}$) fixed in comoving coordinates

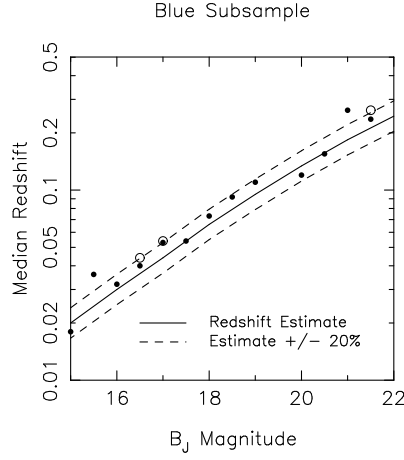


Figure 4.16: The median redshift as a function of magnitude for the blue subsample. Data points from B_J band magnitude limited surveys are shown with circles while data using NED redshifts is shown with dots. The median redshift estimate and data points have been determined using 0.5 magnitude wide bins. As the estimates of the correlation function use wider magnitude bins, the estimates of the median redshift in this plot are higher than in Figure 4.18.

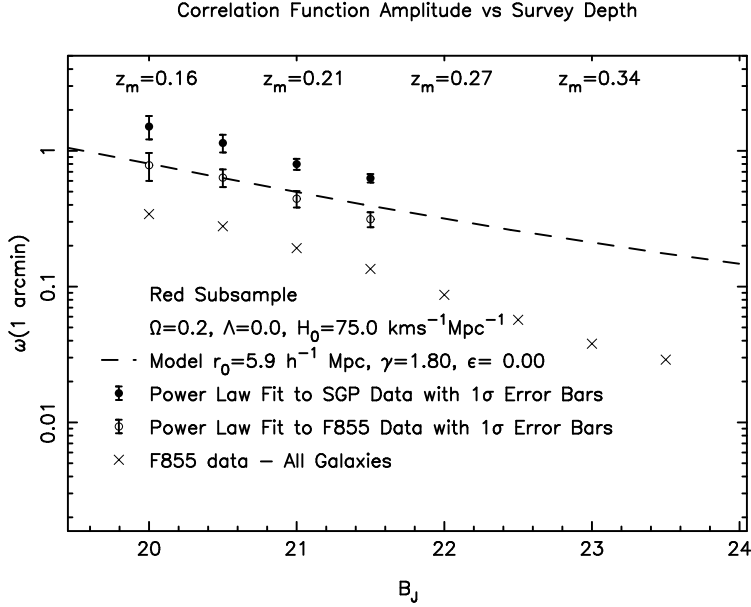


Figure 4.17: The amplitude of the clustering of the red subsamples as a function of magnitude. The value of γ has been fixed to 1.8. The clustering strength in the two fields differs by $\sim 100\%$ at all magnitudes. Both fields show strong clustering, consistent with the red subsamples being dominated by early type galaxies.

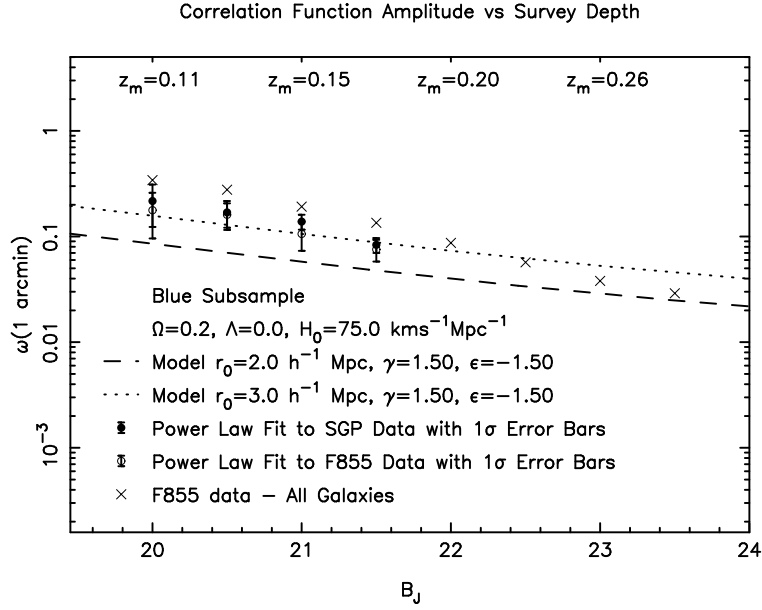


Figure 4.18: The amplitude of the clustering for the blue subsamples as a function of magnitude. The value of γ has been fixed to 1.5. The blue galaxies are extremely weakly clustered with a similar spatial correlation function to faint B_J galaxies. As the $B_J \sim 23$ number counts are dominated by blue galaxies (Guhathakurta, Tyson & Majewski 1990), this is strong evidence for star forming galaxies being weakly clustered from $z \sim 0.4$ until the present epoch.

is also shown in Figure 4.18. The amplitude of the clustering is similar to that estimated for faint galaxies by Efstathiou (1995) and $z \sim 0.5$ galaxies by Le Fèvre *et al.* (1996). The model slightly underestimates the strength of the clustering and a model with stronger clustering, $r_0 = 3h^{-1}\text{Mpc}$, is a better fit to the data. This is significantly weaker than $r_0 \sim 4.4h^{-1}\text{Mpc}$, the measured clustering of late type galaxies in the local Universe (Loveday *et al.* 1995). The only large sample of low z galaxies with similar properties ($r_0 \sim 3h^{-1}\text{Mpc}$, $\gamma \sim 1.8$) are galaxies with [OII] or H α emission lines with large equivalent widths from the Stromlo-APM survey (Loveday, Tresse & Maddox 1999). However, the Stromlo-APM sample has significantly stronger clustering than the blue subsample or faint blue galaxies on scales $\lesssim 2h^{-1}\text{Mpc}$.

An underestimate of the redshift by $\gtrsim 50\%$ could explain the weak clustering at $B_J \sim 20$ but this would be difficult to reconcile with the redshift data in Figure 4.16. Altering the assumed cosmological parameters can change estimates of spatial correlation function but the effect is negligible at $z \sim 0$ and is less than 30% at $z = 0.2$. A plausible explanation is that the clustering of galaxies is more strongly correlated with colour and stellar population than morphology. This would explain why no local population of galaxies selected by morphology displays the weak clustering of faint blue galaxies. This may also be the first detection of large population of galaxies at low redshift with similar clustering properties to faint blue galaxies.

4.7 Summary

The Panoramic Deep Fields have been used to study the clustering of galaxies from $z \sim 0$ to $z \sim 0.4$. The key conclusions are:

(i) The galaxy spatial correlation function is a power law on comoving scales less than $15h^{-1}\text{Mpc}$. At larger scales, the correlation function is consistent with a power law though a break in the correlation function is not inconsistent with the data.

(ii) Despite the large fields-of-view, there are significant differences in the measured amplitude of the clustering; with the possible exception of blue galaxies. It is clear that fields larger than 100arcmin^2 are required to accurately measure the clustering of $B_J \sim 22$ galaxies.

(iii) Dwarf galaxies in relatively nearby clusters ($z \sim 0.11$) may effect estimates

of faint galaxy correlation function. The effect is colour dependent with the clustering of red galaxies varying significantly between the 2 fields observed.

(iv) The clustering properties of galaxies strongly depend on the band used to select the catalogue. Bluer bands show weaker clustering than red bands and there is a rapid decline of the amplitude of the B_J correlation function at faint magnitudes. It is probably inappropriate to fit a simple clustering model to correlation functions derived from single band imaging due to the changing morphological mix with magnitude.

(v) The clustering properties of galaxies strongly depend on colour. Such behaviour is consistent with colour being correlated with morphological type. Red galaxies (early types) exhibit stronger clustering with larger values of γ than blue galaxies (late and irregular types).

(vi) Blue galaxies have extremely weak clustering with $r_0 \lesssim 3h^{-1}\text{Mpc}$. This is considerably weaker than the clustering of late type galaxies and is consistent with the clustering of galaxies being more strongly correlated with colour and stellar population than morphology.

(vii) The clustering of $B_J < 21.5$ blue galaxies is comparable to $B_J > 23$ blue galaxies. This is strong evidence for star forming galaxies being weakly clustered from $z \sim 0.4$ until the present epoch.

Chapter 5

A Survey for Distant Clusters

5.1 Introduction

Clusters are thought to trace the locations of the largest overdensities of baryonic and dark matter in the early Universe (van Albada 1961, Peebles 1970, Frenk *et al.* 1990). Therefore their number density, distribution and evolution place strong constraints on structure formation and cosmological models. The strong clustering of galaxy clusters at the present epoch allows them to be used as tracers of large-scale structure on distance scales where the amplitude of the galaxy autocorrelation function is negligible (Dalton *et al.* 1994). While recent studies of high redshift clusters have placed constraints on the epoch of cluster formation (Postman, Lubin & Oke 1998), the constraints on the number density and autocorrelation function of intermediate redshift clusters ($z \sim 0.5$) are poor.

Several large catalogues of $z < 0.2$ clusters selected from Schmidt telescope plates have been used to determine cluster properties at the current epoch (Abell 1958, Abell, Corwin & Olowin 1989, Lumsden *et al.* 1992, Dalton *et al.* 1997) but there are no equivalent spectroscopic samples at higher redshifts. Smaller spectroscopic samples of $z \gtrsim 0.4$ clusters do exist but are not suitable for studies of large-scale structure as they were selected visually from fields-of-view $\lesssim 2^\circ \times 2^\circ$. (Gunn, Hoesell & Oke 1986, Couch *et al.* 1991). The Panoramic Deep Fields allow the selection of clusters to $z \sim 0.5$ over two $5^\circ \times 5^\circ$ fields. The large size of the fields results in a catalogue of clusters suitable for statistically significant studies of the evolution and distribution of clusters as a function of redshift.

5.2 Methods for Identifying Clusters

The cluster selection method will significantly affect the type, completeness and depth of the samples selected. Most catalogues of clusters selected from photographic material rely on visual inspection and the application of a set of selection criteria (Abell 1958, Gunn, Hoessel & Oke 1986, Abell, Corwin & Olowin 1989, Couch *et al.* 1991). Selection criteria include searching for excess galaxy counts in small regions or cells (Couch *et al.* 1991). However, the resulting catalogues can suffer from non-uniformity due to the varying quality of visual inspection and variations of plate quality. These errors can be reduced if multiple observers inspect plates for clusters (Abell, Corwin & Olowin 1989) or by obtaining photometric calibration of the plates using CCD photometry or galaxy number counts (Gunn, Hoessel & Oke 1986, Couch *et al.* 1991)

A more uniform method for selecting clusters is to apply the selection criteria automatically to a machine readable galaxy catalogue (Lumsden *et al.* 1992, Lidman & Peterson 1996, Dalton *et al.* 1997). For photometrically calibrated datasets, this also allows galaxy magnitudes to be included in the selection criteria. As the apparent magnitude of the cluster galaxies is correlated with the cluster distance, an appropriate weighting scheme can also be used to derive an approximate cluster distance. However, spurious clusters are often detected by automated cell counts near bright stars or at the edges of spiral galaxies where the arms are broken up into multiple objects (Couch *et al.* 1991, Olsen *et al.* 1998).

A particularly useful method for detecting high redshift clusters is the detection of sky background variations (Dalcanton 1996) from the integrated light of (undetected) cluster galaxies. The advantage of this method is that 2m-class telescopes can be used to select $z \sim 1$ clusters. However, the technique requires extremely well flat-fielded images such as those provided by CCD drift scans. If suitable data is used, the success rate for the method is high with $\sim 80\%$ of cluster candidates being high redshift clusters (Zaritsky *et al.* 1997). Unfortunately, this method is not applicable to the Panoramic Deep Fields as the median subtraction of the sky background will reduce any signal present from high redshift clusters.

A recent development for the detection of clusters is the use of matched filters (Postman *et al.* 1996, Olsen *et al.* 1998, Kepner *et al.* 1999). The filter assumes a cluster galaxy luminosity function and a radial profile for the number density of cluster galaxies. A likelihood map of the survey area for a range of redshifts is then

Table 5.1: A Sample of Cluster Surveys and Methods

| Survey | Magnitude Limits | Area (\square°) | Number of Candidates | Method |
|-------------------------------|------------------------------------|-----------------------------|-------------------------|-----------------------|
| Abell (1958) | $B_J \sim 20$ | - | 2712 | Visual Inspection |
| Abell, Corwin & Olowin (1989) | $B_J \sim 20$ | All Sky | 4073 | Visual Inspection |
| Couch <i>et. al</i> (1991) | $B_J \simeq 24.4, R_F \simeq 22.9$ | ~ 80 | 112 | Visual Cell Counts |
| Dalton <i>et al.</i> (1997) | $B_J = 20.5$ | 4300 | 957 | Automated Algorithm |
| Gunn, Hoessel & Oke (1986) | Various | 154.7 | 418 | Visual Cell Counts? |
| Lidman & Peterson (1996) | $I \simeq 22.7$ | 13 | 105 | Automated Cell counts |
| Lumsden <i>et al.</i> (1992) | $B_J = 20.5$ | 1600 | 737 | Weighted Cell Counts |
| Olsen <i>et. al</i> (1998) | $I \simeq 23.0$ | 2.5 | 39 | Matched Filter |
| Postman <i>et. al</i> (1996) | $V \simeq 23.8, I \simeq 22.5$ | 5.1 | 107 | Matched Filter |
| Zaritsky <i>et. al</i> (1997) | $I \simeq 22.5?$ | 140 | ~ 300 | Background Variations |

produced with the peaks corresponding to clusters which have properties similar to the filter. As the apparent luminosity function and radial profile changes with redshift, it is possible to determine approximate cluster redshifts ($\Delta z \leq 0.2$) with a matched filter. The matched filter of Kepner *et al.* (1999) significantly improves on previous filters by allowing the inclusion of spectroscopic and photometric redshift information. As galaxies in the Panoramic Deep Fields are imaged in up to 4 bands, the Kepner *et al.* filter has been employed to uniformly select a catalogue of distant clusters in the SGP and F855 fields.

5.3 The Adaptive Matched Filter

The Adaptive Matched Filter (AMF) method applied here is almost identical to that described by Kepner *et al.* (1999). A summary of the method is provided here though the reader is referred to Kepner *et al.* (1999) for a more thorough discussion of the AMF.

The AMF assumes the number density of observed galaxies per solid angle ($d\Omega$) per apparent luminosity (dl) at angle θ from a redshift z_c cluster is given by

$$n_{model}(\theta, l; z_c) = [n_f(l) + \Lambda n_c(\theta, l; z_c)] d\Omega dl \quad (5.1)$$

where n_f and Λn_c are the number densities due to the field and cluster. The number density of field galaxies can be directly determined from the observed galaxy number counts. The value of Λ is an estimate of the cluster richness in units of luminosity and n_c is the product of the radial profile and luminosity function of cluster galaxies;

$$n_c(\theta, l; z_c) = \Sigma_c(r) \left(\frac{dr}{d\theta} \right)^2 \phi_c(L) \left(\frac{dL}{dl} \right) \quad (5.2)$$

where r is the projected radius and L is the absolute luminosity. The values of r and L are related to the observed θ and l by

$$r(\theta, z_c) = \frac{\theta D_M}{1 + z_c} \quad (5.3)$$

and

$$L = 4\pi \left(\frac{(1 + z_c) D_M}{K(z_c)} \right)^2 l \quad (5.4)$$

where D_M is the transverse comoving distance (Hogg 1999) and $K(z)$ is the k -correction at redshift z . The cluster galaxy luminosity function is modelled with a Schechter function,

$$\phi_c(L) dL \propto (L/L^*)^{-\alpha} e^{-L/L^*} d(L/L^*), \quad (5.5)$$

and the model radial profile is a modified Plummer law given by

$$\Sigma_c(r) = \begin{cases} \frac{\Sigma_c^0}{(1+r^2/r_{core}^2)^{(n-1)/2}} - \frac{\Sigma_c^0}{(1+r^2/r_{max}^2)^{(n-1)/2}} & r \leq r_{max} \\ 0 & r > r_{max}, \end{cases} \quad (5.6)$$

where Σ_c^0 is set by the normalisation. The cluster radial and flux filters are normalised by

$$\int_0^{r_{max}} \Sigma_c(r) 2\pi r dr = 1 \quad (5.7)$$

and

$$\int_0^\infty \phi_c(L) L dL = L^*. \quad (5.8)$$

resulting in the luminosity of the cluster being given by

$$\Lambda L^* = \Lambda \int_0^{r_{max}} \Sigma_c(r) 2\pi r dr \int_0^\infty \phi_c(L) L dL. \quad (5.9)$$

At the location of the i th galaxy, the apparent local overdensity due to a cluster, $\Lambda \delta_i$, is given by

$$\delta_i = \frac{n_c^i}{n_f^i} = \frac{n_c(\theta_i, l_i; z_c) d\Omega dl}{n_f(l_i) d\Omega dl}. \quad (5.10)$$

The apparent overdensity of the cluster as measured from the data is given by

$$\Delta_{data} = \sum_i \delta_i. \quad (5.11)$$

The estimate of the overdensity from the model is given

$$\Delta_{model} = \Lambda \int_{l_{min}}^\infty \int \delta(\theta, l; z_c) n_c(\theta, l; z_c) d\Omega dl. \quad (5.12)$$

Equating Δ_{data} and Δ_{model} provides a solution for Λ :

$$\Lambda = \frac{\sum_i \delta_i}{\int \delta n_c}. \quad (5.13)$$

From the model, a variety of likelihood functions can be derived which are dependent on assumptions made about the distribution of galaxies. Full details of the derivations of the likelihood functions are given in Appendix C of Kepner *et al.* (1999). A cluster is identified by finding the values of z_c and Λ which maximise the likelihood. For matched filters this is done by finding the maximum value of the likelihood for a series of possible cluster redshifts, z_c , by taking the derivative of the log of the likelihood (\mathcal{L}) with respect to Λ and finding the value of Λ where

$$\frac{d\mathcal{L}}{d\Lambda} = 0 \quad (5.14)$$

(Postman *et al.* 1996, Kepner *et al.* 1999). The estimated cluster redshift and Λ are the values which return the maximum value of \mathcal{L} .

Kepner *et al.* (1999) derive two log likelihood equations. The first assumes that if the galaxy catalogue is binned, the number of galaxies in each bin can be described by a Gaussian distribution. This is an approximation but the resulting likelihood is easy to compute. If the noise of the likelihood signal is dominated by field galaxies, the resulting *coarse* estimate of \mathcal{L} is given by

$$\mathcal{L}_{coarse} = - \int \frac{[n_{data} - (n_f + \Lambda n_c)]^2}{n_f} d\Omega dl \quad (5.15)$$

where n_{data} is a sum of Dirac delta functions corresponding to the galaxy locations. If all terms independent of Λ are dropped from this expression, then

$$\mathcal{L}_{coarse} = 2\Lambda_{coarse} \sum_i \delta_i - 2\Lambda_{coarse} \int n_c d\Omega dl + \Lambda^2 \int \delta n_c d\Omega dl \quad (5.16)$$

where

$$\Lambda_{coarse} = \frac{\sum_i \delta_i - \int n_c d\Omega dl}{\int \delta n_c d\Omega dl}. \quad (5.17)$$

Kepner *et al.* (1999) do not include $\int n_c d\Omega dl$ as this is considered to be small compared to the other terms. However, when this form of likelihood was applied to the Panoramic Deep Fields, this term was found to be comparable to the other terms in the equation. Retaining this term also results in the background value of Λ_{coarse} being ~ 0 at all redshifts rather than increasing with redshift.

The second likelihood function, \mathcal{L}_{fine} , assumes that if the galaxy catalogue is binned, the number of galaxies in each bin can be described by a Poisson distribution. The resulting likelihood function,

$$\mathcal{L}_{fine} = -\Lambda_{fine} N_c + \sum_i \ln(1 + \Lambda_{fine} \delta_i), \quad (5.18)$$

is considerably more difficult to solve as

$$N_c = \sum_i \frac{\delta_i}{1 + \Lambda_{fine} \delta_i} \quad (5.19)$$

where N_c is the expected number of observable galaxies in a $\Lambda = 1$ cluster;

$$N_c = \int_{l_{min}}^{\infty} \int_0^{\pi} n_c d\Omega dl. \quad (5.20)$$

As \mathcal{L}_{fine} can only be solved numerically, \mathcal{L}_{coarse} is used to identify clusters and \mathcal{L}_{fine} is used to determine cluster parameters.

By including photometric redshifts, a third filter is applied to the data which uses known limits of each galaxy's redshift. Consider a galaxy catalogue where the i th galaxy has an estimated redshift z_i with error estimate of σ_z^i . The redshift information can be included in the AMF by simply evaluating the redshift z_c filter for galaxies which satisfy $|z_i - z_c| < w\sigma_z^i$, where w is a constant. If w is set to a high value, no redshift information is included in the AMF. However, if $w \sim 1$, a significant fraction of cluster galaxies are excluded from the AMF and the value of Λ has to be corrected. To include redshift information while keeping the correction to Λ negligible, w has been set to 2 for the selection of clusters in the Panoramic Deep Fields.

5.4 Photometric Redshifts

While photometric redshifts have been primarily used to study $z > 1$ galaxies (e.g. Fernandez-Soto, Lanzetta & Yahil 1999), they can also be used to provide strong constraints on the redshift distribution of $z < 1$ galaxies. Where the galaxies being studied are fainter than spectroscopic samples, spectra of low-redshift galaxies and evolution models are used to extrapolate the colours of higher redshift objects (Fernandez-Soto, Lanzetta & Yahil 1999). This requires assumptions about galaxy evolution and cosmological parameters which may not necessarily be correct.

For samples which are brighter than spectroscopic samples, it is possible to use the observed galaxy photometry and redshifts to determine the relationship for photometric redshifts (Connolly *et al.* 1995, Brunner *et al.* 1997, Brunner, Szalay & Connolly 2000). This avoids the need to use (model) spectra and evolution to determine the expected colours of galaxies as a function of redshift. However, it may be biased by the selection effects of the original redshift surveys.

Approximately 700 galaxy redshifts in the SGP and F855 fields are available from the NED database. The redshift and magnitude ranges are $0.0 < z < 0.8$ and $B_J < 24$ which allows the calibration of the relationship between redshift and colour across the observed magnitude range. At bright magnitudes most of the spectroscopic IDs are from the Las Campanas (Schectman *et al.* 1996) and APM (Loveday *et al.* 1992) surveys while at $B_J > 20$ most of the redshifts are from Broadhurst *et al.* (1988), Colless *et al.* (1990) and Glazebrook *et al.* (1995). The relationship between the multicolour photometry and the galaxy redshift

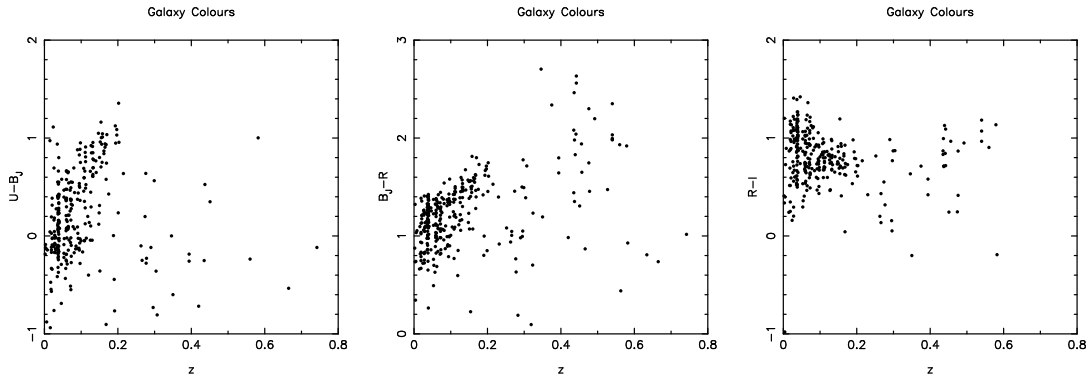


Figure 5.1: The colours of galaxies with known redshifts in the Panoramic Deep Fields.

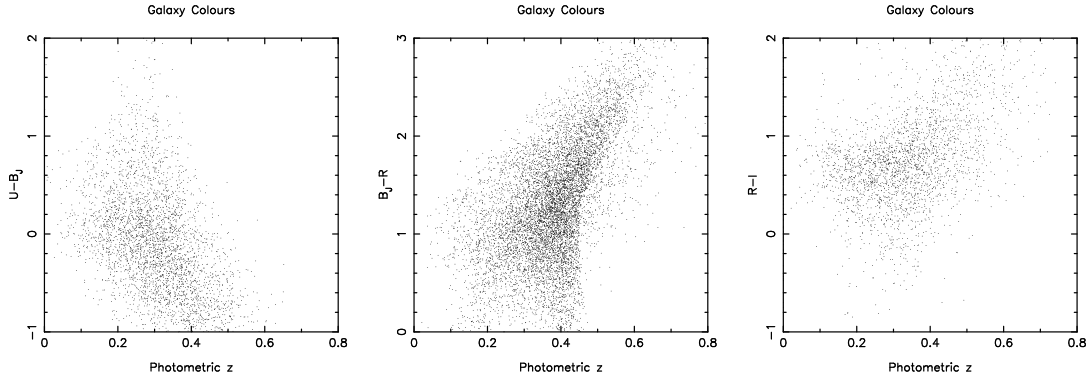


Figure 5.2: The colours and photometric redshifts of galaxies in the SGP field.

was determined by fitting quadratic functions to the data. The relationship was determined for UB_JRI , UB_JR , B_JRI and B_JR photometry as only a small fraction of the catalogue is detected in all 4 bands. Figure 5.1 shows that the spectroscopic surveys do not have uniform coverage of colour-redshift space. In particular, there are few $z \gtrsim 0.2$ galaxies with red $U - B_J$ colours. Because of this, B_JRI photometry has been used to estimate the redshifts of galaxies where $B_J - R > 1.5$ in preference to UB_JRI photometric redshifts which may have systematic errors. To check for artifacts in the photometric redshift estimates, the colours and photometric redshifts of galaxies have been plotted in Figure 5.2. A “boomerang” is produced by the B_J and R magnitude limits but no other artifacts are immediately apparent in the plots.

Figures 5.3 and 5.4 show plots of the photometric redshifts and the spectroscopic redshifts for galaxies in the two fields. It is clear from Figure 5.4 that the

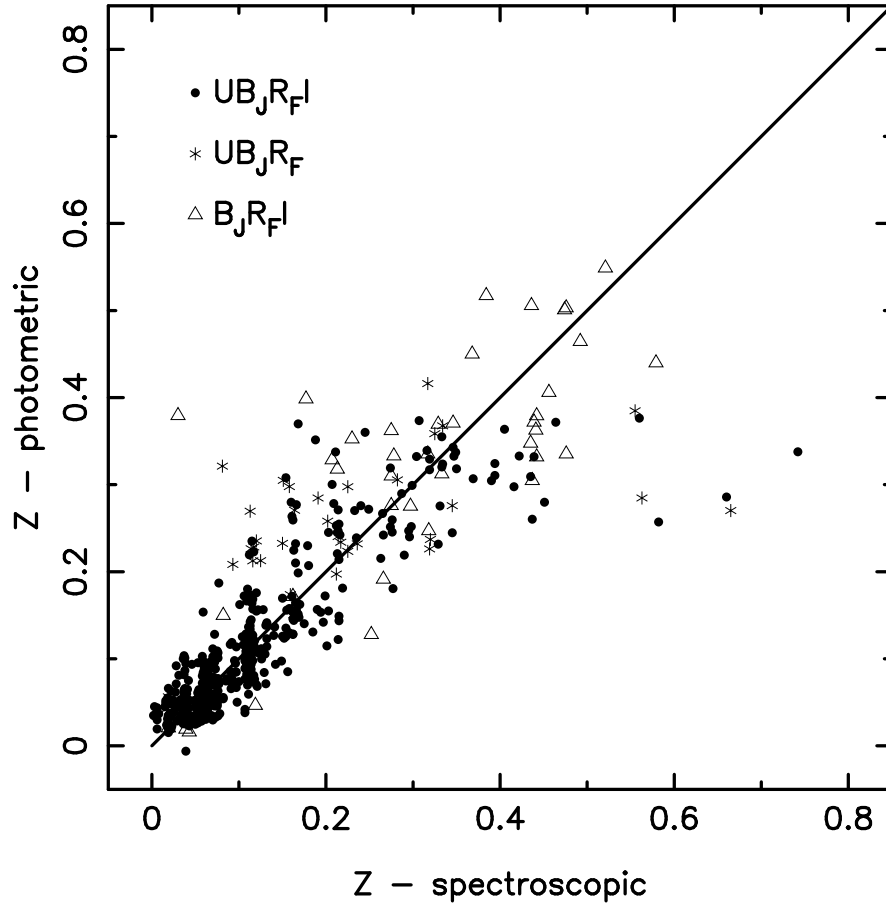


Figure 5.3: Comparison of photometric and spectroscopic redshifts for galaxies with 3 or more colours (including B_J and R).

errors for $B_J R$ photometric redshifts are considerably larger than those of derived from photometry in 3 or more bands. However, the $B_J R$ photometric redshifts do place good constraints on redshifts of red ($B_J - R > 1.5$) galaxies and upper limits can be determined for the redshifts of blue galaxies. This is useful as it lowers the background for AMF, allowing poorer and higher redshift clusters to be successfully detected. Error estimates for the photometric redshifts have been determined by the measuring the rms of the residuals as a function of photometric redshift.

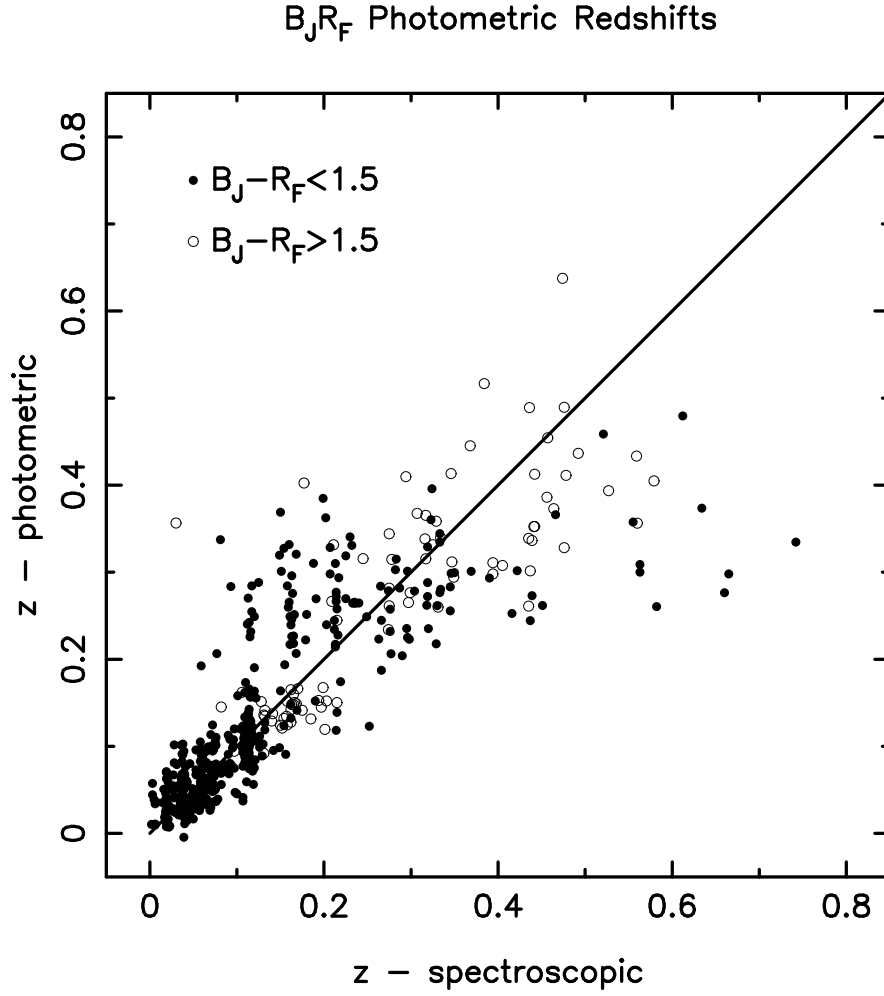


Figure 5.4: Comparison of photometric and spectroscopic redshifts for galaxies with B_J and R photometry. The errors are generally larger than for photometric redshifts determined from photometry in 3 or more bands. However, there is a reasonable correlation between the photometric and spectroscopic redshifts of red ($B_J - R > 1.5$) galaxies and limits can be determined for the redshifts of blue galaxies.

5.5 Implementing the AMF

The successful implementation of the AMF requires accurate estimates of the radial profile and cluster luminosity function. The cluster radial profile and luminosity function parameters used in this chapter are listed in Table 5.5. Where possible, cluster parameters are drawn from the literature to allow comparison with previous cluster surveys. It should be noted that the parameters are estimates for “typical” clusters and the radial profiles and luminosity functions of individual clusters can vary from these values (Colless 1989, Lubin & Postman 1996, Driver, Couch & Phillipps 1998). The variation of cluster parameters will introduce some uncertainty into estimates of the redshift and richness.

The cluster parameters have mostly been determined for clusters at low redshift while the Panoramic Deep Fields image galaxies at up to $z \sim 0.6$. While k -corrections have been included in the AMF, they are only approximations which are valid for non-evolving ellipticals. Spirals comprise a significant fraction of cluster members (Dressler 1980) so the k -corrections will overestimate the average k -correction for all cluster members. Also, the cluster luminosity function evolves by $\delta M_V \sim -0.3$ between $z = 0$ and $z \sim 0.5$ (Smail *et al.* 1997). To correct for these effects, approximations for the “evolution” have been included in the AMF and the estimates are listed in Table 5.5. The parameterisation is simple but is sufficient to prevent the redshift estimates having significant systematic errors (see Section 5.6).

It is possible to estimate the number of field galaxies for the AMF using luminosity functions but this requires accurate photometry, dust extinction estimates, luminosity functions, k -corrections and evolution models. This is difficult to implement and has only been implemented in simulated catalogues (Kepner *et al.* 1999). A simpler method of determining the number of background galaxies is to directly measure it from the galaxy catalogue. This will only slightly overestimate the number of field galaxies as the contribution of rich clusters to the total galaxy number counts is small (Tully 1987). The number of field galaxies as a function of luminosity and redshift is determined by finding the number of galaxies at a given luminosity which satisfy the redshift criteria.

Cluster candidates are identified from maps of \mathcal{L}_{coarse} and Λ_{coarse} which are determined for a series of redshifts for each band and field. At each redshift, the values of \mathcal{L}_{coarse} and Λ_{coarse} are evaluated for a series of positions across the field. The spacing of the positions is equivalent to $0.1h^{-1}\text{Mpc}$ for the highest

Table 5.2: Filter Parameters

| Parameter | Value | Reference or Notes |
|----------------------------------|-----------------------------|----------------------------------|
| Ω | 1 | |
| r_{core} | $0.1h^{-1}\text{Mpc}$ | Postman <i>et al.</i> (1996) |
| r_{max} | $1.0h^{-1}\text{Mpc}$ | Postman <i>et al.</i> (1996) |
| α | 1.1 | Postman <i>et al.</i> (1996) |
| M_U^* | $-19.4 + 5\log h$ | Estimate from Colour-Magnitude |
| $M_{B_J}^*$ | $-19.9 + 5\log h$ | Colless (1989) |
| M_R^* | $-21.0 + 5\log h$ | Driver, Couch & Phillipps (1998) |
| M_I^* | $-21.6 + 5\log h$ | Postman <i>et al.</i> (1996) |
| k -corrections | M31 | Coleman, Wu & Weedman (1980) |
| Evolution | $\delta m_U = -1.6z$ | |
| Evolution | $\delta m_{B_J} = -1.0z$ | |
| Evolution | $\delta m_R = -0.4z$ | |
| Evolution | $\delta m_I = -0.2z$ | |
| Luminosity Range | $0.05L^* < L(z) < 10L^*$ | |
| \mathcal{L}_{coarse} z range | $0.10 \leq z \leq 0.75$ | |
| Δz_{coarse} | 0.05 | |
| \mathcal{L}_{fine} z range | $0.05 < z < 0.80$ | |
| Δz_{fine} | 0.01 | |
| w | 2 | |
| Det. Threshold | $\mathcal{L}_{coarse} > 10$ | |
| Det. Threshold | $\Lambda_{coarse} > 10$ | |
| Det. Threshold (1 band) | $\mathcal{L}_{fine} > 10$ | |
| Det. Threshold (≥ 2 bands) | $\mathcal{L}_{fine} > 7.5$ | |
| Det. Threshold | $\Lambda_{fine} > 15$ | |

redshift slice. As there are drilled regions in the fields, the undrilled area within a projected r_{max} of each position is determined resulting in the running time being increased significantly.

Near drilled regions, the number of galaxies within r_{max} of a given position is significantly reduced and this results in increased noise in the \mathcal{L}_{coarse} maps. To reduce the probability of \mathcal{L}_{coarse} noise spikes entering the catalogue, \mathcal{L}_{coarse} and Λ_{coarse} are only determined for positions where $> 75\%$ of cluster galaxies can be included in the AMF. Low redshift galaxies with spuriously high photometric redshifts and luminosities can bias the estimates of \mathcal{L}_{coarse} and produce spurious clusters. Also, the fraction of dwarf galaxies varies significantly from cluster to cluster (Driver, Couch & Phillips 1998) and the AMF luminosity function can be a poor fit to the data. To prevent very bright and faint objects from biasing estimates of the cluster redshifts, the AMF is only evaluated with $0.05L^* < L < 10L^*$ galaxies. As this decreases the number of galaxies used to estimate \mathcal{L}_{coarse} and Λ_{coarse} , it also increases the speed of the AMF code.

The completed \mathcal{L}_{coarse} and Λ_{coarse} maps are saved to FITS format files with `cfitsio` functions (Pence 1999) before \mathcal{L}_{fine} and Λ_{fine} are evaluated. This allows small changes of the filter parameters without requiring the time-consuming re-evaluation of the maps. An example of an \mathcal{L}_{coarse} map for the SGP is shown in Figure 5.5.

Clusters are identified by searching for peaks in the \mathcal{L}_{coarse} maps and evaluating \mathcal{L}_{fine} and Λ_{fine} . While the value of \mathcal{L}_{coarse} and \mathcal{L}_{fine} are correlated with the cluster richness, they are also correlated with the redshift and poor low redshift clusters can have higher values of \mathcal{L}_{coarse} than rich high redshift clusters. To prevent poor clusters and groups excluding rich clusters at higher redshifts, threshold values of Λ_{coarse} and Λ_{fine} are used to exclude low redshift groups from the catalogue.

The edges of clusters can have values of \mathcal{L}_{coarse} and Λ_{coarse} which are above the threshold values. If the centre of the cluster is within a drilled area, the edge can be detected instead of the cluster core. As this results in incorrect cluster parameters, these objects should be excluded from the cluster catalogue. To prevent these objects entering the cluster catalogue, \mathcal{L}_{fine} and Λ_{fine} are only evaluated for peaks which are not on the edges of drilled regions.

To prevent low probability cluster candidates excluding high probability cluster candidates, peaks in the \mathcal{L}_{coarse} map are searched for in reverse order of \mathcal{L}_{coarse} .

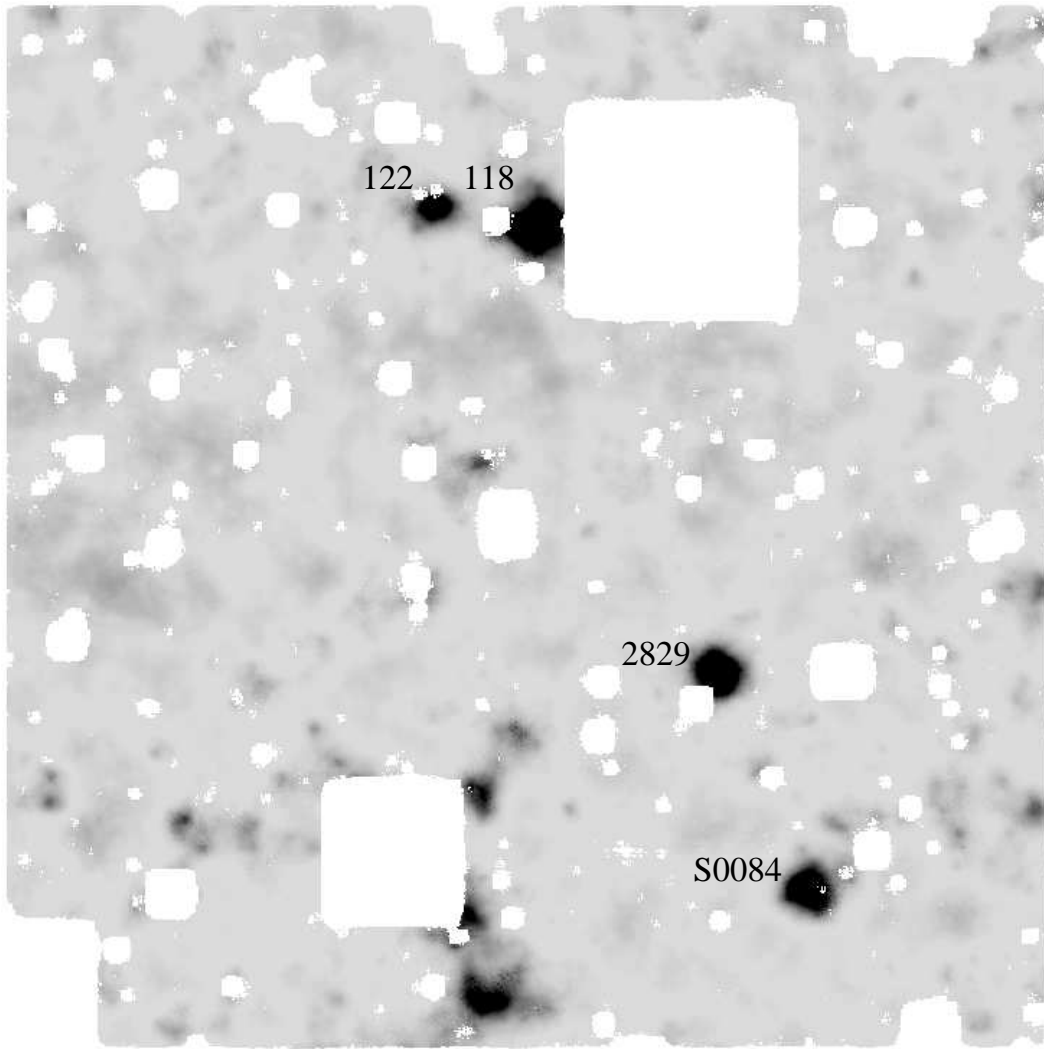


Figure 5.5: The $z = 0.1$ \mathcal{L}_{coarse} filter image for the SGP field. The four most significant detections (from top centre to bottom right) are Abell Clusters 122, 118, 2829 and S0084. The white blocks are regions drilled from the catalogue.

If the \mathcal{L}_{fine} and Λ_{fine} values are above the threshold values, a cluster candidate is recorded in the catalogue. A region within projected r_{max} of the cluster candidate is then flagged and is treated as a drilled region by the cluster finding software. If the values of \mathcal{L}_{fine} and Λ_{fine} do not satisfy the selection criteria, a 5 pixel radius region surrounding the failed candidate is flagged and is treated as a drilled region by the cluster finding software. The cluster detection software searches for clusters until there are no remaining peaks in the \mathcal{L}_{coarse} and Λ_{coarse} maps which satisfy the selection criteria.

The lists of cluster candidates in each band are produced in a format similar to SExtractor object catalogues so cluster candidate astrometry is determined with the same software that is used for the object catalogues. Cluster candidates in the different bands are then matched by searching for candidates with projected distances within $0.25h^{-1}\text{Mpc}$ of each other. Candidates with \mathcal{L}_{fine} values below the single band threshold are rejected if they are not matched to a candidate detected in another band. The final catalogue contains 519 cluster candidates which are listed in Appendix B.

5.6 Redshift Accuracy

Estimates of the errors of redshift estimates derived from matched filter can be determined by adding artificial clusters to real or fake datasets (Postman *et al.* 1996, Kepner *et al.* 1999). However, the redshift errors are typically underestimated as real clusters rarely have the properties of artificial clusters, which are usually generated using idealised cluster luminosity functions and radial profiles (e.g. Kepner *et al.* 1999).

To test the accuracy of cluster redshift estimates, the redshift estimates are compared with spectroscopic redshifts of galaxies and clusters from the NED database. Several of the clusters are from the relatively shallow Abell catalogue (Abell, Corwin & Olowin 1989) though a significant fraction are from the deep catalogue of Couch *et al.* (1991). Figure 5.6 shows a comparison of the redshift estimates and spectroscopic redshifts for clusters in the F855 and SGP fields. There is good agreement between the estimated and spectroscopic redshifts, with almost all clusters within 0.1 of the spectroscopic redshift. This is larger than the $\Delta z \sim 0.05$ errors from simulations by Kepner *et al.* (1999) but this is not unexpected as the simulations used idealised clusters and deeper images.

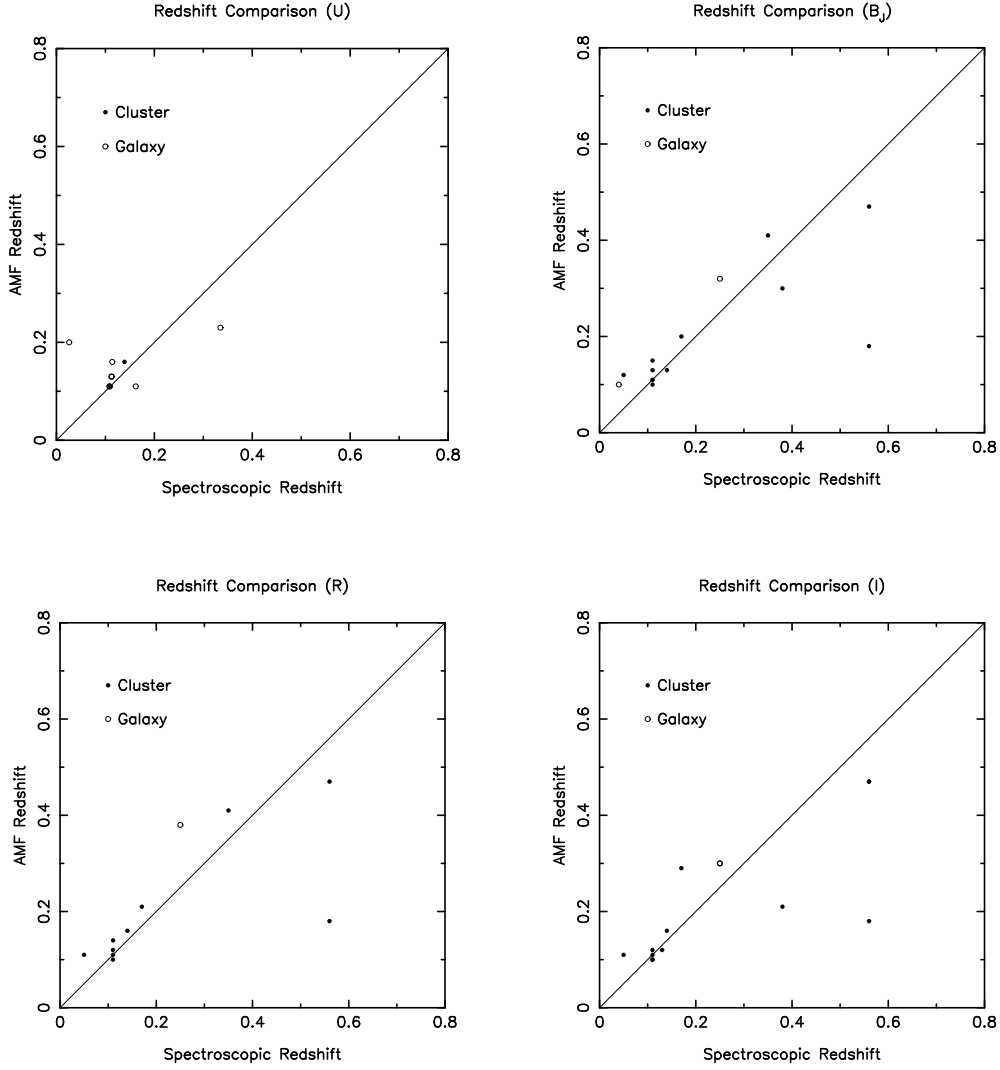


Figure 5.6: A comparison of the estimated redshifts of clusters and spectroscopic redshifts from the NED database. There is reasonable agreement between the estimated and measured redshifts. The outlier with “spectroscopic” redshift 0.56 is Abell 2843 which has a redshift listed in the NED database but no reference to the source of the redshift. The U band is shallow and has relatively large k -corrections resulting in few high redshift cluster detections.

5.7 Detection Limits

The detection limits for clusters can be evaluated by adding artificial clusters to datasets but they probably overestimate the detection limits. An upper limit for the detection of clusters can be found by using cluster detections to determine the minimum value of Λ which satisfies the cluster selection criteria at a given redshift. Plots of the detection limits derived by this method in B_J , R and I are shown in Figure 5.7. As expected, the R band is the most effective band for selecting distant clusters, with $\Lambda \sim 35$ clusters being detectable at $z \sim 0.45$. The estimates of the depth derived from Figure 5.7 can be compared with the estimated comoving density of clusters given in Figures 5.13 and 5.15. The estimates have not been corrected for incompleteness and rapidly decline at redshifts similar to the limits estimated from Figure 5.7.

A useful estimate of the depth of the catalogue is its ability to detect distant clusters from published catalogues. Clusters with projected positions within $0.5h^{-1}\text{Mpc}$ of clusters identified by Couch *et al.* (1991) are listed in Table 5.3. The Couch *et al.* (1991) catalogue was selected from AAT B_J and R_F plates ~ 1 magnitude fainter than the Panoramic Deep Fields. Approximate Abell richness classes have been determined with the significance and redshifts of the Couch *et al.* (1991) detections and Figure 3 from Couch *et al.* (1991). All clusters except J1834.08BL, which is in a drilled region, have been matched to cluster candidates. All the clusters are within 0.1 of the spectroscopic redshifts. Couch *et al.* (1991) note that J1834.03TC is probably a projection effect. Inspection of the individual B_J and R cluster candidates shows that they are offset by the $\sim 5'$ from each other and the published position of J1834.03TC.

5.8 B_J , R and I Cluster Properties

With the correct luminosity function, k -corrections and parameterisation of the cluster evolution, the estimated redshift and richness of the clusters in each band should be the same. If the estimates of the redshifts and richness are systematically different from band-to-band, it is probable that at least one of the filter parameters is incorrect. Figure 5.8 shows a comparison of redshift estimates for clusters from the B_J , R and I selected catalogues. There is a good correlation between the redshift estimates and no large systematic errors are evident.

Figure 5.9 compares estimates of the cluster richness in B_J , R and I for a range

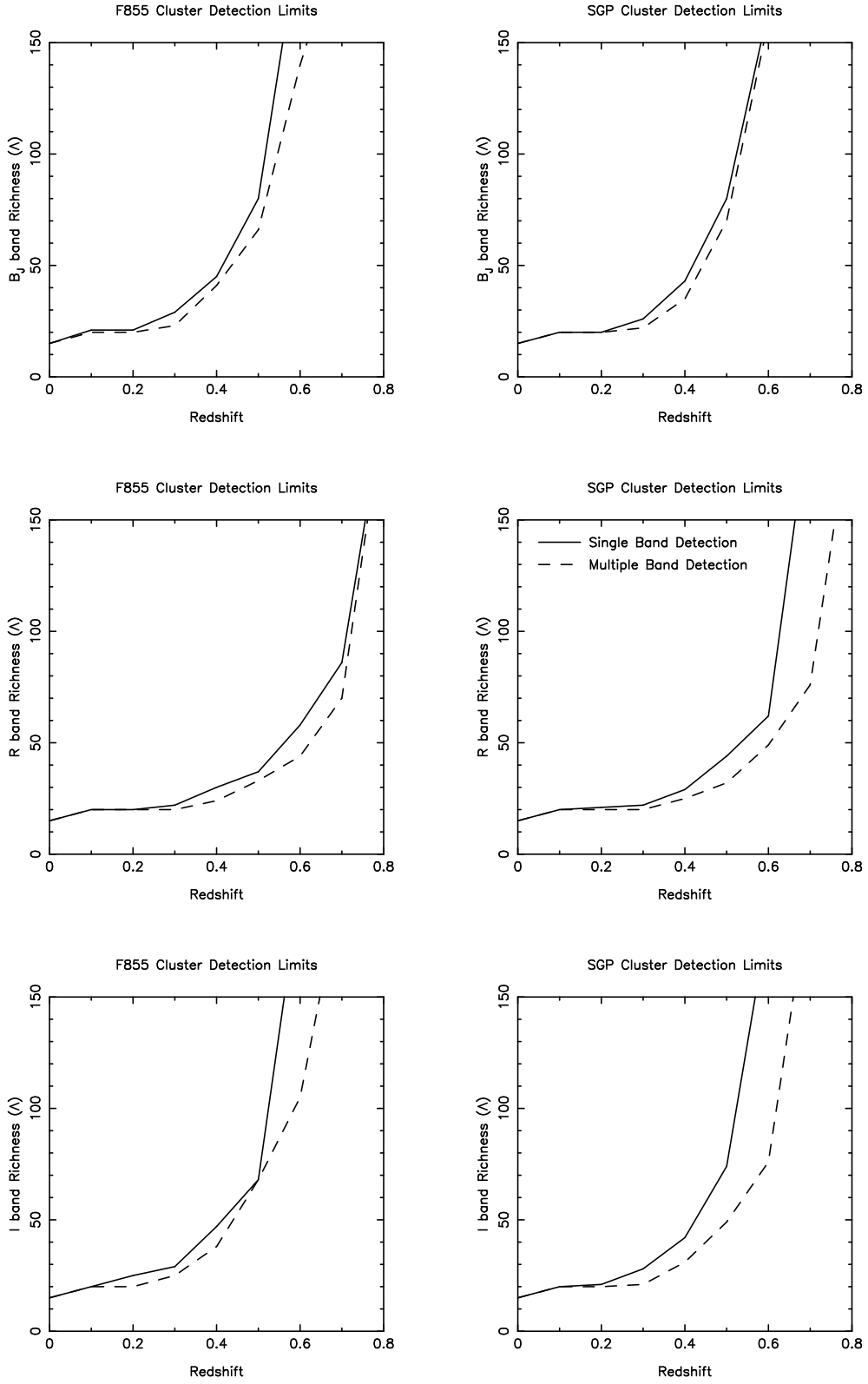


Figure 5.7: The estimated detection limits for clusters in B_J , R and I for the AMF.

Table 5.3: Identifications of Clusters from Couch *et al.* (1991)

| Cluster | Spectroscopic z | Abell Richness | B_J AMF z | R AMF z | $R \Lambda$ |
|-------------|-------------------|----------------|---------------|-------------|-------------|
| J1888.16CL | 0.56 | ~ 2 | 0.47 | 0.47 | 70 |
| J1834.03TC* | - | - | 0.23 | 0.12 | 31 |
| J1834.05BC | 0.44 | ~ 0 | - | 0.40 | 52 |
| J1834.08BL | 0.44 | $\lesssim 0^*$ | - | - | - |
| F1835.02CL | 0.38 | ~ 1 | 0.30 | - | - |
| F1835.22CR | 0.47 | ~ 1 | - | 0.45 | 36 |
| F1835.28BR | 0.35 | ~ 0 | 0.41 | 0.41 | 32 |

* Couch *et al.* note this is probably a projection effect. See text for details.

★ Cluster not detected in R band by Couch *et al.*.

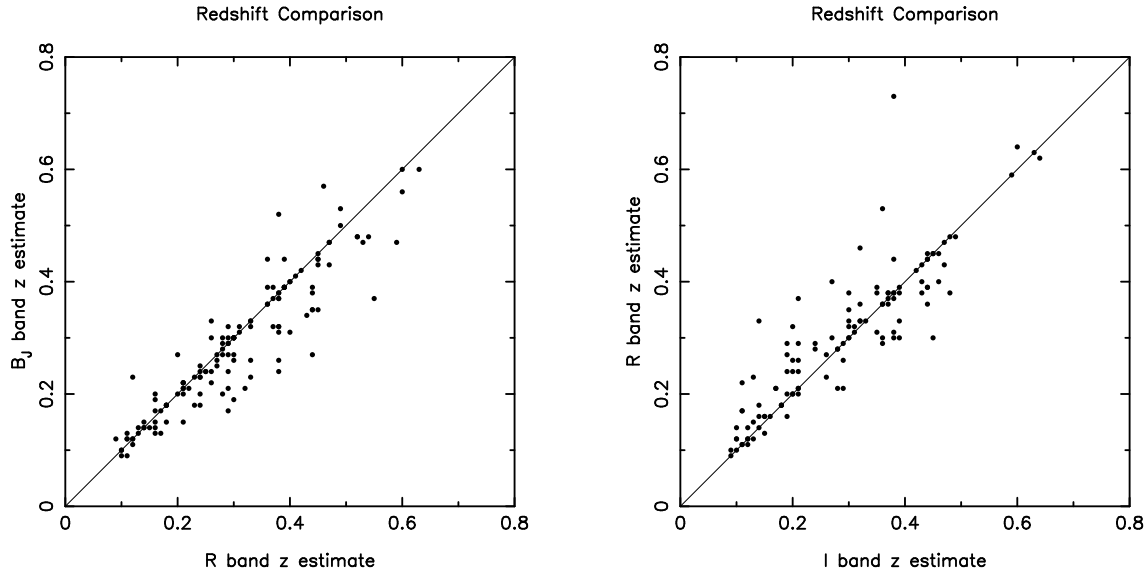


Figure 5.8: Plots of the comparing the B_J , R and I band redshift estimates.

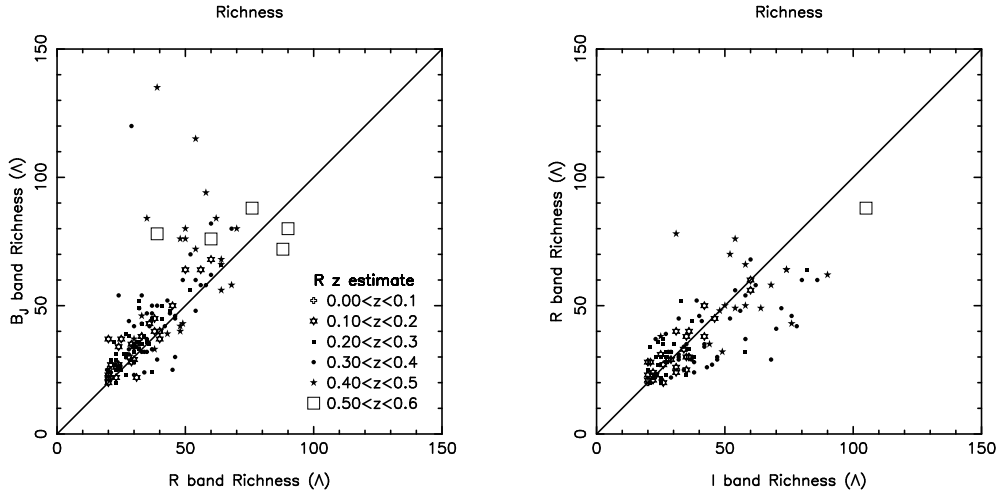


Figure 5.9: A comparison of the richness estimates of clusters derived from the B_J , R and I bands.

of redshifts. The richness estimates are correlated for low redshift clusters though the B_J and I richness estimates are significantly higher than the R estimates for high redshift clusters. All of these clusters have $\mathcal{L}_{fine} < 15$ and most have values of \mathcal{L}_{fine} less than 10 in the B_J and I bands. It is therefore probable that these clusters have Λ estimates with comparatively large errors. Also, as these clusters are at the limits of the B_J and I data, it is possible that Malmquist bias is producing the observed offsets in the richness estimates for high redshift clusters.

5.9 Comparison with the Low z Catalogues

The correct interpretation of results derived from the catalogue requires comparison with low redshift cluster surveys. This being the case, it is useful to compare properties with the Abell (Abell 1958, Abell, Corwin & Olowin 1989) and APM cluster catalogues (Dalton *et al.* 1994).

Figures 5.10 and Figures 5.11 plot the estimated redshift distributions of the Abell, APM and Panoramic Deep Field catalogues. The Panoramic Deep Field catalogue is considerably deeper than the Abell and APM catalogues due to the use of coadded plate scans and the AMF with photometric redshifts. The median redshift of the Panoramic Deep Field cluster candidates is ~ 0.3 compared with ~ 0.15 for the Abell and APM catalogues. It should be noted that while the Abell and APM catalogues have similar redshift distributions, the APM catalogue

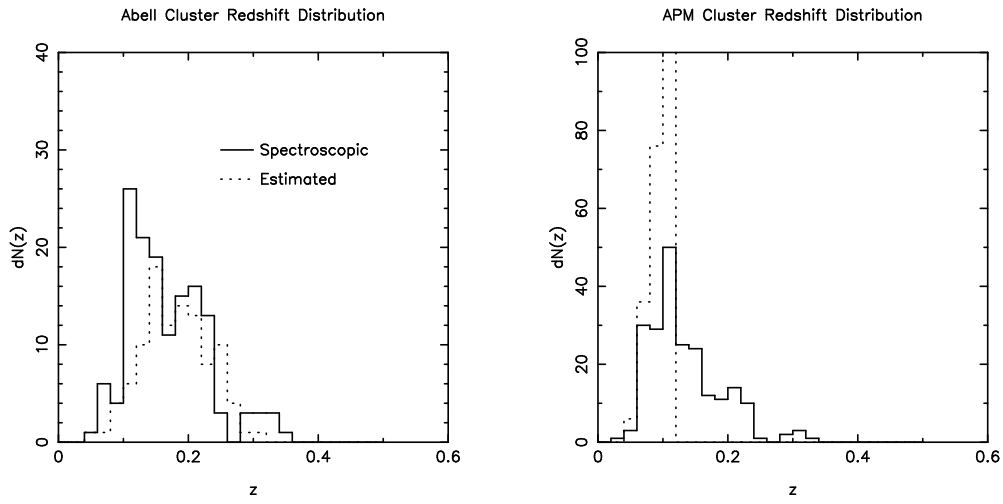


Figure 5.10: Spectroscopic redshift distributions for a sample of the Abell catalogue (Huchra *et al.* 1990) and the APM catalogue (Dalton *et al.* 1994). The dotted lines are estimated redshift distributions by Leir & van den Bergh (1977) and Dalton *et al.* (1994). Leir & van den Bergh (1977) use cluster diameters and the apparent magnitudes of the brightest cluster members to estimate the redshift. Dalton *et al.* (1994) use their cluster detection algorithm and the apparent magnitude of one of brightest cluster members to estimate redshifts.

contains poorer clusters than the Abell catalogue.

The richness distribution of clusters with estimated redshifts less than 0.2 is shown in Figure 5.12. The richness estimates of Abell clusters are also plotted in Figure 5.12, which shows the completeness of the Abell catalogue rapidly decreases below $\Lambda \sim 40$. The range of Λ values for a single Abell richness class is large and richness class 0 clusters have B_J Λ estimates between ~ 30 and ~ 50 . Large errors for richness estimates of Abell clusters have also been determined by Lumsden *et al.* (1992) and it is probable that the dispersion of Λ values is real rather than being caused by errors in the Λ estimates. Several cluster candidates from the APM (Dalton *et al.* 1994) and Edinburgh-Durham (Lumsden *et al.* 1992) catalogues are also within the survey area and APMCC 119, APMCC 120 and EDCC 505 are detected. APMC 121 and EDCC 509 are not detected though visual inspection of the published candidate positions indicates these clusters (if real) must be very poor.

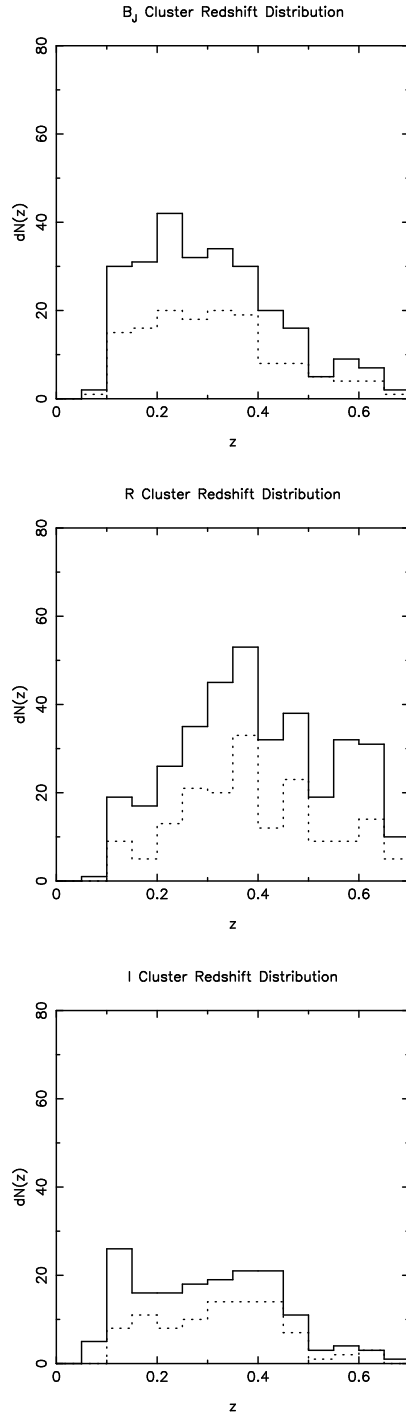


Figure 5.11: Plots of the estimated redshift distributions for the clusters detected in B_J , R and I bands. The solid line is the redshift distribution of all cluster candidates and the dotted line is the redshift distribution of cluster candidates in the SGP.

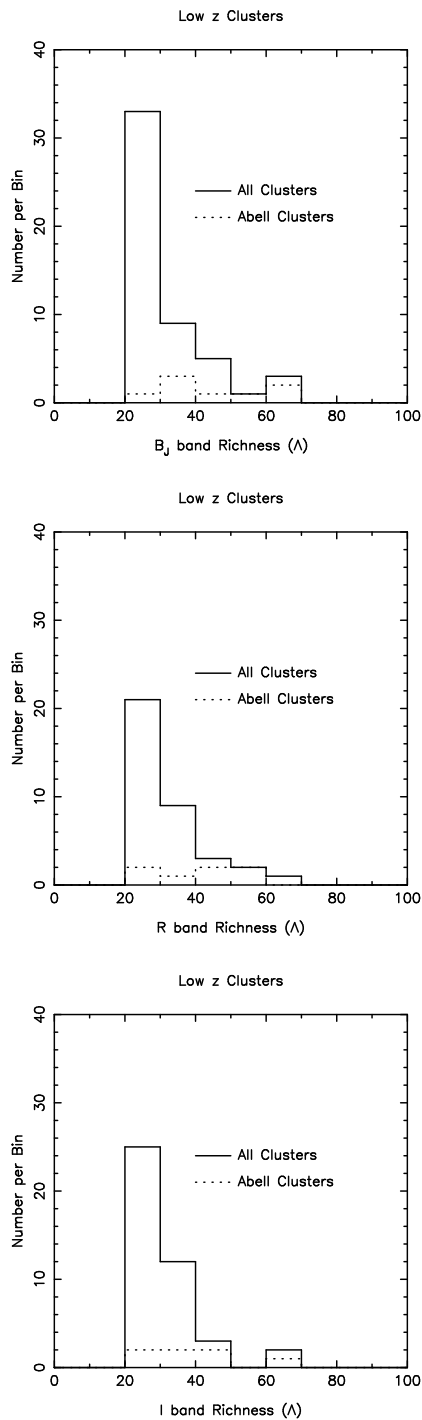


Figure 5.12: The richness distribution of clusters with redshift estimates less than 0.2. The Abell catalogue is significantly incomplete for clusters with $\Lambda < 35$. The $\Lambda \sim 60$ cluster which appears to be missing from the Abell catalogue is associated with Abell 118 which is $\sim 20'$ in diameter.

5.10 Comoving Density of Clusters

One of the primary reasons for obtaining deep cluster catalogues is to study the comoving density of clusters as a function of redshift. If the AMF parameters are accurate and the merger rate at $z < 0.5$ is not significant, the comoving density of clusters in the Panoramic Deep Fields should be approximately constant over the observed redshift range.

The comoving density of $\Lambda > 35$ clusters detected in all B_J and R bands is shown in Figure 5.13. No correction for incompleteness has been applied to the data at high redshift resulting a rapid decline in the observed density at $z \gtrsim 0.5$. The observed comoving density is consistent with a constant value of $\sim 3 \times 10^{-5} h^3 \text{Mpc}^{-3}$ at $z < 0.5$. The observed comoving density is a factor of 3 greater than the observed density of richness class ≥ 0 Abell clusters (Bahcall 1979, Huchra *et al.* 1990) but is similar to the comoving density of clusters observed by Postman *et al.* (1996).

Approximately half the disparity between the estimates of the cluster comoving density can be accounted for by incompleteness in the Abell catalogue (Lumsden *et al.* 1996). Postman *et al.* (1996) account for the remaining disparity with Malmquist bias from the random scatter of the redshift and richness estimates. If the distribution of errors of $\ln z$ is assumed to be Gaussian with standard deviation σ , the overestimate of the comoving density is given by

$$F = \frac{\Lambda_{estimated}}{\Lambda_{true}} = \exp\left(\frac{\gamma^2 \sigma^2}{2}\right) \quad (5.21)$$

(Postman *et al.* 1996) where $\gamma = d\ln N/d\ln z$ and N is the number of clusters. The value of γ is given by

$$\begin{aligned} \gamma &= \frac{d\ln N}{d\ln z} \\ &\propto \frac{d\ln V}{d\ln z} + \frac{d\ln f}{d\ln z} \\ &\propto \frac{d\ln V}{d\ln z} + \frac{d\ln f}{d\ln \Lambda} \frac{d\ln \Lambda}{d\ln z} \end{aligned} \quad (5.22)$$

(Postman *et al.* 1996) where V is the comoving volume and f is the fraction of clusters of richness Λ . The value of $\frac{d\ln f}{d\ln \Lambda}$ is ~ -2.4 (Postman *et al.* 1996) while the value of $\frac{d\ln \Lambda}{d\ln z}$ can be estimated from the data. Figure 5.14 shows plots of $\frac{\ln \Lambda}{\ln z}$ for the clusters detected by the survey. The slope of the data points is close to ~ 2.1 which is the value determined by Postman *et al.* (1996). The values of Λ determined in B_J are more strongly correlated with the redshift estimate

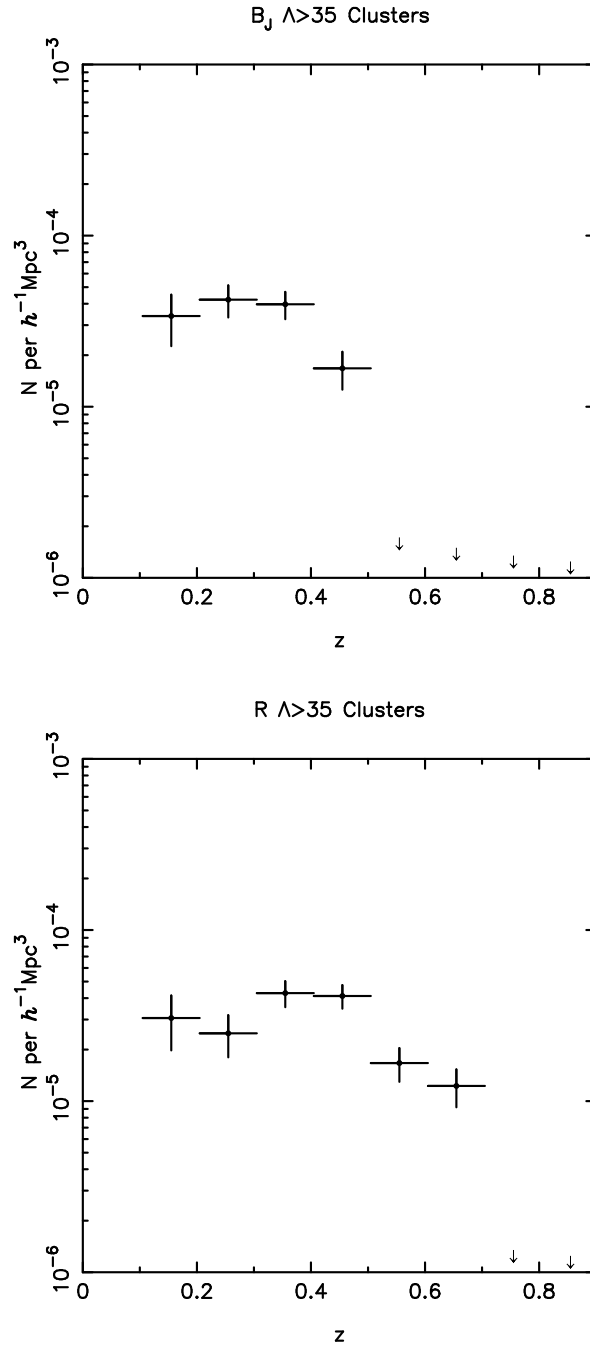


Figure 5.13: Estimated cluster number density as a function of redshift. The number density estimates have not been corrected for incompleteness resulting in the rapid decline of the estimates at high redshifts.

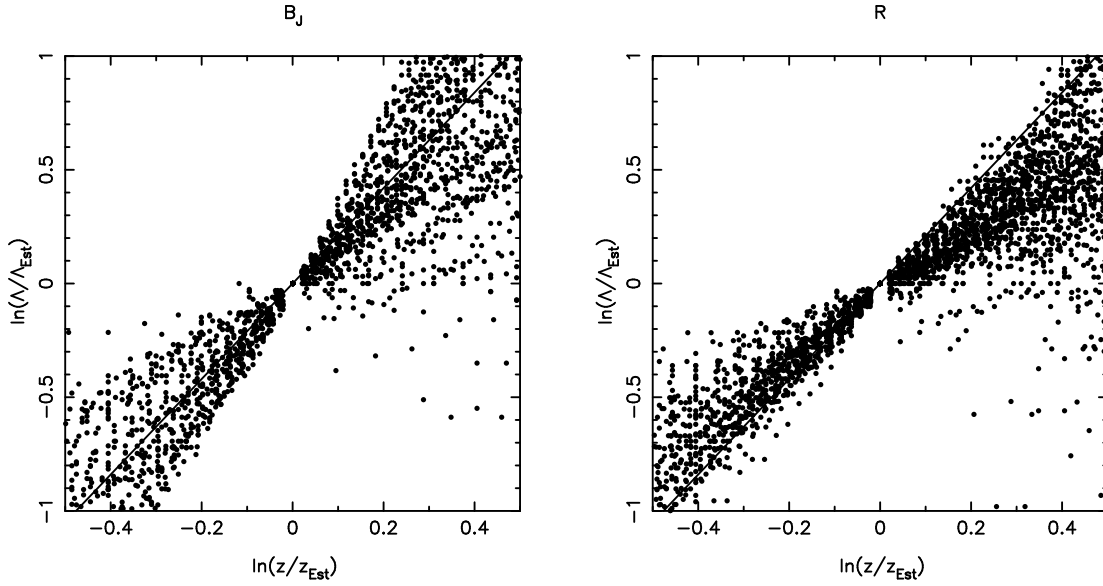


Figure 5.14: Plots of the cluster richness estimate as a function of redshift derived from the cluster candidates. The estimates have been normalised to the best estimate of the cluster richness and redshift. A line with gradient 2.1 is a reasonable fit to the B_J data though the the best-fit to the R data is shallower.

than they are for the R band data and will have larger errors. This is almost certainly due to the larger k -corrections in the B_J band. Assuming $\sigma = 0.2$ and $\frac{d \ln V}{d \ln z} = 2.5$, the value of F is ~ 1.15 .

If the Abell catalogue is $\sim 50\%$ complete for $30 < \Lambda < 50$ clusters and the AMF overestimates the number of $\Lambda > 35$ clusters by $\sim 15\%$, the expected comoving density of $\Lambda > 35$ clusters is $\sim 2.3 \times 10^{-5} h^3 \text{Mpc}^{-3}$ rather than the observed $\sim 3 \times 10^{-5} h^3 \text{Mpc}^{-3}$. A difference of $\sim 30\%$ is probably not significant considering the small number statistics of the sample. The difference could also be due to the richness estimators of Abell, Corwin & Olowin (1989) and Lumsden *et al.* (1992) and the AMF not being equivalent (though they are correlated). The comoving density is also strongly correlated with richness estimate and Figure 5.15 shows the comoving density of $\Lambda > 40$ clusters is $\sim 30\%$ less than the estimate of $\Lambda > 35$ clusters. A small systematic error in any of the cluster richness estimators could be responsible for a $\sim 30\%$ error in the estimated comoving density.

An accurate estimate of the comoving density of clusters will probably require a large uniform imaging survey (such as the SDSS) followed by spectroscopic observations. However, the Panoramic Deep Field cluster catalogue does provide

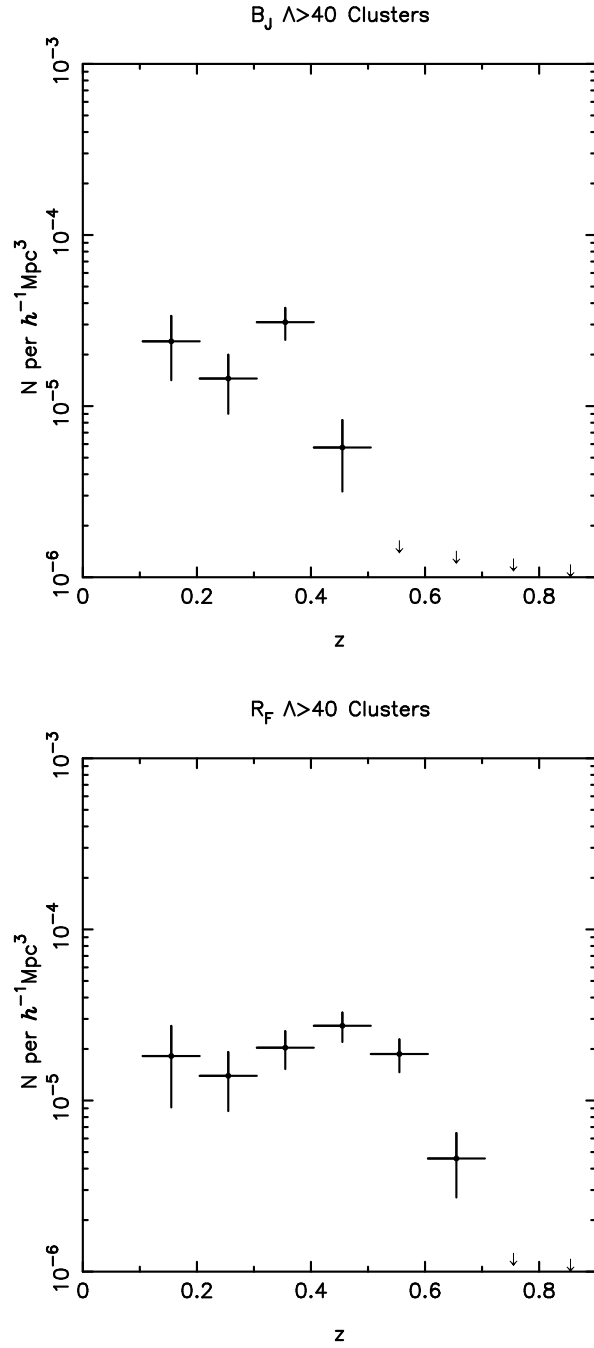


Figure 5.15: Estimated $\Lambda > 40$ cluster number density as a function of redshift. The cluster number density is strongly correlated with richness resulting in the number density of $\Lambda > 40$ being significantly lower than the number density of $\Lambda > 35$ clusters.

useful information on the comoving density of clusters. Comparisons with the Abell catalogue show that the Abell catalogue is substantially incomplete and the comoving density of $\Lambda > 35$ (richness class 0) clusters is $\sim 3 \times 10^{-5} h^3 \text{Mpc}^{-3}$. Also, while there is evolution of the cluster galaxy luminosity function between $z \sim 0.5$ and the present epoch, the estimated number density of clusters is consistent with a constant value to $z \sim 0.5$.

5.11 The Cluster Correlation Function

The cluster angular correlation function has been determined with the estimator

$$\hat{\omega}(\theta) = \frac{DD - 2DR + RR}{RR} \quad (5.23)$$

where DD , DR and RR are the number of cluster-cluster, cluster-random and random-random pairs separated by angle $\theta \pm \delta\theta$. The random objects are copies of the clusters which are randomly positioned around the survey area and obey the selection criteria of the cluster catalogue. The random copies are generated in the same order the clusters were detected and a cluster core cannot be on the edge of a drilled area or within $1h^{-1}\text{Mpc}$ of another random cluster core. To reduce random noise in the estimates of $\omega(\theta)$, multiple random catalogues are generated and the values of DR and RR are renormalised.

For the angular correlation function to be meaningful, it must be compared with the spatial correlation function. To do this, Limber's equation is used to determine the angular correlation from a model of the spatial correlation function. The reader is referred to the previous chapter or Brown, Webster & Boyle (2000) for a discussion of Limber's equation. The redshift distribution of the clusters is required to do this accurately and this has been determined by smoothing the estimated cluster redshifts with a Gaussian with $\sigma = 0.2z$.

The correlation functions of R band selected $\Lambda > 35$ clusters in the SGP and F855 fields have been plotted in Figure 5.16. To prevent clusters associated with the $z \sim 0.11$ Broadhurst spike (Broadhurst *et al.* 1990) from biasing the correlation function estimates, only clusters with $z > 0.15$ are used to estimate the correlation function. Models of the spatial correlation function with $r_0 = 20h^{-1}\text{Mpc}$ (Bahcall & Sonneria 1983, Postman, Huchra & Geller 1992, Miller *et al.* 1999) and $r_0 = 14h^{-1}\text{Mpc}$ (Nichol *et al.* 1992, Croft *et al.* 1997) with clustering fixed in comoving coordinates have been plotted with the data. There is reasonable agreement between the $r_0 = 20h^{-1}\text{Mpc}$ model and the data though

the scatter of the data points is large. The observed clustering is significantly stronger than the $r_0 = 14h^{-1}\text{Mpc}$ model for several angular scales.

The correlation function of the B_J selected clusters is shown in Figure 5.17. The observed clustering in the F855 field is stronger than $r_0 \sim 20h^{-1}\text{Mpc}$ while the SGP data differs significantly from a power law. The differences between the correlation function determined with B_J and R selected clusters are due to the small number of clusters used to measure the correlation function and errors in the Λ estimate producing different catalogues of clusters for each band. As the estimates of Λ are a stronger function redshift in B_J than R , it is probable that the B_J correlation function has larger errors (both random and systematic) than the R band correlation function.

The differences in the estimates of the correlation function in the different bands show that larger catalogues are required for an accurate estimate of the cluster correlation function at intermediate redshifts. As the expected value of $\omega(1^\circ)$ is ~ 0.1 , it is not unexpected that estimates of the correlation function in the two $5^\circ \times 5^\circ$ fields show large variations. However, while the estimates of the correlation function are not conclusive, they support $r_0 \sim 20h^{-1}\text{Mpc}$.

5.12 Comparison of the SGP and F855 fields

A strong motivation for compiling large catalogues of clusters is to use them to trace large-scale structure. The cluster correlation functions for the SGP and F855 fields detect structure on scales of $\sim 1^\circ$ or $\sim 10h^{-1}\text{Mpc}$ at $z \gtrsim 0.2$. This does not exclude the possibility of larger structures which have not been detected by the correlation function. There are significant differences between estimates of the galaxy and cluster autocorrelation functions in the SGP and F855 fields (Brown, Webster & Boyle 2000 and section 5.11). Two possible causes of these differences are dwarf galaxies associated with relatively nearby clusters or structures at $z > 0.2$ on scales $\gtrsim 10h^{-1}\text{Mpc}$.

The distribution of R and B_J cluster candidates in the two fields are plotted in Figures 5.18 to 5.21. Clustering of the candidates is immediately apparent in the images and structure on scales of $> 1^\circ$ is observable. The most prominent structures are a large void in the western half of the F855 field and a cluster of candidates near the centre of the SGP. The void is difficult to explain if it is considered to be a structure several tens of Mpc across which stretches from

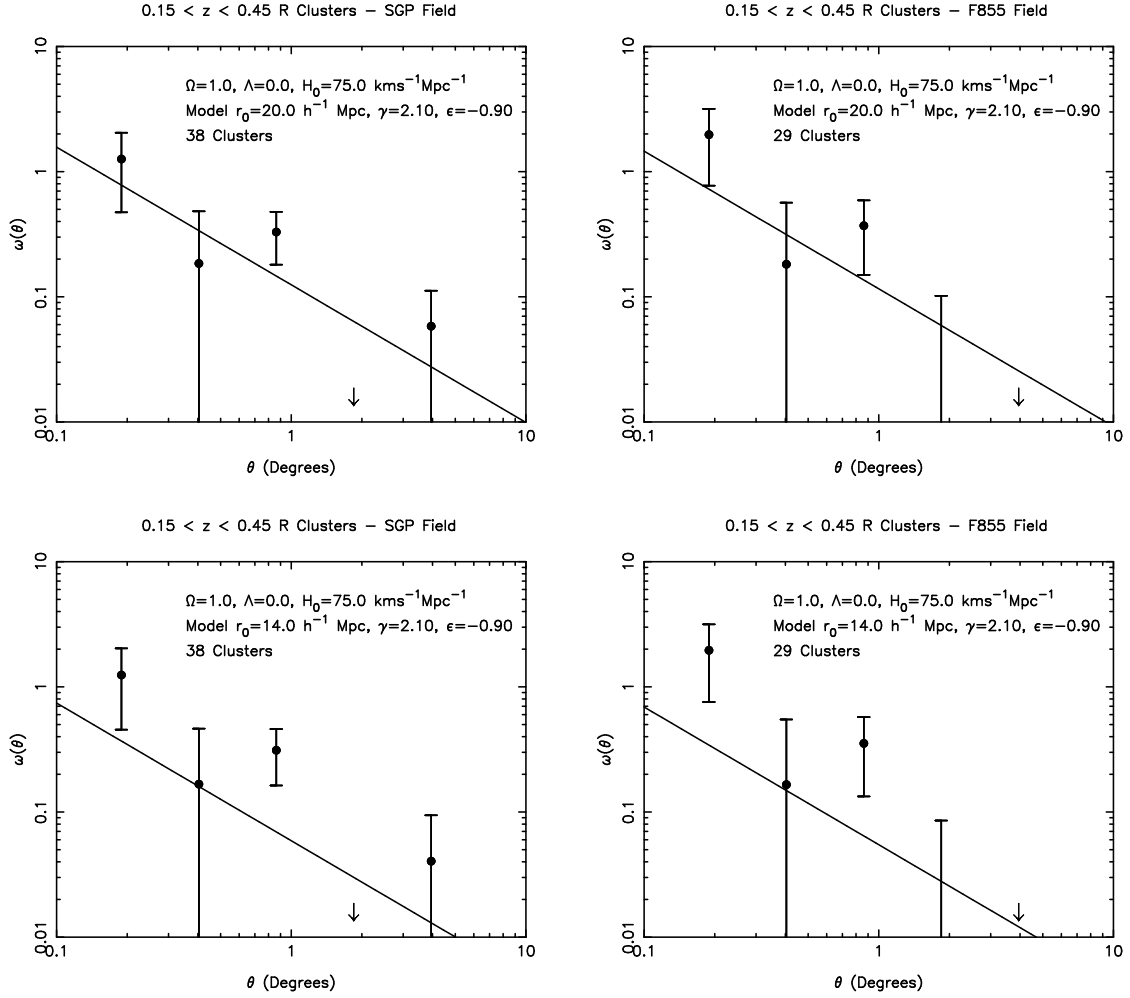


Figure 5.16: The R band $\Lambda > 35$ cluster correlation function for the SGP and F855 fields. The estimates of the correlation function have been corrected for the integral constraint where the amplitude of the correlation function is derived from the models of the spatial correlation function.

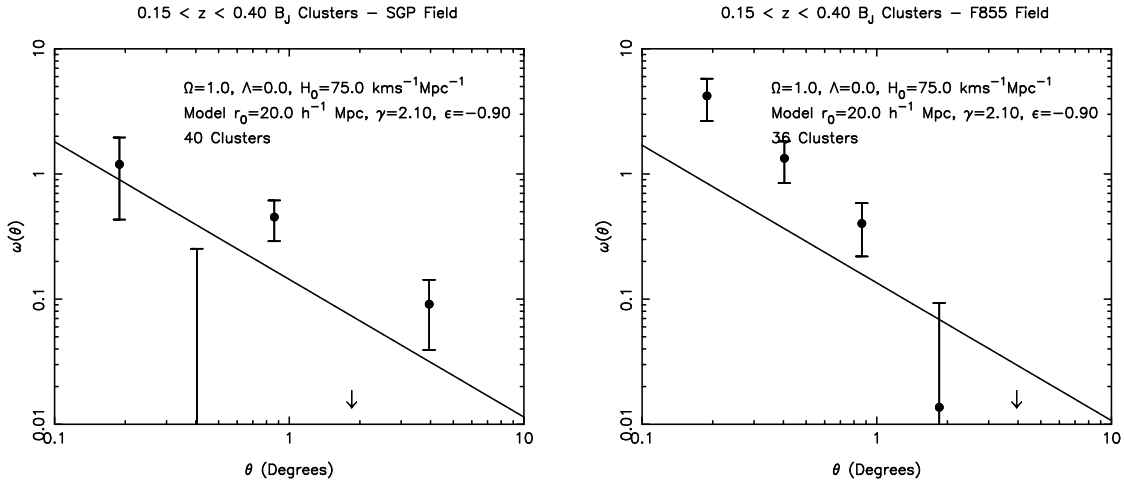


Figure 5.17: The $B_J \Lambda > 35$ cluster correlation functions for the SGP and F855 fields.

$z \sim 0.1$ to $z \sim 0.5$. However, if clusters trace filamentary structures, the void is just a line-of-sight which does not intersect a filament. It is probable that the differences in the clustering of galaxies in the SGP and F855 fields observed in Chapter 4 and by Brown, Webster & Boyle (2000) are due to large-scale structure at $0.2 < z < 0.4$ rather than the effects of relatively local dwarf galaxies or clusters. It is clear that accurate studies of the clustering of strongly clustered objects (red galaxies, clusters) require fields of view greater than $5^\circ \times 5^\circ$ (or $\sim 60h^{-1}\text{Mpc} \times \sim 60h^{-1}\text{Mpc}$) to obtain representative samples.

5.13 Summary

A deep catalogue of galaxy clusters in the SGP and F855 fields has been compiled using uniformly applied selection criteria. Photometric redshifts and an Adaptive Matched Filter have been used to estimate cluster redshifts and richness. The main conclusions which can be derived from the cluster catalogue are

- (i) Comparison of the cluster detections with the Abell catalogue indicates the Abell catalogue is $\sim 50\%$ complete for $z < 0.2$ richness class 0 clusters.
- (ii) The comoving density of clusters is approximately constant at $z < 0.6$ if cluster galaxies undergo mild luminosity evolution (with $\Omega = 1$). The estimated comoving density of $\Lambda > 35$ (richness class ~ 0) clusters is $\sim 3 \times 10^{-5} h^3 \text{Mpc}^{-3}$. This could be a $\sim 30\%$ overestimate of the density of richness class ~ 0 clusters

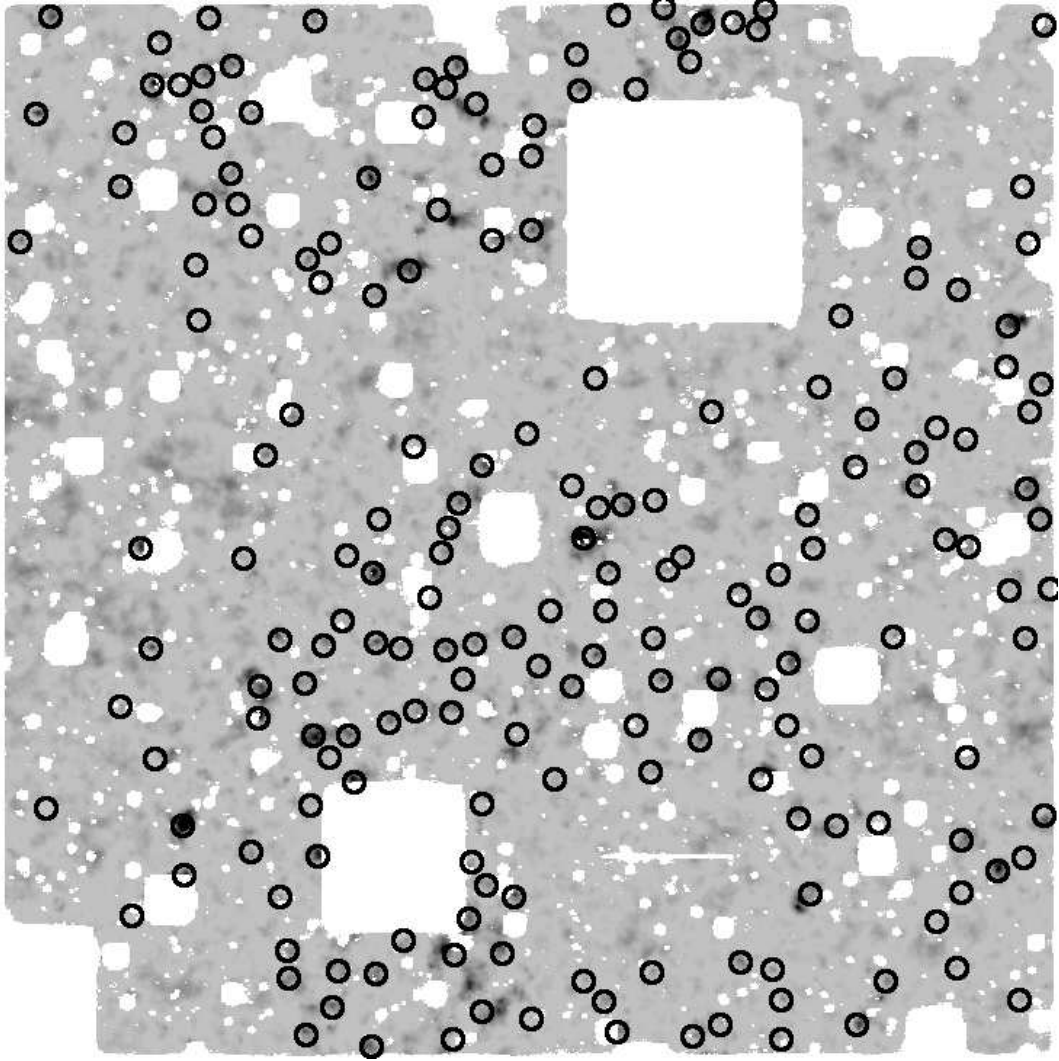


Figure 5.18: The B_J $z = 0.4$ \mathcal{L}_{coarse} map for the SGP with the positions of all $\mathcal{L}_{fine} > 7.5$ cluster candidates. North is to the top and east is to the left of the image. Structure can be clearly observed with an excess of clusters near the centre of the field and a deficit near the eastern edge of the field. Some peaks in the likelihood map do not generate cluster candidates as they are within r_{max} of other cluster candidates.

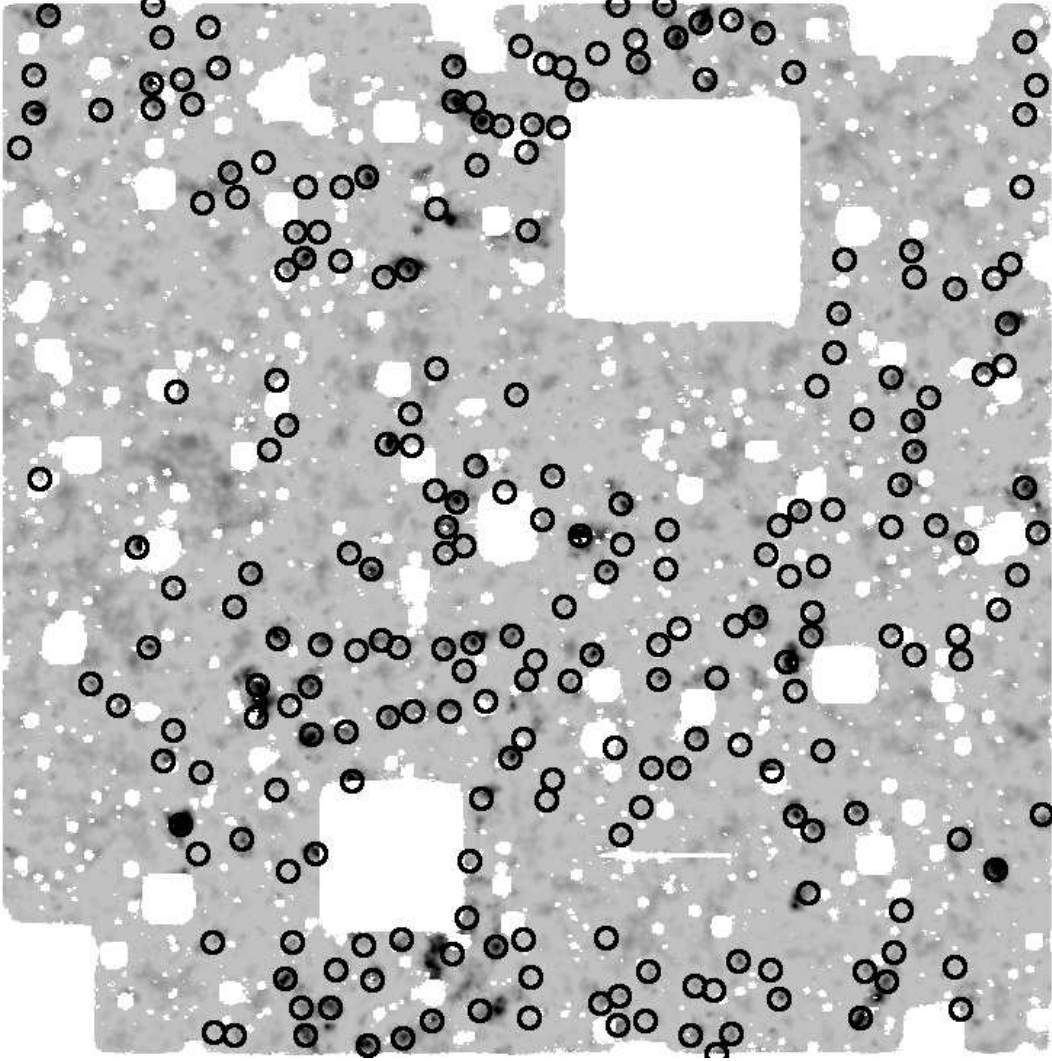


Figure 5.19: The $R\ z = 0.4\ \mathcal{L}_{coarse}$ map for the SGP with the positions of all $\mathcal{L}_{fine} > 7.5$ cluster candidates. North is to the top and east is to the left of the image. Structure can be clearly observed with an excess of clusters near the centre of the field and a deficit near the eastern edge of the field.

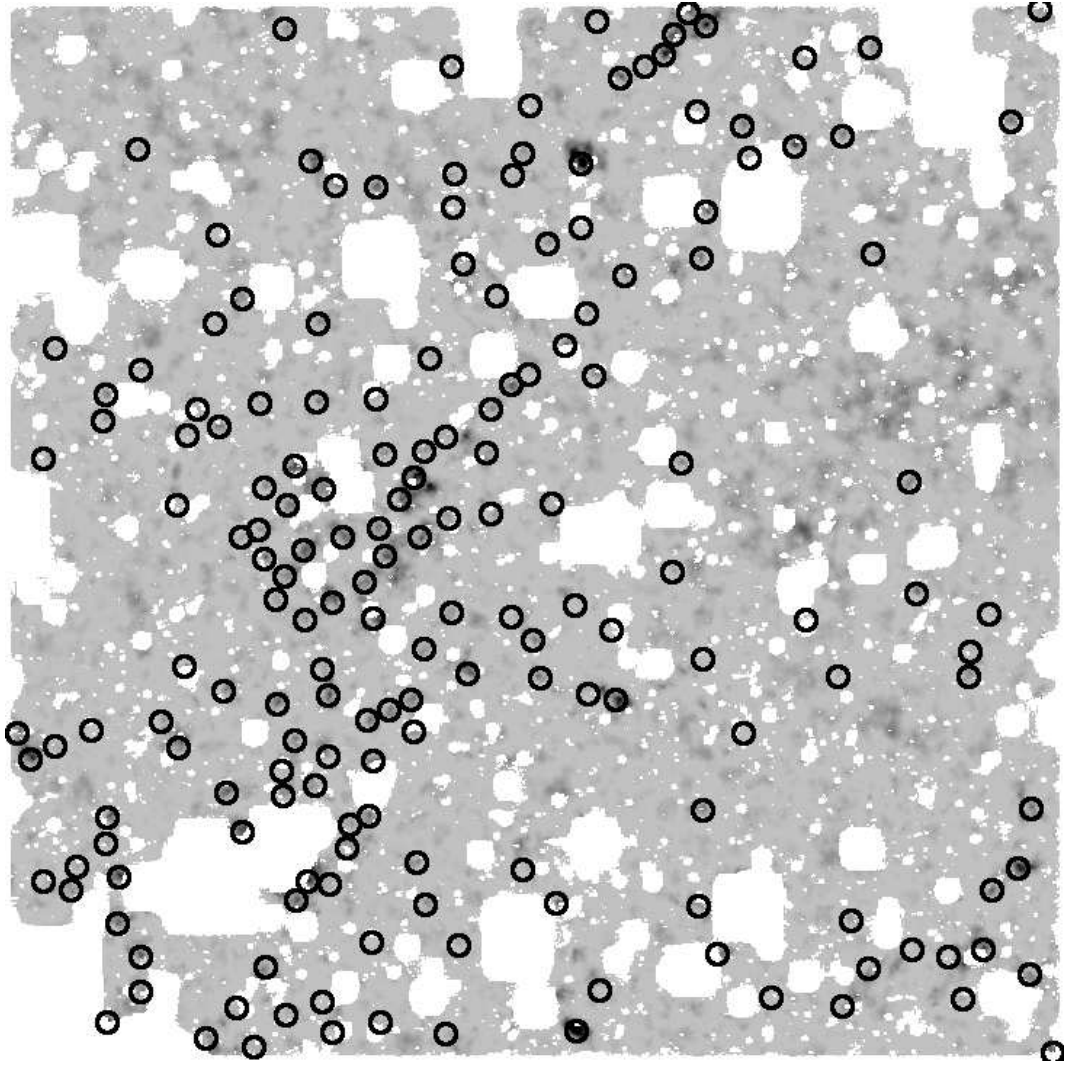


Figure 5.20: The B_J $z = 0.4$ \mathcal{L}_{coarse} map for the F855 field with the positions of all $\mathcal{L}_{fine} > 7.5$ cluster candidates. North is to the top and east is to the left of the image. The slight increase of the \mathcal{L}_{coarse} values in the north western quarter of the field is associated with a deficit of galaxies compared with the entire field. At $z \sim 0.4$, the width of the survey area is $\sim 60h^{-1}\text{Mpc}$.

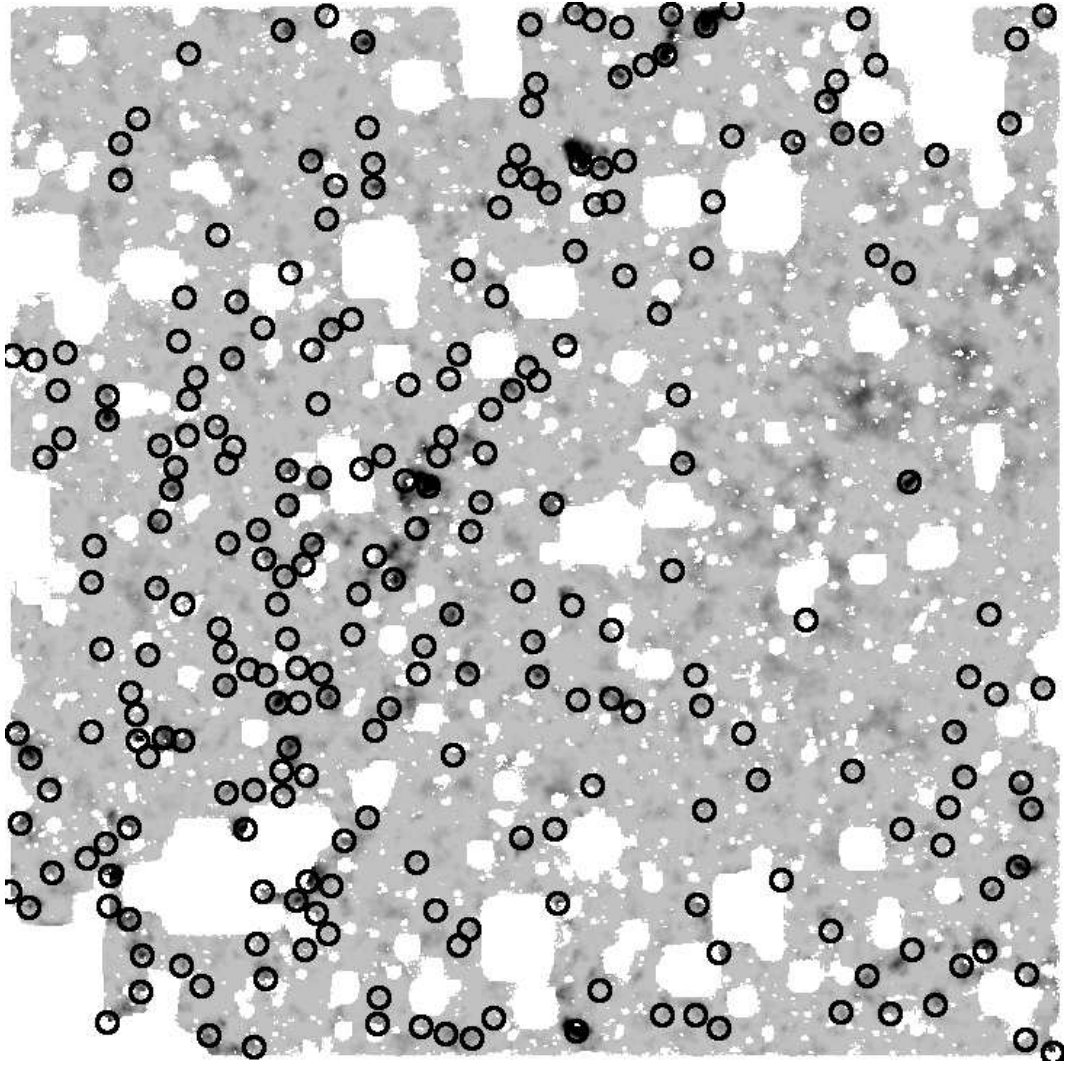


Figure 5.21: The $R\ z = 0.4\ \mathcal{L}_{coarse}$ map for the F855 field with the positions of all $\mathcal{L}_{fine} > 7.5$ cluster candidates. North is to the top and east is to the left of the image. The slight increase of the \mathcal{L}_{coarse} values in the north western quarter of the field is associated with a deficit of galaxies compared with the entire field. At $z \sim 0.4$, the width of the survey area is $\sim 60h^{-1}\text{Mpc}$

as Λ isn't equivalent to Abell richness class (though it is correlated) and the estimate of the comoving density is strongly dependent on Λ .

(iii) The clustering of the candidates is consistent with a spatial correlation function with $r_0 \sim 20h^{-1}\text{Mpc}$. Models of the spatial correlation function with $r_0 \sim 14h^{-1}\text{Mpc}$ underestimate the clustering of the galaxy cluster candidates.

(iv) The distribution of the cluster candidates clearly shows large-scale structure on scales comparable to the size of the fields or $\sim 60h^{-1}\text{Mpc}$ at $z \sim 0.4$.

Chapter 6

The Clustering of AGN and Galaxies

6.1 Introduction

While the association of Active Galactic Nuclei hosts with other galaxies has been well established (Bahcall, Schmidt & Gunn 1969, Yee & Green 1987, Hall & Green 1998, Smith, Boyle & Maddox 1995), it has been unclear if the AGN host environment differs significantly from other galaxies. A correlation between AGN activity and host environment would provide constraints on models for fuelling AGN. As QSOs can be used to trace large-scale-structure at $z \gg 1$ (Boyle *et al.* 1999), a measure of the QSO environment is required to estimate their bias with respect to galaxies which are used to trace large-scale-structure at $z < 1$.

Several previous studies of AGN environments are summarised in Table 6.1. The clustering of galaxies near radio-loud QSOs is consistent with these AGN occupying rich environments similar to galaxy clusters (Yee & Green 1987, Hall & Green 1998). In contrast, studies of radio-quiet QSOs have not produced consistent estimates of their environments (Boyle & Couch 1993, Ellingson, Yee & Green 1991, Smith, Boyle & Maddox 1995, Smith, Boyle & Maddox 2000, Teplitz, McLean & Malkan 1999). From the clustering studies, it would appear that radio emission from QSOs may be triggered by rich galaxy environments while radio-quiet QSO hosts could be in poorer environments.

HST imaging of $z < 0.35$ QSOs (McLure *et al.* 1999), $z < 0.15$ X-ray selected AGN (Schade, Boyle & Letawsky 2000) and $z < 0.5$ BL Lacs (Urry *et al.* 2000) indicates the majority of luminous AGN hosts have early-type morphologies. If

the environment of radio-quiet AGN is similar to field galaxies then they are in unusually poor environments compared to most early-type galaxies. Using colour selection, it should be possible to measure the AGN-early-type and AGN-late-type cross-correlation functions and determine if radio-quiet AGN are in unusual environments compared to early-type galaxies and field galaxies.

6.2 Multicolour imaging and photometric redshifts

A significant problem with most studies of the AGN environment is that they have relied on small samples or single band imaging. Galaxy evolution and k -corrections result in a changing morphological mix of galaxies as a function of limiting magnitude with single band imaging. Galaxy catalogues in bands bluer than R are dominated by weakly clustered (blue) late-type galaxies at magnitudes fainter than $B_J \sim 22$ (Efstathiou *et al.* 1991). This being the case, many studies of the AGN environment at intermediate redshifts have probably measured the cross-correlation of AGN with faint blue galaxies.

Multicolour imaging provides significant advantages for the study of the AGN host environment. Colours and photometric redshifts can be used to select particular galaxy types at faint magnitudes. As galaxy clustering is strongly correlated with colour (Brown, Webster & Boyle 2000, Chapter 4) and morphology (Loveday *et al.* 1995), studying the cross-correlation of AGN with particular galaxy types should determine if AGN hosts are in unusual environments compared with other galaxies with the same morphology.

The relationship between redshift and multicolour photometry was determined with ~ 700 galaxies in the SGP and F855 fields with redshifts in the NED database. The relationship between the multicolour photometry and the galaxy redshifts was fitted with quadratic functions using the method of Connolly *et al.* (1995). Full details of the implementation of the photometric redshifts are provided in Chapter 5. The colour criteria applied to the Panoramic Deep Field galaxy catalogue select galaxies redder or bluer than a non-evolving Sbc in $B_J - R$. The use of $B_J - R$ rather than shallower $U - B_J$ or $R - I$ allows the selection of $B_J = 23.5$ early-type galaxies at $z \sim 0.5$. The $B_J - R$ selection criteria are a function of redshift so photometric redshifts are used to determine the correct value of $B_J - R$ when selecting galaxies. For the remainder of the chapter, the

Table 6.1: A sample of studies of the AGN environment

| Reference | AGN Type | Number of AGN | AGN Redshift Range | Galaxy Magnitude Limit | Correlation Estimate |
|--------------------------------|------------|---------------------|--------------------------|------------------------------|---------------------------------|
| De Robertis, Yee & Hayhoe 1998 | Seyferts | 33 | $z < 0.04$ | $M_R < -19.5$ | $r_0 \sim 5.4h^{-1}\text{Mpc}$ |
| Laurikainen & Salo 1995 | Seyfert 1 | - | $z < 0.05$ | $B_J < 21$ | $r_0 \sim 5h^{-1}\text{Mpc}$ |
| Laurikainen & Salo 1995 | Seyfert 2 | - | $z < 0.05$ | $B_J < 21$ | $r_0 > 5h^{-1}\text{Mpc}$ |
| Smith, Boyle & Maddox 1995 | X-ray QSOs | 169 | $z < 0.3$ | $B_J < 20.5$ | $r_0 \sim 5h^{-1}\text{Mpc}$ |
| Ellingson, Yee & Green 1991 | RQ QSOs | 46 | $0.3 < z < 0.6$ | $r \sim 23.5, g \sim 24$ | $r_0 \sim 5h^{-1}\text{Mpc}$ |
| Smith, Boyle & Maddox 2000 | X-ray QSOs | 83 | $0.3 < z < 0.7$ | $V = 23$ | $r_0 \sim 3h^{-1}\text{Mpc}$ |
| This work | UBR AGN | 66 | $0.3 < z < 0.7$ | $B_J < 23.5$ | $r_0 \sim 8h^{-1}\text{Mpc}$ |
| Boyle & Couch 1993 | QSOs | 27 | $0.9 < z < 1.7$ | $R < 23$ | No correlation |
| Teplitz, McLean & Malkan 1999 | RQ QSOs | 30 | $0.9 < z < 2.1$ | $I, J, H \sim 21, K$ | 2σ correlation |
| Croom & Shanks 1999 | RQ QSOs | 150 | $0.0 < z < 3.2$ | $B_J < 23$ | No correlation |
| Yee & Green 1987 | RL QSOs | 10 | $0.3 < z < 0.5$ | $22 < R < 22.9$ | $r_0 \sim 9h^{-1}\text{Mpc}$ |
| Yee & Green 1987 | RL QSOs | 9 | $0.55 < z < 0.65$ | $22 < R < 22.9$ | $r_0 \sim 18h^{-1}\text{Mpc}$ |
| Wold <i>et al.</i> 2000 | RL QSOs | 21 | $0.50 < z < 0.82$ | $V, R \sim 23.5, I$ | $r_0 \sim 11.7h^{-1}\text{Mpc}$ |
| Hall & Green 1998 | RL QSOs | 31 | $1.0 < z < 2.0$ | $K \gtrsim 19$ | Richness ~ 0 clusters |

early and late subsamples will refer to galaxies redder and bluer than the $B_J - R$ selection criteria.

The AGN sample (which is described in Section 6.4) has a similar absolute magnitude range to Schade, Boyle & Letawsky (2000) and if the AGN are in similar host galaxies, then $\sim 75\%$ should be in host galaxies with earlier morphologies than Sbc galaxies. By comparing the AGN-galaxy cross-correlation with the galaxy-galaxy correlation of similar galaxy types, it should be possible to determine if AGN hosts are in unusual environments. To test the reliability of the colour selection criteria, the colours of galaxies in the SGP with morphologies determined with HST imaging by Abraham *et al.* (1996) and Smail *et al.* (1997) have been plotted in Figure 6.2. The diagram shows elliptical and lenticular galaxies are redder than the selection criteria though the colours of spiral galaxies show considerable scatter.

6.3 The Clustering of Faint Galaxies

Estimates of the clustering of $z \sim 0.5$ galaxies are required if the environment of AGN hosts is to be compared to the “normal” galaxy environment. To make the comparison valid, the same galaxy selection criteria are applied to the study of galaxy-galaxy clustering as AGN-galaxy clustering.

The estimate of the angular autocorrelation function of galaxies is determined with

$$\hat{\omega}(\theta) = \frac{DD - 2DR + RR}{RR} \quad (6.1)$$

(Landy & Szalay 1993) where DD , DR and RR are the number of galaxy-galaxy, galaxy-random and random-random pairs at angular separation $\theta \pm \delta\theta$. The Landy & Szalay (1993) estimator is only applicable to the autocorrelation function so the early-late cross-correlation is determined with

$$\hat{\omega}(\theta) = \frac{EL}{ER} - 1 \quad (6.2)$$

where EL and ER are the number of early-late and early-random pairs at angular separation $\theta \pm \delta\theta$. The estimates of $\hat{\omega}(\theta)$ are corrected for the integral constraint and the spatial correlation function can be estimated with Limber’s equation (Limber 1954, see Chapter 4 for a summary).

The early and late subsample autocorrelation functions and the early-late cross-correlation functions have been determined in the SGP and F855 fields.

Photometric Redshifts (Redder than Sbc galaxies)

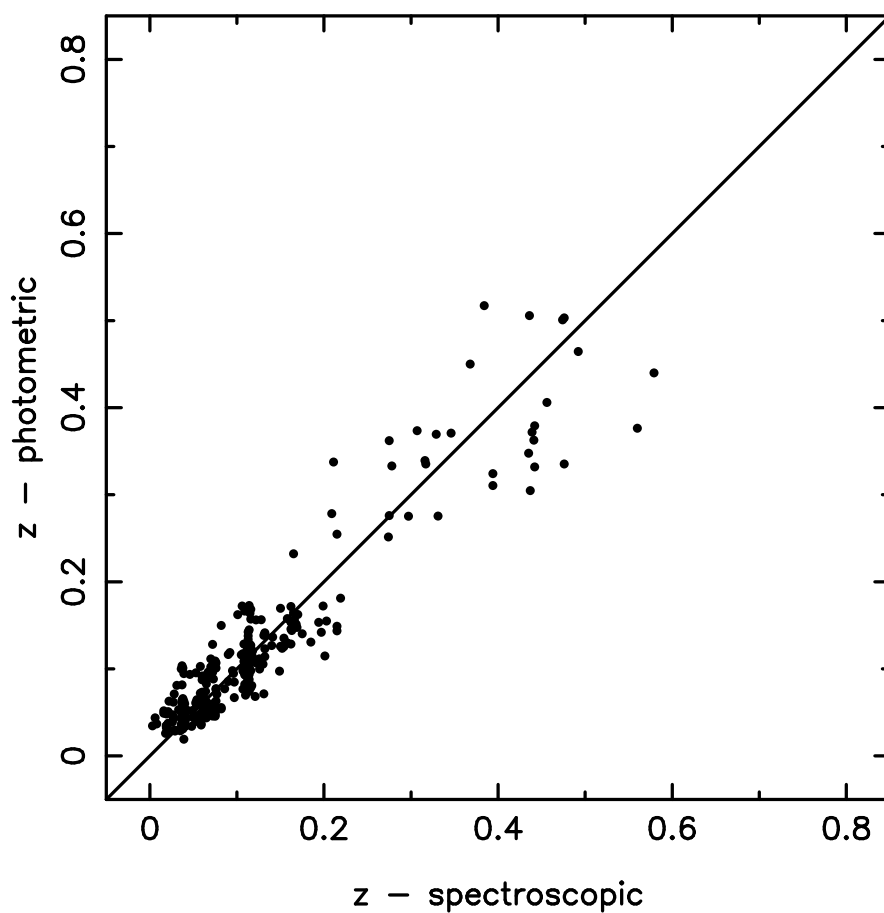


Figure 6.1: Comparison of photometric and spectroscopic redshifts for galaxies with colours redder than non-evolving Sbc galaxies. While some of the galaxies are only detected in B_J and R , the correlation between photometric and spectroscopic redshift is still good.

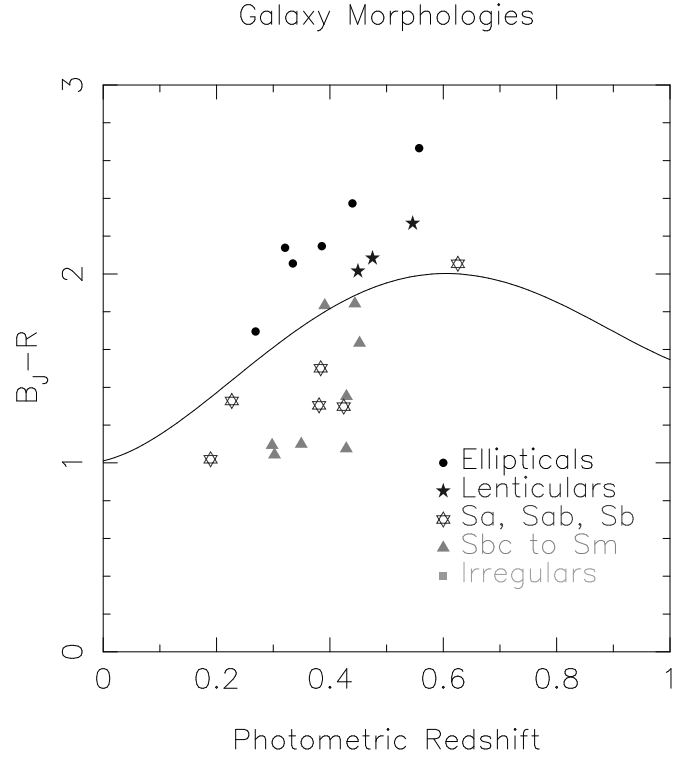


Figure 6.2: The colours and photometric redshifts of galaxies with morphological classifications from Abraham *et al.* (1996) and Smail *et al.* (1997). The curved line is an estimate of the colour of a non-evolving Sbc determined with a polynomial fit to the k -corrections from Coleman, Wu & Weedman (1980). Most early-type galaxies are redder than the non-evolving Sbc.

Plots of the $18.0 < B_J < 23.5$ angular correlation functions are shown in Figures 6.3 to 6.5. The amplitudes and values of the γ as a function of magnitude are summarised in Tables 6.2 to 6.4. As seen previously in Chapter 4, the value of γ and the amplitude of the clustering strongly depend on colour. The values of the γ differ from those determined in Chapter 4 due to the use of different selection criteria. At faint magnitudes, the estimates of γ for the early-late cross-correlation function in the SGP and F855 fields differ significantly. It is possible that this is due to the cross-correlation function estimator having larger errors than predicted by the Poisson estimate (Landy & Szalay 1993). Also, at faint magnitudes the amplitude of the cross-correlation function is comparable to the estimated errors of the dust extinction estimates of Schlegel, Finkbeiner & Davis (1998).

To determine the spatial correlation function, an estimate of the redshift distribution is required. Estimates of the redshift distribution derived from luminosity functions, k -corrections and evolution models are subject to uncertainties as a range of models can reproduce the observed number counts. Models which assume a shape for the redshift distribution (Baugh & Efstathiou 1993) are useful for single band imaging of low redshift galaxies but are not as effective for multicolour selected samples at higher redshifts where the selection criteria and k -corrections skew the redshift distribution.

Photometric redshifts contain information on the redshift distribution but assume that galaxies with the same colours and magnitudes are at the same redshifts. If the errors of the photometric redshifts are dominated by redshift distribution of galaxies with the same multicolour photometry, it should be possible to derive a redshift distribution using the measured errors of the photometric redshifts. Figure 6.6 shows the observed redshift distribution of galaxies from Glazebrook *et al.* (1995) detected in the Panoramic Deep Fields and a model derived from their photometric redshifts. The photometric redshifts have been smoothed by a Gaussian where σ is equal to the rms of the errors of the photometric redshifts. At $z < 0.05$ the redshift distribution has been multiplied by $z/0.05$ to prevent an infinite density of galaxies at $z = 0$. There is reasonable agreement between the measured and model distributions, though the galaxy number counts are limited. While the exact redshift distribution has not been determined, it is unlikely that large errors dominate the redshift distribution.

The estimated redshift distributions of the early and late subsamples are plot-

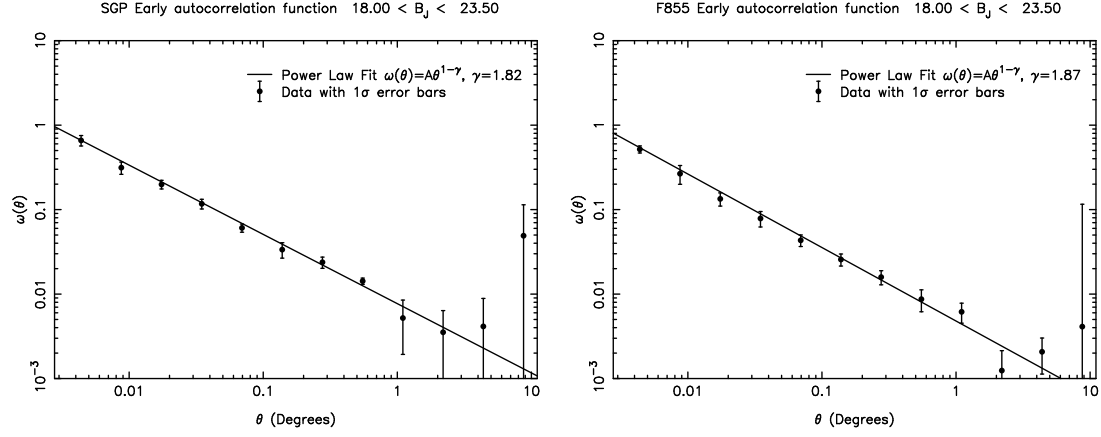


Figure 6.3: The $18.0 < B_J < 23.5$ early subsample autocorrelation function for the SGP and F855 fields.

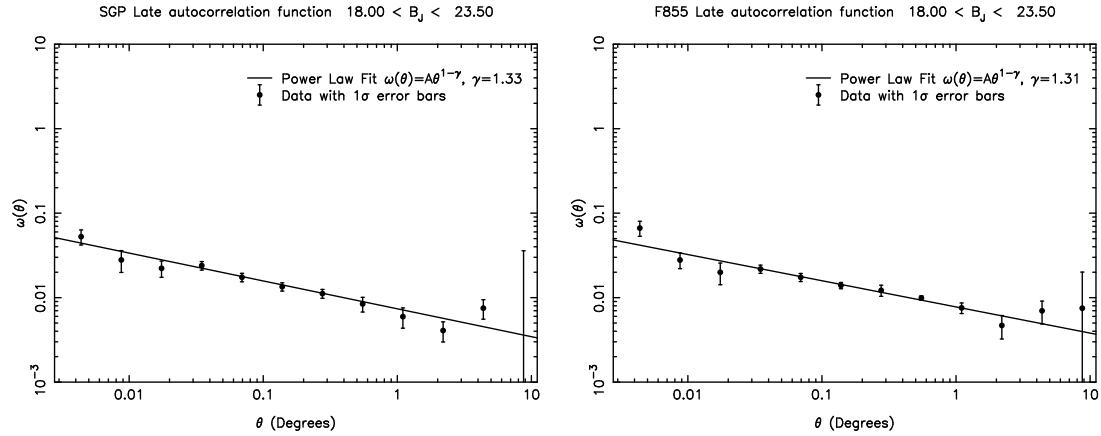


Figure 6.4: The $18.0 < B_J < 23.5$ late subsample autocorrelation function for the SGP and F855 fields. The clustering on small angular scales is an order of magnitude weaker than the autocorrelation function of early subsample galaxies.

Table 6.2: The Early Subsample Angular Correlation Function

| Field | | SGP | | | F855 | | |
|---------------------------|-----------|-----------------|--------------------------|-----------|-----------------|--------------------------|--|
| Magnitude Range | N_{gal} | γ | $\omega(1') \times 10^3$ | N_{gal} | γ | $\omega(1') \times 10^3$ | |
| <hr/> | | | | | | | |
| $18.0 \leq B_J \leq 20.0$ | 2206 | 1.70 ± 0.11 | 1352 ± 233 | 2599 | 1.75 ± 0.21 | 782 ± 196 | |
| $18.0 \leq B_J \leq 21.0$ | 5187 | 1.79 ± 0.08 | 830 ± 83 | 5553 | 1.89 ± 0.14 | 554 ± 81 | |
| $18.0 \leq B_J \leq 22.0$ | 11056 | 1.74 ± 0.04 | 510 ± 51 | 11303 | 1.91 ± 0.09 | 329 ± 34 | |
| $18.0 \leq B_J \leq 23.0$ | 21833 | 1.81 ± 0.05 | 283 ± 28 | 21652 | 1.84 ± 0.07 | 194 ± 19 | |
| $18.0 \leq B_J \leq 23.5$ | 29290 | 1.82 ± 0.06 | 221 ± 22 | 27915 | 1.87 ± 0.05 | 169 ± 17 | |
| <hr/> | | | | | | | |

Table 6.3: The Late Subsample Angular Correlation Function

| Field | | SGP | | | F855 | | |
|---------------------------|-----------|-----------------|--------------------------|-----------|-----------------|--------------------------|--|
| Magnitude Range | N_{gal} | γ | $\omega(1') \times 10^3$ | N_{gal} | γ | $\omega(1') \times 10^3$ | |
| $18.0 \leq B_J \leq 20.0$ | 3854 | 1.37 ± 0.27 | 443 ± 257 | 4648 | 1.53 ± 0.31 | 283 ± 87 | |
| $18.0 \leq B_J \leq 21.0$ | 11952 | 1.40 ± 0.13 | 269 ± 25 | 13866 | 1.55 ± 0.15 | 154 ± 21 | |
| $18.0 \leq B_J \leq 22.0$ | 37785 | 1.34 ± 0.10 | 120 ± 9 | 43047 | 1.41 ± 0.13 | 76 ± 7 | |
| $18.0 \leq B_J \leq 23.0$ | 128278 | 1.28 ± 0.09 | 44 ± 8 | 134331 | 1.26 ± 0.16 | 39 ± 24 | |
| $18.0 \leq B_J \leq 23.5$ | 207390 | 1.33 ± 0.10 | 28 ± 4 | 183347 | 1.31 ± 0.12 | 27 ± 6 | |

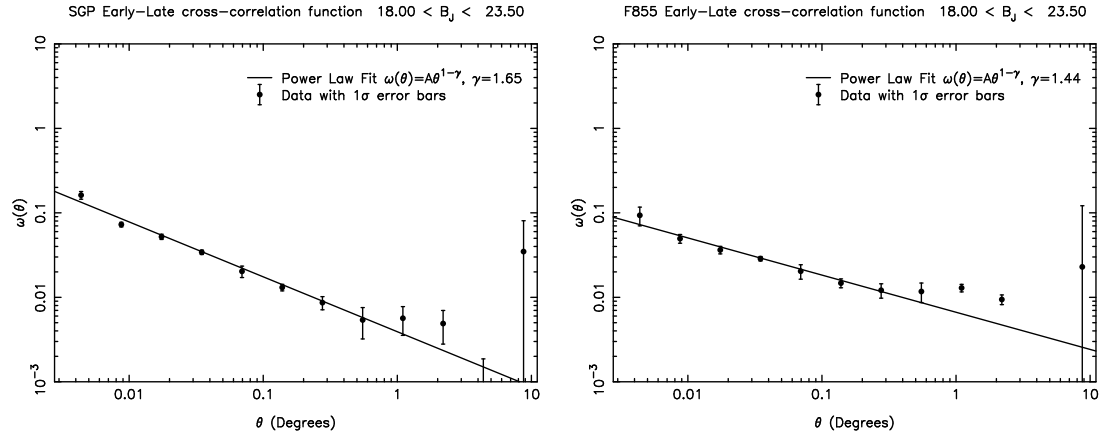


Figure 6.5: The $18.0 < B_J < 23.5$ early-late cross-correlation function. The cross-correlation function is significantly weaker than the autocorrelation of early subsample galaxies.

Table 6.4: The Early-Late Angular Cross-Correlation Function

| Field | SGP | | F855 | |
|---------------------------|-----------------|--------------------------|-----------------|--------------------------|
| Magnitude Range | γ | $\omega(1') \times 10^3$ | γ | $\omega(1') \times 10^3$ |
| $18.0 \leq B_J \leq 20.0$ | 1.43 ± 0.25 | 430 ± 105 | 1.53 ± 0.35 | 194 ± 70 |
| $18.0 \leq B_J \leq 21.0$ | 1.67 ± 0.08 | 322 ± 30 | 1.52 ± 0.11 | 198 ± 20 |
| $18.0 \leq B_J \leq 22.0$ | 1.73 ± 0.06 | 183 ± 10 | 1.60 ± 0.07 | 102 ± 8 |
| $18.0 \leq B_J \leq 23.0$ | 1.76 ± 0.04 | 85 ± 4 | 1.56 ± 0.07 | 52 ± 3 |
| $18.0 \leq B_J \leq 23.5$ | 1.65 ± 0.04 | 56 ± 3 | 1.44 ± 0.07 | 40 ± 2 |

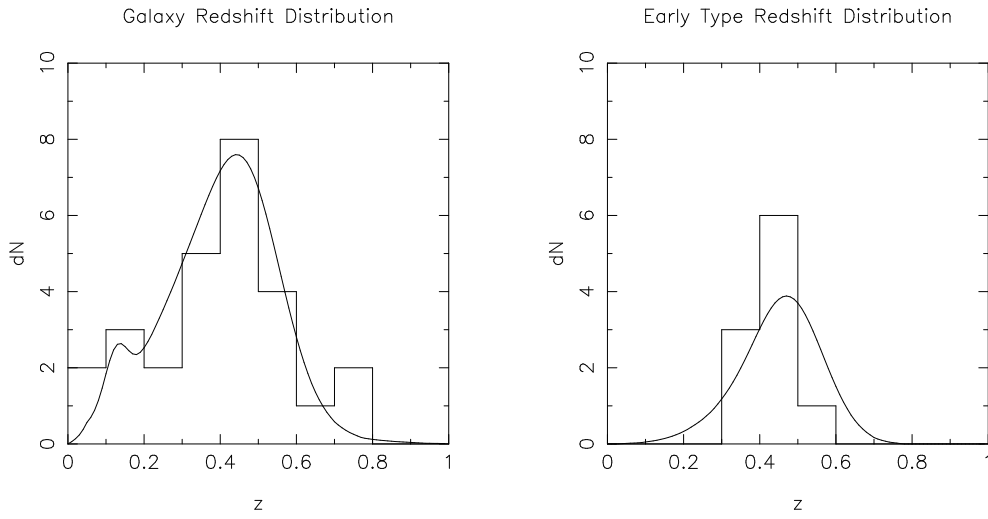


Figure 6.6: A comparison of the observed and model redshift distributions of galaxies from Glazebrook *et al.* (1995) which were detected in the Panoramic Deep Fields. The left panel shows all galaxy types while the right panel shows galaxies with colours redder than Sbc galaxies. While limited by the small number of galaxies available, the model of the redshift distribution is similar to the observed redshift distribution, with both peaking at similar redshifts.

ted in Figures 6.7 and 6.8. The large redshift errors for blue galaxies results in the late subsample redshift distribution being significantly broader than the early subsample redshift distribution. The width of the distribution is consistent with late-type galaxies having smaller k -corrections and a higher fraction of dwarf galaxies than early-type galaxies. It should be noted that while the photometric redshifts are complete to $B_J = 23.5$ for the early subsample, photometric redshifts for $B_J > 22.5$ late subsample galaxies are incomplete and this may slightly skew the redshift distribution.

The amplitude of the early subsample autocorrelation function in the SGP has been plotted in Figure 6.9. To allow the comparison of the amplitude at different magnitudes, the value of γ has been fixed to 1.8. Models with clustering fixed in physical and comoving coordinates have been fitted to the $B_J = 22.5$ data point. The models have been fitted to this data point as it has a large number of galaxy-galaxy pairs while avoiding systematic errors which could be present at the faintest magnitudes of the sample. The models are a reasonable approximation to the data though there are discrepancies between the models and the data for very bright and very faint galaxies. The fit parameters of $r_0 = 6.9 \pm 0.2 h^{-1} \text{Mpc}$ and

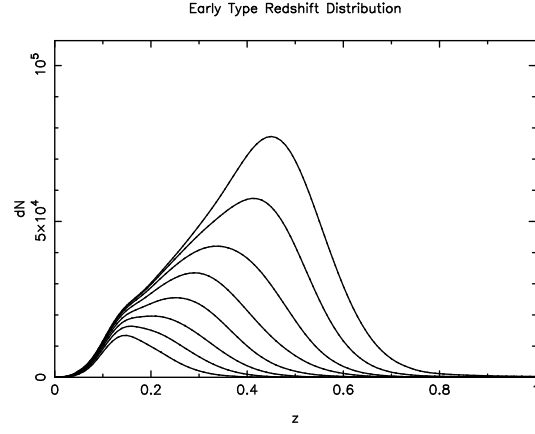


Figure 6.7: The estimated redshift distribution of the early subsample in the SGP. The curves range from $18.0 < B_J < 20.0$ to $18.0 < B_J < 23.5$ in half magnitude steps.

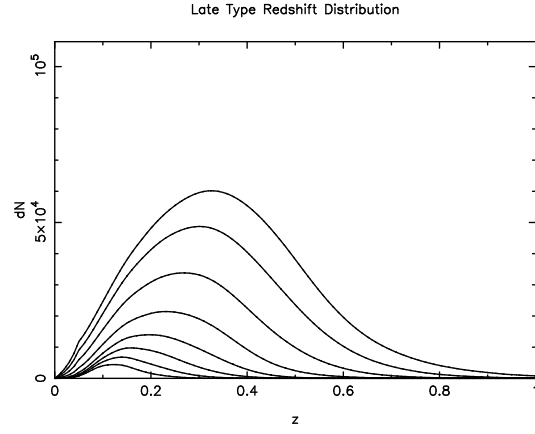


Figure 6.8: The estimated redshift distribution of the late subsample in the SGP. The curves range from $18.0 < B_J < 20.0$ to $18.0 < B_J < 23.5$ in half magnitude steps.

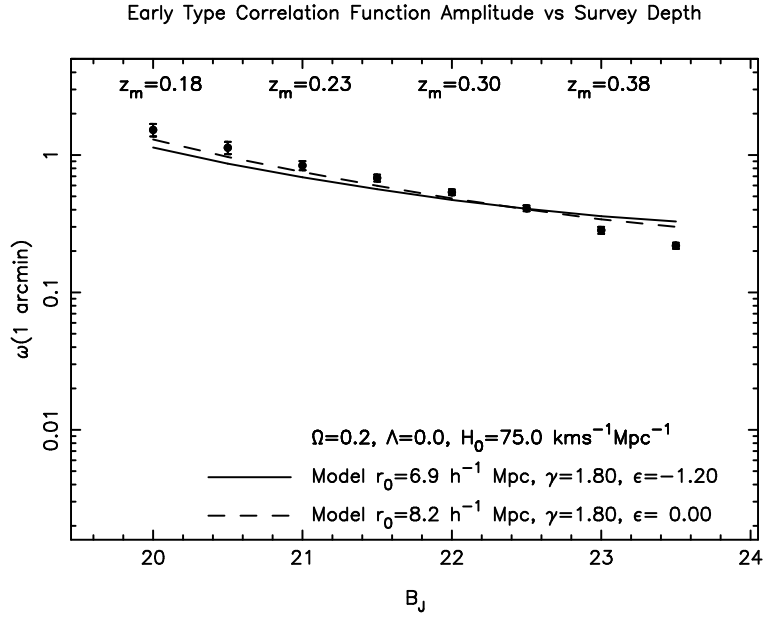


Figure 6.9: The amplitude of the autocorrelation function of the early subsample in the SGP. Models fitted to the $B_J = 22.5$ data point with clustering fixed in comoving and physical coordinates are shown. The median redshift of the sample as a function of depth is listed at the top of the plot.

$r_0 = 8.2 \pm 0.2 h^{-1} \text{Mpc}$ for clustering fixed in comoving and physical coordinates are comparable to estimates of the clustering of early-types in the local Universe (Loveday *et al.* 1995, Guzzo *et al.* 1997). However, it should be noted that the errors quoted for r_0 are underestimates as the uncertainties in the redshift distribution and the effects of large-scale-structure have not been considered.

Figure 6.10 plots the amplitude of the SGP late subsample autocorrelation function as a function of limiting magnitude. At small angular scales the clustering of the late subsample is an order of magnitude weaker than the clustering of the early subsample. Models fitted to the $B_J = 22.5$ data point underpredict the clustering at brighter magnitudes and overpredict the clustering at fainter magnitudes. The observed clustering at bright magnitudes is considerably stronger than the observed clustering of blue galaxies measured in Chapter 4. This is probably due to the use of redder selection criteria and $B_J - R$ being correlated with but not equivalent to $U - B_J$. The rapid decrease of the amplitude of the late subsample autocorrelation function at faint magnitudes is probably due to the faint blue galaxy population which has a similar effect on the correlation function of all B_J galaxies (Chapter 4).

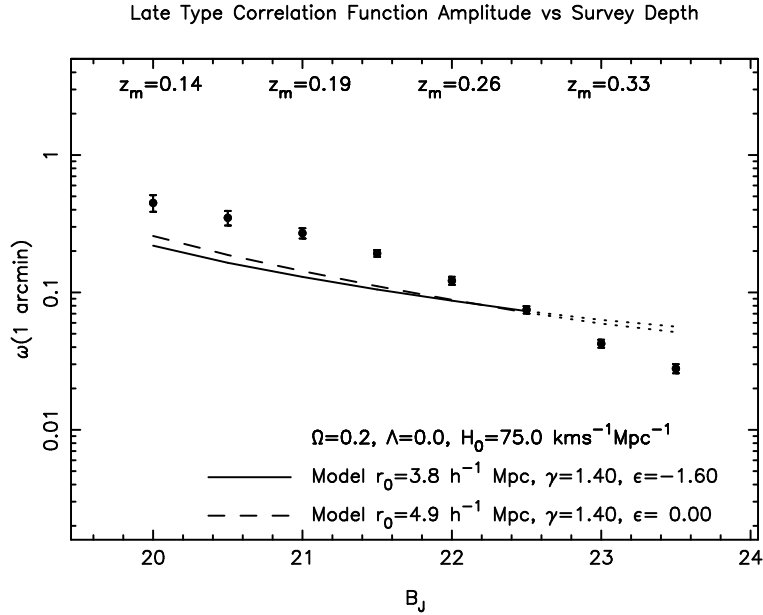


Figure 6.10: The amplitude of the autocorrelation function of the late subsample in the SGP. The models are shown with dotted lines at $B_J > 22.5$ as the photometric redshifts are incomplete at faint magnitudes.

The amplitude of the early-late subsample cross-correlation function is plotted in Figure 6.11. The models fitted to the $B_J = 22.5$ data point have comparable values of r_0 to the late subsample autocorrelation function but at smaller angular scales the clustering is considerably stronger as the value of γ is significantly larger. The models do overpredict the clustering at faint magnitudes and this may be due to the faint blue galaxy population.

6.4 The AGN Sample

The AGN sample consists of *UBR* selected $B_J < 20.5$ broad emission line AGN from La Franca *et al.* (1999). The survey area is the SGP field and while Figure 6.12 shows that the sky coverage is not homogeneous, it is not strongly concentrated in one part of the field. AGN positions were determined with matches to the Panoramic Deep Fields so astrometric errors would not affect estimates of the angular correlation function at small angular scales. When an AGN was matched to multiple objects, the astrometry, magnitudes and colours were compared with published values for the AGN.

The $0.3 < z < 0.7$ catalogue consists of 66 QSOs and Seyfert 1s with

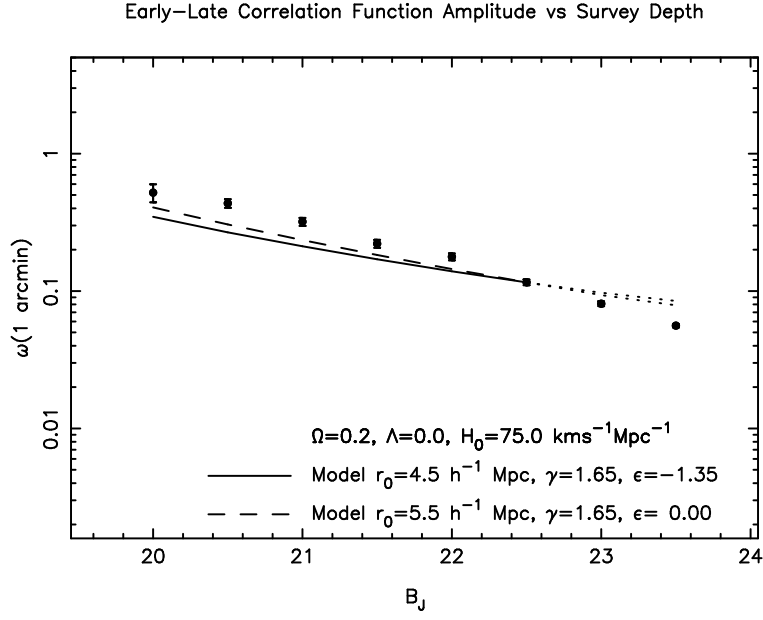


Figure 6.11: The amplitude of the early-late cross-correlation function. The models are shown with dotted lines at $B_J > 22.5$ as the late sample photometric redshifts are incomplete over this magnitude range.

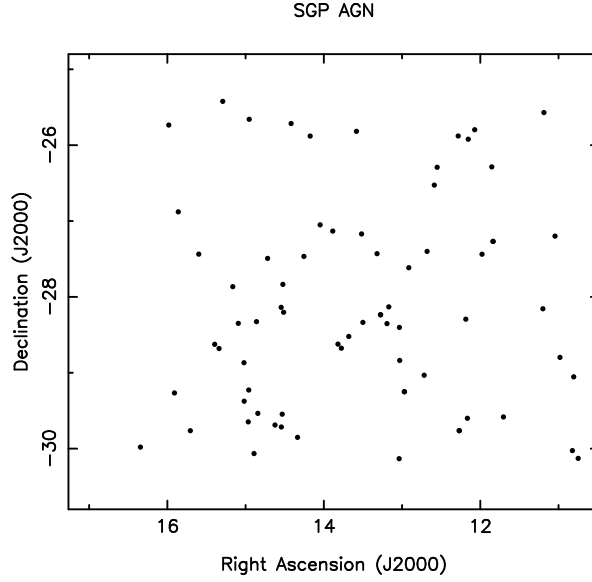


Figure 6.12: The distribution of the $0.3 < z < 0.7$ AGN on the plane of the sky. While the sky coverage is not homogeneous, it is not strongly concentrated in any one region of the field.

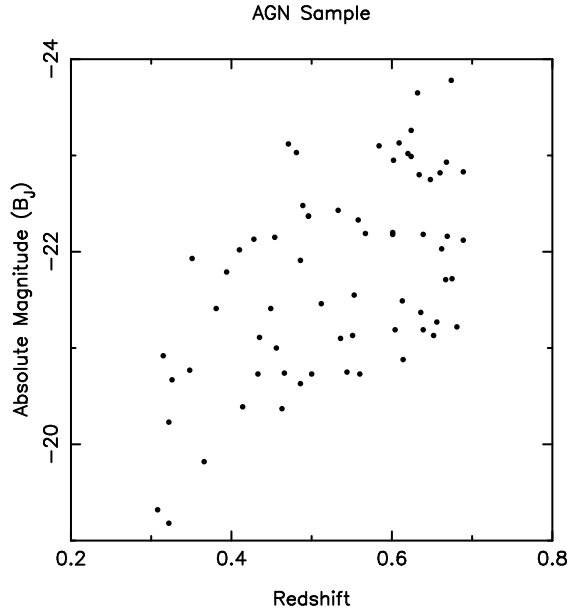


Figure 6.13: The absolute magnitudes and redshifts of the $0.3 < z < 0.7$ AGN selected from the La Franca *et al.* (1999) catalogue. The absolute magnitudes have been determined with $\Omega = 1$, $H_0 = 100 \text{ km s}^{-1} \text{ Mpc}^{-1}$ and k -corrections approximated by $k(z) = -0.4z$.

$-24 < M_{B_J} < -19$. The B_J absolute magnitudes and redshifts of the AGN are plotted in Figure 6.13. The catalogue contains 36 QSOs ($M_{B_J} < -21.5$) and 30 Seyfert 1 galaxies. The range of absolute magnitudes is comparable to the X-ray selected AGN studied by Schade, Boyle & Letawsky (1993) and if the host galaxy morphologies are similar, then $\sim 75\%$ of the AGN sample are in hosts earlier than Sbc galaxies.

6.5 AGN-Galaxy Clustering

The estimator of the angular correlation function used to study AGN-galaxy associations is

$$\hat{\omega}_{ag}(\theta) = \frac{AG}{AR} - 1 \quad (6.3)$$

where AG and AR are the number of AGN-galaxy and normalised AGN-random pairs separated by $\theta \pm \delta\theta$. The random data set consists of multiple copies of the galaxy catalogue with the positions randomised.

Estimates of the cross-correlation of AGN with the early and late subsamples

are summarised in Table 6.5. The AGN-early cross-correlation is significantly stronger on scales $\gtrsim 1'$ while on smaller scales the signal-to-noise is poor. Despite the strength of the AGN-early cross-correlation, inspection of Table 6.5 shows most AGN-galaxy pairs are AGN-late pairs and the cross-correlation of AGN with all galaxies should be similar to the AGN-late cross-correlation function. Figures 6.14 and 6.15 show the AGN-early and AGN-late cross-correlation functions for $B_J < 23.5$ galaxies. The AGN-early cross-correlation is fitted well by a power law with $\gamma = 1.8$. A power law with $\gamma = 1.65$ has been fitted to the AGN-late cross-correlation though the low significance of the detected signal results in a poor fit. The AGN-late cross-correlation shows evidence of a possible artifact of ~ 0.01 at large angular scales. This may be a result of the small size and inhomogeneous sky coverage of the QSO sample. Figure 6.16 confirms that the cross-correlation of AGN with all galaxies is similar to the AGN-late cross-correlation function and is much weaker than the AGN-early cross-correlation function. As the fraction of late-type galaxies increases with survey depth, the cross-correlation function of AGN with all galaxies should decrease with increasing magnitude. This may have already been observed by Smith, Boyle and Maddox (1995, 2000) who find the AGN-galaxy cross-correlation function decreases from $r_0 \sim 5h^{-1}\text{Mpc}$ for $z < 0.3$ QSOs to $r_0 \sim 3h^{-1}\text{Mpc}$ for $0.3 < z < 0.7$ QSOs.

Models of the spatial correlation function have been fitted to the data using Limber's equation (Limber 1954). As the redshifts of the AGN are known, Limber's equation is given by

$$\omega(\theta) = \sum_i^n \left[\int \xi_{ag}(r, z) \frac{dN_g}{dz} dz \right] \bigg/ \sum_i^n \left[\int \frac{dN_g}{dz} dz \right] \quad (6.4)$$

where n is the number of AGN, $\xi_{ag}(r, z)$ is the spatial cross-correlation function, $\frac{dN_g}{dz}$ is the number of galaxies per unit redshift and r is the distance in physical coordinates between an AGN at redshift z_i and a galaxy at redshift z separated by angle θ on the sky.

The amplitude of the AGN-early correlation function is plotted in Figure 6.17 along with models of the cross-correlation with evolution fixed in comoving coordinates. The models fitted to the $B_J = 22.5$ data point have values of r_0 more than 5σ higher than the early subsample autocorrelation function. This is consistent with AGN host galaxies being in environments richer than early-type galaxies and is comparable to the environment of radio-loud QSOs at the same redshift (Yee & Green 1987).

Table 6.5: The cross-correlation function of AGN and galaxies at $0.3 < z < 0.7$. The values of $\hat{\omega}(\theta)$ have been corrected for the integral constraint which is $\sim 10\%$ of the estimate of the correlation function at $1'$.

| Magnitude Range | Angle | AG | $AR \times 20$ | $\hat{\omega}(\theta)$ |
|---------------------------|-----------------------------|-------|----------------|------------------------|
| AGN-Early | | | | |
| $18.0 \leq B_J \leq 22.5$ | $7'' \leq \theta < 14''$ | 6 | 63 | 0.91 ± 1.13 |
| $18.0 \leq B_J \leq 22.5$ | $14'' \leq \theta < 28''$ | 13 | 274 | -0.04 ± 0.35 |
| $18.0 \leq B_J \leq 22.5$ | $28'' \leq \theta < 56''$ | 57 | 994 | 0.15 ± 0.15 |
| $18.0 \leq B_J \leq 22.5$ | $56'' \leq \theta < 112''$ | 264 | 4077 | 0.30 ± 0.07 |
| $18.0 \leq B_J \leq 22.5$ | $112'' \leq \theta < 224''$ | 853 | 15840 | 0.09 ± 0.04 |
| $18.0 \leq B_J \leq 23.5$ | $7'' \leq \theta < 14''$ | 10 | 117 | 0.71 ± 0.73 |
| $18.0 \leq B_J \leq 23.5$ | $14'' \leq \theta < 28''$ | 27 | 506 | 0.07 ± 0.20 |
| $18.0 \leq B_J \leq 23.5$ | $28'' \leq \theta < 56''$ | 109 | 1858 | 0.18 ± 0.11 |
| $18.0 \leq B_J \leq 23.5$ | $56'' \leq \theta < 112''$ | 483 | 7732 | 0.26 ± 0.06 |
| $18.0 \leq B_J \leq 23.5$ | $112'' \leq \theta < 224''$ | 1613 | 30233 | 0.08 ± 0.03 |
| AGN-Late | | | | |
| $18.0 \leq B_J \leq 22.5$ | $7'' \leq \theta < 14''$ | 15 | 288 | 0.04 ± 0.39 |
| $18.0 \leq B_J \leq 22.5$ | $14'' \leq \theta < 28''$ | 51 | 1146 | -0.10 ± 0.12 |
| $18.0 \leq B_J \leq 22.5$ | $28'' \leq \theta < 56''$ | 254 | 4580 | 0.11 ± 0.07 |
| $18.0 \leq B_J \leq 22.5$ | $56'' \leq \theta < 112''$ | 903 | 18264 | -0.01 ± 0.03 |
| $18.0 \leq B_J \leq 22.5$ | $112'' \leq \theta < 224''$ | 3600 | 71550 | 0.01 ± 0.02 |
| $18.0 \leq B_J \leq 23.5$ | $7'' \leq \theta < 14''$ | 42 | 833 | 0.01 ± 0.16 |
| $18.0 \leq B_J \leq 23.5$ | $14'' \leq \theta < 28''$ | 166 | 3211 | 0.04 ± 0.08 |
| $18.0 \leq B_J \leq 23.5$ | $28'' \leq \theta < 56''$ | 725 | 13187 | 0.11 ± 0.04 |
| $18.0 \leq B_J \leq 23.5$ | $56'' \leq \theta < 112''$ | 2663 | 52543 | 0.02 ± 0.02 |
| $18.0 \leq B_J \leq 23.5$ | $112'' \leq \theta < 224''$ | 10587 | 207839 | 0.03 ± 0.01 |

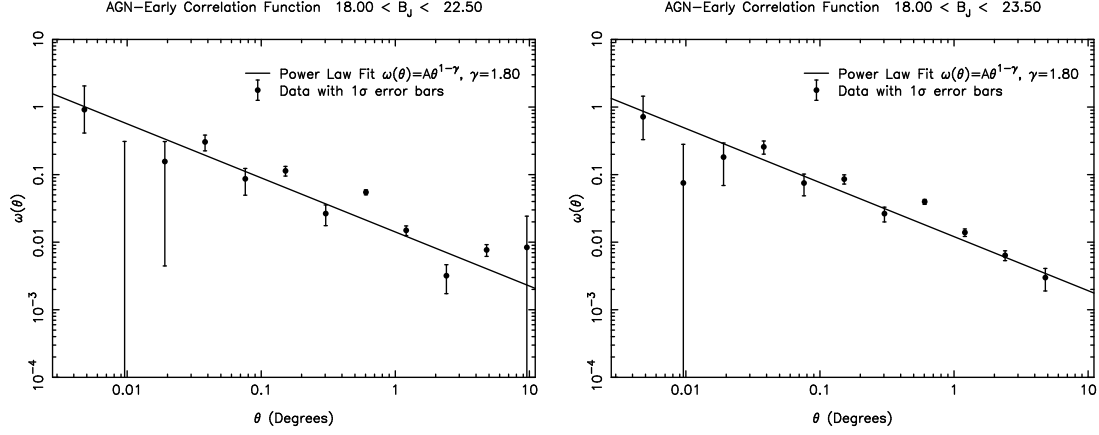


Figure 6.14: The AGN-early subsample angular cross-correlation function. The data is shown with 1σ error bars determined with Poisson statistics. Power law fits with $\gamma = 1.8$ are a good approximation to the observed clustering.

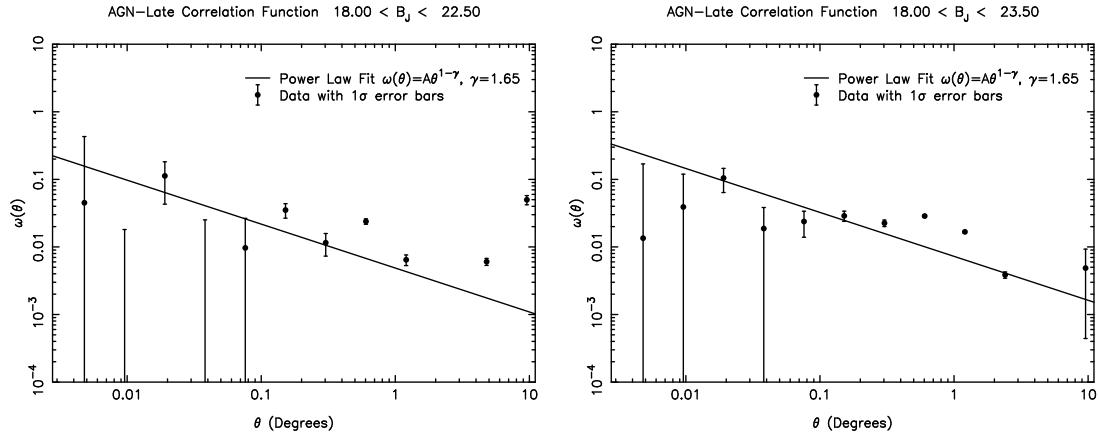


Figure 6.15: The AGN-late subsample angular cross-correlation function. The clustering is considerably weaker than the AGN-early cross-correlation function and the signal-to-noise is poor. A power law with $\gamma = 1.65$ has been fitted to the data though the quality of the fits is poor.

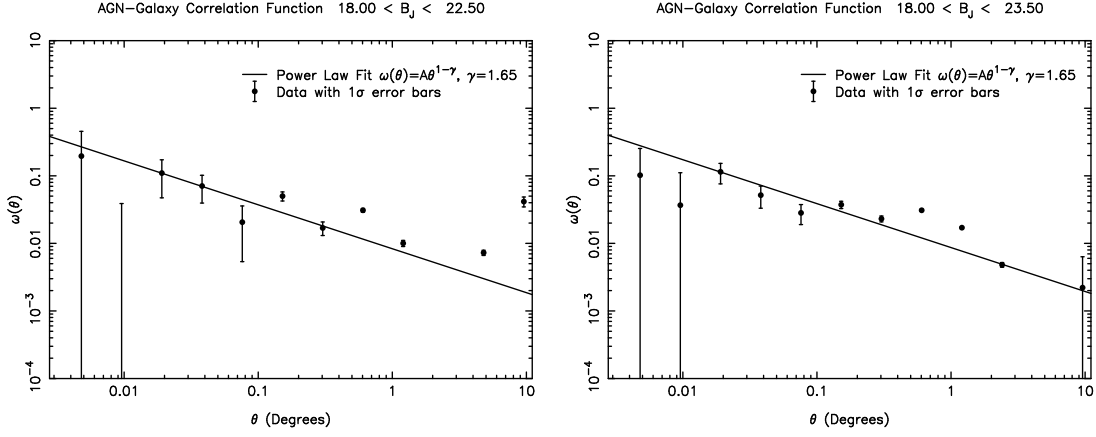


Figure 6.16: The cross-correlation of AGN with all galaxies in the SGP. The clustering is significantly weaker than the AGN-early cross-correlation function and is only slightly stronger than the AGN-late cross-correlation function.

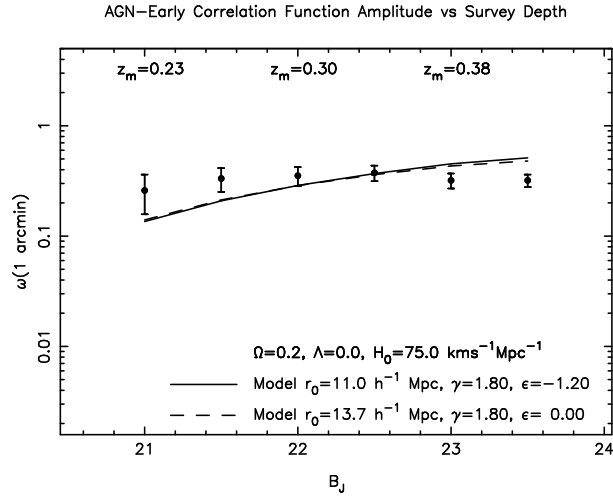


Figure 6.17: The amplitude of the AGN-early angular cross-correlation function. The amplitude of the clustering increases with magnitude as few bright galaxies are at the same redshift as the QSO sample. Models with clustering fixed in comoving and physical coordinates have been fitted to the $B_J = 22.5$ data point. The clustering is significantly stronger than the autocorrelation function of early-type galaxies and similar to the clustering observed near radio-loud QSOs.

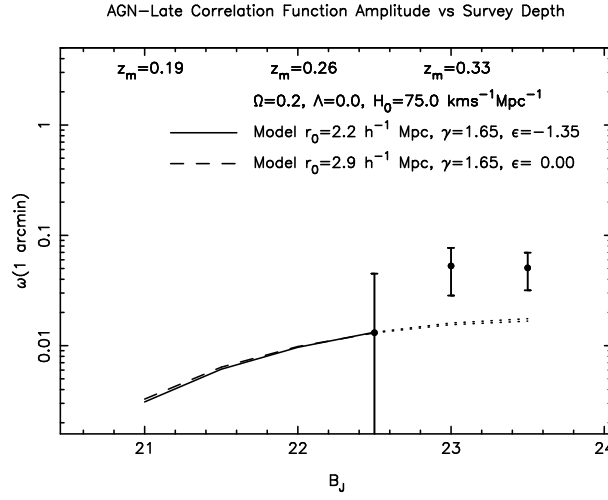


Figure 6.18: The amplitude of the AGN-late cross-correlation function. Models of the spatial correlation function have been fitted to the $B_J = 22.5$ data point. The clustering is considerably weaker than the AGN-early cross-correlation though the poor signal-to-noise of the AGN-late angular cross-correlation function results in the estimates of r_0 having errors of $\sim \pm 2h^{-1}\text{Mpc}$. The models are shown with dotted lines at $B_J > 22.5$ as incompleteness affects the photometric redshift estimates used to derive the redshift distribution at these magnitudes.

The amplitude of the AGN-late cross-correlation function is shown in Figure 6.18. As expected, comparison of the data with Figure 6.17 confirms that the AGN-late cross-correlation function is much weaker than the AGN-early cross-correlation function. However, low signal-to-noise of the angular correlation function results in the estimates of r_0 having considerable uncertainty.

The errors of the estimates of $\omega(\theta)$ are dominated by galaxies along the line-of-sight which are not associated with the AGN. The signal and significance of the correlation function can be improved if the number of unassociated galaxies included in the estimate of $\omega(\theta)$ are reduced. Early-type galaxies have comparatively small photometric redshift errors so it is possible to define a narrow range of photometric redshifts which could be associated with the AGN. Figures 6.19 and 6.20 show the AGN-early cross-correlation function for galaxies with photometric redshifts within 2σ of the AGN redshift. Comparison of the two panels of Figure 6.20 shows the signal-to-noise of the cross-correlation function is significantly improved by including photometric redshift constraints.

The spatial AGN-early cross-correlation can be determined by deriving the

Table 6.6: The cross-correlation of AGN with the early subsample with photometric redshift constraints applied to the data.

| Magnitude Range | Angle | AG | $AR \times 20$ | $\hat{\omega}(\theta)$ |
|---------------------------|-----------------------------|------|----------------|------------------------|
| $18.0 \leq B_J \leq 22.5$ | $7'' \leq \theta < 14''$ | 2 | 29 | 0.39 ± 1.81 |
| $18.0 \leq B_J \leq 22.5$ | $14'' \leq \theta < 28''$ | 4 | 105 | -0.22 ± 0.60 |
| $18.0 \leq B_J \leq 22.5$ | $28'' \leq \theta < 56''$ | 33 | 443 | 0.50 ± 0.26 |
| $18.0 \leq B_J \leq 22.5$ | $56'' \leq \theta < 112''$ | 117 | 1729 | 0.36 ± 0.13 |
| $18.0 \leq B_J \leq 22.5$ | $112'' \leq \theta < 224''$ | 383 | 6955 | 0.11 ± 0.06 |
| $18.0 \leq B_J \leq 22.5$ | $224'' \leq \theta < 448''$ | 1455 | 26358 | 0.11 ± 0.03 |
| $18.0 \leq B_J \leq 23.5$ | $7'' \leq \theta < 14''$ | 6 | 72 | 0.67 ± 0.99 |
| $18.0 \leq B_J \leq 23.5$ | $14'' \leq \theta < 28''$ | 16 | 277 | 0.16 ± 0.29 |
| $18.0 \leq B_J \leq 23.5$ | $28'' \leq \theta < 56''$ | 78 | 1220 | 0.29 ± 0.14 |
| $18.0 \leq B_J \leq 23.5$ | $56'' \leq \theta < 112''$ | 293 | 4652 | 0.27 ± 0.07 |
| $18.0 \leq B_J \leq 23.5$ | $112'' \leq \theta < 224''$ | 993 | 18544 | 0.08 ± 0.03 |
| $18.0 \leq B_J \leq 23.5$ | $224'' \leq \theta < 448''$ | 3854 | 71790 | 0.08 ± 0.02 |

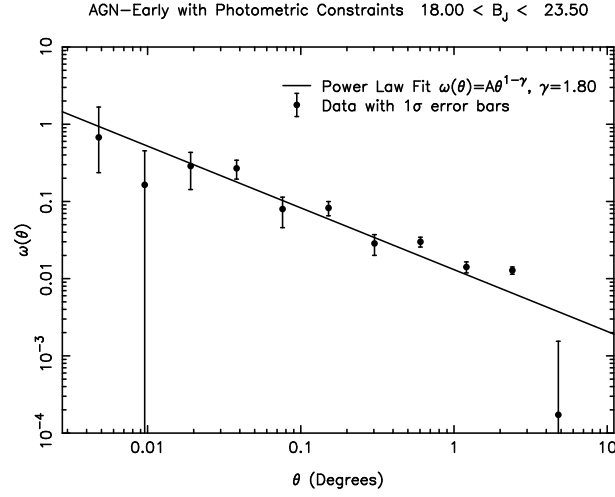


Figure 6.19: The angular cross-correlation of AGN and $B_J < 23.5$ early subsample galaxies with photometric redshift constraints applied to the pair counts. Poisson statistics have been used to determine the 1σ errors shown with the data points. A power law with $\gamma = 1.8$ is a good fit to the data.

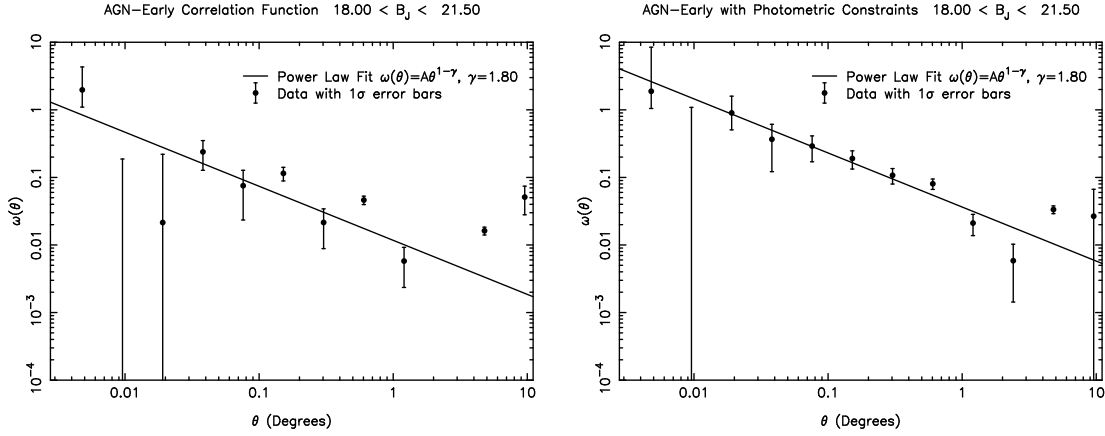


Figure 6.20: Estimates of the cross-correlation of AGN and $B_J < 21.5$ early subsample galaxies without (left panel) and with (right panel) photometric redshift constraints. The improvement in the signal-to-noise and the power law fit to the data is immediately apparent.

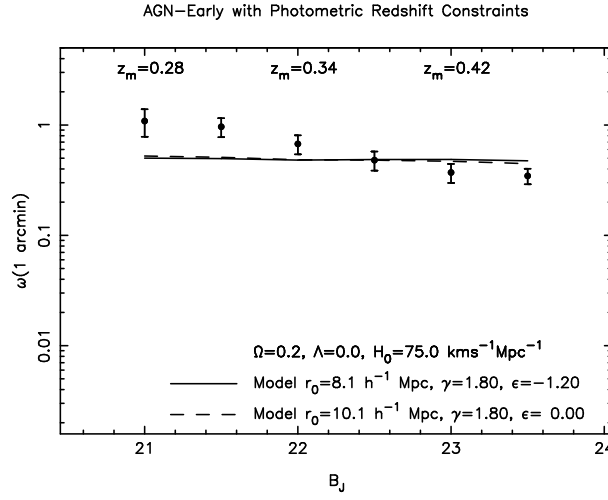


Figure 6.21: The amplitude of the AGN-early cross-correlation function with photometric redshift constraints applied. The errors are significantly reduced and the best fits to the faint data are slightly decreased. However, the amplitude of the clustering is similar to that estimated in Figure 6.17 and is consistent with AGN being in rich environments. The estimated median redshifts are for early subsample galaxies that satisfy the photometric redshift constraints rather than the entire early subsample.

redshift distribution of galaxies within 2σ of each AGN when applying Limber's equation. The amplitude of the AGN-early cross-correlation and models of the spatial cross-correlation are shown in Figure 6.21. The fit to the $B_J = 22.5$ data point is marginally weaker than in Figure 6.17 and underpredicts the amplitude of the correlation function at bright magnitudes.

The variations of the measured clustering from the model could be due to systematic errors, small number statistics at low redshift or evolution of the AGN-early clustering. Systematic errors are difficult to identify though it is probable that they would perturb the shape of the angular correlation from a power law. To determine if small number statistics could be significantly biasing the estimate of the cross-correlation function, the distribution of the number of AGN-early pairs per AGN is plotted in Figure 6.22. The plot shows 4 AGN may have an excess of AGN-early pairs compared with the rest of the sample.

B_J and R images of the 4 AGN (Figures 6.23 and 6.24) show apparent overdensities of galaxies but it isn't conclusive that all 4 AGN are associated with clusters. There are no ROSAT (Voges *et al.* 2000) detections of X-ray emission

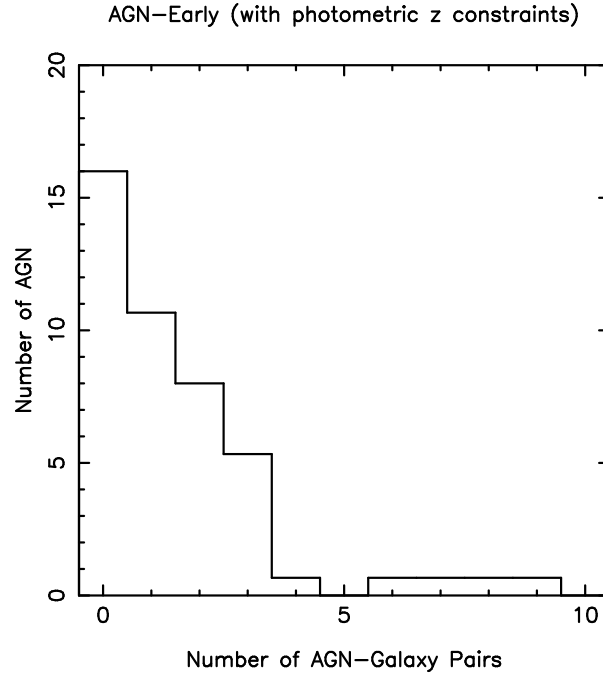


Figure 6.22: The distribution of AGN-early pairs with separations less than $56''$. While most of the AGN sample have less than 5 AGN-early pairs, the 4 AGN with > 5 AGN-early pairs contribute $\sim 30\%$ of the total number of AGN-early pairs.

Table 6.7: AGN with an excess of AGN-galaxy pairs. Photometric redshift constraints have been applied to the estimate of AGN-early pairs but not to the estimate of AGN-late pairs.

| AGN | Redshift | M_{BJ} | AGN-Early Pairs < 56'' | AGN-Late Pairs < 56'' |
|-------------|----------|----------|---------------------------|--------------------------|
| Q 0057-3020 | 0.394 | -21.79 | 9 | 23 |
| Q 0054-2608 | 0.604 | -21.19 | 8 | 24 |
| Q 0058-2856 | 0.322 | -19.18 | 7 | 22 |
| Q 0046-2609 | 0.435 | -21.11 | 5 | 17 |
| Total | - | - | 29 | 86 |
| All AGN | - | - | 100 | 933 |

associated with the 4 AGN. None of the 4 AGN were detected by the NVSS survey and they are presumably radio-quiet ($< 5\text{mJy}$ at 1.4GHz). Table 6.7 lists the number of AGN-galaxy pairs the 4 AGN contribute along with the number of AGN-galaxy pairs for the entire AGN sample. The 4 AGN, which are 6% of the AGN sample, contribute $\sim 30\%$ of the $< 56''$ AGN-early pairs and $\sim 10\%$ of the $< 56''$ AGN-late pairs. Laurikainen & Salo (1995) also found a small fraction of their $z < 0.05$ Seyfert sample were in unusually rich environments though most of these objects were Seyfert 2s. If the 4 AGN are removed from the sample, the amplitude of the cross-correlation function (shown in Figure 6.25) decreases significantly and is comparable to the early subsample autocorrelation function. It is plausible that most AGN hosts are in environments similar to normal galaxies with the same morphology while a small number of AGN are in considerably richer environments.

Radio-loud AGN environments may be correlated with rich environments comparable to galaxy clusters (Yee & Green 1987). To determine if radio-loud AGN

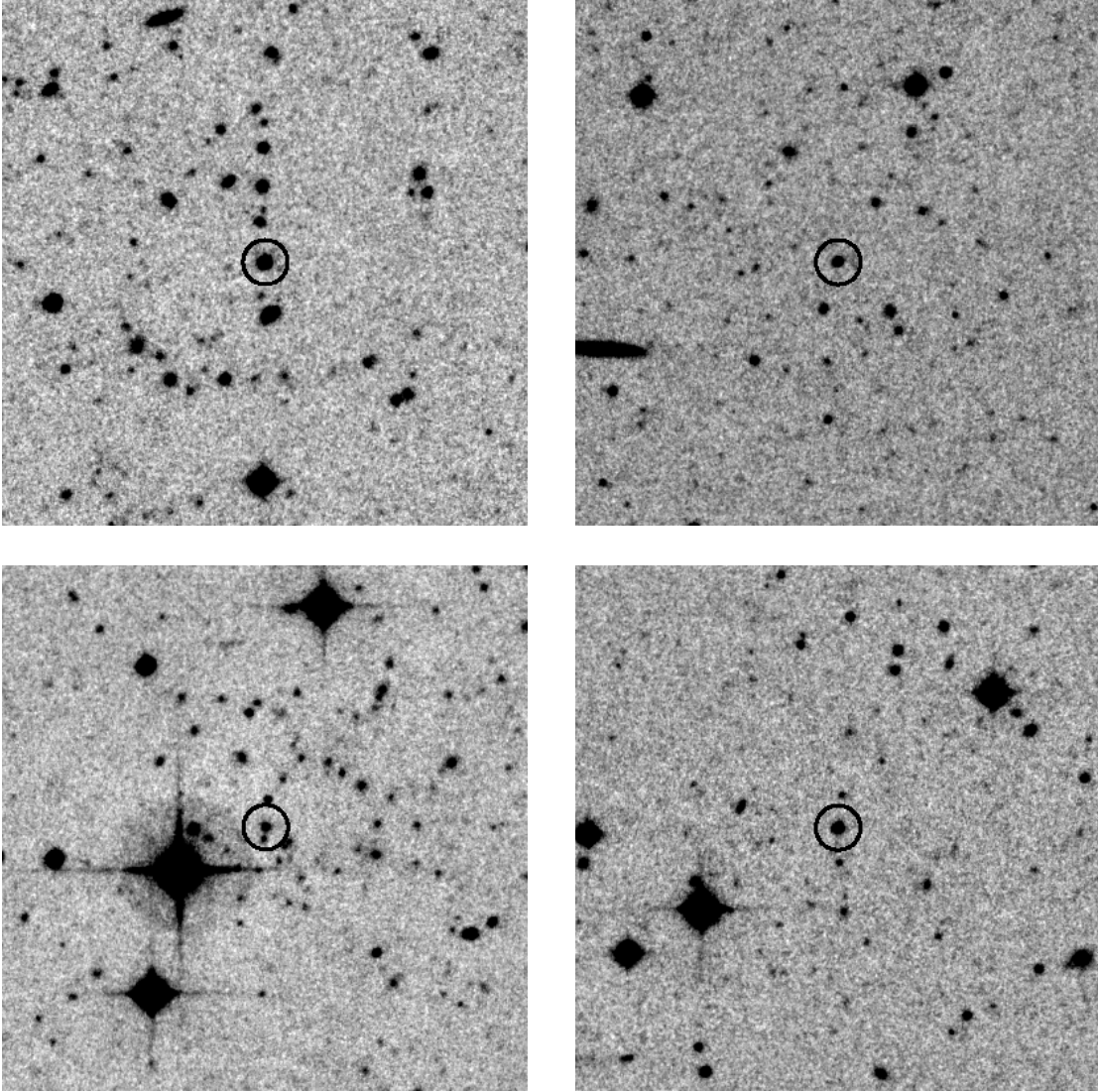


Figure 6.23: B_J band images of Q 0057-3020 (top-left), Q 0054-2608 (top-right), Q 0058-2856 (bottom-left) and Q 0046-2609 (bottom-right). The images are $4.5' \times 4.5'$ with north at the top and east to the left.

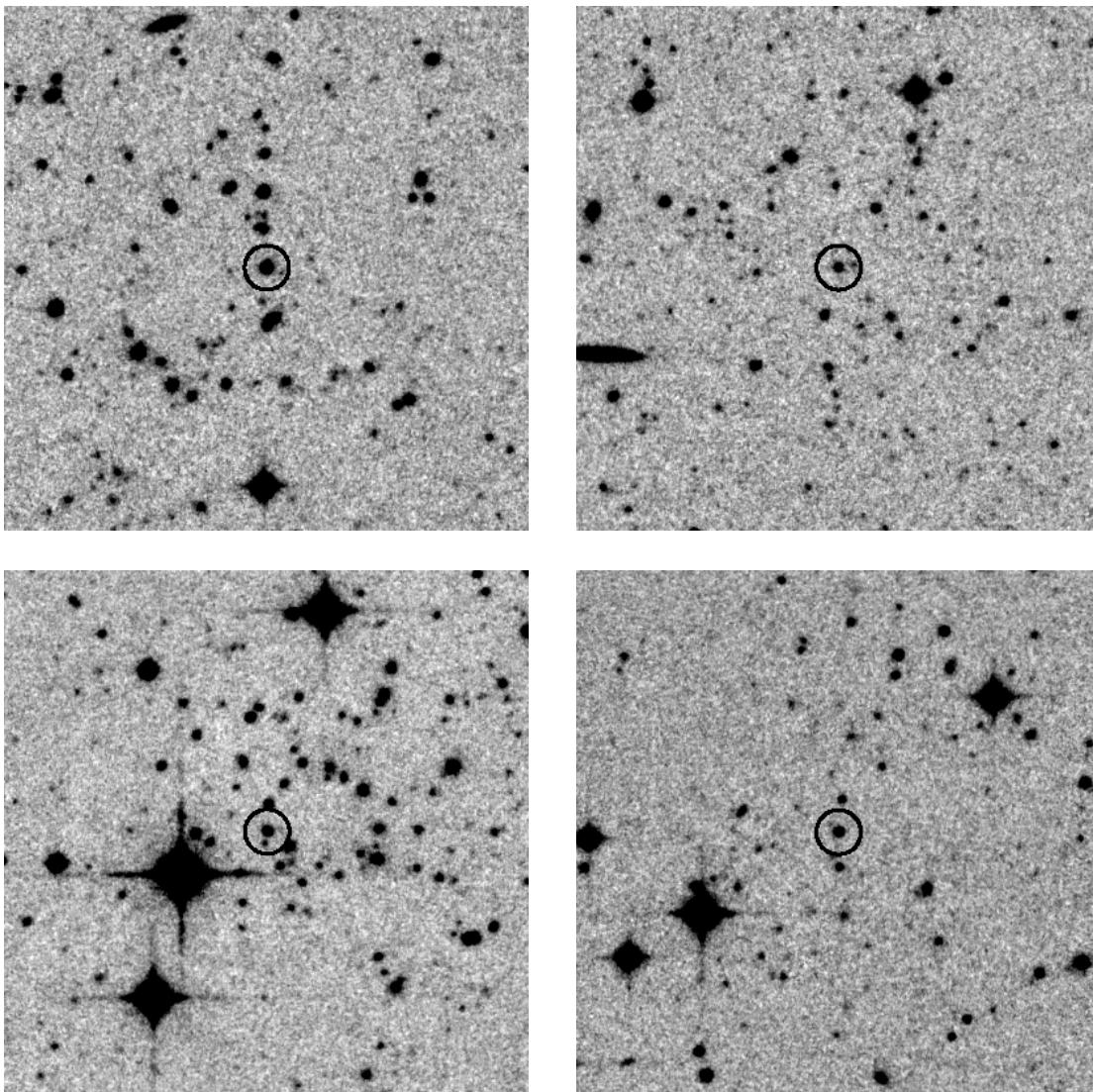


Figure 6.24: R band images of Q 0057-3020 (top-left), Q 0054-2608 (top-right), Q 0058-2856 (bottom-left) and Q 0046-2609 (bottom-right). The images are $4.5' \times 4.5'$ with north at the top and east to the left.

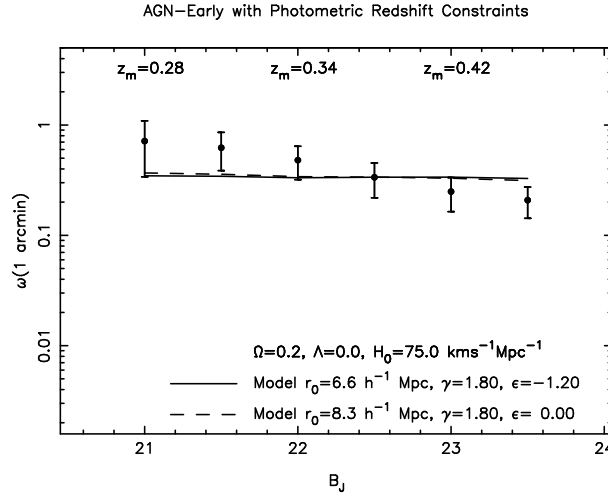


Figure 6.25: The amplitude of the AGN-early cross-correlation with the 4 AGN from Table 6.7 removed from the sample. The amplitude of the correlation function decreases significantly and is comparable to the early subsample autocorrelation function.

significantly bias the estimate of the AGN-galaxy correlation, AGN within $20''$ of NVSS sources and their AGN-galaxy pair counts are listed in Table 6.8. The radio emission associated with the AGN is $< 0.1\text{Jy}$ which is considerably fainter than the radio-loud QSO samples of Yee & Green (1987) and Hall & Green (1998). The 5 AGN contribute 3% of the AGN-early pairs and 7% of the AGN-late pairs with separations $< 56''$. A series of R band images of the AGN in Figure 6.26 do not show any evidence for the AGN being in unusually rich environments.

There may be a correlation between AGN luminosity and host galaxy with luminous AGN occurring more frequently in early-type galaxies than Seyferts (McLure *et al.* 1999). If this is the case, the correlation between galaxy morphology and environment may result in a correlation between AGN luminosity and environment. Figure 6.27 compares the amplitudes of the Seyfert 1 ($M_{B_J} < -21.5$) and QSO ($M_{B_J} > -21.5$) cross-correlations with the early subsample. Fits to the $B_J = 22.5$ data point show QSOs are in slightly richer environments but the significance of the detection is $\sim 1\sigma$. The models also consistently underestimate the clustering at $B_J < 22.5$.

Figures 6.21, 6.25 and 6.27 show evidence the amplitude of the AGN-early cross-correlation weakening with increasing magnitude and redshift. To determine if the AGN-early cross-correlation evolves over the observed redshift range, the

Table 6.8: AGN within $20''$ of NVSS sources. Q 0040-2024 and Q 0057-2555 are within or near drilled regions of the field.

| AGN | Redshift | M_{B_J} | $S_{1.4}$ (mJy) | Optical-Radio Position Offset | AGN-Early Pairs $< 56''$ | AGN-Late Pairs $< 56''$ |
|-------------|----------|-----------|--------------------|----------------------------------|-----------------------------|----------------------------|
| Q 0101-2600 | 0.449 | -21.41 | 52.6 | $2.6''$ | 2 | 23 |
| Q 0058-2808 | 0.308 | -19.32 | 39.7 | $12.6''$ | 0 | 20 |
| Q 0040-2024 | 0.609 | -23.13 | 38.0 | $3.0''$ | 0 | 0 |
| Q 0057-2555 | 0.315 | -20.92 | 6.5 | $5.5''$ | 1 | 5 |
| Q 0051-2726 | 0.689 | -22.83 | 6.4 | $4.0''$ | 0 | 13 |

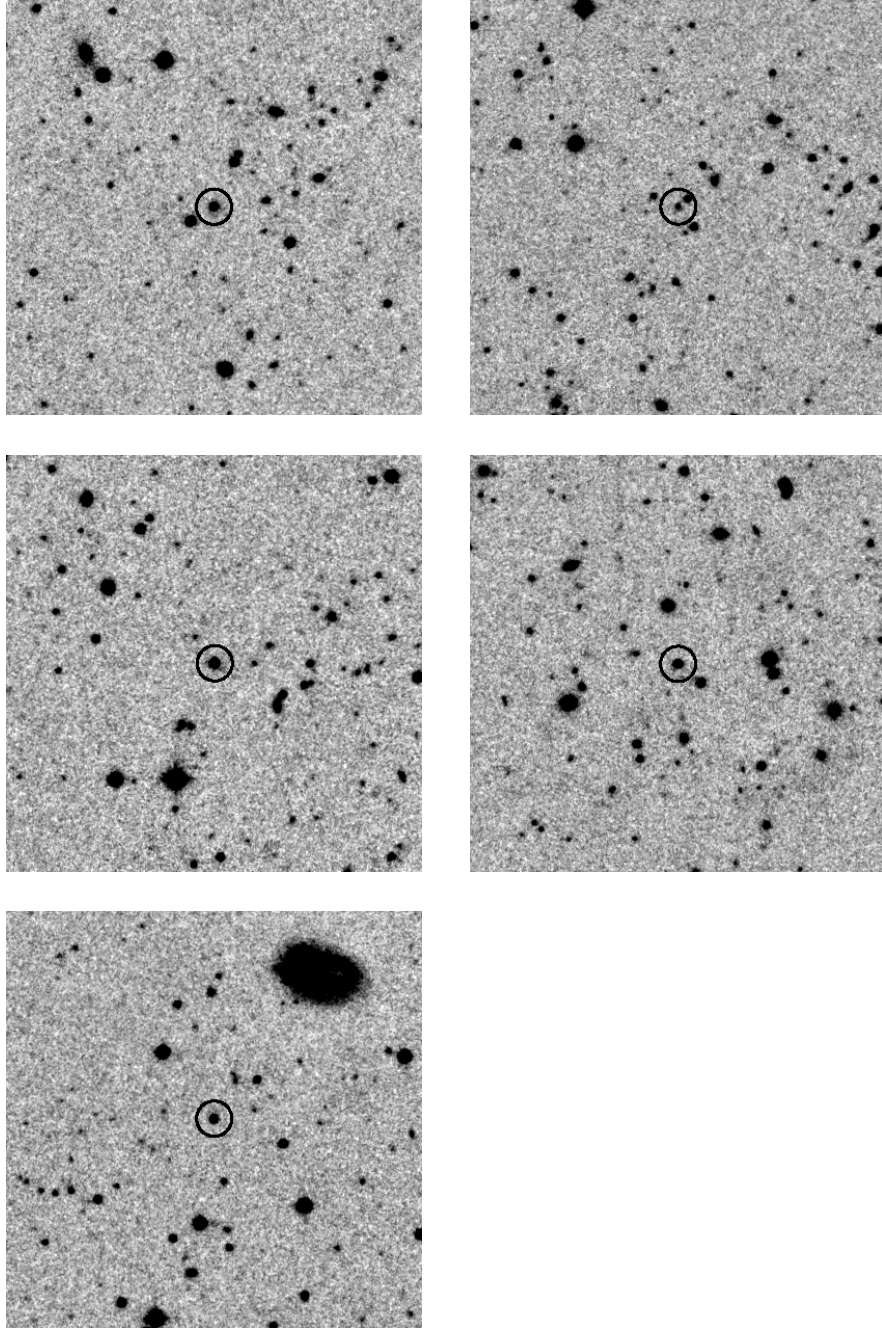


Figure 6.26: *R* band images of AGN within $20''$ of NVSS sources. The AGN are Q 0101-2600 (top-left), Q 0058-2808, Q 0040-2024, Q 0057-2555 and Q 0051-2726 (bottom-left). The images are $4.5' \times 4.5'$ with north at the top and east to the left. The AGN do not appear to be in unusually rich environments.

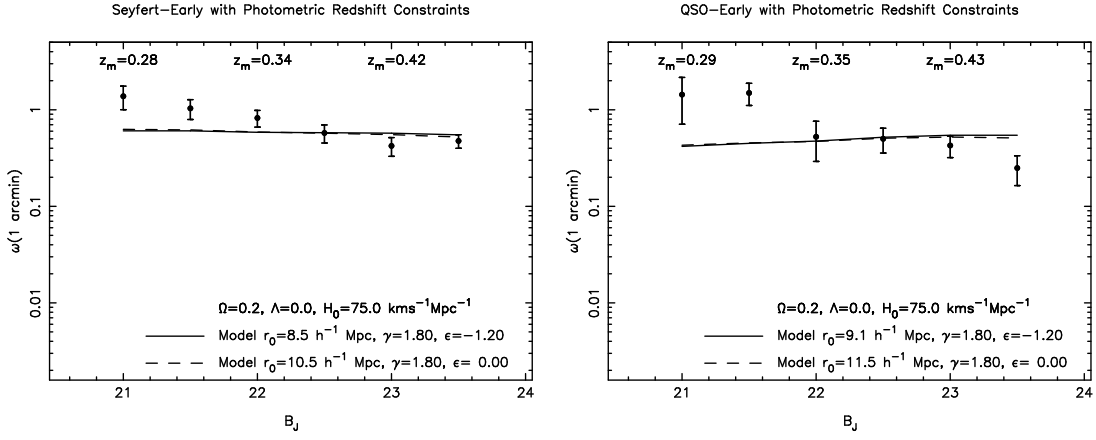


Figure 6.27: The amplitude of the Seyfert 1 and QSO cross-correlation functions. There is no evidence for a strong correlation between AGN luminosity and environment.

amplitude of the cross-correlation has been determined for $0.3 < z < 0.5$ and $0.5 < z < 0.7$ AGN. Figure 6.28 shows plots of the amplitude of the cross-correlation with models of the spatial correlation. While the best fit values of r_0 are higher for $0.5 < z < 0.7$ AGN, the signal-to-noise is poor and the values of r_0 are only $\sim 1\sigma$ higher than the r_0 values for $0.3 < z < 0.5$ AGN.

It is possible that the strong clustering at bright magnitudes is not a property of the AGN but of the galaxy sample with which they are being correlated. The autocorrelation function of early-type galaxies is a function of the absolute magnitude and r_0 decreases from $\sim 7h^{-1}\text{Mpc}$ for $M_{B_J} \sim -21$ galaxies to $\sim 4h^{-1}\text{Mpc}$ for $M_{B_J} \sim -17$ galaxies (Loveday *et al.* 1995). For a sample limited in apparent magnitude, the absolute magnitude will change with redshift resulting in changing clustering properties. The estimated median absolute magnitude of early subsample galaxies which are cross-correlated with $0.3 < z < 0.7$ AGN is shown in Figure 6.29. The median absolute magnitude of the galaxy sample increases with limiting magnitude and it is possible that the stronger clustering observed at bright magnitudes is due to the strong clustering of luminous early-type galaxies. Unfortunately, it is difficult to differentiate between luminous and faint early-type galaxies with photometric redshifts as galaxies with the same multicolour photometry will have the same redshift and magnitude estimates.

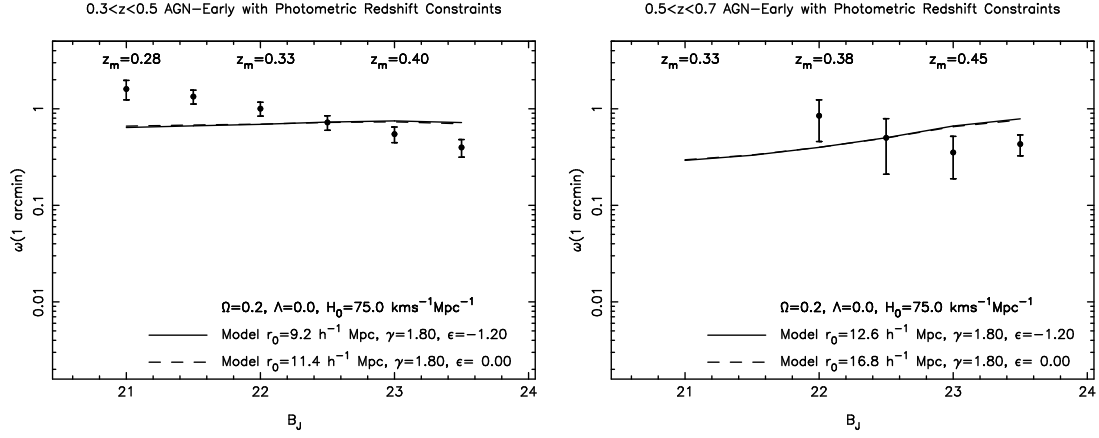


Figure 6.28: The amplitude of the AGN-early cross-correlation function for $0.3 < z < 0.5$ and $0.5 < z < 0.7$ AGN. No significant signal is detected at $B_J < 22$ for the $0.5 < z < 0.7$ AGN sample. There is no clear evidence for a difference in the spatial correlation function of the 2 samples.

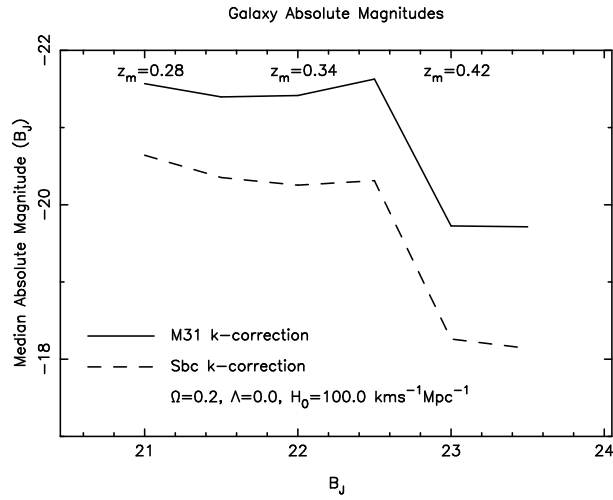


Figure 6.29: The median absolute magnitude of early subsample galaxies which satisfy the photometric redshift constraints with the $0.3 < z < 0.7$ AGN sample. The median absolute magnitude increases with survey depth. As the clustering of early-type galaxies varies with absolute magnitude, the AGN-early cross-correlation would be expected to decrease with limiting magnitude if AGN are a random sample of early-type galaxies.

6.6 Summary

The environments of galaxies and 66 AGN at $z \sim 0.5$ have been measured using photometric redshifts and colour criteria to select galaxy types to $B_J \sim 23.5$. The key conclusions are

- (i) The clustering of early subsample galaxies is strong across the observed magnitude range with $r_0 \sim 7h^{-1}\text{Mpc}$ and $\gamma \sim 1.8$.
- (ii) The autocorrelation function of late subsample galaxies is weak and decreases to $r_0 \sim 2h^{-1}\text{Mpc}$ at $B_J \sim 23.5$.
- (iii) The cross-correlation of $-24 < M_{B_J} < -19$ AGN with the early subsample is stronger than the autocorrelation function of the early subsample. However, the estimate of the correlation function may be biased by $\sim 6\%$ of the AGN sample which could be in rich environments. If these are removed from the sample, the AGN-early cross-correlation function is comparable to the early subsample autocorrelation function.
- (iv) The AGN-late cross-correlation function is very weak. As the fraction of late-type galaxies in magnitude limited samples increases with survey depth, the cross-correlation function of AGN with all galaxies should decrease with increasing magnitude. This may have already been observed by Smith, Boyle & Maddox (1995, 2000).
- (v) The correlation between AGN luminosity and host environment is weak and has not been detected at a significant level in this work.
- (vi) There is no significant evolution of the AGN-early cross-correlation function over the observed redshift range. While the amplitude of the cross-correlation does decrease with magnitude, this may be a selection effect from the early subsample.

Chapter 7

The Evolution of Radio Galaxies

7.1 Introduction

Evolution of radio sources is required to explain the observed number of radio sources and the redshift distribution of radio sources with observed optical counterparts (Condon 1984, Peacock 1985). While the evolution of the radio luminosity function is well established (Dunlop & Peacock 1990, Rowan-Robinson *et al.* 1993), the physical processes responsible for the evolution are not understood. Radio-loud QSOs can be observed over a wide range of redshifts but historically it has been difficult to measure the environment and properties of QSO hosts. Only recently has it been possible to place constraints on the distribution of morphologies of AGN hosts at low redshift (McLure *et al.* 1999, Schade, Boyle & Letawsky 2000, Urry *et al.* 2000) and the environment of radio-quiet AGN at $z > 0.3$ (Chapter 6).

Radio galaxies are relatively easy to study at low redshift as their radio morphology and host galaxies are resolved with ground-based imaging (Matthews, Morgan & Schmidt 1964). Studies of low redshift radio galaxies have established that they are in environments richer than the field (Longair & Seldner 1979, Prestage & Peacock 1988) and their elliptical host galaxies are typically brighter than L_* (Sadler *et al.* 1999, Govoni *et al.* 2000). While radio emission from higher redshift radio galaxies can be detected by radio sky surveys including the NVSS, FIRST and Molonglo, the faint ($B_J \sim 23$) optical counterparts and their low sky surface density ($\sim 5/\square^\circ$) make it difficult to obtain large spectroscopic samples. The properties of radio galaxies at $z \sim 0.5$ have therefore been determined with relatively small numbers of objects. Since strong evolution is apparent at $z \gtrsim 0.5$, this has resulted in poor constraints on the physical processes responsible for radio

galaxy evolution.

With photometric redshifts and colour selection, it is possible to select and estimate the redshifts of $B_J \lesssim 23.5$ early-type galaxies in the Panoramic Deep Fields ($\sim 50^\circ$). By matching early-type galaxies with sources from the NVSS, it is possible to compile a uniformly selected catalogue of $\sim 2 \times 10^2$ radio galaxies to measure the evolution of radio galaxy properties.

7.2 Selection of Radio Galaxies

The radio galaxy sample consists of Panoramic Deep Field galaxies which are associated with NVSS radio sources. As radio galaxies have early-type morphologies (Matthews, Morgan & Schmidt 1964), colour selection criteria are used to select a catalogue of $B_J < 23.5$ early-type galaxies which are then matched to the radio sources. $B_J - R$ colour and photometric redshifts are used to select galaxies which are redder than a non-evolving Sbc. This is the same as the selection criteria used in Chapter 6; Figure 6.2 demonstrates the selection criteria select most early-type galaxies.

As the evolution of the radio galaxy population is to be studied, the criteria used for matching radio and optical sources can not be a function of redshift. The completeness must be high so the luminosity function is not dominated by corrections for incompleteness. Also, the contamination of the sample should be low so estimates of radio galaxy luminosity function and environment are not dominated by galaxies which are not associated with radio sources.

The NVSS source catalogues have 1σ error estimates for the position of each source. Figure 7.1, which is a plot of the estimated errors of the radio source position as a function of flux, shows that the errors are a strong function of radio flux. The positions of bright radio sources have 1σ errors of $\sim 1''$ while the faintest ($\sim 2.5\text{mJy}$) source positions have errors of $\gtrsim 15''$. The sky surface density of $B_J < 23.5$ galaxies which meet the colour selection criteria is $\sim 0.5/\square'$ so $\sim 40\%$ of $\sim 2.5\text{mJy}$ sources will have an unassociated optical galaxy within 2σ of the radio source position. To prevent the catalogue being dominated by spurious matches to faint radio sources, the radio flux limit has been set to 5mJy which is also the completeness limit of the NVSS catalogue.

An obvious criteria for selecting optical counterparts to radio sources is to match objects within $\sim 3\sigma$ of the radio source centroid. This assumes that

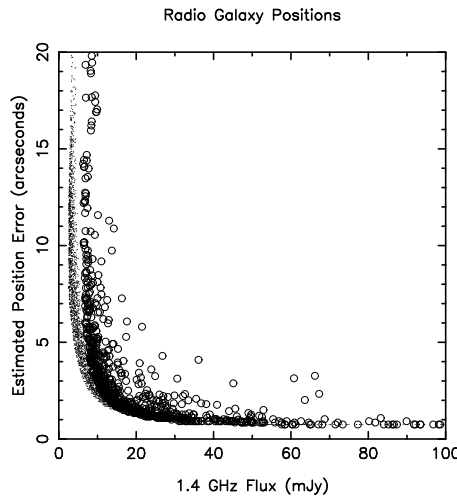


Figure 7.1: The 1σ errors estimated for the NVSS radio source positions as a function of flux. NVSS point sources are shown with dots and extended sources are shown with circles. The estimated error of the positions is strongly correlated with the object flux.

the radio source position and the optical position are not significantly offset. Figure 7.2 shows radio and optical images of three radio sources with nearby counterparts where this assumption is not correct. While radio emission overlaps the optical galaxy position for all three sources, the offset between the NVSS radio and optical centroids is $> 5\sigma$ as the peak of the radio emission is often offset from the optical galaxy.

Selection criteria using only the angular separation between radio and optical sources can select a large fraction of all radio sources. However, for a fixed angular scale, the projected distance increases with redshift introducing selection effects which are a function of redshift. Large radio sources will be excluded at low redshift but will be included at high redshift where the angular size of the radio sources is less than the selection criteria.

As the optical counterparts of radio sources are physical associations, selection criteria based on the physical separation of the optical and radio sources can be used to select radio galaxies. While the NVSS catalogue does not contain redshift information, photometric redshifts can be used to estimate the redshifts of optical galaxies and the projected distance between the optical and radio sources. As the size (in physical coordinates) of radio sources does not rapidly evolve between $z \sim 1$ and $z \sim 0$ (Buchalter *et al.* 1998), selection criteria determined using a

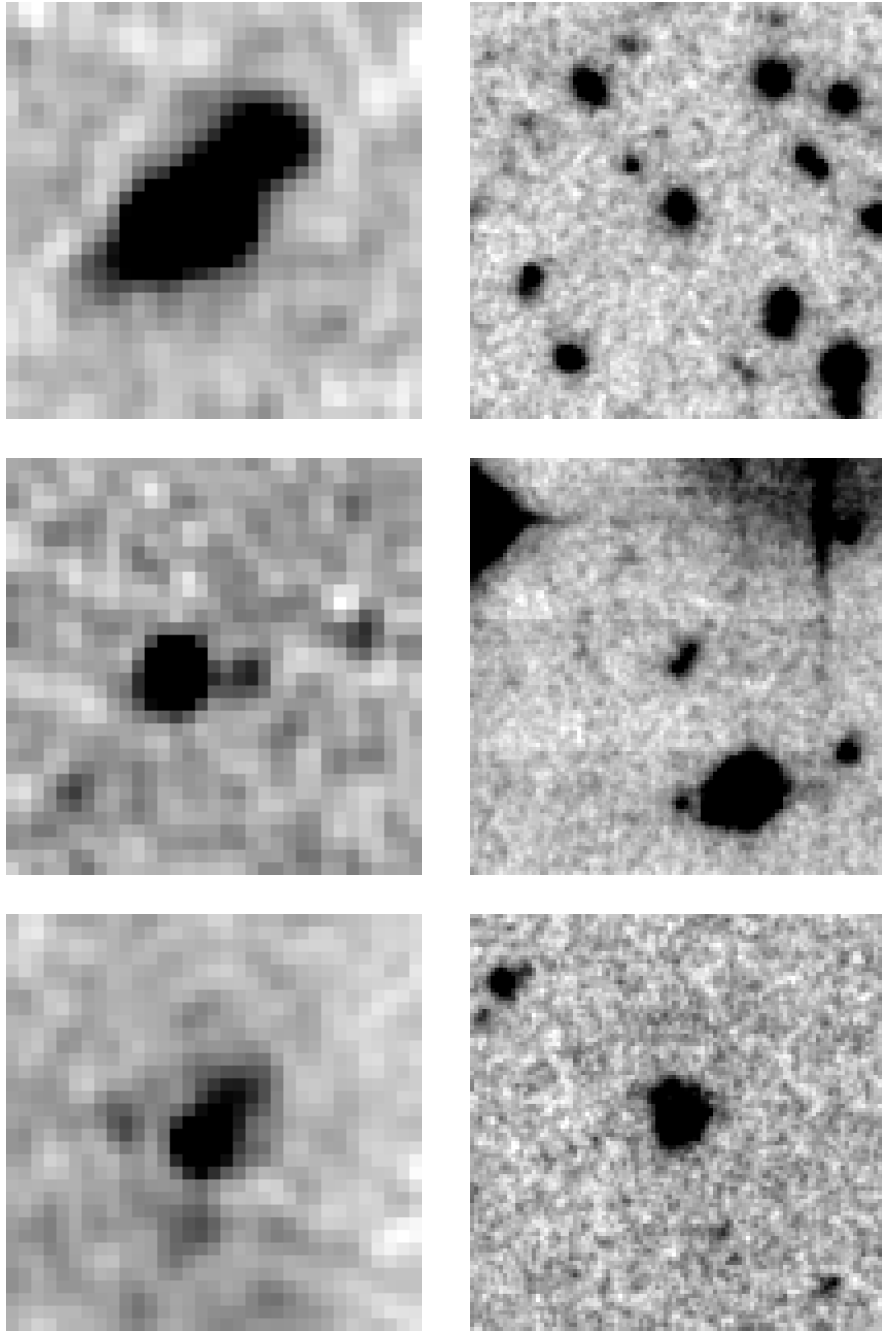


Figure 7.2: Radio (FIRST, White *et al.* 1997) and R band images of the positions of galaxies near NVSS radio sources. All images are $1' \times 1'$ with north at the top and east to the left. The offsets of the NVSS radio position and the optical positions are $4.2''$, $4.0''$ and $4.5''$. None of the galaxies are within 5σ of the radio position though radio emission overlaps the galaxy position in the FIRST images. While FIRST has significantly better resolution than the NVSS, it is not used for the radio galaxy survey as it does not include the SGP.

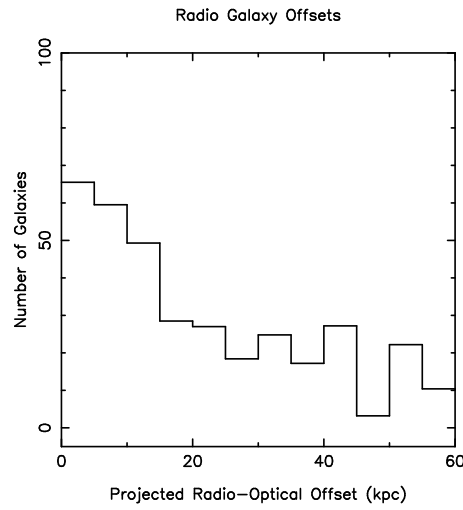


Figure 7.3: The projected distances between radio sources and optical galaxies with angular separations $< 30''$.

fixed projected distance should not introduce selection effects which are a function of redshift.

To determine the projected distance used as the selection criteria for optical counterparts, the distribution of projected distances between NVSS sources and optical galaxies within $30''$ of NVSS sources is plotted in Figure 7.3. The number of optical counterparts declines rapidly on scales $< 20h^{-1}\text{kpc}$ after which the distribution has a long tail. Approximately 25% of the NVSS sources with optical galaxies within $30''$ have more than 1 optical counterpart which is consistent with much of the tail in Figure 7.3 being contamination. To remove the contamination, optical galaxies $> 20h^{-1}\text{kpc}$ from NVSS sources have been excluded from the radio galaxy sample.

The $20h^{-1}\text{kpc}$ selection criteria will exclude large luminous radio sources. This should not affect estimates of the evolution of radio sources as radio source sizes do not rapidly evolve (Buchalter *et al.* 1998) but it will result in the luminosity function being steeper at the bright end. Also, while contamination has been reduced, it is still present in the radio galaxy catalogue. A portion of the catalogue will be matches of unassociated radio sources and optical galaxies. To prevent these objects from biasing the estimate of the luminosity function, a control sample is constructed by randomly repositioning the radio sources and matching them to the galaxy catalogue. This process is repeated 10 times so the control sample size is large enough to not be a significant source of noise in the estimate of the

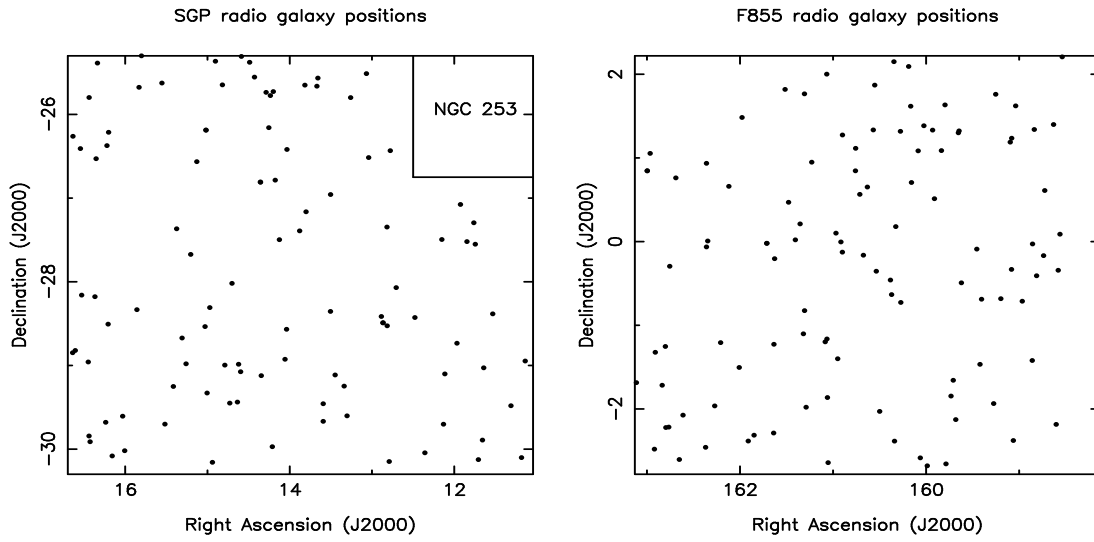


Figure 7.4: The distribution of the radio galaxies on the plane of the sky. Structure is evident in the distribution of radio galaxies and some of the underdensities in the plots are coincident with voids in the distribution of cluster candidates in Figures 5.18 to 5.21.

luminosity function.

Approximately 5% of radio sources with optical counterparts have 2 optical counterparts resulting in ambiguous redshift estimates. As this is a small fraction of the total catalogue, rejecting these objects from the radio galaxy and control samples should only reduce the completeness of the sample by 5% and not significantly bias estimates of the evolution of radio galaxies. The estimates of the space density and luminosity function parameters are renormalised to account for the 5% of radio galaxies removed from the catalogue. The final catalogue of radio galaxy candidates contains 213 objects while the control sample (generated with 10 times as many radio sources) contains 192 objects.

The distribution of the radio galaxies on the plane of the sky is shown in Figure 7.4. The radio galaxies are not randomly distributed across the fields and some $\sim 1^\circ$ regions contain no radio galaxy candidates. Near the north-western edge of the SGP, this is due to interference from starburst NGC 253. However, several of the other regions appear to be associated with underdensities of clusters shown in Figures 5.18 to 5.21 and are probably voids in the distribution of radio galaxies.

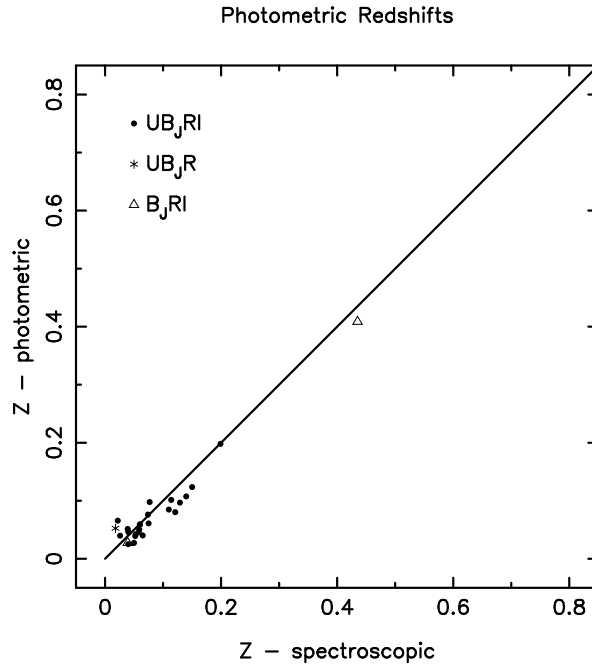


Figure 7.5: A comparison of photometric and spectroscopic redshifts of galaxies which have been matched to the NVSS catalogue. The photometric redshifts for radio galaxies are 15% larger than the redshifts of radio-quiet galaxies with the same multicolour photometry.

7.3 Redshift Distribution

Initial estimates for the redshifts of radio galaxies were obtained with the photometric redshift solutions determined for Chapter 5. Comparison of the photometric redshifts of radio galaxies with spectroscopic redshifts showed that radio galaxy redshifts were systematically underestimated by $\sim 15\%$. This is almost certainly due to radio-galaxies being more luminous than radio-quiet galaxies (Sadler *et al.* 1999, Govoni *et al.* 2000). To correct for this, the photometric redshifts of radio galaxies in this chapter have been increased by 15% and Figure 7.5 shows there is good agreement between the corrected photometric and spectroscopic redshifts.

The B_J and R Hubble diagrams for the optical counterparts of NVSS sources are shown in Figure 7.6. There is a strong correlation between redshift and magnitude though this is partially due to the use of photometric redshifts which result in objects with the same multicolour photometry having the same redshift estimate. Comparison of R band plot in Figure 7.6 with the Hubble diagram

of the control sample (Figure 7.7) shows the radio galaxy sample is generally brighter than the control sample at a given photometric redshift. This is not unexpected as the control sample (and contamination of the radio galaxy sample) includes early spiral galaxies while radio galaxies are typically matched with more luminous elliptical galaxies. The R band Hubble diagram shows evidence for incompleteness at $\log z > -0.25$ ($z > 0.55$) due to the B_J magnitude limit. As the apparent magnitude of a $M_{B_J} \sim -20$ elliptical at $z \sim 0.55$ is $B_J \sim 23$, this is not unexpected. As this incompleteness of the $z > 0.55$ radio galaxies could introduce biases into the estimates of radio galaxy evolution, the sample is limited to redshifts $z < 0.55$. The redshift distributions of the radio-galaxies and the control sample are shown in Figure 7.8. The contamination shows a small peak at high redshift but the contamination is $\lesssim 15\%$ for all redshift bins and contamination should not bias estimates of the luminosity evolution.

7.4 Colour Distribution

The colour selection criteria applied to the radio galaxy candidates will affect the sample completeness at some level. If a large fraction of radio galaxies have colours bluer than the selection criteria, significantly uncertainty is introduced into estimates of the luminosity function and its evolution.

The colours of galaxies in the radio galaxy and control samples are shown as a function of redshift in Figures 7.9 and 7.10. While most radio galaxies have red colours, some do have colours similar to the selection criteria. For comparison, a plot of the colours of radio galaxies from the Dunlop *et al.* (1989) sample is shown in Figure 7.11. While $\sim 50\%$ of the radio galaxies in Figure 7.11 have colours bluer than the selection criteria, most have been flagged by Dunlop *et al.* (1989) as having poor photometry (errors $\gtrsim 0.5$ magnitudes). Comparison of the Figures 7.10 and 7.11 shows that the Dunlop *et al.* (1989) colours have larger scatter than the Panoramic Deep Field colours. Of the 9 $z < 0.8$ radio galaxies from Dunlop *et al.* (1989) with $B_J - R$ estimates with errors less than 0.5, 6 are redder than the selection criteria.

Figure 7.9 contains $\sim 10\%$ contamination which would be expected to introduce an excess of blue galaxies as these comprise most of the faint galaxy population. Figure 7.12 is a plot of the distribution of difference between the radio galaxy colours and the colour selection criteria. Contamination has been

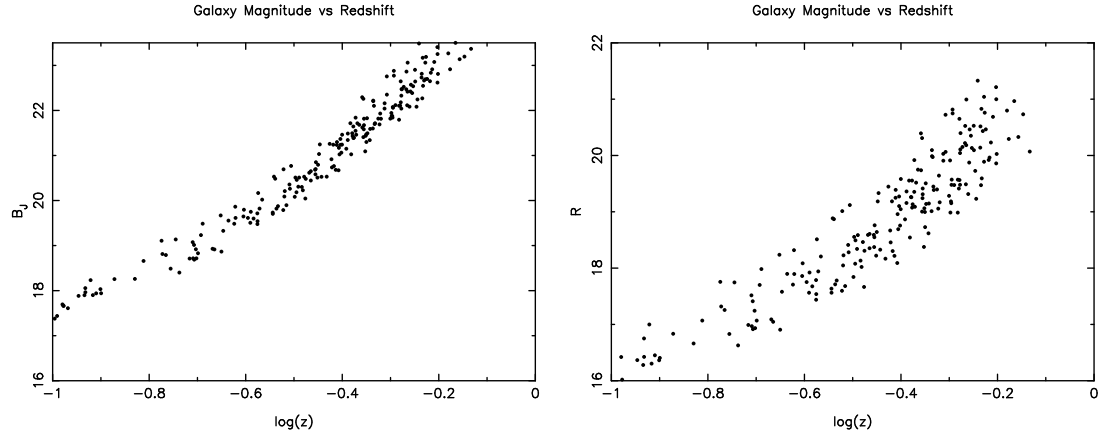


Figure 7.6: The B_J and R Hubble diagrams of $B_J < 23.5$ radio-galaxies in the Panoramic Deep Fields.

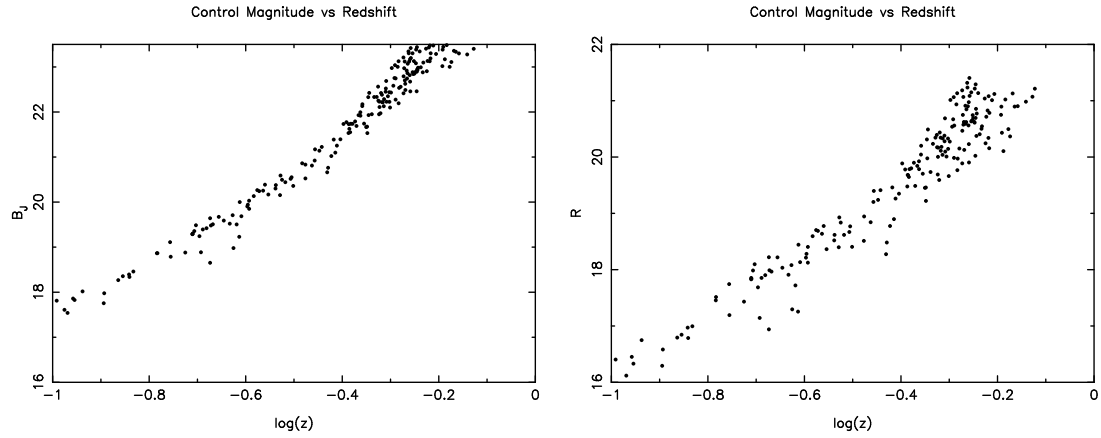


Figure 7.7: The B_J and R Hubble diagrams of control objects.

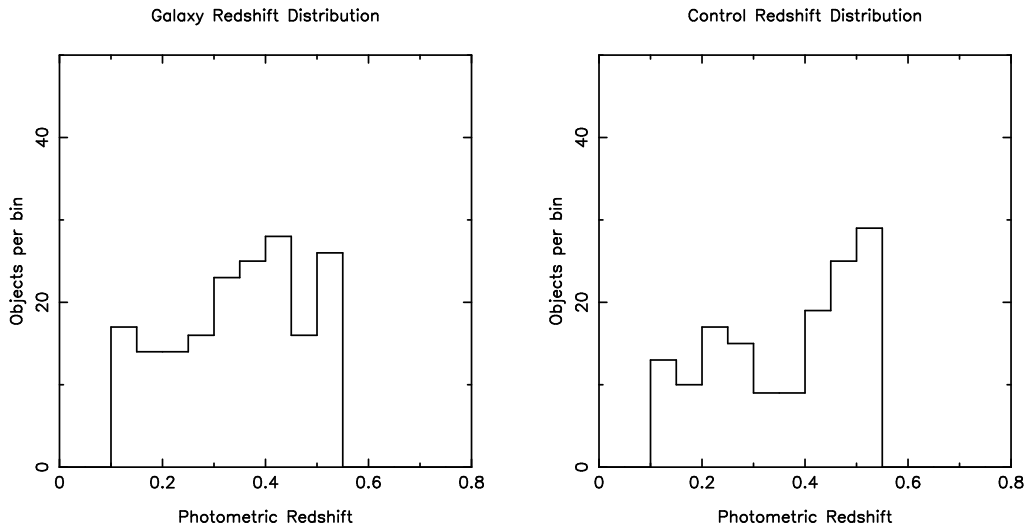


Figure 7.8: The redshift distributions of $0.10 < z < 0.55$ radio galaxies and control objects in the Panoramic Deep Fields.

removed by subtracting the renormalised distribution of the control sample. The peak of the distribution is redder than the selection criteria and the radio galaxy sample is not dominated by blue galaxies. The shape of the distribution is a function of redshift as k -corrections result in redder colours for elliptical galaxies as a function of redshift.

The estimated restframe colours of the radio galaxy sample is plotted in Figure 7.13. Restframe colours have been estimated with linear extrapolations from the E and Sbc k -corrections from Coleman, Wu and Weedman (1980). The peak of the distribution is ~ 0.2 magnitudes redder than the $B_J - R = 1.01$ selection criteria. For comparison, the distribution of radio galaxy colours from Govoni *et al.* (2000) is shown in Figure 7.14. If the Govoni *et al.* sample is representative of all radio galaxies, then $\sim 85\%$ of radio galaxies are selected by the colour selection criteria. However, the distributions in Figures 7.13 and 7.14 are not identical and a systematic $\delta B_J - R = 0.05$ difference between the Govoni *et al.* (2000) and Panoramic Deep Field colours could alter the completeness by $\sim 5\%$. For the remainder of the Chapter, the completeness is assumed to be 85%.

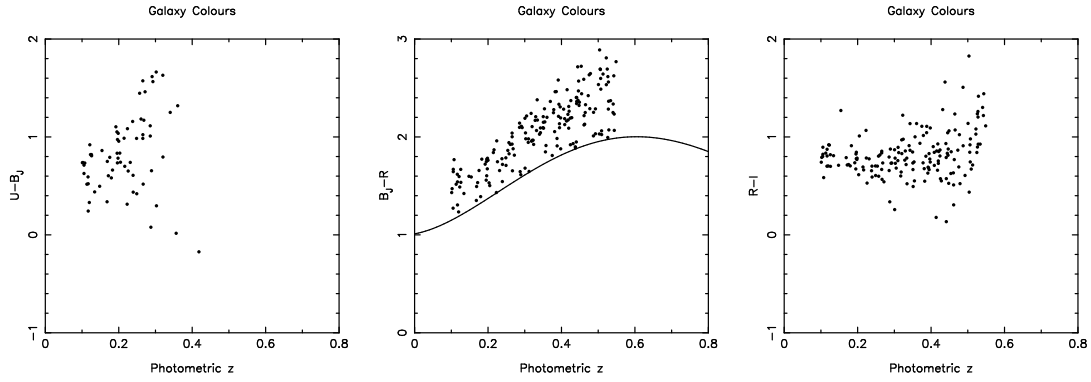


Figure 7.9: The colours of radio galaxies as a function of photometric redshift. The colour selection criteria is shown with the curved line in the $B_J - R$ plot. Most radio galaxies have $B_J - R$ colours significantly redder than the selection criteria.

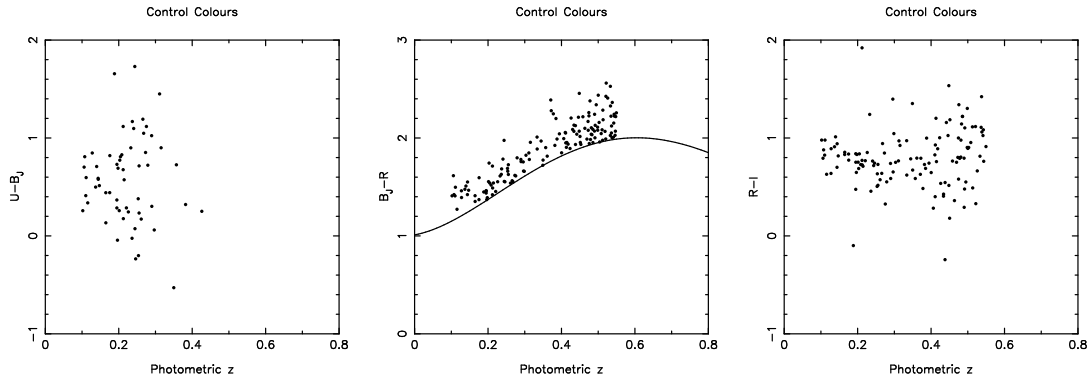


Figure 7.10: The colours of the control sample as a function of photometric redshift.

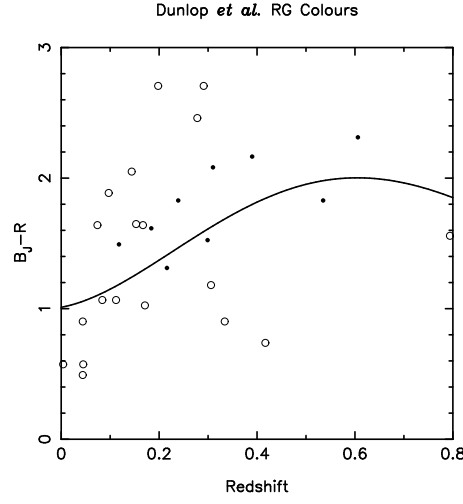


Figure 7.11: The colours of Dunlop *et al.* (1989) radio galaxies as a function of redshift. The colour selection criteria used in this chapter is shown with the curved line and $B_J - R$ colours have been estimated with $B_J - R = 0.82(B - R)$. Radio galaxies with poor photometry are shown with circles while radio galaxies with good photometry are shown with dots.

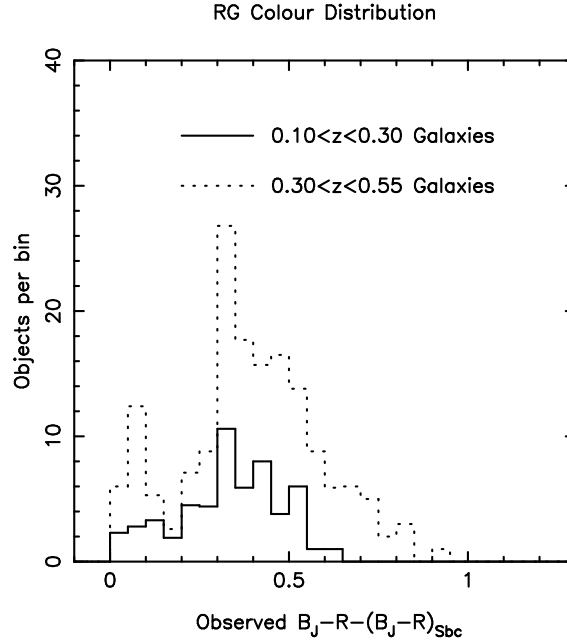


Figure 7.12: The distribution of the difference of the $B_J - R$ colours of the radio galaxy sample and the colour selection criteria. The peak of the distribution is significantly redder than the selection criteria.

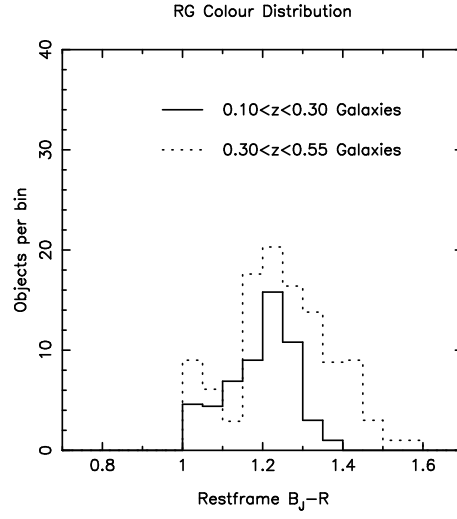


Figure 7.13: The restframe $B_J - R$ colours of the radio galaxy sample. The control sample has been subtracted from the distribution to remove the effects of contamination.

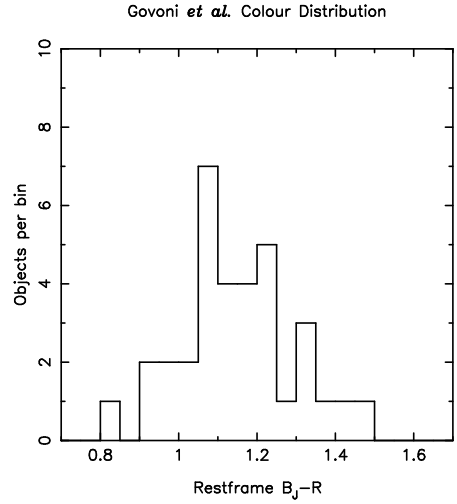


Figure 7.14: The restframe colours of Govoni *et al.* (1989) radio galaxies. The $B_J - R$ colours have been estimated with $B_J - R = 0.88(B - R)$.

7.5 The 1.4 GHz Luminosity Function

The radio power of the sources is estimated by

$$\log P_{1.4}(\text{WHz}^{-1}) = \log S_{1.4}(\text{mJy}) - (1 - \alpha_r) \log(1 + z) + 2 \log D_l(\text{Mpc}) - 17.08 \quad (7.1)$$

where $S_{1.4}$ is the 1.4GHz radio flux, D_l is the luminosity distance and α_r is the radio spectral index which is assumed to be 0.7. The radio luminosity function is estimated by

$$\Phi(P_{1.4}) = \sum_i \frac{1}{V_{max,i}} \quad (7.2)$$

(Schmidt 1968) where $V_{max,i}$ is the maximum comoving volume in which the i th source would be included in the sample. The value of $V_{max,i}$ is given by

$$V_{max,i} = \eta_i \int_{z_{min}}^{z_{max}} \frac{dV_c}{dz} dz \quad (7.3)$$

where η_i is the completeness of the survey for sources with the properties of source i , z_{min} and z_{max} are the minimum and maximum redshifts where source i would be included in the sample and V_c is the comoving volume. The derivative of the comoving volume is given by

$$\frac{dV_c}{dz} = \frac{c}{H_0} \frac{D_M^2}{E(z)} \Omega \quad (7.4)$$

where D_M is the transverse comoving distance, Ω is the survey area and

$$E(z) \equiv \sqrt{\Omega_M(1+z)^3 + \Omega_k(1+z)^2 + \Omega_\Lambda}. \quad (7.5)$$

The values of z_{min} and z_{max} are set by the bright and faint flux limits (optical and radio) for the sample and the lower and upper limits for the redshifts over which the luminosity function is determined.

The radio luminosity function of radio galaxies for $0.10 < z < 0.30$ and $0.3 < z < 0.55$ is shown in Figure 7.15 and listed in Table 7.1. The $0.10 < z < 0.30$ space density is slightly higher than the low redshift sample of Sadler, Jenkins & Kotanyi (1989) and has a considerably higher space density than the non-evolving luminosity function of Mobasher *et al.* (1999). The disagreement with Mobasher *et al.* (1999) is not unexpected as the most luminous radio-galaxies in the Mobasher sample are $\sim 10^{24} \text{WHz}^{-1}$. The space density of $0.30 < z < 0.55$ radio galaxies is significantly higher than the $0.10 < z < 0.30$ sample which is consistent with evolution occurring over the observed redshift range.

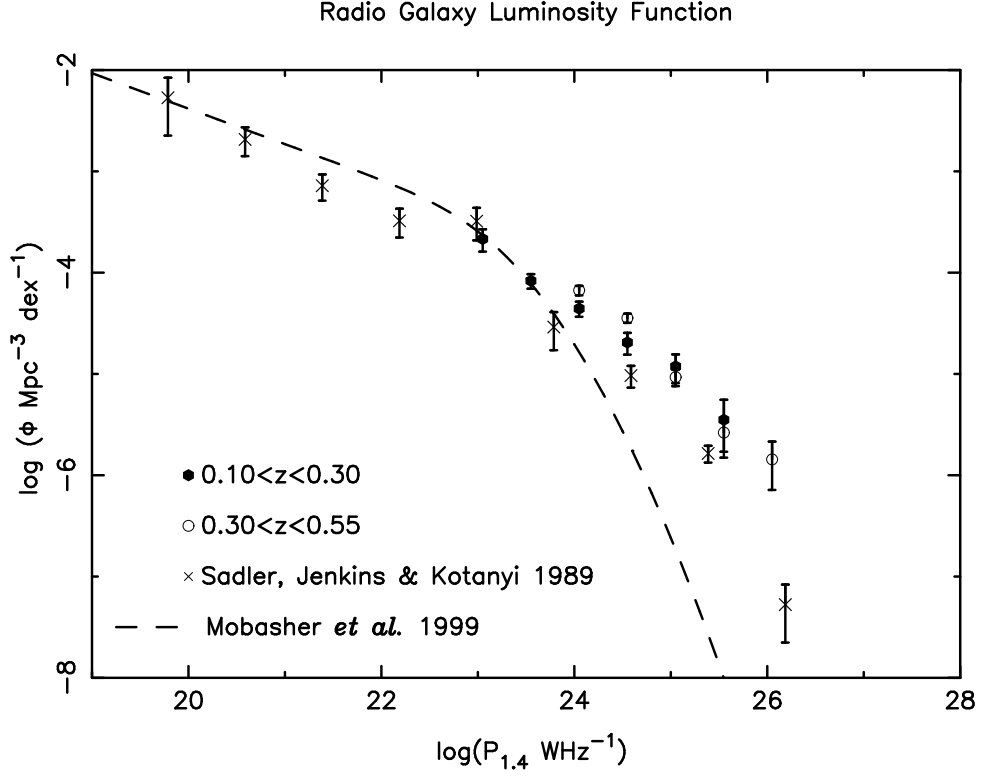


Figure 7.15: The luminosity function of radio galaxies detected in the Panoramic Deep Fields. The space density of $z > 0.1$ radio galaxies is significantly higher than the estimates of space density of $z < 0.1$ radio galaxies (Sadler, Jenkins & Kotanyi 1989). For several luminosity bins, the estimate of the space density of $0.30 < z < 0.55$ radio galaxies is significantly higher than the estimates for $0.1 < z < 0.30$ radio galaxies.

Table 7.1: The Radio Galaxy Luminosity Function. Where $k_L \neq 0$, the radio powers have been divided by the luminosity evolution to estimate the luminosity function at $z \sim 0$.

| Redshift Range | k_L | $\text{Log}P_{1.4}$ | N_{gal} | Φ ($h^3\text{Mpc}^{-3}\text{dex}^{-1}$) |
|-------------------|-------|---------------------|-----------|--|
| $0.10 < z < 0.30$ | 0.0 | 23.05 | 16 | $2.1 \pm 0.5 \times 10^{-6}$ |
| $0.10 < z < 0.30$ | 0.0 | 23.55 | 37 | $8.3 \pm 1.3 \times 10^{-5}$ |
| $0.10 < z < 0.30$ | 0.0 | 24.05 | 35 | $4.4 \pm 0.7 \times 10^{-5}$ |
| $0.10 < z < 0.30$ | 0.0 | 24.55 | 17 | $2.0 \pm 0.5 \times 10^{-5}$ |
| $0.10 < z < 0.30$ | 0.0 | 25.05 | 10 | $1.1 \pm_{0.2}^{0.4} \times 10^{-5}$ |
| $0.10 < z < 0.30$ | 0.0 | 25.55 | 3 | $3.5 \pm_{1.2}^{3.5} \times 10^{-4}$ |
| $0.30 < z < 0.55$ | 0.0 | 24.05 | 85 | $6.5 \pm 0.7 \times 10^{-5}$ |
| $0.30 < z < 0.55$ | 0.0 | 24.55 | 92 | $3.5 \pm 0.4 \times 10^{-5}$ |
| $0.30 < z < 0.55$ | 0.0 | 25.05 | 29 | $9.3 \pm 1.7 \times 10^{-5}$ |
| $0.30 < z < 0.55$ | 0.0 | 25.55 | 8 | $2.6 \pm_{0.5}^{1.2} \times 10^{-6}$ |
| $0.30 < z < 0.55$ | 0.0 | 26.05 | 4 | $1.4 \pm_{0.4}^{1.1} \times 10^{-6}$ |
| $0.10 < z < 0.55$ | 3.4 | 22.95 | 29 | $2.3 \pm 0.4 \times 10^{-6}$ |
| $0.10 < z < 0.55$ | 3.4 | 23.45 | 120 | $9.3 \pm 0.9 \times 10^{-5}$ |
| $0.10 < z < 0.55$ | 3.4 | 23.95 | 133 | $4.8 \pm 0.5 \times 10^{-5}$ |
| $0.10 < z < 0.55$ | 3.4 | 24.45 | 48 | $1.2 \pm 0.2 \times 10^{-5}$ |
| $0.10 < z < 0.55$ | 3.4 | 24.95 | 17 | $4.5 \pm 1.1 \times 10^{-5}$ |
| $0.10 < z < 0.55$ | 3.4 | 25.45 | 5 | $1.4 \pm_{0.4}^{0.9} \times 10^{-4}$ |

To measure the evolution of the radio galaxy luminosity function, the data has been fitted with a 2 power-law function

$$\Phi(P)d(\log P) = C^* \left[\left(\frac{P^*(z)}{P} \right)^\alpha + \left(\frac{P^*(z)}{P} \right)^\beta \right]^{-1} d(\log P) \quad (7.6)$$

(Boyle, Shanks & Peterson 1988, Dunlop & Peacock 1990). The evolution of the luminosity function is assumed to be pure luminosity evolution where

$$P^*(z) = P^*(0)(1+z)^{k_L} \quad (7.7)$$

(Boyle, Shanks & Peterson 1988). The best-fit values for the C^* , $P^*(0)$, α , β and k_L are obtained by minimising

$$S = -2\ln L \quad (7.8)$$

(Marshall *et al.* 1983) where L is the likelihood. The value of S is given by

$$S = -2\sum_{i=1}^N \ln[\Phi(P, z_i)] + 2 \int \int \Phi(P, z) \Omega(P, z) \frac{dV}{dz} dz dP \quad (7.9)$$

(Marshall *et al.* 1983). Error estimates for the measured parameters are determined by computing ΔS for each parameter in turn while allowing the other values for the parameters to float (Lampton, Margon & Bowyer 1976, Boyle, Shanks & Peterson 1988). The errors quoted for the remainder of the chapter are determined for $\Delta S = 1$ which is equivalent to 1σ .

The best-fit estimate of the luminosity function is shown in Figure 7.16 and the estimates of C^* , $P^*(0)$, α , β and k_L are listed in Table 7.2. To allow comparison with low redshift samples, the radio power of sources used to estimate the space density has been divided by the estimate of the luminosity evolution. The luminosity function model agrees well with the data and the low redshift sample of Sadler, Jenkins & Kotanyi (1989). The estimate of the luminosity parameter, $k_L \sim 3.4$, is similar to previous estimates of the evolution of radio galaxies (Rowan-Robinson *et al.* 1993) and is similar to the evolution of optically selected QSOs (Boyle, Shanks & Peterson 1988).

7.6 The Environment of Radio Galaxies

Radio galaxies and other radio-loud AGN are often detected in environments considerably richer than field galaxies (Yee & Green 1987, Prestage & Peacock

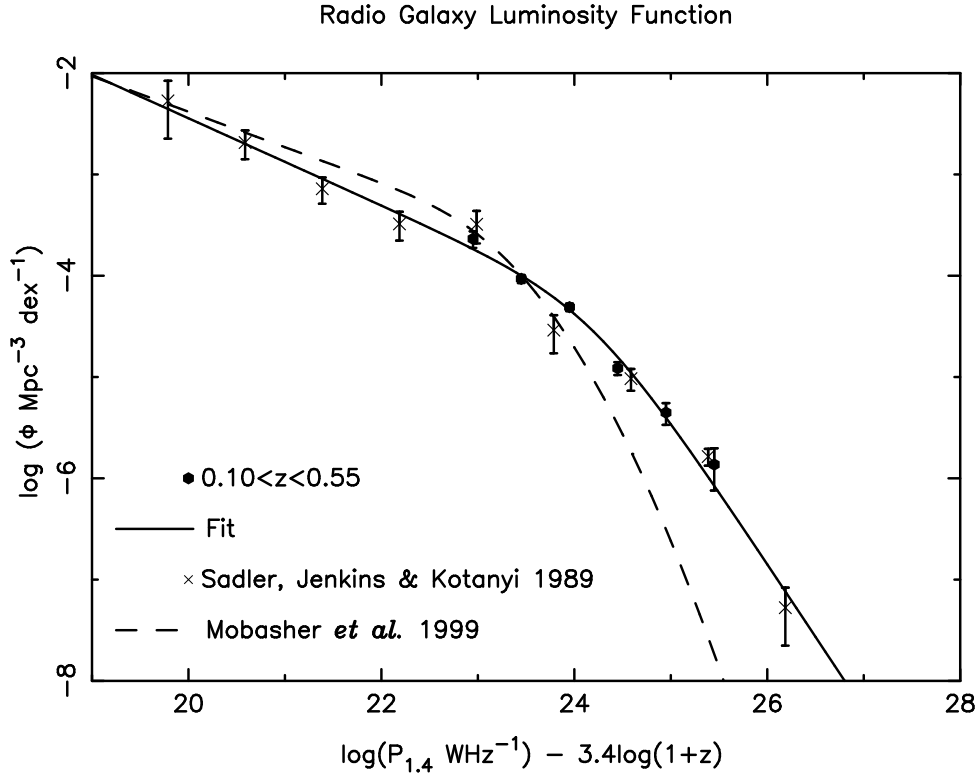


Figure 7.16: The luminosity function of radio galaxies at the current epoch where the luminosity at $z \sim 0$ has been estimated by dividing the radio power by $(1+z)^{3.4}$. There is reasonable agreement between the model of the luminosity function, the data and Sadler, Jenkins & Kotanyi (1989).

Table 7.2: The Radio Galaxy Luminosity Function Parameters

| L.F. Parameter | Best-Fit Estimate |
|----------------|--|
| $C_{1.4}^*$ | $(5.6 \pm 4.0) \times 10^{-4} h^3 \text{Mpc}^{-3}$ |
| $P_{1.4}^*$ | $(1.6 \pm 1.0) \times 10^{24} \text{WHz}^{-1}$ |
| α | -1.44 ± 0.08 |
| β | -0.43 ± 0.07 |
| k_L | 3.4 ± 1.4 |

1988, Wurtz *et al.* 1997, Hall & Green 1998, Miller *et al.* 1999). However, as radio galaxies can occur in poor environments (Rogstad & Ekers 1969), the physical processes responsible for radio emission are only correlated with but not exclusive to rich environments. If environment does have a significant effect on radio luminosity, evolution of the radio galaxy environment could be responsible for the evolution of the radio galaxy luminosity function. Several studies have detected evolution of radio galaxy and radio-loud AGN environments (Yee & Green 1987, Hill & Lilly *et al.* 1991, Wurtz *et al.* 1997) but the sample sizes are generally small and the detections of evolution are associated with $\lesssim 10$ objects. The depth and area of the Panoramic Deep Fields result in the environments of ~ 180 $0.1 < z < 0.55$ radio galaxies being imaged and allow the accurate measurement of the evolution of radio galaxy environment.

The estimator of the angular correlation function is

$$\hat{\omega}_{ag}(\theta) = \frac{AG}{AR} - 1 \quad (7.10)$$

where AG and AR are the number of AGN-galaxy and normalised AGN-random pairs separated by $\theta \pm \delta\theta$. If the spatial cross-correlation function is given by

$$\epsilon(r) = \left(\frac{r_0}{r}\right)^\gamma \quad (7.11)$$

then the angular correlation function is given by

$$\omega(\theta) = A\theta^{1-\gamma}. \quad (7.12)$$

The relationship between the value of A and r_0 is given by Limber's equation which is discussed Chapters 4 and 6. The redshift distributions of the galaxies (including radio-galaxies) are determined by smoothing the photometric redshift distribution with a Gaussian where σ is given by the estimated errors of the photometric redshifts. As the galaxy correlation function is strongly dependent on morphology and colour (Chapters 4 & 6), galaxies bluer and redder than a non-evolving Sbc have been used to determine the angular cross-correlation function of radio-galaxies and particular galaxy types.

Estimates of the radio galaxy-galaxy cross correlation function are listed in Table 7.3. The cross-correlation with early subsample galaxies is consistently stronger than the cross-correlation with late subsample galaxies. The average environment of the radio galaxies in the SGP is also richer than the environment of radio galaxies in the F855 field. Similar behaviour is seen for the autocorrelation

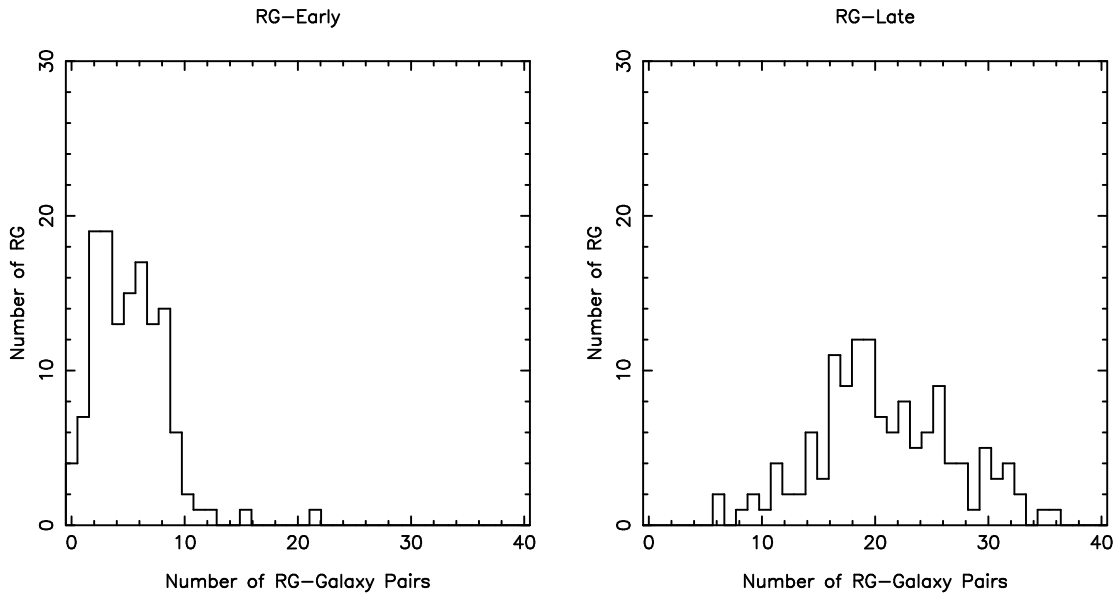


Figure 7.17: The distribution of radio galaxy-galaxy pairs with separations less than $56''$ for early and late subsamples. The mean number of radio galaxy-late pairs is higher than the number of radio galaxy-early pairs due to the higher sky-surface density of faint late subsample galaxies. There is no evidence of outliers significantly biasing the estimates of the pair-counts.

function of red galaxies in Chapter 4. To check estimates of the cross-correlation have not been biased by contamination or a small number of objects, the distribution of radio galaxy-galaxy pairs with separations $< 56''$ is plotted in Figure 7.17. There is no evidence for outliers significantly biasing estimates of the pair-counts. As the late subsample is ~ 5 times the size of the early subsample, it dominates the pair-counts and the cross-correlation of radio galaxies with all galaxies is much weaker than the cross-correlation with the early subsample.

The signal-to-noise of the cross-correlation with the early subsample is sufficient to estimate the value of γ . Estimates of the amplitude and γ of the radio galaxy-early cross-correlation function are listed in Table 7.4. Plots of the cross-correlation function in Figure 7.18 show the power laws to be good approximations to the data though there are significant deviations from the power law fits on scales $> 0.1^\circ$. The values of γ are ~ 2.1 in both fields though the amplitude of the cross-correlation function is twice as high in the SGP as F855. While the value of γ is higher than the autocorrelation function of the early subsample, it is comparable to the autocorrelation function of elliptical galaxies at $z \sim 0$ (Guzzo

Table 7.3: The cross-correlation function of radio galaxies with other galaxies in the SGP and F855 fields

| Magnitude Range | Galaxy Subsample | Angle | SGP $\hat{\omega}(\theta)$ | F855 $\hat{\omega}(\theta)$ |
|---------------------------|---------------------|-----------------------------|----------------------------|-----------------------------|
| $18.0 \leq B_J \leq 23.5$ | Early | $7'' \leq \theta < 14''$ | 2.48 ± 0.62 | 1.18 ± 0.46 |
| $18.0 \leq B_J \leq 23.5$ | Early | $14'' \leq \theta < 28''$ | 1.56 ± 0.27 | 1.02 ± 0.22 |
| $18.0 \leq B_J \leq 23.5$ | Early | $28'' \leq \theta < 56''$ | 0.85 ± 0.12 | 0.42 ± 0.09 |
| $18.0 \leq B_J \leq 23.5$ | Early | $56'' \leq \theta < 112''$ | 0.36 ± 0.05 | 0.15 ± 0.04 |
| $18.0 \leq B_J \leq 23.5$ | Early | $112'' \leq \theta < 224''$ | 0.14 ± 0.02 | 0.05 ± 0.02 |
| $18.0 \leq B_J \leq 23.5$ | Late | $7'' \leq \theta < 14''$ | 0.36 ± 0.15 | 0.40 ± 0.15 |
| $18.0 \leq B_J \leq 23.5$ | Late | $14'' \leq \theta < 28''$ | 0.25 ± 0.07 | 0.14 ± 0.07 |
| $18.0 \leq B_J \leq 23.5$ | Late | $28'' \leq \theta < 56''$ | 0.13 ± 0.04 | 0.02 ± 0.03 |
| $18.0 \leq B_J \leq 23.5$ | Late | $56'' \leq \theta < 112''$ | 0.11 ± 0.02 | 0.07 ± 0.02 |
| $18.0 \leq B_J \leq 23.5$ | Late | $112'' \leq \theta < 224''$ | 0.06 ± 0.01 | -0.02 ± 0.01 |
| $18.0 \leq B_J \leq 23.5$ | All | $7'' \leq \theta < 14''$ | 0.73 ± 0.17 | 0.51 ± 0.15 |
| $18.0 \leq B_J \leq 23.5$ | All | $14'' \leq \theta < 28''$ | 0.41 ± 0.07 | 0.29 ± 0.07 |
| $18.0 \leq B_J \leq 23.5$ | All | $28'' \leq \theta < 56''$ | 0.22 ± 0.04 | 0.10 ± 0.03 |
| $18.0 \leq B_J \leq 23.5$ | All | $56'' \leq \theta < 112''$ | 0.14 ± 0.02 | 0.07 ± 0.02 |
| $18.0 \leq B_J \leq 23.5$ | All | $112'' \leq \theta < 224''$ | 0.06 ± 0.01 | 0.00 ± 0.01 |

Table 7.4: The cross-correlation function of $B_J < 23.5$ radio galaxies with early subsample galaxies. The parameters for the angular correlation function have been determined with fits to the data on angular scales $< 0.1^\circ$.

| Early Subsample Magnitude Range | SGP | | F855 | |
|------------------------------------|-----------------|--------------------------|-----------------|--------------------------|
| | γ | $\omega(1') \times 10^3$ | γ | $\omega(1') \times 10^3$ |
| $18.0 \leq B_J \leq 21.0$ | 2.04 ± 0.17 | 110 ± 18 | 2.50 ± 0.43 | 28 ± 12 |
| $18.0 \leq B_J \leq 22.0$ | 2.10 ± 0.11 | 114 ± 13 | 2.06 ± 0.22 | 42 ± 9 |
| $18.0 \leq B_J \leq 23.0$ | 2.18 ± 0.08 | 95 ± 10 | 2.02 ± 0.13 | 46 ± 6 |
| $18.0 \leq B_J \leq 23.5$ | 2.20 ± 0.07 | 87 ± 7 | 2.07 ± 0.13 | 40 ± 5 |

et al. 1997).

The cross-correlation of radio galaxies with the late subsample is shown in Figure 7.19. The signal-to-noise is much poorer than Figure 7.18 and power laws have been fitted to the data with γ fixed at 1.65, the value for the early-late cross-correlation function (Chapter 6). While the fit to the SGP data is good, the F855 data is poorly fitted by a power law. The cross-correlation function is considerably weaker than the radio galaxy-early cross-correlation function on most angular scales.

The amplitude of the angular cross-correlation function of radio galaxies with the early subsample as a function of limiting magnitude is shown in Figure 7.21. Models of the spatial correlation function have been fitted to the the $B_J \sim 22.5$ data points for the SGP and F855 fields. The values of r_0 determined in the SGP and F855 fields differ significantly with stronger clustering observed in the SGP. The clustering in both fields is stronger than the clustering of field galaxies. The environments of radio galaxies in the SGP are comparable to the average environment of *UBR* selected AGN in the same field (Chapter 6). However, if the 4 AGN associated with unusually rich environments are rejected from the *UBR* selected sample, the environments of radio galaxies are significantly richer than *UBR* selected AGN. While the radio galaxy sample spans a large range of redshifts, Figure 7.21 does not show evidence for a consistent increase or decrease

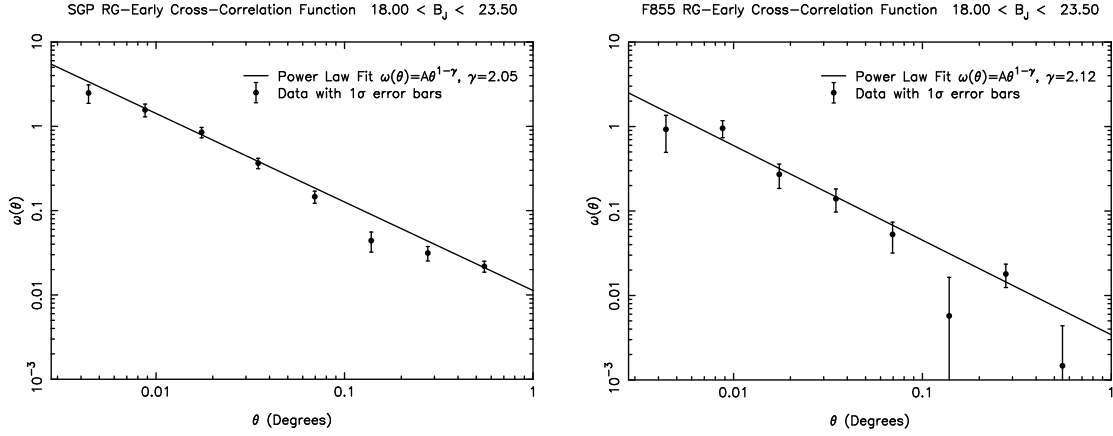


Figure 7.18: The angular cross-correlation function of radio galaxies with the early subsample.

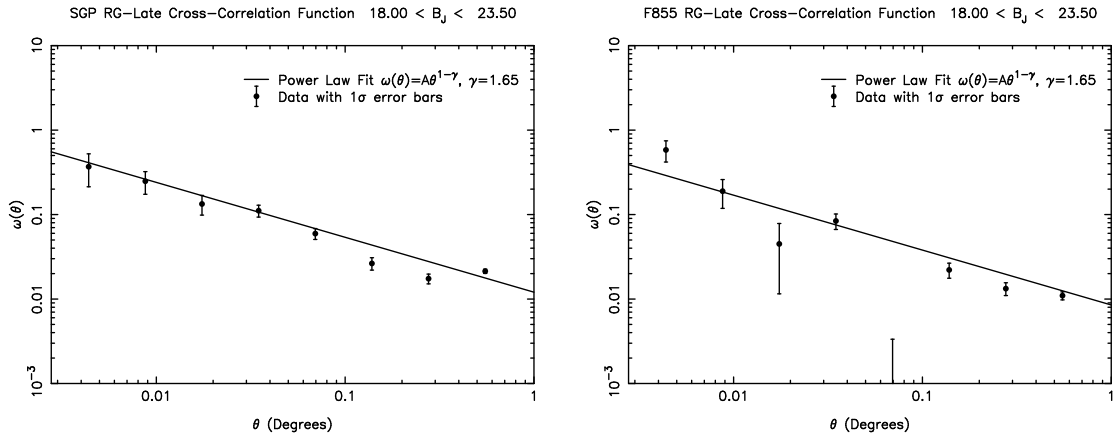


Figure 7.19: The cross-correlation function of $B_J < 23.5$ radio galaxies and late type galaxies. While a power law is a good approximation to the SGP data, the fit to the F855 data is poor. On small angular scales, the cross-correlation is an order of magnitude weaker than the cross-correlation with the early subsample.

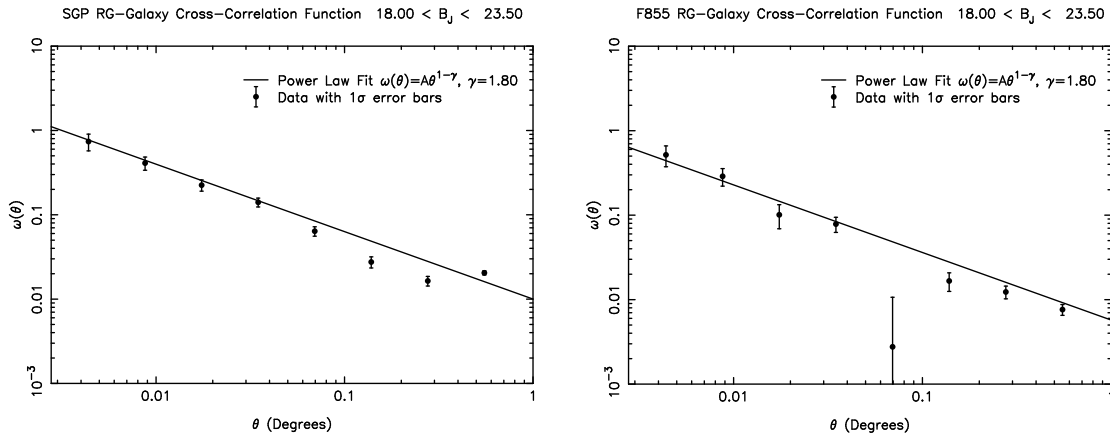


Figure 7.20: The angular cross-correlation function of $B_J < 23.5$ radio galaxies with all galaxies.

in the richness of the radio galaxy environments over the observed redshift range.

The amplitude of the angular cross-correlation function of radio galaxies with late subsample galaxies as a function of limiting magnitude is shown in Figure 7.22. While the values of r_0 are smaller in the F855 field than the SGP, the fits to the F855 data are poor and it is possible that large systematic errors exist in the estimates of the F855 cross-correlation function amplitudes. The values of r_0 are comparable to Figure 7.21 but the smaller value of γ results in weaker clustering at small scales. Except for the 2 faintest magnitude slices of the SGP plot, the data in shows no evidence for the evolution of radio galaxy environments.

The lack of evolution of the clustering is surprising as Yee & Green (1987), Hill & Lilly *et al.* (1991) and Wurtz *et al.* (1997) claim detections of evolution of the environment of radio-galaxies and radio-loud AGN over a similar range of redshifts. To confirm that the evolution of the clustering is negligible, the cross-correlation with the early subsample has been determined for radio galaxies with photometric redshifts $0.10 \leq z < 0.30$ and $0.30 \leq z < 0.55$. The amplitude of the angular cross-correlation function as a function of magnitude for the two subsets of radio galaxies is shown in Figures 7.24 and 7.25.

The environments of $0.10 \leq z < 0.30$ radio galaxies are marginally richer than $0.30 \leq z < 0.55$ radio galaxies. However, the values of r_0 differ by only $\sim 10\%$ and it is entirely plausible that systematic errors in the galaxy selection criteria or redshift distribution model could introduce a signal at this level. There is no evidence for a positive correlation between the richness and redshift of

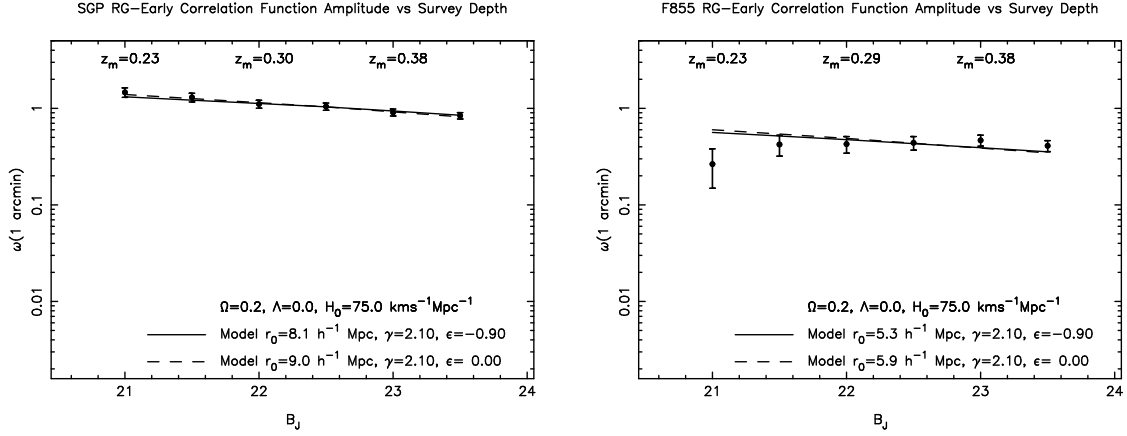


Figure 7.21: The amplitude of the angular cross-correlation function of radio galaxies with early subsample galaxies. The strength of the clustering does not consistently increase or decrease with increasing magnitude or redshift.

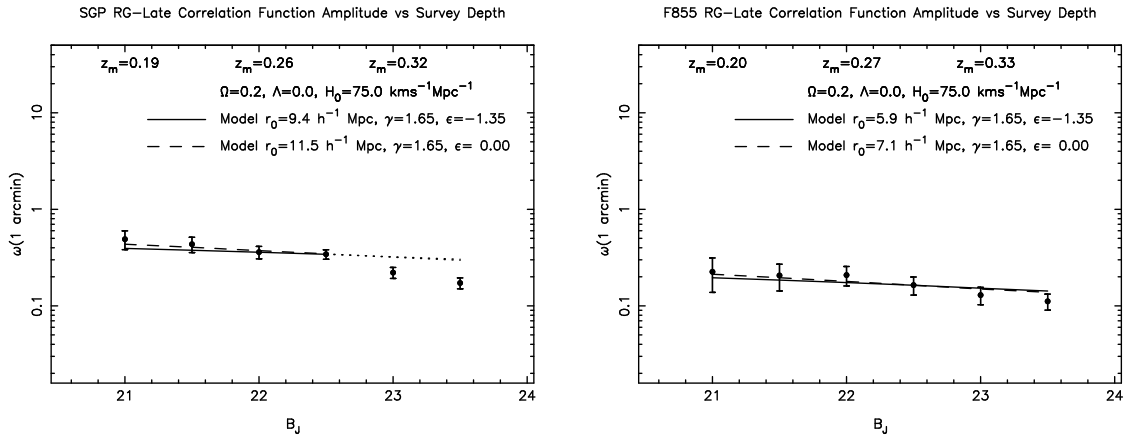


Figure 7.22: The amplitude of the angular cross-correlation function of radio galaxies with the late subsample. The strength of the clustering does not consistently increase or decrease with increasing magnitude or redshift.

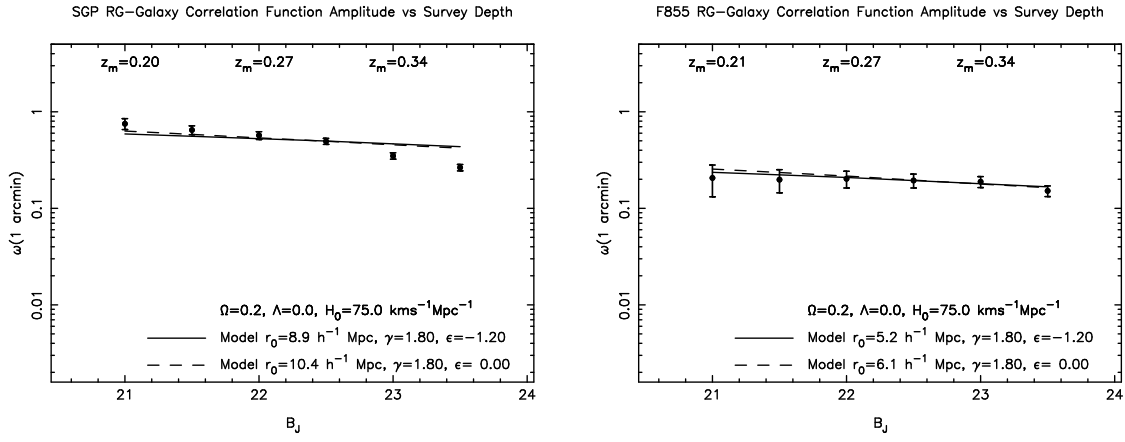


Figure 7.23: The amplitude of the angular cross-correlation function of radio galaxies and all galaxies. While the values of r_0 are comparable to the cross-correlation with early subsample galaxies, the smaller value of γ results in $\sim 50\%$ weaker clustering on scales $< 1h^{-1}\text{Mpc}$.

radio galaxy environments. This does not exclude the possibility of a correlation between richness and redshift for luminous ($P > 10^{26}\text{WHz}^{-1}$) radio galaxies (Hill & Lilly 1991) as few luminous sources are contained in this sample. However, if there is a strong correlation between richness and redshift for luminous radio galaxies, it is surprising that a weaker correlation isn't present for fainter sources. The lack of a correlation between richness and redshift in this sample implies that, for most radio galaxies, the evolution of the radio luminosity function is not directly caused by evolution of the richness of the radio galaxy environment.

While there isn't a strong correlation between the evolution of the luminosity function and richness, this does not exclude a correlation between radio galaxy luminosity at a given epoch and environment. To determine if there is a correlation between radio luminosity and environment, the radio luminosity of galaxies at the current epoch has been estimated using the luminosity evolution estimate from the Section 7.5. The cross-correlation with early type galaxies has been determined with $P(z = 0) > 10^{24.0}\text{WHz}^{-1}$ and $P(z = 0) < 10^{24.0}\text{WHz}^{-1}$ radio galaxies. Plots of the amplitude of the angular cross-correlation function for the 2 subsamples are shown in Figures 7.26 and 7.27. In a given field, the estimates of r_0 vary by $\sim 10\%$ between the bright and faint subsamples. There is no consistent trend between environment and luminosity in the two fields. If there is a correlation between radio power and environment, radio galaxy samples spanning

$0.10 \leq z < 0.30$ Radio Galaxies

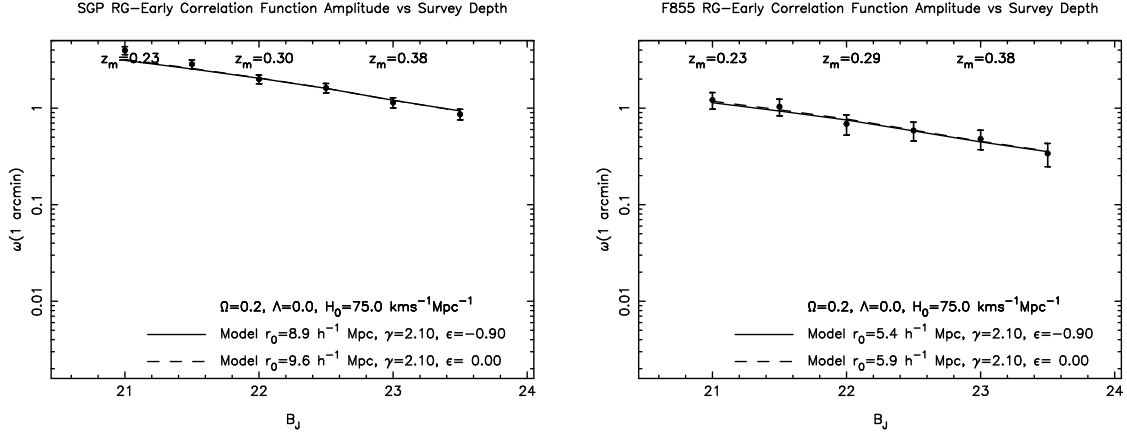


Figure 7.24: The amplitude of the angular cross-correlation function of $0.10 \leq z < 0.30$ radio galaxies and early subsample galaxies.

$0.40 \leq z < 0.55$ Radio Galaxies

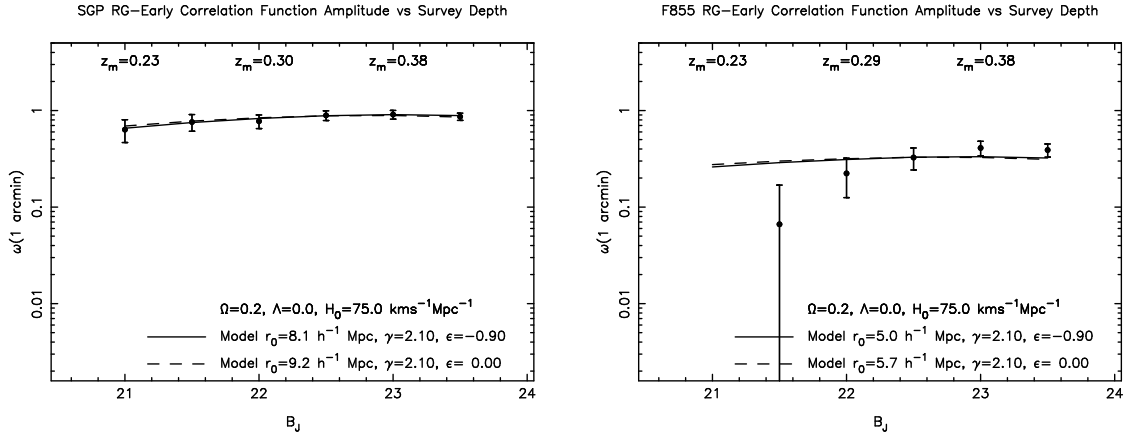


Figure 7.25: The amplitude of the angular cross-correlation function of $0.30 \leq z < 0.55$ radio galaxies and early subsample galaxies.

larger ranges of luminosity or containing $\gg 10^2$ objects are required if a detection is to be made with the angular cross-correlation function.

7.7 Summary

The Panoramic Deep Fields and the NVSS have been used to compile a catalogue of $0.1 < z < 0.55$ $B_J < 23.5$ radio galaxies. Radio fluxes, multicolour photometry and photometric redshifts have been used to select ~ 180 radio galaxies and to measure the evolution of their luminosity and environments. The key conclusions are

- (i) The evolution of the radio galaxy luminosity function can be approximated by luminosity evolution where $P(z) \sim P(0)(1+z)^{3.4}$. The measured evolution of the luminosity function is similar to previous estimates of the evolution of radio sources (Rowan-Robinson *et al.* 1993) and is similar to the evolution of optically selected AGN (Boyle, Shanks & Peterson 1988).
- (ii) Radio galaxies are typically found in environments richer than field galaxies. Over the redshift range observed, the environments of radio galaxies are comparable to or slightly richer than the environments of early-type galaxies and *UBR* selected AGN.
- (iii) While the radio luminosity function rapidly evolves from $z \sim 0.1$ to $z \sim 0.55$, no significant evolution of the environment of radio galaxies was detected.
- (iv) There is no evidence for a correlation between radio luminosity and environment in the Panoramic Deep Field sample. If a correlation between richness and luminosity does exist, samples containing $\gg 10^2$ radio galaxies or spanning a large range of luminosities are required to detect the correlation.

$P(0) > 10^{24.0} \text{WHz}^{-1}$ Radio Galaxies

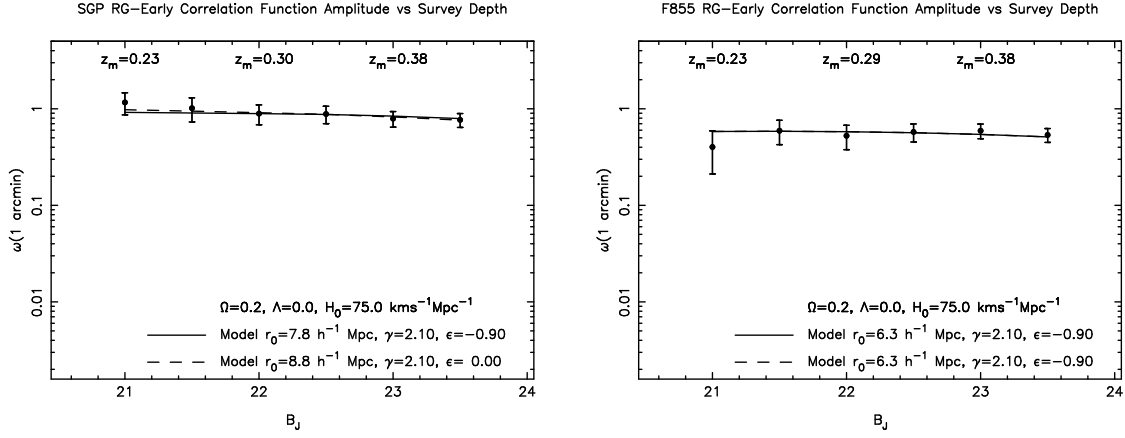


Figure 7.26: The amplitude of the angular cross-correlation function of $P(0) > 10^{24.0} \text{WHz}^{-1}$ radio galaxies and early subsample galaxies.

$P(0) < 10^{24.0} \text{WHz}^{-1}$ Radio Galaxies

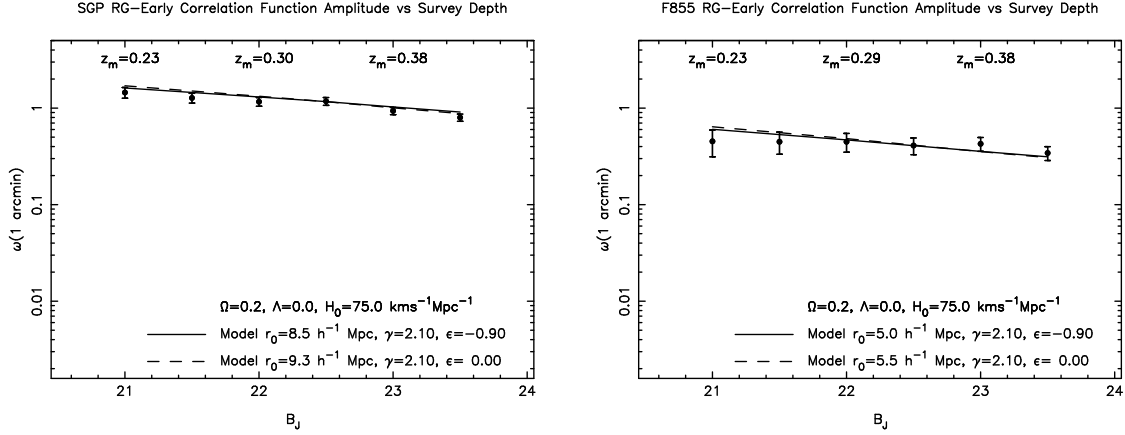


Figure 7.27: The amplitude of the angular cross-correlation function of $P(0) < 10^{24.0} \text{WHz}^{-1}$ radio galaxies and early subsample galaxies.

Chapter 8

Conclusions and Future Prospects

8.1 The Panoramic Deep Fields

The Panoramic Deep Fields are a deep wide-field multicolour survey of two high galactic latitude fields. The size and depth of the fields allows the accurate statistical measurement of the environments and evolution of galaxies and AGN.

The survey images have been constructed by digitally stacking scans of UK Schmidt photographic plates. The use of photographic plates provides a $\sim 25^\circ$ field-of-view (with low vignetting) and allows archival material to be used for the production of deep images. The successful coaddition of the scans requires accurate background subtraction and robust bad pixel rejection to achieve deep clean images. SExtractor has been used to construct and classify the object catalogue. Photometry has been calibrated with deep CCD images and astrometry has been determined with a solution derived from Tycho-2 stars.

The successful construction and use of the catalogue would not have been possible without visual inspection of the data and the availability of published data on the Internet. Visual inspection is particularly effective for finding spurious objects in images (Chapter 2). Online databases (NED and CDS in particular) have been used to calibrate or confirm the accuracy of object classifications, astrometry, photometry, dust extinction, photometric redshifts, radio fluxes, galaxy selection criteria and the cluster catalogue. The science derived from surveys is significantly improved by the availability of other data for the same field and this must be considered when surveys are planned. For this reason, surveys and object

catalogues are much more effective if they are available online. The Panoramic Deep Fields will be available online after the completion of this thesis.

8.2 Galaxy and Cluster Environments

The environments of galaxies and clusters have been measured from $z \sim 0.4$ until the current epoch with the Panoramic Deep Fields. Despite the large field-of-view of each of the fields, there are significant differences between the observed clustering of galaxies. This is particularly true for red early-type galaxies and galaxy clusters, both of which are strongly clustered in both fields. The distribution of galaxy clusters in the two fields is consistent with the differences being caused by large-scale-structure at $z \sim 0.4$ rather than smaller structures at $z \sim 0$.

The strong correlation between galaxy colour and environment has been measured by applying colour selection criteria to the galaxy catalogue. The clustering of blue $U - B_J$ selected galaxies is weaker than any morphologically selected sample described in the published literature and is comparable to the clustering of $B_J > 23$ field galaxies. The weak clustering ($r_0 \lesssim 3h^{-1}\text{Mpc}$) implies galaxy colour and stellar population are more strongly correlated with environment than galaxy morphology.

Since there is a strong correlation between galaxy colour and environment, single power-law models for the clustering of all galaxies are not meaningful. At the very least, the clustering of galaxies is a function of colour (Chapter 4), luminosity (Loveday *et al.* 1995) and redshift. To measure the correlation function as a function of these parameters, a large catalogue of galaxy redshifts and multicolour photometry is required. This should be provided by wide-field surveys including 2dFGRS and SDSS.

The correlation between galaxy colour and environment has significant implications for the study of the evolution of large-scale-structure. Single band imaging cannot measure the evolution of clustering. Single band images will select different galaxy populations as a function of redshift and changes in the measured clustering properties will be dominated by the correlation between colour and environment. It should be possible to measure the evolution of galaxy clustering by applying colour selection criteria to multicolour catalogues. However, red early-type galaxies will require survey volumes considerably larger than the Panoramic Deep Fields ($\gg 1000 \times 60 \times 60h^{-3}\text{Mpc}$) to prevent individual structures bias-

ing estimates of the correlation function. While blue galaxies could be used to measure the evolution of clustering, constraints on their luminosity evolution and redshift distribution are poor (Ellis 1997). Both issues must be addressed if galaxy clustering is to be used to constrain galaxy evolution and cosmological parameters.

8.3 AGN Evolution and Environments

The evolution of radio galaxies has been measured from $z \sim 0.5$ to the current epoch with the Panoramic Deep Fields. Photometric redshifts, colour selection and matches to the NVSS have been used to select a catalogue of ~ 180 $z < 0.55$ radio galaxies. By selecting radio sources within a fixed projected distance of red galaxies, the selection criteria for radio galaxies is not strongly correlated with redshift and it is possible to measure the evolution of radio galaxies. The evolution of the radio galaxy luminosity function is consistent with luminosity evolution where the radio luminosity is given by $L(z) \sim L(0)(1+z)^{3.4}$. The observed evolution is similar to previous estimates of the evolution of radio galaxies (Dunlop & Peacock 1990, Rowan-Robinson *et al.* 1993) and is similar to the evolution of the QSO optical luminosity function. While it could be argued the same physical processes are responsible for the luminosity evolution of different AGN types, it is plausible that the observed similarity is purely coincidental.

The Panoramic Deep Fields have been used to measure the environments of *UBR*-selected AGN and radio galaxies at intermediate redshifts. Colour selection criteria and photometric redshifts have been used to select specific galaxy-types and to significantly improve the signal-to-noise of the angular cross-correlation function. *UBR*-selected AGN and radio galaxies occur in significantly richer environments than field galaxies. However, this is not unexpected as $M_B \sim -21$ AGN often occur in early-type hosts (Schade, Boyle, Letawsky 2000) and radio galaxies have bulge dominated morphologies (Matthews, Morgan & Schmidt 1964). Most *UBR* selected AGN hosts have environments similar to other galaxies with the same morphology, but $\sim 6\%$ may be associated with unusually rich environments. While radio galaxies are in richer environments than most *UBR*-selected AGN, the observed clustering properties are similar to elliptical galaxies at low redshift (Guzzo *et al.* 1997). The Panoramic Deep Fields do not provide evidence of AGN hosts being in unusual galaxy environments compared with

other galaxies with similar morphologies.

The environments of *UBR*-selected AGN and radio galaxies do not exhibit rapid evolution over the observed redshift range. Previous studies of AGN environments at intermediate redshifts have claimed detections of evolution (Yee & Green 1987, Hill & Lilly *et al.* 1991, Wurtz *et al.* 1997) but the detections have usually relied on small number of objects and have been derived from single-band imaging. The evolution of the AGN luminosity function is not associated with or caused by rapid evolution richness of AGN environments.

The luminosities of *UBR*-selected AGN and radio galaxies are not strongly correlated with environment. It can be argued that the occurrence of radio galaxies in richer environments than *UBR* selected AGN could be due to a correlation between environment and radio luminosity. However, this argument assumes unified models of AGN are valid. While no correlation was detected between optical luminosity and environment in Chapter 6, such a correlation must occur if AGN host environments are the same as galaxies with the same morphology, as Seyferts occur more frequently in late-type galaxies than QSOs (McLure *et al.* 1999, Schade, Boyle & Letawsky 2000). If this correlation does exist, it should be detectable in larger samples of uniformly selected AGN. It will be possible to use the 2dFQRS and the Panoramic Deep Fields to place further constraints on the environments of *UBR*-selected AGN.

The Panoramic Deep Field estimate of the radio galaxy luminosity function provides good constraints on the evolution of radio galaxies at low redshift. However, at higher redshifts the constraints are poor as they have been derived from small samples or with redshifts derived from *K* band photometry (Dunlop & Peacock 1990). The techniques used to select $z < 0.5$ radio galaxies in the Panoramic Deep Fields should also be applicable to surveys of $z \gg 1$ radio galaxies with CCD mosaics. In particular, it should be possible to use photometric redshifts, colour selection and projected distance criteria to uniformly select large samples of radio galaxies over a wide range of redshifts.

While the environments of radio galaxies and AGN have been measured at $z < 0.5$, the constraints on their environments at higher redshifts (Hall & Green 1998) have only been determined with small samples and with low signal-to-noise. While the environment does not evolve at $z < 0.5$, significant evolution may occur at redshifts where the rate of galaxy formation and evolution is significantly higher than the current epoch. The bias of QSOs with respect to galaxies must also be

determined as a function of redshift if QSOs are to be used to trace large-scale-structure at $z > 1$ (Boyle *et al.* 1999).

Appendix A

References

- Abell, G.O., 1958, ApJS, 211, 3
- Abell, G.O., Corwin, H.G., & Olowin, R.P., 1989, ApJS, 70, 1
- Bahcall, J.N., Schmidt, M., & Gunn, J.E., 1969, ApJ 157, 77
- Bahcall, J.N., & Soneira, R.M., 1983, ApJ, 270, 20
- Bahcall, N.A., 1979, ApJ, 232, 689
- Bailey, J., & Glazebrook, K., 1999,
http://www.aao.gov.au/2df/manual/2df_manual.html
- Barger, A.J., Aragon-Salamanca, A., Ellis, R.S., Couch, W.J., Smail, I., & Sharples, R.M., 1996, MNRAS, 279, 1
- Baugh, C.M., & Efstathiou, G., 1993, MNRAS, 265, 145
- Baugh, C.M., Cole, S., Frenk, C.S., 1996, MNRAS, 283, 1361
- Baugh, C.M., Benson, A.J., Cole, S., Frenk, C.S., & Lacey, C.G., MNRAS, 1999, 305, L21
- Beard, S.M., MacGillivray, H.T., & Thanisch, P.F., 1990, MNRAS, 247, 311
- Bertin, E., & Arnouts, S., 1996, A&Ass, 117, 393
- Blair, M., & Gilmore, G., 1982, PASP, 94, 742
- Bland-Hawthorn, J., Shopbell P.L., & Malin, D.F., 1993, AJ, 106, 2154
- Boyle, B.J., Shanks, T., & Peterson, B.A., 1988, MNRAS, 238, 957
- Boyle, B.J., & Couch, W.J., 1993, MNRAS, 264, 604

- Boyle, B.J., Croom, S.M., Smith, R.J., Shanks, T., Miller, L., Loaring, N., 1999, in *Looking Deep in the Southern Sky, Proceedings of the ESO/Australia Workshop*, 16
- Broadhurst, T.J., Ellis, R.S., & Shanks, T., 1988, MNRAS, 235, 827
- Brunner, R.J., Connolly, A.J., Szalay, A.S., & Bershad, M.A., 1997, ApJ, 482, L21
- Brunner, R.J., Szalay, A.S., & Connolly, A.J., 2000, astro-ph/0005312
- Caldwell, J.A.R., & Schechter, P.L., 1996, AJ, 112, 772
- Coleman, G.D., Wu, C.C., & Weedman, D.W., 1980, ApJS, 43, 393
- Colless, M., 1989, MNRAS, 237, 799
- Colless, M., Ellis, R.S., Taylor, K., Hook, R.N., MNRAS, 1990, 244, 408
- Condon, J.J., 1984, ApJ, 287, 461
- Condon, J.J., Cotton, W.D., Greisen, E.W., Yin, Q.F., Perley, R.A., Taylor, G.B., & Broderick, J.J., 1998, AJ, 115, 1693
- Connolly, A.J., Csabai, I., Szalay, A.S., Koo, D.C., Kron, R.G., & Munn, J.A., 1995, AJ, 110, 2655
- Couch, W.J., Ellis, R.S., Malin, D.F., & MacLaren, I., MNRAS, 1991, 249, 606
- Croom, S.M., Ratcliffe, A., Parker, Q.A., Shanks, T., Boyle, B.J., & Smith, R.J., 1999, MNRAS, 306, 592
- Croom, S.M., & Shanks, T., 1999, MNRAS, 303, 411
- Dalcanton, J.J., 1996, ApJ, 466, 92
- Dalton, G.B., Croft, R.A.C., Efstathiou, G., Sutherland, W.J., Maddox, S.J., & Davis, M., 1994, MNRAS, 271, L47
- Dalton, G.B., Maddox, S.J., Sutherland, W.J., & Efstathiou, G., 1997, MNRAS, 289, 263
- Davis, M., & Geller, M.J., 1976, ApJ, 203, 13
- De Robertis, M.N., Yee, H.K.C., & Hayhoe, K., 1998, ApJ, 496, 93
- de Vaucouleurs G., de Vaucouleurs A., Corwin H.G., Buta R.J., Paturel G., & Fouque P., 1991, Third Reference Catalogue of Bright Galaxies, Springer-Verlag: New York

- Dressler, A., 1980, *ApJ*, 236, 351
- Driver, S.P., Couch, W.J., & Phillipps, S., 1998, *MNRAS*, 301, 369
- Dunlop, J.S, Peacock, J.A., Savage, A., Lilly, S.J., Heasley, J.N., & Simon, A.J.B, 1989, *MNRAS*, 238, 1171
- Efstathiou, G., Bernstein, G., Katz, N., Tyson, J.A., & Guhathakurta, P., 1991, *ApJ*, 380, L47
- Ellingson, E., Yee, H.K.C., & Green, R.F., 1991, *ApJ*, 1991, 371, 49
- Ellis, R., 1998, *Nature*, 395, 3
- Epchtein, N., de Batz, B., Copet, E., Fouque, P., Lacombe, F., Le Bertre, T., Mamon, G., Rouan, D., Tiphene, D., Burton, W. B., Deul, E., Habing, H., Boersenberger, J., Dennefeld, M., Omont, A., Renault, J. C., Rocca-Volmerange, B., Kimeswenger, S., Appenzeller, I., Bender, R., Forveille, T., Garzon, F., Hron, J., Persi, P., Ferrari-Toniolo, M., & Vauglin, I., 1994, *Ap&SS*, 217, 3
- ESA, 1997, *The Hipparcos & Tycho Catalogues*, ESA SP-1200
- Fernandez-Soto, F., Lanzetta, K.M., Yahil, A., 1999, *ApJ*, 513, 34
- Frenk, C.S., White, S.D.M., Efstathiou, G., & Davis, M., 1990, *ApJ*, 351, 10
- Glazebrook, K., Ellis, R., Colless, M., Broadhurst, T., Allington-Smith, J., and Tanvir, N., 1995, *MNRAS*, 273, 157
- Govoni, F., Falomo, R., Fasano, G., & Scarpa, R., 2000, *A&A*, 353, 507
- Graham, J.A., 1982, *PASP*, 94, 244
- Groth, E.J. & Peebles, P.J.E., 1977, *ApJ*, 217, 385
- Guhathakurta P., Tyson J.A., Majewski, S.R., 1990, *ApJ*, 357, L9
- Gunn, J.E., Hoessel, J.G., & Oke, J.B., 1986, *ApJ*, 306, 30
- Guzzo, L., Strauss, M.A., Fisher, K.B., Giovanelli, R., & Haynes, M.P., 1997, *ApJ*, 1997, 489, 37
- Hall, P.B., & Green, R.F., 1998, *ApJ*, 507, 558
- Hambly, N.C., & Miller, L., 1997, *SuperCOSMOS Technical Manual*, Royal Observatory Edinburgh
- Hambly, N.C., 1998, *Beginner's Guide to SuperCOSMOS data*, Royal Observatory Edinburgh

- Hambly, N.C., 1998b, *The SuperCOSMOS data processing guides: Photometry*, Royal Observatory Edinburgh
- Hambly, N.C., Miller, L., Hawkins, M.R.S., & MacGillivray, H.T., 1998, MNRAS, 297, 839
- Hawkins, M.R.S., 1994, in *Astronomy from wide-field imaging: proceedings of the 161st Symposium of the International Astronomical Union*, 177
- Hawkins, M.R.S., 1995, in *The future utilisation of Schmidt telescopes. Astronomical Society of the Pacific Conference Series, Volume 84; Proceedings of IAU Colloquium 148*, 192
- Hill, G.J., & Lilly, S.J., 1991, ApJ, 367, 1
- Høg, E., Fabricius, C., Makarov, V.V., Urban, S., Corbin, T., Wycoff, G., Bastian, U., Schwekendiek, P., & Wicenec, A., 2000, A&A, 355, L19
- Hogg, D.W., 1999, astro-ph/9905116
- Huchra, J.P., Henry, J.P., Postman, M., & Geller, M.J., 1990, ApJ, 365, 66
- Infante, L., & Pritchett, C.J., 1995, ApJ, 439, 565
- Irwin, M.J., 1985, MNRAS, 214, 575
- Jenkins A., Frenk, C.S., Pearce, F.R., Thomas, P.A., Colberg, J.M., White, S.D.M., Couchman, H.M.P., Peacock, J.A., Efstathiou, G., Nelson, A.H., 1998, ApJ, 499, 20
- Kaiser, N., 1986, MNRAS, 222, 323
- Katsiyannis, A.C., Kemp, S.N., Berry, D.S., & Meaburn, J., 1998, A&Ass, 133, 387
- Kemp, S.N., & Meaburn, J., 1995, in *The future utilisation of Schmidt telescopes. Astronomical Society of the Pacific Conference Series, Volume 84; Proceedings of IAU Colloquium 148*, 200
- Kibblewhite, E.J., Bridgeland, M.T., Bunclark, P., & Irwin, M.J., 1984, *Astronomical Microdensitometry Conference*, NASA Conf Publ, 2317, 277
- Kepner, J., Fan, X., Bahcall, N., Gunn, J., Lupton, R., & Xu, G., 1999, ApJ, 517, 78
- Knox, R.A., Hambly, N.C., Hawkins, M.R.S., & MacGillivray, H.T., 1998, MNRAS, 297, 839

- Knox, R.A., Hawkins, M.R.S., & Hambly, N.C., 1999, MNRAS, 306, 736
- Koo, D.C., 1988, ApJ, 311, 651
- La Franca, F., Lissandrini, C., Cristiani, S., Miller, S., Hawkins, M.R.S, & MacGillivray, H.T., A&A, 1999, 140, 351
- Landolt, A.U., 1992, AJ, 104, 340
- Lampton, M., Margon, B., & Bowyer, S., 1976, ApJ, 208, 177
- Laurikainen, E., & Salo, H., 1995, A&A, 293, 683
- Leir, A., & van den Bergh, S., 1977, ApJS, 34 381
- Lidman, C.E., & Peterson, B.A., 1996, AJ, 112, 2454
- Limber, D.N., 1954, ApJ, 119, 655
- Lin, H., Yee, H.K.C., Carlberg, R.G., Morris, S.L., Sawickim M., Patton, D.R., Wirth, G., & Shepherd, C.W., ApJ, 1999, In Press
- Longair, M.S., & Seldner, M., 1979, MNRAS, 189, 433
- Lubin, L.M., & Postman, M., 1996, AJ, 111, 1795
- Lumsden, S.L., Nichol, R.C., Collins, C.A., & Guzzo, L., 1992, 258, 1
- MacGillivray, H.T., & Stobie, R.S., 1984, Vistas Astr., 27, 433
- Maddox, S.J., Efstathiou, G. & Sutherland, W.J. 1996, MNRAS, 283, 1227
- Marston, A.P., 1988, MNRAS, 230, 97
- Martini, P., & Osmer, P.S., 1998, AJ, 116, 2513
- Matthews, T.A., Morgan, W.W., & Schmidt, M., 1964, ApJ, 140, 35
- Mermilliod, J.-C., Mermilliod, M., & Hauck, B., 1997, A&AS, 124, 349
- McLure, R.J., Kukula, M.J., Dunlop, J.S., Baum, S.A., O'Dea, C.P., & Hughes, D.H., 1999, MNRAS, 308, 377
- McNally, S.J., Peacock, J.A., & Hawkins, M.R.S., 1995, in *The future utilisation of Schmidt telescopes. Astronomical Society of the Pacific Conference Series, Volume 84; Proceedings of IAU Colloquium 148*, 478
- Metcalfe, N., Shanks, T., Fong, R. & Jones, L.R., 1991, MNRAS, 249, 498
- Metcalfe, N., Shanks, T., Campos, A., McCracken, H.J., & Fong, R., MNRAS, 323, 795

- Miller, C.J., Batuski, D.J., Singlend, K.A., & Hill, J.M., 1999, *AJ*, 523, 492
- Morgan, D.H. & Parker, Q.A., in McLean B.J., Golombek D.A., Hayes, J.J.E., Payne E., eds, *IAU Symp. 179, New Horizons from Multi-Wavelength Sky Surveys*, Kluwer, Dordrecht, p. 291.
- Munn, J.A., Koo, D.C., Kron, R.G., Majewski, S.R., Bershad, M.A., & Smetanka, J.J., 1997, *ApJS*, 109, 45
- Newberg, H.J., & Yanny, B., 1997, *ApJs*, 113, 89
- Olsen, L.F., Scoddeggio, M., da Costa, L., Benoist, C., Bertin, E., Deul, E., Erben, T., Guarnieri, M.D., Hook, R., Nonino, M., Prandoni, I., Slijkhuis, R., Wicenec, A., & Wichmann, R., 1999, *A&A*, 345, 681
- Peacock, J.A., 1985, *MNRAS*, 217, 601
- Peebles, P.J.E., 1970, *AJ*, 75, 13
- Pence, W.D., 1999, in *ASP Conf. Ser., Vol. 172, Astronomical Data Analysis Software and Systems VIII*, ed. D. Mehringer, R. Plante, and D. Roberts (San Francisco: ASP), 487
- Poggianti, B.M., Smail, I., Dressler, A., Couch, W.J., Barger, A.J., Butcher, H., Ellis, R.S., & Oemler, A., Jr., 1999, *ApJ*, 518, 576
- Postman, M., Huchra, J.P., & Geller, M.J., 1992, *ApJ*, 384, 404
- Postman, M., Lubin, L.M., Gunn, J.E., Oke, J.B., Hoessel, J.G., Schneider, D.P., & Christensen, J.A., 1996, *AJ*, 111, 615
- Postman, M., Lubin, L.M., & Oke, J.B., 1998, *AJ*, 116, 560
- Postman, M., Lauer, T.R., Szapudi, I. & Oegerle, W., 1998, *ApJ*, 506, 33
- Prandoni, I., Wichmann, R., da Costa, L., Benoist, C., Méndez, R., Nonino, M., Olsen, L.F., Wicenec, A., Zaggia, S., Bertin, E., Deul, E., Erben, T., Guarnieri, M.D., Hook, I., Hook, R., Scoddeggio, M., & Slijkhuis, R., *A&A*, accepted
- Prugniel P., & Heraudeau P., 1998, *A&Ass*, 128, 299
- Roche, N., Shanks, T., Metcalfe, N., & Fong, R., 1996, *MNRAS*, 280, 397
- Rogstad, D.H., & Ekers, R.D., 1969, *ApJ*, 157, 481
- Rowan-Robinson, M., Benn, C.R., Lawrence, A., McMahon, R.G., & Broadhurst, T.J., 1993, *MNRAS*, 263, 123

- Savage, A., & Cannon R.D., 1995, in *The future utilisation of Schmidt telescopes: proceedings of IAU Colloquiu, 148*, 245
- Schade, D., Boyle, B.J., & Letawsky, M., 2000, MNRAS, 315, 498
- Schmidt, M., 1968, ApJ, 151, 393
- Schwartzenberg, J.M., 1996, PhD thesis, University of Bristol
- Schwartzenberg, J.M., Phillipps, S., & Parker, Q., 1996, A&AS, 117, 179
- Sloan Digital Sky Survey (SDSS), 2000, <http://www.sdss.org>
- Smail, I., Dressler, A., Couch, W.J., Ellis, R.S., Oemler, A., Butcher, H., & Sharples, R.M., 1997, ApJS, 110, 213
- Smith, R.J., Boyle, B.J., & Maddox, S.J., 1995, MNRAS, 277, 270
- Smith, R.J., 1998, PhD thesis, Cambridge University
- Smith, R.J., Boyle, B.J., & Maddox, S.J., 2000, MNRAS, 313, 252
- Tinsley, 1978, in *The large scale structure of the Universe; Proceedings of the Symposium*, 343
- Tritton, K., 1983, *Schmidt Telescope Handbook*, AAO UM21
- Tully, B.R., 1987, ApJ, 321, 280
- Urry, M.C., Scarpa, R., O'Dowd, M., & Giavalisco, M., Falomo, R., Pesce, J.E., & Treves, A., ApJ, 2000, 532, 816
- van Albada, G.B., 1961, AJ, 66, 590
- Veron-Cetty, M.P., & Veron, P., 2000, ESO Scientific Report, in press
- Voges, W., Aschenbach, B., Boller, T., Brauningner, H., Briel, U., Burkert, W., Dennerl, K., Englhauser, J., Gruber, R., Haberl, F., Hartner, G., Hasinger, G., Pfeffermann, E., Pietsch, W., Predehl, P., Schmitt, J., Trumper, J., & Zimmermann, U., 2000, IAUC, 7432
- White, R. L., Becker, R. H., Helfand, D. J., & Gregg, M. D. 1997, AJ, 475, 479
- Wold, M., Lacy, M., Lilje, P.B., & Serjeant, S., 2000, MNRAS, 316, 267
- Yee, H.K.C., & Green, R.F., 1987, ApJ, 319, 28
- Zaritsky, D., Nelson, A.E., Dalcanton, J.J., & Gonzalez, A.H., 1997, ApJL, 480, 91

Appendix B

Cluster Candidates

The tables in this appendix provide a full list of the galaxy cluster candidates from Chapter 5. The AMF estimates of the redshift, richness and likelihood are listed for the B_J , R and I bands (where available). If a previously identified cluster is within a projected distance of $0.25h^{-1}\text{Mpc}$ from the cluster candidate, the name and redshift from the NED database are provided. If a galaxy with a spectroscopic identification is within $0.1h^{-1}\text{Mpc}$ of the cluster position, the redshift is listed with the superscript g .

Table B.1: Cluster Candidate Catalogue

| Cluster | RA (J2000) | Declination (J2000) | B_J AMF | | | z | R AMF | | | z | I AMF | | | NED z | Previous ID |
|----------------|---------------|------------------------|-----------|-----------|---------------|-----|---------|-----------|---------------|------|---------|-----------|---------------|------------|----------------|
| | | | z | Λ | \mathcal{L} | | z | Λ | \mathcal{L} | | z | Λ | \mathcal{L} | | |
| PDF J0044-2803 | 00 44 16.6 | -28 03 42 | 0.13 | 21.0 | 19.33 | | | | | | | | | | |
| PDF J0044-2908 | 00 44 18.3 | -29 08 02 | 0.17 | 26.0 | 23.79 | | 0.16 | 23.0 | 24.45 | 0.15 | 23.0 | 23.94 | | | |
| PDF J0044-2748 | 00 44 31.0 | -27 48 05 | | | | | 0.37 | 32.0 | 14.52 | | | | | | |
| PDF J0044-2743 | 00 44 31.4 | -27 43 58 | 0.33 | 35.0 | 11.39 | | | | | | | | | | |
| PDF J0044-2705 | 00 44 32.8 | -27 05 37 | 0.30 | 25.0 | 10.56 | | | | | | | | | | |
| PDF J0044-2523 | 00 44 37.4 | -25 23 47 | 0.25 | 32.0 | 15.14 | | | | | | | | | | |
| PDF J0044-2541 | 00 44 43.3 | -25 41 08 | | | | | 0.72 | 110.0 | 11.74 | | | | | | |
| PDF J0044-2920 | 00 44 43.7 | -29 20 06 | 0.24 | 21.0 | 10.19 | | | | | | | | | | |
| PDF J0044-2735 | 00 44 48.9 | -27 35 23 | 0.30 | 37.0 | 19.49 | | 0.30 | 35.0 | 26.67 | 0.30 | 35.0 | 18.76 | | | |
| PDF J0044-2625 | 00 44 52.7 | -26 25 42 | 0.16 | 21.0 | 10.86 | | | | | | | | | | |
| PDF J0044-2800 | 00 44 56.1 | -28 00 09 | | | | | 0.35 | 25.0 | 10.81 | | | | | | |
| PDF J0044-2549 | 00 44 57.3 | -25 49 26 | | | | | 0.56 | 62.0 | 15.02 | | | | | | |
| PDF J0044-2528 | 00 44 58.9 | -25 28 50 | | | | | 0.37 | 27.0 | 10.99 | | | | | | |
| PDF J0044-2610 | 00 44 59.4 | -26 10 04 | 0.18 | 22.0 | 13.02 | | 0.18 | 21.0 | 15.09 | 0.18 | 22.0 | 14.76 | | | |
| PDF J0045-2647 | 00 45 03.8 | -26 47 36 | | | | | | | | 0.28 | 34.0 | 20.14 | | | |
| PDF J0045-2804 | 00 45 08.9 | -28 04 20 | 0.17 | 23.0 | 17.19 | | | | | | | | | | |
| PDF J0045-2635 | 00 45 14.0 | -26 35 41 | | | | | | | | 0.44 | 45.0 | 10.61 | | | |
| PDF J0045-2648 | 00 45 14.8 | -26 48 53 | 0.27 | 50.0 | 36.21 | | 0.28 | 41.0 | 36.51 | | | | | | |
| PDF J0045-2923 | 00 45 17.4 | -29 23 57 | 0.33 | 58.0 | 30.36 | | 0.33 | 58.0 | 49.94 | 0.33 | 62.0 | 38.08 | | | EIS J0045-2923 |
| PDF J0045-2700 | 00 45 17.6 | -27 00 51 | 0.18 | 25.0 | 12.46 | | 0.24 | 23.0 | 11.53 | | | | | | |
| PDF J0045-2810 | 00 45 19.6 | -28 10 08 | | | | | 0.67 | 76.0 | 11.69 | | | | | | |
| PDF J0045-2653 | 00 45 27.4 | -26 53 53 | | | | | | | | 0.28 | 28.0 | 14.23 | | | |
| PDF J0045-2902 | 00 45 39.9 | -29 02 35 | | | | | | | | 0.72 | 200.0 | 10.84 | | | |
| PDF J0045-2703 | 00 45 43.3 | -27 03 26 | | | | | | | | 0.41 | 42.0 | 11.95 | | | |
| PDF J0045-2851 | 00 45 59.6 | -28 51 56 | 0.26 | 30.0 | 11.79 | | | | | | | | | | |
| PDF J0045-3003 | 00 45 59.7 | -30 03 41 | | | | | 0.72 | 110.0 | 11.69 | | | | | | |
| PDF J0046-2751 | 00 46 02.2 | -27 51 20 | | | | | 0.33 | 22.0 | 10.75 | 0.32 | 29.0 | 12.75 | | | |
| PDF J0046-2915 | 00 46 05.3 | -29 15 28 | 0.20 | 34.0 | 30.84 | | 0.24 | 30.0 | 27.28 | 0.19 | 25.0 | 20.68 | | | |
| PDF J0046-2824 | 00 46 07.3 | -28 24 20 | | | | | 0.47 | 38.0 | 10.47 | | | | | | |
| PDF J0046-2639 | 00 46 22.0 | -26 39 14 | | | | | 0.37 | 29.0 | 13.85 | | | | | | |
| PDF J0046-2746 | 00 46 41.7 | -27 46 31 | | | | | 0.30 | 20.0 | 10.71 | | | | | | |
| PDF J0046-2710 | 00 46 53.3 | -27 10 16 | | | | | 0.23 | 20.0 | 12.36 | | | | | | |
| PDF J0047-2718 | 00 47 07.6 | -27 18 33 | | | | | | | | 0.61 | 100.0 | 12.01 | | | |
| PDF J0047-2735 | 00 47 08.5 | -27 35 03 | 0.39 | 49.0 | 12.83 | | | | | | | | | | |
| PDF J0047-2725 | 00 47 10.9 | -27 25 34 | 0.37 | 43.0 | 12.56 | | 0.55 | 86.0 | 26.55 | | | | | | |

Table B.2: Cluster Candidate Catalogue

| Cluster | RA (J2000) | Declination (J2000) | z | B_J AMF Λ | \mathcal{L} | z | R AMF Λ | \mathcal{L} | z | I AMF Λ | \mathcal{L} | NED z | Previous ID |
|----------------|---------------|------------------------|------|------------------------|---------------|------|----------------------|---------------|------|----------------------|---------------|-------------------|-------------|
| PDF J0047-2716 | 00 47 13.3 | -27 16 55 | | | | 0.46 | 54.0 | 22.49 | | | | | |
| PDF J0047-2636 | 00 47 13.9 | -26 36 06 | 0.23 | 26.0 | 18.29 | 0.24 | 24.0 | 19.46 | | | | | |
| PDF J0047-2628 | 00 47 18.0 | -26 28 41 | | | | 0.39 | 26.0 | 11.54 | | | | | |
| PDF J0047-2728 | 00 47 21.9 | -27 28 05 | | | | | | | 0.58 | 76.0 | 10.06 | | |
| PDF J0047-2735 | 00 47 28.9 | -27 35 07 | | | | 0.31 | 26.0 | 17.24 | 0.35 | 43.0 | 17.60 | | |
| PDF J0047-2956 | 00 47 37.4 | -29 56 10 | 0.47 | 72.0 | 11.99 | 0.47 | 54.0 | 19.76 | | | | | |
| PDF J0047-2818 | 00 47 37.6 | -28 18 01 | | | | 0.49 | 39.0 | 12.02 | | | | | |
| PDF J0047-2704 | 00 47 41.8 | -27 04 38 | 0.57 | 135.0 | 10.06 | 0.46 | 39.0 | 13.20 | | | | | |
| PDF J0047-3000 | 00 47 50.4 | -30 00 44 | | | | | | | 0.47 | 68.0 | 11.74 | | |
| PDF J0047-2910 | 00 47 53.4 | -29 10 51 | 0.18 | 23.0 | 14.48 | | | | | | | | |
| PDF J0048-2953 | 00 48 06.1 | -29 53 21 | | | | 0.47 | 39.0 | 11.11 | | | | | |
| PDF J0048-3006 | 00 48 11.0 | -30 06 34 | | | | 0.45 | 66.0 | 31.26 | 0.45 | 58.0 | 15.07 | | |
| PDF J0048-2716 | 00 48 18.2 | -27 16 41 | 0.60 | 190.0 | 11.98 | 0.60 | 64.0 | 10.68 | | | | | |
| PDF J0048-3008 | 00 48 18.6 | -30 08 14 | 0.45 | 80.0 | 18.27 | | | | | | | | |
| PDF J0048-2908 | 00 48 19.9 | -29 08 27 | | | | 0.43 | 42.0 | 16.96 | | | | | |
| PDF J0048-2911 | 00 48 48.1 | -29 11 49 | 0.18 | 21.0 | 15.77 | | | | | | | | |
| PDF J0048-2647 | 00 48 49.3 | -26 47 04 | 0.27 | 23.0 | 10.84 | | | | | | | | |
| PDF J0048-2657 | 00 48 54.3 | -26 57 48 | | | | 0.68 | 86.0 | 10.26 | | | | | |
| PDF J0049-2850 | 00 49 04.2 | -28 50 49 | | | | 0.26 | 25.0 | 15.47 | | | | | |
| PDF J0049-2707 | 00 49 16.2 | -27 07 20 | 0.30 | 29.0 | 11.44 | 0.29 | 21.0 | 11.51 | | | | | |
| PDF J0049-2913 | 00 49 16.3 | -29 13 31 | | | | 0.55 | 68.0 | 18.07 | | | | | |
| PDF J0049-2811 | 00 49 19.0 | -28 11 40 | | | | 0.59 | 60.0 | 10.17 | | | | | |
| PDF J0049-2818 | 00 49 20.6 | -28 18 16 | | | | 0.39 | 37.0 | 16.54 | | | | | |
| PDF J0049-2852 | 00 49 21.1 | -28 52 05 | 0.21 | 21.0 | 12.67 | | | | | | | | |
| PDF J0049-2931 | 00 49 21.2 | -29 31 16 | 0.10 | 50.0 | 110.44 | 0.10 | 45.0 | 105.56 | 0.10 | 46.0 | 103.48 | 0.11 ^c | ABELL S0084 |
| PDF J0049-2813 | 00 49 28.3 | -28 13 45 | 0.46 | 96.0 | 14.87 | | | | | | | | |
| PDF J0049-2743 | 00 49 29.5 | -27 43 39 | 0.54 | 120.0 | 11.13 | | | | | | | | |
| PDF J0049-2817 | 00 49 30.1 | -28 17 03 | | | | | | | 0.54 | 98.0 | 15.91 | | |
| PDF J0049-2742 | 00 49 37.0 | -27 42 50 | | | | 0.65 | 100.0 | 15.70 | | | | | |
| PDF J0049-2909 | 00 49 39.2 | -29 09 27 | | | | 0.39 | 38.0 | 22.18 | | | | | |
| PDF J0049-2732 | 00 49 39.3 | -27 32 57 | | | | | | | 0.48 | 54.0 | 10.42 | | |
| PDF J0049-2833 | 00 49 40.6 | -28 33 59 | | | | 0.54 | 52.0 | 11.55 | | | | | |
| PDF J0049-2538 | 00 49 49.0 | -25 38 19 | | | | 0.56 | 58.0 | 13.49 | | | | | |
| PDF J0049-2801 | 00 49 49.4 | -28 01 25 | | | | 0.72 | 110.0 | 10.34 | | | | | |
| PDF J0049-2825 | 00 49 52.2 | -28 25 45 | 0.40 | 56.0 | 15.37 | 0.40 | 64.0 | 38.77 | 0.46 | 74.0 | 21.83 | | |

Table B.3: Cluster Candidate Catalogue

| Cluster | RA (J2000) | Declination (J2000) | z | B_J AMF Λ | \mathcal{L} | z | R AMF Λ | \mathcal{L} | z | I AMF Λ | \mathcal{L} | NED z | Previous ID |
|----------------|---------------|------------------------|------|------------------------|---------------|------|----------------------|---------------|------|----------------------|---------------|-------------------|--------------------|
| PDF J0049-2843 | 00 49 53.4 | -28 43 29 | 0.14 | 21.0 | 16.38 | | | | | | | | |
| PDF J0049-3001 | 00 49 58.0 | -30 01 26 | 0.53 | 115.0 | 12.96 | 0.49 | 54.0 | 18.74 | | | | | [LP96] Cl0048-3018 |
| PDF J0050-2800 | 00 50 06.2 | -28 00 37 | 0.63 | 270.0 | 12.36 | | | | | | | | |
| PDF J0050-2856 | 00 50 09.9 | -28 56 43 | | | | 0.31 | 27.0 | 16.81 | 0.38 | 45.0 | 14.28 | | |
| PDF J0050-2755 | 00 50 19.5 | -27 55 17 | | | | 0.71 | 105.0 | 11.48 | | | | | |
| PDF J0050-2858 | 00 50 26.7 | -28 58 48 | 0.14 | 21.0 | 16.49 | | | | | | | | |
| PDF J0050-2527 | 00 50 27.7 | -25 27 15 | | | | 0.37 | 28.0 | 12.50 | 0.37 | 38.0 | 13.18 | | |
| PDF J0050-2521 | 00 50 27.9 | -25 21 04 | | | | | | | 0.41 | 43.0 | 10.33 | | |
| PDF J0050-2813 | 00 50 32.0 | -28 13 02 | 0.24 | 25.0 | 15.99 | 0.38 | 45.0 | 26.13 | 0.37 | 52.0 | 19.25 | | |
| PDF J0050-2526 | 00 50 36.8 | -25 26 02 | 0.37 | 45.0 | 13.99 | | | | | | | | |
| PDF J0050-2805 | 00 50 47.2 | -28 05 38 | | | | | | | 0.35 | 34.0 | 10.09 | | |
| PDF J0050-2950 | 00 50 51.6 | -29 50 48 | 0.39 | 44.0 | 12.20 | 0.39 | 28.0 | 13.29 | | | | | |
| PDF J0050-2806 | 00 50 56.5 | -28 06 28 | 0.26 | 24.0 | 10.07 | | | | | | | | |
| PDF J0051-3011 | 00 51 00.5 | -30 11 26 | | | | 0.35 | 23.0 | 10.07 | | | | | |
| PDF J0051-2523 | 00 51 07.9 | -25 23 36 | 0.33 | 36.0 | 13.01 | 0.26 | 22.0 | 15.64 | 0.29 | 25.0 | 11.58 | | |
| PDF J0051-3008 | 00 51 17.8 | -30 08 34 | 0.27 | 30.0 | 10.72 | | | | | | | | |
| PDF J0051-3017 | 00 51 19.4 | -30 17 14 | | | | 0.32 | 21.0 | 11.56 | 0.31 | 25.0 | 10.32 | | |
| PDF J0051-2830 | 00 51 22.1 | -28 30 25 | 0.12 | 64.0 | 128.24 | 0.11 | 56.0 | 125.04 | 0.11 | 60.0 | 126.46 | 0.05 ^c | ABELL 2829 |
| PDF J0051-2714 | 00 51 33.1 | -27 14 33 | 0.66 | 290.0 | 10.28 | | | | | | | | |
| PDF J0051-2540 | 00 51 40.5 | -25 40 32 | | | | 0.21 | 32.0 | 28.25 | 0.17 | 29.0 | 25.00 | | |
| PDF J0051-2521 | 00 51 40.8 | -25 21 59 | | | | | | | 0.33 | 41.0 | 19.63 | | |
| PDF J0051-2524 | 00 51 46.2 | -25 24 27 | 0.30 | 52.0 | 33.40 | 0.30 | 43.0 | 37.83 | | | | | |
| PDF J0051-2847 | 00 51 48.0 | -28 47 46 | 0.36 | 49.0 | 18.02 | 0.36 | 32.0 | 16.16 | 0.32 | 28.0 | 11.85 | | |
| PDF J0051-3011 | 00 51 53.9 | -30 11 54 | 0.24 | 36.0 | 20.64 | 0.25 | 31.0 | 19.54 | | | | | |
| PDF J0052-2535 | 00 52 02.5 | -25 35 12 | 0.21 | 23.0 | 15.79 | | | | | | | | |
| PDF J0052-2755 | 00 52 09.6 | -27 55 50 | 0.48 | 70.0 | 10.46 | | | | | | | | |
| PDF J0052-2856 | 00 52 10.5 | -28 56 02 | | | | 0.38 | 25.0 | 10.19 | | | | | |
| PDF J0052-2528 | 00 52 17.2 | -25 28 36 | 0.32 | 45.0 | 21.92 | 0.29 | 37.0 | 31.37 | 0.19 | 26.0 | 18.85 | | |
| PDF J0052-2748 | 00 52 26.5 | -27 48 25 | | | | 0.63 | 62.0 | 10.60 | | | | | |
| PDF J0052-2759 | 00 52 28.2 | -27 59 33 | 0.51 | 150.0 | 21.07 | | | | | | | | |
| PDF J0052-2519 | 00 52 31.9 | -25 19 33 | 0.32 | 32.0 | 13.29 | 0.38 | 35.0 | 19.10 | | | | | |
| PDF J0052-2830 | 00 52 37.2 | -28 30 54 | 0.45 | 76.0 | 17.58 | 0.45 | 48.0 | 20.97 | 0.45 | 48.0 | 13.53 | | |
| PDF J0052-2953 | 00 52 49.4 | -29 53 48 | | | | 0.46 | 33.0 | 10.12 | | | | | |
| PDF J0052-3007 | 00 52 53.1 | -30 07 49 | | | | 0.61 | 80.0 | 14.10 | | | | | |
| PDF J0052-2907 | 00 52 59.4 | -29 07 12 | | | | 0.61 | 74.0 | 11.87 | | | | | |

Table B.4: Cluster Candidate Catalogue

| Cluster | RA (J2000) | Declination (J2000) | B_J AMF | | | R AMF | | | I AMF | | | NED z | Previous ID |
|----------------|---------------|------------------------|-----------|-----------|---------------|---------|-----------|---------------|---------|-----------|---------------|-------------------|-------------|
| | | | z | Λ | \mathcal{L} | z | Λ | \mathcal{L} | z | Λ | \mathcal{L} | | |
| PDF J0053-2535 | 00 53 04.7 | -25 35 38 | | | | 0.40 | 35.0 | 15.94 | 0.43 | 44.0 | 10.60 | | |
| PDF J0053-2543 | 00 53 11.9 | -25 43 04 | 0.19 | 22.0 | 16.11 | | | | 0.26 | 21.0 | 11.73 | | |
| PDF J0053-2741 | 00 53 26.2 | -27 41 01 | 0.31 | 42.0 | 20.09 | 0.38 | 42.0 | 22.76 | 0.43 | 78.0 | 22.45 | | |
| PDF J0053-3000 | 00 53 27.4 | -30 00 49 | | | | 0.49 | 43.0 | 13.50 | | | | | |
| PDF J0053-3009 | 00 53 29.3 | -30 09 04 | | | | 0.33 | 24.0 | 11.85 | | | | | |
| PDF J0053-2519 | 00 53 30.3 | -25 19 34 | | | | 0.39 | 29.0 | 10.84 | | | | | |
| PDF J0053-3010 | 00 53 33.1 | -30 10 43 | 0.25 | 26.0 | 10.48 | | | | | | | | |
| PDF J0053-2800 | 00 53 44.8 | -28 00 24 | 0.38 | 40.0 | 11.59 | 0.44 | 48.0 | 21.19 | | | | | |
| PDF J0053-3002 | 00 53 52.2 | -30 02 53 | 0.48 | 76.0 | 10.91 | 0.52 | 60.0 | 16.32 | | | | | |
| PDF J0053-2533 | 00 53 55.8 | -25 33 10 | | | | 0.66 | 76.0 | 10.72 | | | | | |
| PDF J0053-2741 | 00 53 57.8 | -27 41 51 | 0.61 | 210.0 | 11.71 | | | | | | | | |
| PDF J0054-2705 | 00 54 01.5 | -27 05 08 | 0.54 | 130.0 | 11.17 | | | | | | | | |
| PDF J0054-2823 | 00 54 03.5 | -28 23 55 | 0.32 | 33.0 | 14.66 | 0.38 | 37.0 | 21.92 | 0.30 | 23.0 | 11.47 | 0.25 ^c | [VMF98] 004 |
| PDF J0054-2542 | 00 54 06.8 | -25 42 15 | | | | | | | 0.28 | 24.0 | 10.94 | | |
| PDF J0054-2956 | 00 54 16.9 | -29 56 17 | 0.62 | 210.0 | 11.02 | | | | | | | | |
| PDF J0054-2750 | 00 54 18.3 | -27 50 05 | 0.26 | 60.0 | 44.23 | 0.30 | 49.0 | 46.80 | 0.38 | 72.0 | 33.67 | | |
| PDF J0054-2543 | 00 54 21.5 | -25 43 29 | 0.39 | 54.0 | 16.57 | 0.37 | 33.0 | 16.53 | | | | | |
| PDF J0054-2831 | 00 54 31.6 | -28 31 20 | 0.35 | 37.0 | 11.88 | 0.44 | 30.0 | 10.55 | | | | | |
| PDF J0054-2814 | 00 54 40.9 | -28 14 50 | | | | | | | 0.60 | 88.0 | 10.44 | | |
| PDF J0054-2554 | 00 54 45.4 | -25 54 12 | | | | 0.26 | 23.0 | 11.51 | | | | | |
| PDF J0054-2811 | 00 54 59.6 | -28 11 06 | 0.58 | 200.0 | 11.29 | | | | | | | | |
| PDF J0055-2905 | 00 55 02.0 | -29 05 08 | | | | 0.63 | 78.0 | 12.49 | | | | | |
| PDF J0055-2745 | 00 55 06.8 | -27 45 32 | | | | 0.64 | 82.0 | 11.36 | | | | | |
| PDF J0055-3006 | 00 55 08.4 | -30 06 10 | | | | | | | 0.12 | 25.0 | 21.62 | | |
| PDF J0055-2826 | 00 55 14.8 | -28 26 46 | 0.56 | 160.0 | 13.99 | | | | | | | | |
| PDF J0055-2842 | 00 55 14.9 | -28 42 26 | | | | | | | 0.49 | 60.0 | 11.93 | | |
| PDF J0055-2553 | 00 55 18.3 | -25 53 21 | 0.20 | 20.0 | 13.60 | 0.28 | 23.0 | 17.17 | 0.24 | 23.0 | 15.43 | | |
| PDF J0055-2623 | 00 55 24.3 | -26 23 27 | 0.13 | 68.0 | 124.24 | 0.11 | 60.0 | 122.87 | 0.11 | 60.0 | 117.30 | 0.11 ^c | APMCC 119 |
| PDF J0055-3006 | 00 55 25.6 | -30 06 59 | 0.13 | 43.0 | 39.81 | 0.13 | 36.0 | 33.87 | | | | | |
| PDF J0055-2601 | 00 55 25.8 | -26 01 11 | | | | 0.21 | 22.0 | 12.00 | | | | | |
| PDF J0055-2830 | 00 55 27.9 | -28 30 53 | | | | 0.60 | 78.0 | 12.84 | | | | | |
| PDF J0055-2720 | 00 55 28.8 | -27 20 47 | 0.63 | 250.0 | 10.38 | | | | | | | | |
| PDF J0055-2847 | 00 55 32.0 | -28 47 47 | 0.09 | 23.0 | 24.93 | 0.11 | 20.0 | 18.08 | | | | | ABELL S0100 |
| PDF J0055-2531 | 00 55 32.7 | -25 31 04 | | | | 0.50 | 40.0 | 10.11 | | | | | |
| PDF J0055-2710 | 00 55 39.7 | -27 10 03 | | | | 0.65 | 78.0 | 12.63 | | | | | |

Table B.5: Cluster Candidate Catalogue

| Cluster | RA (J2000) | Declination (J2000) | B_J AMF | | | R AMF | | | I AMF | | | NED z | Previous ID |
|----------------|---------------|------------------------|-----------|-----------|---------------|---------|-----------|---------------|---------|-----------|---------------|-------------------|--------------------|
| | | | z | Λ | \mathcal{L} | z | Λ | \mathcal{L} | z | Λ | \mathcal{L} | | |
| PDF J0055-2818 | 00 55 46.5 | -28 18 30 | 0.48 | 88.0 | 14.34 | 0.54 | 76.0 | 21.92 | | | | | |
| PDF J0055-2932 | 00 55 47.8 | -29 32 19 | 0.39 | 52.0 | 15.14 | | | | | | | | |
| PDF J0055-2853 | 00 55 49.0 | -28 53 08 | | | | 0.46 | 62.0 | 27.99 | | | | | |
| PDF J0055-2553 | 00 55 56.8 | -25 53 44 | | | | 0.48 | 32.0 | 11.19 | 0.48 | 49.0 | 11.70 | | |
| PDF J0055-2719 | 00 55 58.4 | -27 19 06 | | | | | | | 0.45 | 44.0 | 10.29 | | |
| PDF J0056-2948 | 00 56 03.3 | -29 48 23 | 0.24 | 29.0 | 17.96 | | | | | | | | [LP96] Cl0054-3005 |
| PDF J0056-2946 | 00 56 09.0 | -29 46 44 | | | | 0.36 | 45.0 | 26.57 | 0.36 | 32.0 | 10.85 | | |
| PDF J0056-2604 | 00 56 11.7 | -26 04 26 | 0.25 | 23.0 | 12.17 | | | | | | | | |
| PDF J0056-2625 | 00 56 12.2 | -26 25 53 | 0.10 | 24.0 | 17.43 | | | | | | | 0.04 ^g | |
| PDF J0056-2837 | 00 56 20.6 | -28 37 01 | | | | 0.31 | 25.0 | 10.85 | | | | | |
| PDF J0056-2552 | 00 56 20.6 | -25 52 28 | | | | 0.53 | 98.0 | 39.21 | 0.36 | 31.0 | 11.84 | | |
| PDF J0056-2904 | 00 56 26.9 | -29 04 39 | 0.14 | 35.0 | 41.21 | 0.14 | 31.0 | 38.73 | 0.10 | 25.0 | 31.07 | | ABELL S0105 |
| PDF J0056-2604 | 00 56 28.2 | -26 04 50 | | | | 0.27 | 23.0 | 13.57 | | | | | |
| PDF J0056-3004 | 00 56 30.3 | -30 04 51 | 0.15 | 64.0 | 84.44 | 0.14 | 50.0 | 70.09 | 0.12 | 42.0 | 55.09 | 0.11 ^c | ABELL 2844 |
| PDF J0056-2547 | 00 56 31.5 | -25 47 06 | 0.24 | 31.0 | 19.69 | 0.25 | 27.0 | 18.69 | | | | | |
| PDF J0056-2730 | 00 56 32.1 | -27 30 12 | 0.18 | 37.0 | 36.94 | 0.18 | 25.0 | 28.58 | 0.18 | 35.0 | 35.37 | 0.56 ^c | ABELL 2843 |
| PDF J0056-2820 | 00 56 37.1 | -28 20 30 | 0.39 | 45.0 | 12.00 | 0.39 | 46.0 | 25.12 | | | | | |
| PDF J0056-2922 | 00 56 42.5 | -29 22 22 | | | | 0.56 | 68.0 | 15.03 | | | | | |
| PDF J0056-2938 | 00 56 46.7 | -29 38 26 | 0.18 | 35.0 | 38.68 | 0.18 | 29.0 | 33.82 | 0.18 | 29.0 | 30.98 | | |
| PDF J0056-2740 | 00 56 56.6 | -27 40 29 | 0.47 | 80.0 | 14.99 | 0.47 | 70.0 | 33.17 | 0.47 | 52.0 | 11.13 | 0.56 ^c | J1888.16CL |
| PDF J0056-2536 | 00 56 56.9 | -25 36 45 | 0.39 | 70.0 | 21.26 | 0.39 | 52.0 | 26.94 | 0.39 | 39.0 | 10.39 | | |
| PDF J0056-2546 | 00 56 57.1 | -25 46 39 | | | | 0.46 | 78.0 | 39.45 | 0.32 | 31.0 | 13.02 | | |
| PDF J0057-2822 | 00 57 03.4 | -28 22 57 | | | | | | | 0.49 | 50.0 | 10.92 | | |
| PDF J0057-2948 | 00 57 06.0 | -29 48 43 | 0.14 | 30.0 | 24.05 | 0.16 | 28.0 | 24.66 | 0.15 | 21.0 | 17.27 | | |
| PDF J0057-2839 | 00 57 07.7 | -28 39 51 | 0.21 | 25.0 | 16.69 | 0.29 | 25.0 | 17.03 | 0.21 | 20.0 | 13.34 | | |
| PDF J0057-3012 | 00 57 08.7 | -30 12 38 | 0.10 | 20.0 | 14.00 | | | | | | | | |
| PDF J0057-2747 | 00 57 09.8 | -27 47 28 | 0.37 | 60.0 | 16.78 | 0.37 | 54.0 | 26.54 | 0.38 | 58.0 | 21.63 | | |
| PDF J0057-2754 | 00 57 11.9 | -27 54 53 | | | | 0.46 | 39.0 | 11.29 | | | | | |
| PDF J0057-2822 | 00 57 14.6 | -28 22 06 | 0.35 | 42.0 | 14.97 | 0.45 | 48.0 | 18.65 | | | | | |
| PDF J0057-2754 | 00 57 19.4 | -27 54 28 | 0.50 | 84.0 | 11.15 | | | | | | | | |
| PDF J0057-2617 | 00 57 20.0 | -26 17 08 | 0.11 | 40.0 | 69.95 | 0.12 | 40.0 | 71.18 | 0.10 | 36.0 | 64.97 | 0.11 ^c | ABELL 0122 |
| PDF J0057-2702 | 00 57 21.4 | -27 02 30 | | | | 0.68 | 90.0 | 13.88 | | | | | |
| PDF J0057-2737 | 00 57 24.4 | -27 37 08 | | | | 0.56 | 49.0 | 10.05 | | | | | |
| PDF J0057-3007 | 00 57 33.3 | -30 07 39 | | | | 0.48 | 78.0 | 29.90 | | | | | |
| PDF J0057-2807 | 00 57 34.7 | -28 07 14 | 0.11 | 23.0 | 20.07 | | | | | | | | |

Table B.6: Cluster Candidate Catalogue

| Cluster | RA (J2000) | Declination (J2000) | B_J AMF | | | R AMF | | | I AMF | | | NED z | Previous ID |
|----------------|---------------|------------------------|-----------|-----------|---------------|---------|-----------|---------------|---------|-----------|---------------|------------|--------------------|
| | | | z | Λ | \mathcal{L} | z | Λ | \mathcal{L} | z | Λ | \mathcal{L} | | |
| PDF J0057-2540 | 00 57 35.4 | -25 40 00 | 0.39 | 43.0 | 11.08 | | | | | | | | |
| PDF J0057-2856 | 00 57 42.1 | -28 56 42 | | | | | | | 0.42 | 42.0 | 10.48 | | |
| PDF J0057-2724 | 00 57 53.7 | -27 24 18 | 0.20 | 24.0 | 15.93 | 0.20 | 20.0 | 13.97 | 0.19 | 21.0 | 13.46 | | |
| PDF J0057-2839 | 00 57 54.7 | -28 39 46 | | | | 0.48 | 38.0 | 10.66 | | | | | |
| PDF J0057-2715 | 00 57 55.2 | -27 15 14 | | | | 0.64 | 82.0 | 14.32 | | | | | |
| PDF J0057-2634 | 00 57 57.4 | -26 34 24 | 0.39 | 68.0 | 21.95 | 0.44 | 64.0 | 29.99 | 0.44 | 74.0 | 20.07 | | |
| PDF J0058-3012 | 00 58 11.6 | -30 12 32 | | | | 0.36 | 41.0 | 23.60 | 0.44 | 70.0 | 19.91 | | |
| PDF J0058-2944 | 00 58 12.3 | -29 44 29 | | | | 0.28 | 21.0 | 13.79 | | | | | |
| PDF J0058-2821 | 00 58 12.7 | -28 21 36 | | | | 0.39 | 29.0 | 11.25 | 0.35 | 32.0 | 10.10 | | |
| PDF J0058-2723 | 00 58 25.3 | -27 23 50 | | | | 0.62 | 150.0 | 41.49 | 0.64 | 185.0 | 21.12 | | |
| PDF J0058-2841 | 00 58 26.7 | -28 41 22 | | | | 0.45 | 49.0 | 18.67 | | | | | |
| PDF J0058-2636 | 00 58 27.0 | -26 36 24 | | | | 0.39 | 28.0 | 10.88 | | | | | |
| PDF J0058-2842 | 00 58 28.6 | -28 42 36 | 0.45 | 70.0 | 14.05 | | | | | | | | |
| PDF J0058-2819 | 00 58 35.1 | -28 19 29 | | | | 0.49 | 50.0 | 15.92 | | | | | |
| PDF J0058-2819 | 00 58 44.5 | -28 19 53 | 0.37 | 48.0 | 16.91 | | | | | | | | |
| PDF J0058-2759 | 00 58 47.3 | -27 59 15 | 0.27 | 52.0 | 38.77 | 0.29 | 32.0 | 28.18 | 0.36 | 58.0 | 26.51 | | |
| PDF J0058-2607 | 00 58 47.9 | -26 07 54 | 0.42 | 76.0 | 23.00 | 0.42 | 50.0 | 27.86 | 0.42 | 50.0 | 16.25 | | |
| PDF J0058-2953 | 00 58 48.9 | -29 53 54 | 0.43 | 78.0 | 16.82 | | | | | | | | |
| PDF J0058-2955 | 00 58 50.9 | -29 55 57 | | | | 0.57 | 140.0 | 31.51 | | | | | |
| PDF J0058-3014 | 00 58 57.5 | -30 14 30 | 0.37 | 46.0 | 14.39 | 0.38 | 46.0 | 27.23 | 0.37 | 40.0 | 13.39 | | |
| PDF J0059-2946 | 00 59 01.8 | -29 46 02 | | | | 0.62 | 88.0 | 15.28 | | | | | |
| PDF J0059-2859 | 00 59 14.6 | -28 59 24 | 0.26 | 36.0 | 23.76 | 0.27 | 35.0 | 31.69 | 0.19 | 26.0 | 21.93 | | |
| PDF J0059-2754 | 00 59 15.1 | -27 54 39 | | | | 0.63 | 100.0 | 20.14 | 0.63 | 100.0 | 10.98 | | |
| PDF J0059-2845 | 00 59 21.4 | -28 45 22 | 0.52 | 120.0 | 15.37 | 0.38 | 29.0 | 12.67 | 0.39 | 47.0 | 12.39 | | |
| PDF J0059-2631 | 00 59 22.1 | -26 31 44 | | | | 0.47 | 34.0 | 10.16 | | | | | |
| PDF J0059-2813 | 00 59 27.3 | -28 13 35 | 0.26 | 25.0 | 11.12 | | | | | | | | |
| PDF J0059-2952 | 00 59 38.3 | -29 52 57 | 0.25 | 28.0 | 14.95 | 0.24 | 21.0 | 13.09 | | | | | |
| PDF J0059-2852 | 00 59 46.2 | -28 52 18 | 0.17 | 20.0 | 12.39 | | | | | | | | |
| PDF J0059-3003 | 00 59 46.5 | -30 03 39 | 0.27 | 35.0 | 21.83 | 0.27 | 36.0 | 30.15 | 0.26 | 24.0 | 12.94 | | |
| PDF J0059-2523 | 00 59 53.5 | -25 23 12 | 0.48 | 82.0 | 12.66 | | | | | | | | |
| PDF J0059-2820 | 00 59 53.9 | -28 20 32 | 0.19 | 23.0 | 17.95 | 0.30 | 30.0 | 23.68 | 0.30 | 32.0 | 18.00 | | |
| PDF J0100-2919 | 01 00 02.9 | -29 19 54 | 0.30 | 39.0 | 25.55 | 0.26 | 27.0 | 25.80 | 0.20 | 24.0 | 20.23 | | [LP96] C10058-2936 |
| PDF J0100-2846 | 01 00 06.6 | -28 46 04 | 0.27 | 49.0 | 38.05 | 0.20 | 32.0 | 39.41 | 0.20 | 29.0 | 29.91 | | |
| PDF J0100-2832 | 01 00 07.7 | -28 32 27 | | | | 0.39 | 42.0 | 21.56 | | | | | |
| PDF J0100-2630 | 01 00 08.1 | -26 30 47 | 0.43 | 58.0 | 12.96 | 0.47 | 68.0 | 34.27 | | | | | |

Table B.7: Cluster Candidate Catalogue

| Cluster | RA (J2000) | Declination (J2000) | B_J AMF | | | R AMF | | | I AMF | | | NED z | Previous ID |
|----------------|---------------|------------------------|-----------|-----------|---------------|---------|-----------|---------------|---------|-----------|---------------|------------|--------------------|
| | | | z | Λ | \mathcal{L} | z | Λ | \mathcal{L} | z | Λ | \mathcal{L} | | |
| PDF J0100-2831 | 01 00 17.0 | -28 31 11 | 0.23 | 20.0 | 10.47 | | | | | | | | |
| PDF J0100-2623 | 01 00 18.8 | -26 23 20 | | | | 0.58 | 62.0 | 13.64 | | | | | |
| PDF J0100-3011 | 01 00 19.4 | -30 11 24 | 0.30 | 32.0 | 15.39 | 0.30 | 34.0 | 24.95 | 0.39 | 42.0 | 14.31 | | [LP96] Cl0058-3029 |
| PDF J0100-3003 | 01 00 24.6 | -30 03 33 | | | | 0.49 | 54.0 | 16.90 | | | | | |
| PDF J0100-2634 | 01 00 30.5 | -26 34 01 | | | | 0.62 | 88.0 | 18.60 | | | | | |
| PDF J0100-2718 | 01 00 33.1 | -27 18 09 | | | | 0.73 | 130.0 | 12.82 | 0.38 | 37.0 | 12.33 | | |
| PDF J0100-2944 | 01 00 34.8 | -29 44 57 | | | | 0.54 | 46.0 | 11.44 | | | | | |
| PDF J0100-2946 | 01 00 44.4 | -29 46 59 | 0.32 | 31.0 | 10.76 | | | | | | | | |
| PDF J0100-2955 | 01 00 45.0 | -29 55 14 | 0.43 | 66.0 | 14.23 | 0.45 | 64.0 | 30.65 | | | | | |
| PDF J0100-2705 | 01 00 45.3 | -27 05 19 | | | | 0.49 | 44.0 | 10.62 | | | | | |
| PDF J0100-2818 | 01 00 48.1 | -28 18 43 | 0.21 | 29.0 | 18.34 | 0.32 | 39.0 | 27.15 | 0.20 | 27.0 | 18.40 | | |
| PDF J0100-2956 | 01 00 48.9 | -29 56 28 | | | | | | | 0.43 | 49.0 | 13.08 | | |
| PDF J0100-2901 | 01 00 52.8 | -29 01 36 | | | | 0.24 | 22.0 | 12.69 | | | | | |
| PDF J0100-2931 | 01 00 52.9 | -29 31 42 | 0.20 | 23.0 | 10.90 | | | | | | | | |
| PDF J0100-2725 | 01 00 55.8 | -27 25 05 | | | | 0.67 | 86.0 | 10.25 | | | | | |
| PDF J0101-2831 | 01 01 15.2 | -28 31 50 | 0.21 | 56.0 | 46.99 | 0.21 | 52.0 | 53.43 | 0.17 | 33.0 | 34.53 | | |
| PDF J0101-2840 | 01 01 17.7 | -28 40 54 | 0.32 | 58.0 | 28.50 | 0.31 | 56.0 | 46.77 | 0.31 | 54.0 | 30.83 | | |
| PDF J0101-2800 | 01 01 22.4 | -28 00 03 | | | | 0.46 | 44.0 | 16.53 | | | | | |
| PDF J0101-2918 | 01 01 29.9 | -29 18 48 | 0.18 | 34.0 | 29.93 | | | | | | | | ABELL S0114 |
| PDF J0101-2613 | 01 01 31.7 | -26 13 12 | | | | 0.65 | 98.0 | 19.34 | | | | | |
| PDF J0101-2755 | 01 01 35.1 | -27 55 04 | 0.22 | 20.0 | 11.61 | | | | 0.25 | 23.0 | 13.36 | | |
| PDF J0101-2535 | 01 01 38.4 | -25 35 39 | 0.42 | 56.0 | 12.17 | | | | | | | | |
| PDF J0101-2915 | 01 01 39.1 | -29 15 28 | | | | 0.20 | 35.0 | 38.40 | 0.20 | 30.0 | 25.66 | | |
| PDF J0101-2606 | 01 01 40.4 | -26 06 10 | 0.29 | 30.0 | 14.59 | 0.28 | 27.0 | 18.65 | | | | | |
| PDF J0101-2536 | 01 01 53.0 | -25 36 25 | | | | 0.33 | 37.0 | 17.38 | | | | | |
| PDF J0102-2538 | 01 02 15.1 | -25 38 00 | 0.29 | 32.0 | 15.79 | | | | 0.27 | 24.0 | 13.38 | | |
| PDF J0102-2614 | 01 02 16.0 | -26 14 42 | 0.24 | 31.0 | 20.55 | 0.26 | 26.0 | 18.37 | | | | | |
| PDF J0102-2944 | 01 02 19.2 | -29 44 36 | | | | 0.64 | 94.0 | 17.51 | | | | | |
| PDF J0102-2546 | 01 02 26.7 | -25 46 37 | | | | 0.52 | 44.0 | 10.07 | | | | | |
| PDF J0102-2919 | 01 02 36.1 | -29 19 23 | | | | 0.14 | 21.0 | 23.16 | 0.14 | 20.0 | 21.93 | | |
| PDF J0102-2540 | 01 02 44.6 | -25 40 46 | 0.17 | 24.0 | 15.48 | 0.29 | 37.0 | 22.92 | | | | | |
| PDF J0102-2925 | 01 02 57.4 | -29 25 04 | 0.24 | 27.0 | 15.86 | | | | | | | | |
| PDF J0102-2911 | 01 02 58.1 | -29 11 03 | 0.30 | 80.0 | 79.21 | 0.30 | 68.0 | 87.88 | 0.27 | 60.0 | 59.81 | | ABELL S0119 |
| PDF J0103-2528 | 01 03 09.2 | -25 28 42 | 0.32 | 34.0 | 10.53 | | | | | | | | |
| PDF J0103-2518 | 01 03 13.9 | -25 18 22 | | | | 0.51 | 50.0 | 16.06 | | | | | |

Table B.8: Cluster Candidate Catalogue

| Cluster | RA (J2000) | Declination (J2000) | B_J AMF | | | R AMF | | | I AMF | | | NED z | Previous ID |
|----------------|---------------|------------------------|-----------|-----------|---------------|---------|-----------|---------------|---------|-----------|---------------|------------|-------------|
| | | | z | Λ | \mathcal{L} | z | Λ | \mathcal{L} | z | Λ | \mathcal{L} | | |
| PDF J0103-2547 | 01 03 16.2 | -25 47 39 | | | | 0.36 | 29.0 | 15.47 | | | | | |
| PDF J0103-2540 | 01 03 17.5 | -25 40 38 | 0.32 | 48.0 | 25.73 | 0.37 | 54.0 | 37.13 | 0.21 | 28.0 | 20.46 | | |
| PDF J0103-2852 | 01 03 19.1 | -28 52 49 | | | | 0.26 | 26.0 | 19.72 | | | | | |
| PDF J0103-2851 | 01 03 32.2 | -28 51 56 | 0.19 | 21.0 | 15.91 | | | | | | | | |
| PDF J0103-2820 | 01 03 35.0 | -28 20 34 | 0.29 | 27.0 | 13.95 | 0.29 | 22.0 | 16.77 | 0.29 | 25.0 | 12.85 | | |
| PDF J0103-2752 | 01 03 47.3 | -27 52 04 | 0.39 | 47.0 | 14.18 | 0.39 | 37.0 | 22.09 | 0.44 | 58.0 | 17.85 | | |
| PDF J0104-2936 | 01 04 06.7 | -29 36 19 | 0.13 | 20.0 | 13.87 | | | | | | | | |
| PDF J0104-2836 | 01 04 15.9 | -28 36 53 | | | | 0.30 | 25.0 | 15.27 | 0.36 | 34.0 | 11.02 | | |
| PDF J0104-2547 | 01 04 22.2 | -25 47 46 | | | | 0.37 | 30.0 | 12.44 | | | | | |
| PDF J0104-2830 | 01 04 51.0 | -28 30 32 | | | | 0.44 | 38.0 | 14.21 | | | | | |
| PDF J0105-2520 | 01 05 25.4 | -25 20 39 | 0.22 | 36.0 | 30.65 | 0.21 | 32.0 | 34.23 | 0.21 | 27.0 | 22.51 | | |
| PDF J0105-2537 | 01 05 45.4 | -25 37 27 | | | | 0.45 | 34.0 | 11.09 | | | | | |
| PDF J0105-2548 | 01 05 46.5 | -25 48 10 | 0.37 | 47.0 | 18.47 | 0.38 | 44.0 | 30.56 | 0.35 | 41.0 | 19.53 | | |
| PDF J0105-2905 | 01 05 55.0 | -29 05 15 | 0.13 | 24.0 | 25.61 | | | | | | | | |
| PDF J0106-2624 | 01 06 10.5 | -26 24 19 | 0.39 | 41.0 | 10.43 | | | | | | | | |
| PDF J1032-0244 | 10 32 43.2 | -02 44 01 | 0.39 | 42.0 | 10.09 | 0.39 | 36.0 | 18.92 | | | | | |
| PDF J1032+0210 | 10 32 53.3 | +02 10 21 | 0.13 | 27.0 | 25.64 | 0.17 | 24.0 | 24.16 | 0.11 | 22.0 | 21.12 | | |
| PDF J1033-0134 | 10 33 08.3 | -01 34 45 | 0.23 | 28.0 | 18.42 | 0.24 | 30.0 | 23.63 | 0.21 | 23.0 | 13.51 | | |
| PDF J1033-0221 | 10 33 13.1 | -02 21 45 | 0.21 | 38.0 | 33.25 | 0.22 | 34.0 | 30.87 | 0.11 | 21.0 | 18.59 | | |
| PDF J1033-0127 | 10 33 19.8 | -01 27 20 | | | | 0.45 | 52.0 | 18.43 | | | | | |
| PDF J1033-0151 | 10 33 23.1 | -01 51 15 | 0.44 | 94.0 | 25.52 | 0.45 | 58.0 | 29.07 | 0.46 | 68.0 | 14.40 | | |
| PDF J1033+0203 | 10 33 24.6 | +02 03 45 | | | | 0.57 | 45.0 | 10.39 | | | | | |
| PDF J1033+0139 | 10 33 33.0 | +01 39 50 | 0.50 | 84.0 | 11.94 | 0.49 | 35.0 | 11.68 | | | | | |
| PDF J1033+0200 | 10 33 41.1 | +02 00 02 | | | | | | | 0.10 | 20.0 | 16.58 | | |
| PDF J1033-0040 | 10 33 44.7 | -00 40 45 | | | | | | | 0.13 | 20.0 | 14.63 | | |
| PDF J1033-0157 | 10 33 52.7 | -01 57 26 | 0.30 | 38.0 | 18.83 | 0.28 | 28.0 | 18.79 | 0.28 | 27.0 | 10.69 | | |
| PDF J1033-0039 | 10 33 56.2 | -00 39 30 | 0.22 | 33.0 | 19.00 | 0.21 | 32.0 | 22.37 | | | | | |
| PDF J1034-0215 | 10 34 00.9 | -02 15 10 | 0.18 | 48.0 | 46.17 | 0.23 | 44.0 | 42.56 | 0.13 | 37.0 | 33.79 | | |
| PDF J1034-0105 | 10 34 17.6 | -01 05 54 | | | | | | | 0.44 | 52.0 | 11.41 | | |
| PDF J1034-0050 | 10 34 17.6 | -00 50 14 | 0.24 | 30.0 | 12.94 | | | | | | | | |
| PDF J1034-0057 | 10 34 19.3 | -00 57 14 | 0.29 | 31.0 | 14.59 | 0.29 | 23.0 | 12.99 | | | | | |
| PDF J1034-0219 | 10 34 27.3 | -02 19 17 | | | | 0.31 | 33.0 | 20.89 | | | | | |
| PDF J1034-0112 | 10 34 35.7 | -01 12 54 | | | | 0.48 | 38.0 | 12.32 | | | | | |
| PDF J1034-0216 | 10 34 42.2 | -02 16 49 | 0.12 | 23.0 | 14.16 | | | | | | | | |
| PDF J1034-0213 | 10 34 53.7 | -02 13 31 | | | | | | | 0.11 | 21.0 | 10.97 | | |

Table B.9: Cluster Candidate Catalogue

| Cluster | RA (J2000) | Declination (J2000) | B_J AMF | | | R AMF | | | I AMF | | | NED z | Previous ID |
|----------------|---------------|------------------------|-----------|-----------|---------------|---------|-----------|---------------|---------|-----------|---------------|------------|-------------|
| | | | z | Λ | \mathcal{L} | z | Λ | \mathcal{L} | z | Λ | \mathcal{L} | | |
| PDF J1034+0130 | 10 34 55.5 | +01 30 46 | | | | 0.57 | 47.0 | 11.40 | | | | | |
| PDF J1034-0230 | 10 34 57.0 | -02 30 26 | | | | 0.44 | 37.0 | 14.18 | | | | | |
| PDF J1035-0214 | 10 35 23.4 | -02 14 46 | 0.15 | 22.0 | 17.33 | 0.16 | 20.0 | 17.11 | | | | | |
| PDF J1035-0001 | 10 35 26.9 | -00 01 59 | | | | 0.48 | 62.0 | 31.35 | 0.49 | 90.0 | 18.07 | | |
| PDF J1036+0102 | 10 36 03.1 | +01 02 19 | | | | 0.63 | 56.0 | 11.68 | | | | | |
| PDF J1036+0136 | 10 36 09.7 | +01 36 58 | | | | 0.39 | 24.0 | 11.42 | | | | | |
| PDF J1036-0222 | 10 36 14.6 | -02 22 11 | 0.12 | 28.0 | 22.67 | 0.12 | 29.0 | 28.90 | 0.12 | 28.0 | 25.47 | | |
| PDF J1036-0124 | 10 36 31.2 | -01 24 03 | | | | 0.30 | 25.0 | 11.47 | | | | | |
| PDF J1036-0206 | 10 36 32.8 | -02 06 31 | 0.23 | 28.0 | 16.07 | | | | | | | | |
| PDF J1036+0136 | 10 36 42.7 | +01 36 58 | | | | 0.49 | 47.0 | 18.27 | | | | | |
| PDF J1036-0232 | 10 36 44.2 | -02 32 30 | | | | 0.58 | 54.0 | 12.41 | | | | | |
| PDF J1036-0057 | 10 36 47.7 | -00 57 15 | 0.64 | 230.0 | 10.50 | | | | | | | | |
| PDF J1036+0151 | 10 36 49.2 | +01 51 48 | | | | 0.62 | 84.0 | 18.34 | | | | | |
| PDF J1036-0209 | 10 36 55.8 | -02 09 25 | | | | 0.23 | 23.0 | 14.35 | 0.26 | 27.0 | 10.98 | | |
| PDF J1037+0146 | 10 37 00.8 | +01 46 02 | | | | 0.42 | 38.0 | 17.98 | | | | | |
| PDF J1037-0041 | 10 37 24.0 | -00 41 10 | 0.12 | 25.0 | 21.05 | 0.09 | 20.0 | 20.85 | 0.09 | 20.0 | 19.39 | | |
| PDF J1037+0133 | 10 37 37.1 | +01 33 15 | 0.34 | 39.0 | 14.96 | 0.43 | 43.0 | 19.20 | 0.47 | 76.0 | 14.85 | | |
| PDF J1038-0228 | 10 38 03.5 | -02 28 23 | 0.17 | 27.0 | 17.35 | | | | | | | | |
| PDF J1038-0126 | 10 38 18.4 | -01 26 32 | | | | 0.59 | 58.0 | 14.61 | | | | | |
| PDF J1038-0113 | 10 38 34.9 | -01 13 20 | 0.14 | 20.0 | 15.40 | 0.13 | 20.0 | 18.65 | | | | | |
| PDF J1038+0139 | 10 38 36.5 | +01 39 02 | 0.46 | 70.0 | 12.92 | | | | | | | | |
| PDF J1038+0136 | 10 38 48.0 | +01 36 08 | | | | 0.59 | 50.0 | 11.62 | | | | | |
| PDF J1038-0115 | 10 38 49.7 | -01 15 24 | | | | | | | 0.14 | 25.0 | 17.31 | | |
| PDF J1039-0215 | 10 39 02.9 | -02 15 36 | 0.15 | 27.0 | 18.74 | 0.18 | 21.0 | 15.13 | | | | | |
| PDF J1039+0117 | 10 39 09.5 | +01 17 35 | | | | 0.12 | 27.0 | 28.25 | 0.12 | 26.0 | 24.60 | | |
| PDF J1039+0207 | 10 39 17.6 | +02 07 29 | 0.38 | 62.0 | 22.13 | 0.38 | 60.0 | 43.04 | 0.38 | 80.0 | 30.80 | | |
| PDF J1039+0114 | 10 39 17.7 | +01 14 42 | 0.13 | 29.0 | 25.96 | | | | | | | | |
| PDF J1039-0135 | 10 39 21.1 | -01 35 12 | 0.43 | 80.0 | 16.90 | | | | | | | | |
| PDF J1039-0052 | 10 39 21.1 | -00 52 18 | 0.19 | 24.0 | 15.97 | | | | | | | | |
| PDF J1039+0101 | 10 39 22.7 | +01 01 30 | 0.12 | 45.0 | 59.22 | 0.11 | 38.0 | 48.54 | 0.12 | 42.0 | 51.41 | | |
| PDF J1039-0105 | 10 39 22.7 | -01 05 55 | | | | | | | 0.39 | 52.0 | 15.48 | | |
| PDF J1039-0202 | 10 39 27.6 | -02 02 00 | 0.26 | 30.0 | 11.17 | 0.38 | 46.0 | 20.30 | 0.48 | 76.0 | 11.06 | | |
| PDF J1039-0056 | 10 39 29.3 | -00 56 50 | | | | 0.20 | 20.0 | 13.14 | 0.21 | 25.0 | 14.36 | | |
| PDF J1039+0211 | 10 39 37.4 | +02 11 12 | 0.39 | 44.0 | 10.78 | | | | | | | | |
| PDF J1039+0003 | 10 39 44.2 | +00 03 21 | | | | 0.64 | 78.0 | 16.48 | | | | | |

Table B.10: Cluster Candidate Catalogue

| Cluster | RA (J2000) | Declination (J2000) | B_J AMF | | | R AMF | | | I AMF | | | NED z | Previous ID |
|----------------|---------------|------------------------|-----------|-----------|---------------|---------|-----------|---------------|---------|-----------|---------------|-------------------|-----------------|
| | | | z | Λ | \mathcal{L} | z | Λ | \mathcal{L} | z | Λ | \mathcal{L} | | |
| PDF J1039+0022 | 10 39 49.1 | +00 22 44 | | | | 0.40 | 31.0 | 10.48 | | | | | |
| PDF J1039+0205 | 10 39 53.9 | +02 05 01 | 0.42 | 90.0 | 21.80 | | | | | | | | |
| PDF J1039+0210 | 10 39 57.2 | +02 10 47 | | | | 0.60 | 74.0 | 21.06 | | | | | |
| PDF J1040+0159 | 10 40 03.8 | +01 59 14 | 0.44 | 82.0 | 21.02 | 0.39 | 60.0 | 44.01 | 0.44 | 86.0 | 21.53 | | |
| PDF J1040+0045 | 10 40 10.5 | +00 45 50 | | | | 0.64 | 60.0 | 11.81 | | | | | |
| PDF J1040-0107 | 10 40 40.2 | -01 07 09 | | | | 0.26 | 24.0 | 12.28 | | | | | |
| PDF J1040+0129 | 10 40 50.1 | +01 29 08 | | | | 0.49 | 35.0 | 10.46 | | | | | |
| PDF J1040+0056 | 10 40 50.1 | +00 56 33 | 0.28 | 29.0 | 14.04 | 0.28 | 23.0 | 13.62 | 0.28 | 35.0 | 17.17 | | |
| PDF J1040+0153 | 10 40 55.0 | +01 53 03 | 0.39 | 43.0 | 12.17 | 0.36 | 33.0 | 19.02 | | | | | |
| PDF J1041-0044 | 10 41 05.0 | -00 44 04 | 0.12 | 38.0 | 41.13 | 0.12 | 33.0 | 36.41 | 0.10 | 34.0 | 37.98 | | |
| PDF J1041-0103 | 10 41 05.0 | -01 03 27 | 0.22 | 43.0 | 34.57 | 0.26 | 33.0 | 25.44 | 0.21 | 36.0 | 26.58 | | |
| PDF J1041+0127 | 10 41 16.5 | +01 27 04 | | | | 0.36 | 30.0 | 17.18 | 0.37 | 47.0 | 14.69 | | |
| PDF J1041-0226 | 10 41 18.2 | -02 26 20 | 0.10 | 22.0 | 17.99 | 0.10 | 23.0 | 20.20 | 0.09 | 20.0 | 17.78 | | |
| PDF J1041+0116 | 10 41 23.1 | +01 16 46 | | | | 0.62 | 58.0 | 12.19 | | | | | |
| PDF J1041+0209 | 10 41 24.7 | +02 09 08 | | | | 0.60 | 60.0 | 12.37 | | | | | |
| PDF J1041-0102 | 10 41 31.4 | -01 02 12 | 0.25 | 40.0 | 19.02 | | | | | | | | |
| PDF J1041+0128 | 10 41 39.5 | +01 28 18 | 0.40 | 84.0 | 30.38 | 0.40 | 62.0 | 44.32 | | | | | |
| PDF J1041+0110 | 10 41 39.6 | +01 10 10 | 0.10 | 26.0 | 19.84 | | | | 0.09 | 20.0 | 16.90 | | |
| PDF J1041-0237 | 10 41 44.6 | -02 37 53 | 0.21 | 66.0 | 78.63 | 0.21 | 64.0 | 91.16 | 0.28 | 82.0 | 63.28 | | |
| PDF J1041+0211 | 10 41 46.1 | +02 11 12 | | | | 0.54 | 50.0 | 14.26 | | | | | |
| PDF J1041+0103 | 10 41 46.2 | +01 03 34 | | | | 0.35 | 27.0 | 13.11 | | | | | |
| PDF J1041+0132 | 10 41 49.4 | +01 32 01 | | | | | | | 0.44 | 150.0 | 48.03 | | |
| PDF J1041-0037 | 10 41 49.5 | -00 37 03 | 0.14 | 26.0 | 24.24 | 0.14 | 24.0 | 21.62 | | | | | |
| PDF J1041+0036 | 10 41 57.7 | +00 36 45 | 0.60 | 170.0 | 10.88 | 0.63 | 76.0 | 17.22 | | | | | |
| PDF J1042-0201 | 10 42 06.0 | -02 01 35 | | | | 0.47 | 33.0 | 13.21 | | | | | |
| PDF J1042-0140 | 10 42 09.3 | -01 40 34 | | | | 0.42 | 39.0 | 12.69 | | | | | |
| PDF J1042-0008 | 10 42 12.6 | -00 08 11 | 0.13 | 29.0 | 28.32 | 0.16 | 30.0 | 26.87 | 0.16 | 36.0 | 31.81 | 0.14 ^c | RX J1042.3-0008 |
| PDF J1042+0120 | 10 42 15.8 | +01 20 04 | | | | 0.60 | 54.0 | 12.38 | | | | | |
| PDF J1042+0105 | 10 42 17.5 | +01 05 37 | 0.30 | 27.0 | 13.02 | | | | | | | | |
| PDF J1042-0057 | 10 42 29.1 | -00 57 15 | 0.23 | 24.0 | 15.71 | 0.33 | 34.0 | 23.96 | 0.30 | 34.0 | 14.85 | | |
| PDF J1042-0047 | 10 42 34.0 | -00 47 22 | 0.44 | 54.0 | 10.53 | 0.36 | 24.0 | 11.47 | 0.36 | 38.0 | 11.02 | | |
| PDF J1042+0144 | 10 42 35.6 | +01 44 48 | | | | 0.50 | 54.0 | 15.68 | | | | | |
| PDF J1042+0124 | 10 42 35.6 | +01 24 11 | | | | 0.38 | 38.0 | 16.77 | | | | | |
| PDF J1042+0207 | 10 42 37.3 | +02 07 54 | | | | 0.49 | 42.0 | 12.64 | | | | | |
| PDF J1042+0030 | 10 42 40.6 | +00 30 34 | | | | 0.64 | 82.0 | 17.76 | 0.60 | 110.0 | 12.38 | | |

Table B.11: Cluster Candidate Catalogue

| Cluster | RA (J2000) | Declination (J2000) | B_J AMF | | | R AMF | | | I AMF | | | NED z | Previous ID |
|----------------|---------------|------------------------|-----------|-----------|---------------|---------|-----------|---------------|---------|-----------|---------------|-------------------|--------------------|
| | | | z | Λ | \mathcal{L} | z | Λ | \mathcal{L} | z | Λ | \mathcal{L} | | |
| PDF J1042-0152 | 10 42 45.6 | -01 52 06 | 0.11 | 21.0 | 22.21 | | | | | | | | |
| PDF J1042-0143 | 10 42 47.3 | -01 43 02 | | | | 0.18 | 21.0 | 14.96 | | | | | |
| PDF J1042+0023 | 10 42 57.1 | +00 23 58 | | | | 0.32 | 31.0 | 18.08 | 0.30 | 32.0 | 14.55 | | |
| PDF J1042+0025 | 10 42 58.7 | +00 25 37 | 0.45 | 120.0 | 25.53 | | | | | | | | |
| PDF J1043+0125 | 10 43 00.4 | +01 25 00 | | | | 0.60 | 58.0 | 13.14 | | | | | |
| PDF J1043-0039 | 10 43 00.4 | -00 39 56 | 0.25 | 24.0 | 12.45 | | | | 0.23 | 24.0 | 12.68 | | |
| PDF J1043+0115 | 10 43 11.9 | +01 15 56 | | | | 0.56 | 44.0 | 10.25 | | | | | |
| PDF J1043+0050 | 10 43 15.2 | +00 50 47 | 0.14 | 34.0 | 44.18 | 0.15 | 30.0 | 39.40 | 0.13 | 35.0 | 45.26 | | |
| PDF J1043-0234 | 10 43 18.6 | -02 34 10 | | | | 0.29 | 29.0 | 11.74 | | | | | |
| PDF J1043+0018 | 10 43 21.8 | +00 18 37 | 0.48 | 78.0 | 12.37 | 0.52 | 39.0 | 10.38 | | | | | |
| PDF J1043-0011 | 10 43 21.8 | -00 11 04 | 0.20 | 25.0 | 11.13 | | | | | | | | |
| PDF J1043+0006 | 10 43 28.4 | +00 06 14 | 0.20 | 34.0 | 26.56 | 0.16 | 24.0 | 22.05 | 0.14 | 31.0 | 25.56 | | |
| PDF J1043-0007 | 10 43 33.4 | -00 07 46 | | | | 0.30 | 22.0 | 13.50 | | | | | |
| PDF J1043+0016 | 10 43 40.0 | +00 16 58 | | | | | | | 0.09 | 22.0 | 18.41 | | |
| PDF J1043-0239 | 10 43 43.4 | -02 39 57 | | | | 0.59 | 54.0 | 11.43 | | | | | |
| PDF J1043-0016 | 10 43 44.9 | -00 16 01 | | | | 0.39 | 26.0 | 10.50 | | | | | |
| PDF J1043-0209 | 10 43 46.7 | -02 09 01 | | | | 0.31 | 24.0 | 10.85 | | | | | |
| PDF J1043-0056 | 10 43 48.3 | -00 56 26 | 0.24 | 35.0 | 24.73 | 0.24 | 30.0 | 26.94 | 0.20 | 27.0 | 20.48 | | |
| PDF J1043+0058 | 10 43 53.1 | +00 58 12 | 0.09 | 38.0 | 40.22 | 0.10 | 33.0 | 34.90 | | | | | |
| PDF J1043+0107 | 10 43 54.8 | +01 07 16 | | | | | | | 0.10 | 28.0 | 22.47 | | ABELL 1080 |
| PDF J1043+0034 | 10 43 58.1 | +00 34 17 | | | | 0.44 | 43.0 | 14.23 | | | | | |
| PDF J1043-0213 | 10 43 58.2 | -02 13 33 | | | | 0.59 | 48.0 | 10.79 | | | | | |
| PDF J1044+0053 | 10 44 06.3 | +00 53 15 | | | | | | | 0.09 | 35.0 | 31.34 | | |
| PDF J1044-0039 | 10 44 06.4 | -00 39 31 | | | | 0.33 | 29.0 | 18.60 | 0.32 | 37.0 | 15.89 | | |
| PDF J1044+0027 | 10 44 09.6 | +00 27 16 | | | | 0.43 | 36.0 | 12.02 | | | | | |
| PDF J1044-0012 | 10 44 09.7 | -00 12 18 | 0.15 | 21.0 | 13.46 | | | | | | | | |
| PDF J1044+0010 | 10 44 12.9 | +00 10 46 | 0.30 | 33.0 | 10.28 | 0.30 | 28.0 | 12.28 | | | | | |
| PDF J1044-0238 | 10 44 13.1 | -02 38 42 | | | | 0.30 | 27.0 | 16.86 | | | | | |
| PDF J1044+0005 | 10 44 21.2 | +00 05 25 | | | | 0.52 | 42.0 | 10.91 | | | | | |
| PDF J1044-0003 | 10 44 32.7 | -00 03 14 | | | | 0.43 | 84.0 | 56.88 | | | | | [LP96] C11042+0013 |
| PDF J1044-0048 | 10 44 37.7 | -00 48 36 | 0.26 | 24.0 | 12.68 | 0.33 | 21.0 | 10.52 | | | | | |
| PDF J1044-0015 | 10 44 45.9 | -00 15 11 | 0.23 | 37.0 | 27.39 | 0.12 | 20.0 | 18.50 | 0.13 | 26.0 | 23.32 | | J1834.03TC |
| PDF J1044-0150 | 10 44 46.0 | -01 50 03 | 0.32 | 30.0 | 10.28 | | | | | | | | |
| PDF J1044-0000 | 10 44 49.2 | -00 00 45 | 0.30 | 58.0 | 34.08 | | | | 0.21 | 40.0 | 27.61 | 0.38 ^c | F1835.02CL |
| PDF J1044-0104 | 10 44 57.5 | -01 04 16 | 0.38 | 43.0 | 11.82 | | | | 0.33 | 36.0 | 11.71 | | |

Table B.12: Cluster Candidate Catalogue

| Cluster | RA (J2000) | Declination (J2000) | B_J AMF | | | R AMF | | | I AMF | | | NED z | Previous ID |
|----------------|---------------|------------------------|-----------|-----------|---------------|---------|-----------|---------------|---------|-----------|---------------|-------------------|----------------------------------|
| | | | z | Λ | \mathcal{L} | z | Λ | \mathcal{L} | z | Λ | \mathcal{L} | | |
| PDF J1044-0001 | 10 44 59.1 | -00 01 35 | | | | 0.26 | 44.0 | 29.27 | | | | | |
| PDF J1045-0006 | 10 45 05.7 | -00 06 57 | 0.32 | 43.0 | 19.61 | | | | | | | | [LP96] Cl1043+0009 J1834.05BC |
| PDF J1045-0029 | 10 45 12.3 | -00 29 37 | | | | 0.40 | 52.0 | 28.43 | | | | | |
| PDF J1045-0106 | 10 45 17.3 | -01 06 20 | 0.31 | 31.0 | 11.95 | 0.31 | 28.0 | 16.97 | | | | | |
| PDF J1045+0005 | 10 45 22.2 | +00 05 49 | 0.42 | 52.0 | 10.63 | | | | | | | | |
| PDF J1045-0023 | 10 45 22.2 | -00 23 02 | 0.24 | 39.0 | 27.96 | | | | | | | | |
| PDF J1045-0216 | 10 45 27.3 | -02 16 01 | | | | | | | 0.19 | 22.0 | 10.51 | | |
| PDF J1045-0015 | 10 45 28.8 | -00 15 11 | 0.26 | 26.0 | 13.77 | | | | | | | 0.04 ^g | |
| PDF J1045-0228 | 10 45 29.0 | -02 28 24 | | | | 0.28 | 22.0 | 12.78 | | | | | |
| PDF J1045-0235 | 10 45 30.7 | -02 35 49 | | | | 0.29 | 26.0 | 14.56 | | | | | |
| PDF J1045-0023 | 10 45 33.8 | -00 23 02 | | | | 0.13 | 26.0 | 20.18 | 0.15 | 31.0 | 22.85 | | |
| PDF J1045-0112 | 10 45 33.8 | -01 12 31 | | | | 0.26 | 20.0 | 11.03 | | | | | |
| PDF J1045+0121 | 10 45 35.4 | +01 21 42 | 0.56 | 140.0 | 12.93 | 0.60 | 80.0 | 21.89 | | | | | |
| PDF J1045+0128 | 10 45 35.4 | +01 28 18 | | | | 0.45 | 29.0 | 10.18 | | | | | |
| PDF J1045-0040 | 10 45 35.4 | -00 40 46 | 0.25 | 41.0 | 21.77 | | | | | | | | |
| PDF J1045-0121 | 10 45 35.5 | -01 21 10 | 0.28 | 27.0 | 12.35 | | | | | | | | |
| PDF J1045-0212 | 10 45 37.2 | -02 12 43 | 0.19 | 21.0 | 13.94 | | | | | | | | |
| PDF J1045-0136 | 10 45 40.4 | -01 36 51 | 0.50 | 86.0 | 12.33 | | | | | | | | |
| PDF J1045+0138 | 10 45 42.0 | +01 38 37 | | | | 0.42 | 31.0 | 10.07 | | | | | |
| PDF J1045-0109 | 10 45 42.1 | -01 09 38 | 0.47 | 66.0 | 11.46 | | | | | | | | |
| PDF J1045-0030 | 10 45 45.3 | -00 30 27 | 0.42 | 54.0 | 11.63 | | | | | | | | |
| PDF J1045+0202 | 10 45 47.0 | +02 02 57 | | | | 0.61 | 86.0 | 22.08 | | | | | |
| PDF J1045-0033 | 10 45 51.9 | -00 33 45 | | | | 0.59 | 54.0 | 10.46 | | | | | |
| PDF J1045-0045 | 10 45 58.5 | -00 45 18 | | | | | | | 0.70 | 220.0 | 11.84 | | |
| PDF J1046+0044 | 10 46 00.1 | +00 44 11 | | | | 0.60 | 72.0 | 12.28 | | | | | |
| PDF J1046-0145 | 10 46 05.2 | -01 45 55 | 0.43 | 68.0 | 11.69 | | | | | | | | |
| PDF J1046-0143 | 10 46 08.5 | -01 43 51 | | | | 0.30 | 36.0 | 19.26 | | | | | |
| PDF J1046-0017 | 10 46 10.0 | -00 17 40 | 0.62 | 260.0 | 16.59 | | | | | | | | [LP96] Cl1044-0004 ABELL 1092 |
| PDF J1046+0122 | 10 46 18.3 | +01 22 07 | 0.36 | 50.0 | 13.91 | 0.36 | 37.0 | 15.00 | | | | | |
| PDF J1046-0036 | 10 46 21.6 | -00 36 13 | 0.24 | 33.0 | 18.02 | | | | | | | | |
| PDF J1046+0041 | 10 46 23.2 | +00 41 17 | | | | 0.66 | 70.0 | 12.98 | | | | | |
| PDF J1046-0156 | 10 46 23.4 | -01 56 38 | 0.18 | 22.0 | 11.84 | 0.18 | 31.0 | 21.88 | | | | | |
| PDF J1046-0103 | 10 46 26.6 | -01 03 02 | 0.31 | 33.0 | 15.82 | 0.40 | 38.0 | 18.34 | 0.27 | 25.0 | 11.82 | | |
| PDF J1046-0119 | 10 46 26.6 | -01 19 56 | 0.59 | 170.0 | 11.74 | | | | | | | | |
| PDF J1046+0112 | 10 46 28.2 | +01 12 38 | | | | 0.47 | 36.0 | 11.45 | | | | | |

Table B.13: Cluster Candidate Catalogue

| Cluster | RA (J2000) | Declination (J2000) | B_J AMF | | | R AMF | | | I AMF | | | NED z | Previous ID |
|----------------|---------------|------------------------|-----------|-----------|---------------|---------|-----------|---------------|---------|-----------|---------------|-------------------|-------------|
| | | | z | Λ | \mathcal{L} | z | Λ | \mathcal{L} | z | Λ | \mathcal{L} | | |
| PDF J1046+0210 | 10 46 28.2 | +02 10 22 | | | | 0.63 | 105.0 | 29.58 | | | | | |
| PDF J1046-0004 | 10 46 31.5 | -00 04 03 | 0.38 | 44.0 | 10.94 | | | | | | | | |
| PDF J1046-0055 | 10 46 33.2 | -00 55 11 | 0.43 | 74.0 | 13.27 | | | | | | | | |
| PDF J1046-0116 | 10 46 33.2 | -01 16 38 | | | | | | | 0.55 | 94.0 | 11.66 | | |
| PDF J1046-0056 | 10 46 34.8 | -00 56 26 | | | | 0.54 | 42.0 | 10.15 | | | | | |
| PDF J1046-0000 | 10 46 36.4 | -00 00 45 | | | | 0.37 | 28.0 | 10.98 | | | | | |
| PDF J1046+0042 | 10 46 38.0 | +00 42 56 | 0.67 | 350.0 | 11.64 | | | | | | | | |
| PDF J1046+0127 | 10 46 38.1 | +01 27 29 | 0.17 | 40.0 | 43.85 | 0.17 | 38.0 | 48.76 | 0.11 | 35.0 | 44.86 | | |
| PDF J1046+0020 | 10 46 39.7 | +00 20 40 | 0.56 | 135.0 | 12.54 | | | | | | | | |
| PDF J1046-0204 | 10 46 39.9 | -02 04 28 | | | | 0.55 | 39.0 | 10.50 | | | | | |
| PDF J1046-0128 | 10 46 41.5 | -01 28 11 | 0.19 | 21.0 | 10.79 | | | | | | | | |
| PDF J1046+0035 | 10 46 44.6 | +00 35 31 | | | | 0.67 | 78.0 | 11.76 | | | | | |
| PDF J1046-0019 | 10 46 44.7 | -00 19 44 | | | | 0.35 | 32.0 | 18.22 | 0.30 | 29.0 | 11.08 | | |
| PDF J1046+0110 | 10 46 49.6 | +01 10 09 | | | | | | | 0.28 | 27.0 | 10.14 | | |
| PDF J1046-0155 | 10 46 49.8 | -01 55 24 | 0.38 | 47.0 | 14.60 | 0.38 | 35.0 | 19.67 | 0.38 | 42.0 | 11.92 | | |
| PDF J1046-0041 | 10 46 52.9 | -00 41 10 | 0.24 | 26.0 | 13.82 | | | | | | | | |
| PDF J1046-0214 | 10 46 53.1 | -02 14 47 | | | | 0.34 | 31.0 | 12.41 | | | | | |
| PDF J1046-0021 | 10 46 54.6 | -00 21 23 | 0.28 | 35.0 | 18.55 | | | | | | | | |
| PDF J1046-0025 | 10 46 54.6 | -00 25 30 | | | | 0.45 | 36.0 | 11.09 | | | | 0.47 ^c | F1835.22CR |
| PDF J1047-0054 | 10 47 01.2 | -00 54 47 | | | | 0.64 | 92.0 | 12.73 | | | | | |
| PDF J1047-0200 | 10 47 03.0 | -02 00 45 | 0.35 | 43.0 | 15.83 | 0.44 | 49.0 | 23.47 | 0.44 | 54.0 | 10.29 | | |
| PDF J1047+0002 | 10 47 04.4 | +00 02 32 | 0.22 | 42.0 | 26.01 | | | | | | | | |
| PDF J1047-0115 | 10 47 04.5 | -01 15 24 | 0.39 | 54.0 | 13.94 | | | | | | | | |
| PDF J1047-0117 | 10 47 11.1 | -01 17 27 | | | | 0.64 | 125.0 | 36.79 | | | | | |
| PDF J1047+0001 | 10 47 12.7 | +00 01 17 | | | | 0.23 | 24.0 | 16.86 | | | | | |
| PDF J1047-0008 | 10 47 12.7 | -00 08 35 | | | | 0.39 | 25.0 | 10.33 | | | | | |
| PDF J1047-0028 | 10 47 16.0 | -00 28 48 | | | | 0.39 | 29.0 | 11.73 | | | | 0.08 ^g | |
| PDF J1047+0206 | 10 47 17.7 | +02 06 15 | 0.47 | 72.0 | 12.33 | 0.59 | 88.0 | 25.77 | 0.59 | 105.0 | 10.28 | | |
| PDF J1047-0131 | 10 47 17.8 | -01 31 04 | 0.32 | 42.0 | 17.39 | 0.33 | 30.0 | 15.48 | | | | | |
| PDF J1047-0124 | 10 47 19.4 | -01 24 03 | 0.25 | 35.0 | 14.53 | 0.27 | 33.0 | 15.11 | | | | | |
| PDF J1047-0104 | 10 47 24.3 | -01 04 40 | 0.47 | 80.0 | 14.65 | 0.53 | 90.0 | 42.71 | | | | | |
| PDF J1047-0219 | 10 47 37.7 | -02 19 43 | 0.17 | 23.0 | 16.77 | | | | | | | | |
| PDF J1047-0223 | 10 47 37.7 | -02 23 01 | | | | 0.18 | 28.0 | 21.10 | 0.14 | 20.0 | 13.17 | | |
| PDF J1047-0003 | 10 47 39.1 | -00 03 39 | 0.57 | 150.0 | 11.63 | | | | | | | | |
| PDF J1047-0023 | 10 47 39.1 | -00 23 51 | 0.41 | 46.0 | 11.15 | 0.41 | 33.0 | 13.67 | | | | 0.35 ^c | F1835.28BR |

Table B.14: Cluster Candidate Catalogue

| Cluster | RA (J2000) | Declination (J2000) | B_J AMF | | | R AMF | | | I AMF | | | NED z | Previous ID |
|----------------|---------------|------------------------|-----------|-----------|---------------|---------|-----------|---------------|---------|-----------|---------------|------------|-------------|
| | | | z | Λ | \mathcal{L} | z | Λ | \mathcal{L} | z | Λ | \mathcal{L} | | |
| PDF J1047-0158 | 10 47 40.9 | -01 58 17 | | | | 0.41 | 30.0 | 11.05 | | | | | |
| PDF J1047-0015 | 10 47 45.7 | -00 15 36 | | | | 0.51 | 49.0 | 16.17 | | | | | |
| PDF J1047-0129 | 10 47 50.7 | -01 29 25 | | | | 0.39 | 31.0 | 10.81 | | | | | |
| PDF J1047-0242 | 10 47 50.9 | -02 42 24 | 0.15 | 23.0 | 14.73 | 0.21 | 27.0 | 18.54 | | | | | |
| PDF J1047-0055 | 10 47 57.3 | -00 55 11 | | | | 0.59 | 60.0 | 14.60 | | | | | |
| PDF J1048-0140 | 10 48 00.7 | -01 40 33 | 0.27 | 32.0 | 17.81 | 0.30 | 33.0 | 20.89 | | | | | |
| PDF J1048+0049 | 10 48 10.4 | +00 49 08 | | | | 0.33 | 28.0 | 14.49 | | | | | |
| PDF J1048-0231 | 10 48 10.7 | -02 31 16 | 0.11 | 21.0 | 11.02 | | | | | | | | |
| PDF J1048+0007 | 10 48 13.7 | +00 07 53 | | | | 0.61 | 58.0 | 11.38 | | | | | |
| PDF J1048+0033 | 10 48 15.3 | +00 33 03 | | | | 0.46 | 39.0 | 14.36 | | | | | |
| PDF J1048-0019 | 10 48 20.3 | -00 19 19 | | | | 0.61 | 62.0 | 14.73 | | | | | |
| PDF J1048+0003 | 10 48 21.9 | +00 03 21 | | | | 0.56 | 45.0 | 10.01 | | | | | |
| PDF J1048-0130 | 10 48 22.1 | -01 30 14 | 0.24 | 27.0 | 15.57 | 0.29 | 22.0 | 14.39 | 0.24 | 22.0 | 11.46 | | |
| PDF J1048-0059 | 10 48 23.7 | -00 59 43 | | | | 0.43 | 34.0 | 13.11 | | | | | |
| PDF J1048-0101 | 10 48 25.3 | -01 01 22 | 0.50 | 80.0 | 11.04 | | | | | | | | |
| PDF J1048+0108 | 10 48 31.8 | +01 08 06 | 0.22 | 25.0 | 15.04 | 0.21 | 20.0 | 15.25 | 0.21 | 25.0 | 16.90 | | |
| PDF J1048+0013 | 10 48 33.5 | +00 13 40 | 0.44 | 80.0 | 16.49 | 0.45 | 50.0 | 19.50 | 0.44 | 58.0 | 11.62 | | |
| PDF J1048-0239 | 10 48 42.1 | -02 39 06 | 0.19 | 37.0 | 30.01 | 0.16 | 40.0 | 36.24 | 0.19 | 31.0 | 21.50 | | |
| PDF J1049+0021 | 10 49 04.8 | +00 21 30 | | | | 0.44 | 46.0 | 14.58 | | | | | |
| PDF J1049-0036 | 10 49 11.5 | -00 36 38 | | | | 0.51 | 48.0 | 12.88 | | | | | |
| PDF J1049-0115 | 10 49 11.5 | -01 15 23 | | | | 0.33 | 46.0 | 25.27 | | | | | |
| PDF J1049-0219 | 10 49 13.4 | -02 19 18 | | | | 0.55 | 50.0 | 13.37 | | | | | |
| PDF J1049-0008 | 10 49 18.0 | -00 08 35 | 0.15 | 20.0 | 11.12 | | | | 0.15 | 20.0 | 12.31 | | |
| PDF J1049-0117 | 10 49 18.1 | -01 17 52 | 0.23 | 26.0 | 17.10 | | | | 0.26 | 29.0 | 15.30 | | |
| PDF J1049+0002 | 10 49 19.7 | +00 02 07 | | | | 0.60 | 64.0 | 14.08 | | | | | |
| PDF J1049-0004 | 10 49 24.6 | -00 04 03 | | | | 0.64 | 98.0 | 24.07 | | | | | |
| PDF J1049-0114 | 10 49 33.0 | -01 14 34 | | | | 0.55 | 90.0 | 31.09 | | | | | |
| PDF J1049-0110 | 10 49 36.3 | -01 10 02 | 0.65 | 270.0 | 11.94 | | | | | | | | |
| PDF J1049+0008 | 10 49 37.8 | +00 08 18 | | | | 0.60 | 80.0 | 22.70 | | | | | |
| PDF J1049-0013 | 10 49 37.8 | -00 13 07 | | | | 0.68 | 92.0 | 18.20 | | | | | |
| PDF J1049-0032 | 10 49 41.1 | -00 32 05 | | | | 0.49 | 48.0 | 16.28 | | | | | |
| PDF J1049-0216 | 10 49 57.9 | -02 16 25 | 0.27 | 34.0 | 17.59 | 0.44 | 76.0 | 33.08 | 0.38 | 54.0 | 13.65 | | |
| PDF J1049-0226 | 10 49 59.6 | -02 26 43 | | | | 0.35 | 32.0 | 15.09 | | | | | |
| PDF J1050+0141 | 10 50 02.6 | +01 41 05 | | | | 0.67 | 86.0 | 14.36 | | | | | |
| PDF J1050-0115 | 10 50 02.7 | -01 15 23 | | | | 0.57 | 96.0 | 43.14 | | | | | |

Table B.15: Cluster Candidate Catalogue

| Cluster | RA (J2000) | Declination (J2000) | B_J AMF | | | z | R AMF | | | z | I AMF | | | NED z | Previous ID |
|----------------|---------------|------------------------|-----------|-----------|---------------|-----|---------|-----------|---------------|-----|---------|-----------|---------------|-------------------|-------------|
| | | | z | Λ | \mathcal{L} | | z | Λ | \mathcal{L} | | z | Λ | \mathcal{L} | | |
| PDF J1050-0107 | 10 50 04.3 | -01 07 58 | | | | | 0.60 | 72.0 | 11.47 | | | | | | |
| PDF J1050+0120 | 10 50 07.5 | +01 20 28 | | | | | | | | | 0.53 | 68.0 | 10.33 | | |
| PDF J1050-0140 | 10 50 12.6 | -01 40 07 | | | | | 0.30 | 29.0 | 18.48 | | 0.45 | 68.0 | 11.90 | | |
| PDF J1050-0206 | 10 50 12.7 | -02 06 06 | | | | | 0.34 | 43.0 | 24.65 | | | | | | |
| PDF J1050+0123 | 10 50 22.4 | +01 23 46 | | | | | 0.67 | 100.0 | 21.41 | | | | | | |
| PDF J1050-0154 | 10 50 24.2 | -01 54 08 | 0.38 | 46.0 | 14.78 | | | | | | | | | | |
| PDF J1050-0207 | 10 50 25.9 | -02 07 20 | 0.31 | 36.0 | 15.73 | | | | | | | | | | |
| PDF J1050-0153 | 10 50 34.1 | -01 53 44 | | | | | 0.33 | 48.0 | 35.35 | | 0.39 | 56.0 | 16.55 | | |
| PDF J1050-0202 | 10 50 35.8 | -02 02 23 | | | | | 0.29 | 21.0 | 10.93 | | | | | | |
| PDF J1050+0015 | 10 50 37.2 | +00 15 43 | | | | | 0.64 | 130.0 | 38.76 | | | | | | |
| PDF J1050-0137 | 10 50 37.4 | -01 37 14 | 0.33 | 36.0 | 13.50 | | | | | | | | | | |
| PDF J1050-0235 | 10 50 37.6 | -02 35 22 | 0.20 | 32.0 | 33.28 | | 0.21 | 30.0 | 36.96 | | 0.29 | 38.0 | 23.82 | 0.17 ^c | ABELL 1111 |
| PDF J1050-0144 | 10 50 39.0 | -01 44 39 | | | | | 0.43 | 49.0 | 17.50 | | 0.43 | 64.0 | 10.97 | | |
| PDF J1050-0020 | 10 50 52.0 | -00 20 08 | | | | | 0.59 | 52.0 | 11.74 | | | | | | |
| PDF J1050-0030 | 10 50 55.3 | -00 30 26 | | | | | 0.48 | 33.0 | 10.19 | | | | | | |
| PDF J1050-0112 | 10 50 55.4 | -01 12 54 | | | | | 0.18 | 20.0 | 11.74 | | | | | | |
| PDF J1051-0148 | 10 51 00.5 | -01 48 47 | | | | | 0.28 | 20.0 | 10.29 | | | | | | |
| PDF J1051-0157 | 10 51 18.7 | -01 57 51 | 0.29 | 26.0 | 11.32 | | | | | | | | | | |
| PDF J1051+0010 | 10 51 26.6 | +00 10 22 | | | | | 0.63 | 76.0 | 17.01 | | | | | | |
| PDF J1051-0152 | 10 51 40.1 | -01 52 54 | | | | | 0.31 | 26.0 | 13.12 | | | | | | |
| PDF J1051-0129 | 10 51 43.3 | -01 29 24 | | | | | 0.49 | 39.0 | 12.55 | | | | | | |
| PDF J1051+0004 | 10 51 49.7 | +00 04 36 | 0.17 | 26.0 | 14.98 | | | | | | | | | | |
| PDF J1051-0155 | 10 51 50.0 | -01 55 22 | 0.21 | 23.0 | 10.73 | | | | | | | | | | |
| PDF J1051+0032 | 10 51 59.6 | +00 32 38 | | | | | 0.62 | 68.0 | 10.15 | | | | | | |
| PDF J1052-0202 | 10 52 06.5 | -02 02 47 | | | | | 0.49 | 52.0 | 19.75 | | | | | | |
| PDF J1052-0118 | 10 52 08.0 | -01 18 40 | 0.33 | 50.0 | 22.15 | | 0.33 | 39.0 | 26.02 | | 0.14 | 28.0 | 19.50 | | |
| PDF J1052-0138 | 10 52 16.3 | -01 38 52 | | | | | 0.46 | 37.0 | 14.50 | | | | | | |
| PDF J1052-0113 | 10 52 19.5 | -01 13 19 | 0.23 | 45.0 | 31.11 | | 0.23 | 41.0 | 31.67 | | | | | | |
| PDF J1052+0033 | 10 52 24.3 | +00 33 52 | | | | | 0.73 | 84.0 | 10.64 | | | | | | |

Appendix C

Radio Galaxies

The tables in this appendix provide a full list of the radio galaxies identified in Chapter 7. NVSS source names, optical position, multicolour photometry, photometric redshift and the offset between the radio and optical positions are provided. Objects with photometric redshifts $z > 0.55$ and multiple matches to NVSS sources are listed in the tables but were not used for the estimates of radio galaxy evolution or environments in Chapter 7.

Table C.1: Radio Galaxy Catalogue

| NVSS Source | RA (J2000) | Declination (J2000) | $S_{1.4\text{mJy}}$ | B_J | $U - B_J$ | $B_J - R$ | $R - I$ | z | Optical-Radio Offset |
|---------------------|---------------|------------------------|---------------------|-------|-----------|-----------|---------|-------|-------------------------|
| NVSS J004407-294749 | 00 44 07.8 | -29 47 49.6 | 95.7 | 23.17 | - | 2.34 | - | 0.584 | 1.8'' |
| NVSS J004432-285648 | 00 44 32.9 | -28 56 48.7 | 8.3 | 22.33 | - | 2.28 | 1.26 | 0.528 | 1.7'' |
| NVSS J004443-300604 | 00 44 43.6 | -30 06 04.5 | 5.6 | 21.93 | - | 2.29 | 1.02 | 0.477 | 1.6'' |
| NVSS J004514-292851 | 00 45 14.5 | -29 28 51.3 | 16.0 | 22.08 | - | 2.60 | 0.75 | 0.507 | 2.6'' |
| NVSS J004607-282258 | 00 46 07.7 | -28 22 58.9 | 5.7 | 21.64 | - | 2.09 | 0.76 | 0.420 | 2.6'' |
| NVSS J004633-290140 | 00 46 33.9 | -29 01 40.3 | 7.2 | 18.69 | 0.97 | 1.77 | 0.84 | 0.196 | 3.3'' |
| NVSS J004637-295330 | 00 46 37.7 | -29 53 30.9 | 37.2 | 20.48 | 0.66 | 1.61 | 0.88 | 0.289 | 7.1'' |
| NVSS J004649-300728 | 00 46 49.5 | -30 07 28.8 | 29.2 | 22.76 | - | 2.03 | - | 0.492 | 1.9'' |
| NVSS J004702-271742 | 00 47 02.8 | -27 17 42.7 | 7.7 | 21.88 | - | 2.69 | 0.84 | 0.505 | 3.1'' |
| NVSS J004722-273110 | 00 47 23.0 | -27 31 10.7 | 17.4 | 22.08 | - | 2.77 | 1.11 | 0.549 | 0.9'' |
| NVSS J004724-292200 | 00 47 24.9 | -29 22 00.4 | 8.1 | 22.81 | - | 2.78 | 1.24 | 0.628 | 5.1'' |
| NVSS J004752-284404 | 00 47 52.1 | -28 44 04.3 | 39.8 | 23.06 | - | 2.07 | - | 0.544 | 1.0'' |
| NVSS J004808-281052 | 00 48 08.5 | -28 10 52.2 | 14.3 | 22.62 | - | 2.76 | 1.48 | 0.627 | 2.8'' |
| NVSS J004827-290603 | 00 48 27.3 | -29 06 03.5 | 15.5 | 18.83 | 0.96 | 1.76 | - | 0.200 | 5.8'' |
| NVSS J004831-294209 | 00 48 31.4 | -29 42 09.6 | 7.7 | 22.39 | - | 2.04 | 1.92 | 0.556 | 2.7'' |
| NVSS J004836-272942 | 00 48 36.2 | -27 29 42.9 | 6.9 | 20.53 | 1.32 | 2.20 | 1.14 | 0.361 | 5.2'' |
| NVSS J004925-300237 | 00 49 25.6 | -30 02 37.6 | 8.4 | 19.67 | 0.31 | 1.43 | 1.07 | 0.223 | 1.1'' |
| NVSS J004940-274236 | 00 49 40.3 | -27 42 36.8 | 9.4 | 22.42 | - | 2.23 | 1.44 | 0.543 | 5.4'' |
| NVSS J004954-282535 | 00 49 54.8 | -28 25 36.0 | 8.9 | 21.03 | - | 2.48 | 0.86 | 0.415 | 1.9'' |
| NVSS J005049-280410 | 00 50 49.3 | -28 04 10.5 | 33.8 | 21.82 | - | 2.40 | 0.14 | 0.442 | 0.8'' |
| NVSS J005106-262601 | 00 51 06.6 | -26 26 01.5 | 5.0 | 22.22 | - | 2.12 | 0.51 | 0.461 | 4.8'' |
| NVSS J005115-283132 | 00 51 15.6 | -28 31 32.7 | 53.8 | 17.38 | 0.74 | 1.43 | 0.74 | 0.101 | 14.0'' |
| NVSS J005116-272046 | 00 51 16.4 | -27 20 46.6 | 12.9 | 21.24 | - | 2.19 | 0.74 | 0.398 | 3.3'' |
| NVSS J005127-282923 | 00 51 27.5 | -28 29 23.6 | 77.8 | 18.08 | 0.74 | 1.41 | 0.84 | 0.125 | 2.8'' |
| NVSS J005128-282927 | 00 51 28.0 | -28 29 27.1 | 77.8 | 17.64 | 0.58 | 1.47 | 0.97 | 0.103 | 10.4'' |
| NVSS J005132-282451 | 00 51 32.5 | -28 24 51.8 | 92.1 | 17.44 | 0.74 | 1.47 | 0.79 | 0.102 | 9.1'' |
| NVSS J005209-263055 | 00 52 09.6 | -26 30 55.6 | 10.1 | 22.21 | - | 2.22 | 0.31 | 0.462 | 2.4'' |
| NVSS J005216-253042 | 00 52 16.2 | -25 30 43.0 | 11.0 | 21.69 | - | 2.63 | 0.69 | 0.476 | 2.8'' |
| NVSS J005223-284110 | 00 52 23.9 | -28 41 10.3 | 7.8 | 23.50 | - | 2.53 | 1.37 | 0.683 | 3.4'' |
| NVSS J005241-284123 | 00 52 41.6 | -28 41 23.2 | 6.6 | 20.58 | - | 2.21 | 0.73 | 0.350 | 6.3'' |
| NVSS J005302-254756 | 00 53 02.4 | -25 47 56.2 | 22.0 | 22.11 | - | 2.62 | 1.22 | 0.543 | 4.3'' |
| NVSS J005304-281614 | 00 53 04.9 | -28 16 14.0 | 9.9 | 23.06 | - | 2.02 | - | 0.592 | 2.9'' |
| NVSS J005321-291450 | 00 53 21.2 | -29 14 50.0 | 47.5 | 21.03 | 0.02 | 1.85 | 1.00 | 0.356 | 1.6'' |
| NVSS J005400-265727 | 00 54 00.9 | -26 57 27.7 | 16.6 | 21.43 | -0.17 | 2.17 | 0.93 | 0.418 | 1.8'' |
| NVSS J005401-282116 | 00 54 01.1 | -28 21 16.0 | 9.5 | 20.74 | - | 2.28 | 1.02 | 0.379 | 2.7'' |

Table C.2: Radio Galaxy Catalogue

| NVSS Source | RA (J2000) | Declination (J2000) | $S_{1.4\text{mJy}}$ | B_J | $U - B_J$ | $B_J - R$ | $R - I$ | z | Optical-Radio Offset |
|---------------------|---------------|------------------------|---------------------|-------|-----------|-----------|---------|-------|-------------------------|
| NVSS J005422-292727 | 00 54 22.3 | -29 27 27.8 | 19.9 | 19.33 | 0.65 | 1.75 | 0.53 | 0.226 | 8.4'' |
| NVSS J005422-294003 | 00 54 22.4 | -29 40 03.6 | 18.0 | 22.04 | - | 2.01 | 1.51 | 0.487 | 3.3'' |
| NVSS J005437-253356 | 00 54 37.8 | -25 33 56.6 | 5.3 | 21.72 | - | 2.33 | 1.07 | 0.466 | 3.3'' |
| NVSS J005440-253943 | 00 54 40.7 | -25 39 43.5 | 7.0 | 18.26 | 0.44 | 1.42 | 0.81 | 0.134 | 3.8'' |
| NVSS J005512-270947 | 00 55 12.5 | -27 09 47.3 | 11.3 | 19.86 | 0.61 | 1.54 | 0.70 | 0.239 | 0.9'' |
| NVSS J005513-275207 | 00 55 13.3 | -27 52 07.8 | 19.1 | 22.66 | - | 2.23 | 1.70 | 0.588 | 3.6'' |
| NVSS J005515-253859 | 00 55 15.7 | -25 38 59.7 | 7.8 | 20.65 | - | 2.04 | 0.86 | 0.343 | 1.2'' |
| NVSS J005531-272330 | 00 55 31.0 | -27 23 30.2 | 6.5 | 21.82 | - | 2.42 | 0.87 | 0.473 | 1.5'' |
| NVSS J005542-275056 | 00 55 42.1 | -27 50 56.1 | 6.2 | 23.19 | -1.61 | 2.46 | - | 0.713 | 4.7'' |
| NVSS J005548-283605 | 00 55 48.6 | -28 36 05.6 | 10.4 | 21.30 | - | 1.91 | 1.11 | 0.388 | 4.6'' |
| NVSS J005608-262505 | 00 56 08.2 | -26 25 05.9 | 163.7 | 21.72 | - | 2.16 | 0.18 | 0.414 | 1.7'' |
| NVSS J005609-283403 | 00 56 09.3 | -28 34 03.6 | 48.4 | 18.03 | 0.82 | 1.67 | 0.82 | 0.126 | 3.9'' |
| NVSS J005613-285535 | 00 56 13.7 | -28 55 35.8 | 8.0 | 17.90 | 0.92 | 1.60 | 0.92 | 0.121 | 1.3'' |
| NVSS J005630-272950 | 00 56 30.1 | -27 29 50.2 | 86.1 | 19.55 | 0.74 | 1.66 | 0.78 | 0.231 | 0.5'' |
| NVSS J005642-254144 | 00 56 42.3 | -25 41 44.3 | 68.7 | 22.91 | - | 2.62 | 1.75 | 0.666 | 0.7'' |
| NVSS J005642-264707 | 00 56 42.5 | -26 47 07.6 | 22.9 | 20.04 | - | 2.38 | 0.78 | 0.334 | 3.7'' |
| NVSS J005648-254337 | 00 56 48.0 | -25 43 37.3 | 8.6 | 22.52 | - | 2.37 | 0.93 | 0.534 | 2.5'' |
| NVSS J005650-295814 | 00 56 50.9 | -29 58 14.4 | 9.3 | 18.79 | 0.60 | 1.53 | 0.71 | 0.172 | 2.3'' |
| NVSS J005656-254628 | 00 56 56.4 | -25 46 28.5 | 16.2 | 22.10 | - | 2.53 | 1.08 | 0.522 | 3.2'' |
| NVSS J005700-260928 | 00 57 00.9 | -26 09 28.5 | 5.3 | 22.47 | - | 2.36 | 0.93 | 0.528 | 0.6'' |
| NVSS J005708-254409 | 00 57 08.8 | -25 44 09.9 | 12.2 | 21.88 | - | 2.89 | 0.44 | 0.504 | 2.2'' |
| NVSS J005722-290718 | 00 57 22.9 | -29 07 18.7 | 6.8 | 21.40 | - | 2.26 | 0.85 | 0.421 | 5.1'' |
| NVSS J005725-264837 | 00 57 25.5 | -26 48 37.8 | 9.5 | 19.57 | 0.41 | 1.44 | 0.61 | 0.211 | 7.6'' |
| NVSS J005725-264825 | 00 57 25.7 | -26 48 25.5 | 9.5 | 18.42 | 0.59 | 1.51 | 0.77 | 0.150 | 6.2'' |
| NVSS J005742-253315 | 00 57 42.8 | -25 33 15.8 | 238.4 | 21.46 | - | 1.88 | 1.09 | 0.398 | 1.5'' |
| NVSS J005756-252237 | 00 57 57.0 | -25 22 37.1 | 301.9 | 18.92 | 0.78 | 1.67 | 0.77 | 0.198 | 0.9'' |
| NVSS J005820-251826 | 00 58 20.9 | -25 18 26.6 | 19.1 | 19.82 | 1.62 | 2.11 | 0.73 | 0.291 | 3.5'' |
| NVSS J005823-290429 | 00 58 23.3 | -29 04 29.0 | 17.7 | 18.93 | 0.99 | 1.84 | 0.69 | 0.214 | 1.0'' |
| NVSS J005832-292616 | 00 58 32.7 | -29 26 16.0 | 56.2 | 23.37 | - | 3.30 | 1.13 | 0.736 | 2.4'' |
| NVSS J005833-263225 | 00 58 33.3 | -26 32 25.9 | 25.1 | 22.90 | - | 2.37 | 0.81 | 0.563 | 1.2'' |
| NVSS J005848-280107 | 00 58 48.5 | -28 01 07.6 | 19.2 | 19.71 | 0.99 | 1.93 | 0.67 | 0.265 | 2.5'' |
| NVSS J005909-285944 | 00 59 09.3 | -28 59 44.5 | 448.2 | 17.79 | 0.94 | 1.76 | 0.76 | 0.117 | 8.5'' |
| NVSS J005916-253849 | 00 59 16.4 | -25 38 49.9 | 6.6 | 20.08 | - | 2.24 | 0.60 | 0.317 | 2.2'' |
| NVSS J005936-252153 | 00 59 36.9 | -25 21 53.9 | 8.4 | 21.15 | - | 2.28 | 0.90 | 0.406 | 1.6'' |
| NVSS J005945-300925 | 00 59 45.6 | -30 09 25.8 | 8.9 | 21.30 | - | 2.57 | 0.88 | 0.447 | 2.6'' |

Table C.3: Radio Galaxy Catalogue

| NVSS Source | RA (J2000) | Declination (J2000) | $S_{1.4\text{mJy}}$ | B_J | $U - B_J$ | $B_J - R$ | $R - I$ | z | Optical-Radio Offset |
|---------------------|---------------|------------------------|---------------------|-------|-----------|-----------|---------|-------|-------------------------|
| NVSS J005953-281829 | 00 59 53.3 | -28 18 29.1 | 5.1 | 20.31 | - | 1.97 | 1.22 | 0.323 | 3.7'' |
| NVSS J010001-291946 | 01 00 01.1 | -29 19 47.0 | 19.0 | 19.61 | - | 1.86 | 0.70 | 0.254 | 3.0'' |
| NVSS J010004-261116 | 01 00 04.2 | -26 11 16.8 | 12.6 | 21.23 | - | 1.98 | 1.04 | 0.388 | 2.6'' |
| NVSS J010006-283210 | 01 00 07.0 | -28 32 10.1 | 16.9 | 20.44 | - | 2.09 | 1.14 | 0.343 | 5.1'' |
| NVSS J010010-260655 | 01 00 10.8 | -26 06 55.3 | 5.3 | 22.47 | - | 2.25 | 1.30 | 0.540 | 4.5'' |
| NVSS J010022-272342 | 01 00 22.9 | -27 23 42.1 | 9.1 | 22.81 | - | 2.30 | 1.33 | 0.582 | 4.2'' |
| NVSS J010031-263352 | 01 00 31.0 | -26 33 52.7 | 98.8 | 22.08 | - | 2.36 | 1.96 | 0.567 | 1.8'' |
| NVSS J010049-274023 | 01 00 49.1 | -27 40 23.9 | 20.0 | 20.18 | 1.63 | 2.11 | 0.97 | 0.320 | 2.9'' |
| NVSS J010102-285847 | 01 01 02.4 | -28 58 47.2 | 18.7 | 19.73 | 1.11 | 2.10 | 0.80 | 0.286 | 7.3'' |
| NVSS J010114-284018 | 01 01 14.1 | -28 40 18.5 | 18.9 | 20.48 | - | 2.17 | 0.52 | 0.334 | 3.8'' |
| NVSS J010129-272201 | 01 01 29.9 | -27 22 01.7 | 8.6 | 19.60 | 1.18 | 1.92 | 0.82 | 0.261 | 1.1'' |
| NVSS J010132-275444 | 01 01 32.3 | -27 54 44.8 | 18.4 | 22.73 | -2.20 | 2.59 | 0.99 | 0.581 | 0.4'' |
| NVSS J010204-294203 | 01 02 04.1 | -29 42 03.8 | 26.9 | 21.83 | - | 2.32 | 0.53 | 0.448 | 4.5'' |
| NVSS J010213-253731 | 01 02 13.0 | -25 37 31.3 | 6.3 | 20.79 | - | 2.15 | 0.55 | 0.355 | 4.4'' |
| NVSS J010312-251801 | 01 03 12.5 | -25 18 01.5 | 16.6 | 21.43 | - | 2.15 | 1.07 | 0.422 | 3.3'' |
| NVSS J010312-251754 | 01 03 12.7 | -25 17 54.9 | 16.6 | 21.90 | - | 2.66 | 0.38 | 0.481 | 4.1'' |
| NVSS J010319-254035 | 01 03 19.8 | -25 40 35.1 | 8.2 | 20.02 | 1.46 | 1.81 | 0.54 | 0.272 | 4.3'' |
| NVSS J010325-282000 | 01 03 26.0 | -28 20 00.6 | 12.4 | 19.48 | 1.16 | 1.78 | 0.66 | 0.238 | 1.9'' |
| NVSS J010401-300107 | 01 04 01.4 | -30 01 07.2 | 6.1 | 20.76 | - | 2.46 | 0.55 | 0.383 | 2.7'' |
| NVSS J010407-293621 | 01 04 07.5 | -29 36 21.7 | 5.8 | 17.94 | 0.82 | 1.49 | 0.92 | 0.123 | 6.3'' |
| NVSS J010437-300452 | 01 04 37.9 | -30 04 52.7 | 12.0 | 20.68 | - | 2.09 | 0.85 | 0.350 | 4.1'' |
| NVSS J010448-261250 | 01 04 48.5 | -26 12 50.1 | 8.2 | 22.42 | - | 2.55 | 1.06 | 0.551 | 4.2'' |
| NVSS J010449-283024 | 01 04 49.9 | -28 30 24.7 | 8.9 | 21.79 | - | 2.81 | 1.03 | 0.522 | 5.3'' |
| NVSS J010451-251725 | 01 04 51.6 | -25 17 25.1 | 10.0 | 20.51 | - | 1.92 | 0.98 | 0.324 | 5.7'' |
| NVSS J010453-262221 | 01 04 53.4 | -26 22 21.0 | 18.7 | 21.49 | - | 2.23 | 0.66 | 0.418 | 0.4'' |
| NVSS J010456-294043 | 01 04 56.9 | -29 40 43.7 | 30.2 | 19.88 | 1.57 | 2.10 | 0.73 | 0.293 | 1.5'' |
| NVSS J010520-252310 | 01 05 20.9 | -25 23 10.9 | 8.3 | 18.71 | 1.10 | 1.72 | 0.74 | 0.192 | 2.6'' |
| NVSS J010525-263145 | 01 05 25.1 | -26 31 45.0 | 5.0 | 20.77 | - | 1.65 | 0.84 | 0.312 | 4.2'' |
| NVSS J010528-281043 | 01 05 28.2 | -28 10 43.3 | 10.9 | 19.08 | 1.05 | 1.56 | 0.67 | 0.195 | 4.6'' |
| NVSS J010542-295443 | 01 05 42.5 | -29 54 43.1 | 7.0 | 20.85 | - | 2.09 | 0.49 | 0.351 | 1.9'' |
| NVSS J010545-254752 | 01 05 45.3 | -25 47 52.4 | 34.5 | 19.90 | - | 2.21 | 0.68 | 0.305 | 1.3'' |
| NVSS J010545-295032 | 01 05 45.6 | -29 50 32.8 | 12.3 | 21.17 | - | 2.21 | 0.69 | 0.392 | 1.8'' |
| NVSS J010547-285729 | 01 05 47.8 | -28 57 29.2 | 18.2 | 19.01 | 0.74 | 1.60 | 0.78 | 0.196 | 0.7'' |
| NVSS J010607-280934 | 01 06 07.2 | -28 09 34.9 | 10.9 | 22.88 | -1.33 | 2.06 | - | 0.509 | 0.3'' |
| NVSS J010610-262430 | 01 06 10.7 | -26 24 30.7 | 63.9 | 20.23 | - | 2.21 | 0.86 | 0.330 | 1.3'' |

Table C.4: Radio Galaxy Catalogue

| NVSS Source | RA (J2000) | Declination (J2000) | $S_{1.4\text{mJy}}$ | B_J | $U - B_J$ | $B_J - R$ | $R - I$ | z | Optical-Radio Offset |
|---------------------|---------------|------------------------|---------------------|-------|-----------|-----------|---------|-------|-------------------------|
| NVSS J010625-284917 | 01 06 25.9 | -28 49 17.5 | 12.1 | 21.60 | - | 2.59 | 0.63 | 0.461 | 4.6'' |
| NVSS J010633-285054 | 01 06 33.5 | -28 50 54.2 | 12.0 | 20.46 | 0.80 | 1.97 | 0.83 | 0.320 | 2.5'' |
| NVSS J103241+013423 | 10 32 41.1 | +01 34 23.7 | 9.2 | 22.70 | - | 2.24 | 1.75 | 0.597 | 1.2'' |
| NVSS J103409+021224 | 10 34 09.0 | +02 12 24.5 | 9.2 | 20.21 | 0.30 | 1.98 | 0.73 | 0.303 | 4.1'' |
| NVSS J103414+000521 | 10 34 14.6 | +00 05 21.1 | 254.8 | 19.14 | 0.58 | 1.39 | 0.70 | 0.180 | 4.6'' |
| NVSS J103419-002032 | 10 34 19.1 | -00 20 32.4 | 5.0 | 18.23 | 0.33 | 1.23 | 0.70 | 0.120 | 2.6'' |
| NVSS J103424-021103 | 10 34 24.4 | -02 11 03.1 | 123.5 | 20.17 | 0.52 | 1.65 | 0.57 | 0.267 | 1.1'' |
| NVSS J103431+012354 | 10 34 31.2 | +01 23 54.8 | 15.9 | 22.54 | - | 2.40 | 1.23 | 0.559 | 1.3'' |
| NVSS J103453+003637 | 10 34 53.9 | +00 36 37.7 | 139.1 | 22.16 | - | 2.25 | 0.91 | 0.488 | 0.8'' |
| NVSS J103456-001004 | 10 34 56.9 | -00 10 04.5 | 6.3 | 21.37 | - | 2.09 | 0.67 | 0.395 | 3.5'' |
| NVSS J103520+012022 | 10 35 20.9 | +01 20 22.8 | 5.5 | 22.65 | - | 1.99 | 1.24 | 0.526 | 3.6'' |
| NVSS J103525-000140 | 10 35 25.4 | -00 01 40.8 | 7.8 | 21.58 | - | 2.34 | 0.79 | 0.441 | 4.5'' |
| NVSS J103526-012513 | 10 35 26.2 | -01 25 13.7 | 7.3 | 21.24 | - | 2.13 | 0.83 | 0.394 | 2.1'' |
| NVSS J103551-004245 | 10 35 52.0 | -00 42 46.0 | 6.1 | 21.84 | - | 2.69 | 0.92 | 0.506 | 0.7'' |
| NVSS J103608+013719 | 10 36 09.0 | +01 37 20.0 | 11.0 | 21.39 | - | 2.31 | 0.73 | 0.420 | 1.5'' |
| NVSS J103619-001955 | 10 36 19.7 | -00 19 55.8 | 8.4 | 20.35 | - | 1.94 | 0.76 | 0.309 | 0.8'' |
| NVSS J103622+011119 | 10 36 22.9 | +01 11 19.8 | 5.8 | 21.83 | - | 2.54 | 1.14 | 0.502 | 2.1'' |
| NVSS J103647-004056 | 10 36 47.2 | -00 40 56.5 | 12.9 | 18.81 | 0.75 | 1.49 | 0.79 | 0.169 | 2.6'' |
| NVSS J103700+014539 | 10 37 00.5 | +01 45 39.1 | 44.7 | 22.18 | - | 2.62 | 0.90 | 0.526 | 4.2'' |
| NVSS J103736-004117 | 10 37 36.9 | -00 41 17.6 | 29.4 | 17.89 | 0.59 | 1.62 | 0.70 | 0.116 | 7.9'' |
| NVSS J103741-012800 | 10 37 41.0 | -01 28 00.2 | 81.8 | 21.55 | - | 2.19 | 0.81 | 0.424 | 4.2'' |
| NVSS J103749-000522 | 10 37 49.2 | -00 05 22.7 | 32.0 | 21.26 | - | 1.81 | 1.11 | 0.375 | 2.3'' |
| NVSS J103829-002934 | 10 38 29.0 | -00 29 34.0 | 5.3 | 20.68 | - | 2.46 | 0.80 | 0.386 | 4.5'' |
| NVSS J103834+011923 | 10 38 34.8 | +01 19 23.2 | 6.8 | 20.62 | 1.25 | 2.03 | 0.91 | 0.340 | 1.7'' |
| NVSS J103836+011800 | 10 38 36.7 | +01 18 00.8 | 321.4 | 19.49 | 0.74 | 1.50 | 1.01 | 0.205 | 6.9'' |
| NVSS J103843-020736 | 10 38 43.4 | -02 07 36.3 | 6.6 | 21.41 | - | 2.40 | 0.93 | 0.440 | 4.0'' |
| NVSS J103849-013925 | 10 38 50.0 | -01 39 25.9 | 10.9 | 20.69 | - | 1.68 | 0.26 | 0.301 | 3.9'' |
| NVSS J103853-024059 | 10 38 53.9 | -02 40 59.1 | 5.8 | 22.47 | - | 2.07 | 1.42 | 0.529 | 1.0'' |
| NVSS J103855-015043 | 10 38 55.6 | -01 50 43.9 | 9.9 | 20.92 | - | 2.25 | 0.74 | 0.378 | 4.2'' |
| NVSS J103908-023923 | 10 39 08.7 | -02 39 23.2 | 26.5 | 20.53 | 0.08 | 1.65 | 0.34 | 0.288 | 5.9'' |
| NVSS J103911+013801 | 10 39 11.2 | +01 38 01.0 | 24.0 | 21.24 | - | 2.05 | 0.68 | 0.381 | 1.0'' |
| NVSS J103920+010514 | 10 39 20.4 | +01 05 14.9 | 8.3 | 18.40 | 0.66 | 1.77 | 0.91 | 0.183 | 6.4'' |
| NVSS J103938+003046 | 10 39 38.4 | +00 30 46.6 | 8.4 | 17.96 | 0.52 | 1.54 | 0.81 | 0.117 | 1.4'' |
| NVSS J103944-021128 | 10 39 44.2 | -02 11 28.5 | 29.7 | 22.65 | - | 2.73 | 1.22 | 0.605 | 3.5'' |
| NVSS J103956-024043 | 10 39 57.0 | -02 40 43.6 | 5.3 | 22.10 | - | 2.13 | 0.77 | 0.463 | 2.1'' |

Table C.5: Radio Galaxy Catalogue

| NVSS Source | RA (J2000) | Declination (J2000) | $S_{1.4\text{mJy}}$ | B_J | $U - B_J$ | $B_J - R$ | $R - I$ | z | Optical-Radio Offset |
|---------------------|---------------|------------------------|---------------------|-------|-----------|-----------|---------|-------|-------------------------|
| NVSS J104005+012303 | 10 40 05.8 | +01 23 03.8 | 5.3 | 21.70 | - | 2.25 | 1.24 | 0.465 | 2.6'' |
| NVSS J104014-023504 | 10 40 14.9 | -02 35 04.1 | 17.3 | 22.11 | - | 2.69 | 0.84 | 0.525 | 1.1'' |
| NVSS J104020+010505 | 10 40 20.3 | +01 05 05.9 | 11.2 | 22.26 | - | 1.95 | - | 0.441 | 2.7'' |
| NVSS J104037+004222 | 10 40 37.8 | +00 42 22.3 | 15.9 | 21.44 | - | 2.37 | 1.04 | 0.445 | 0.9'' |
| NVSS J104039+013703 | 10 40 39.7 | +01 37 03.8 | 5.6 | 19.48 | 1.57 | 2.04 | 0.84 | 0.266 | 5.5'' |
| NVSS J104044+020533 | 10 40 44.8 | +02 05 33.8 | 20.0 | 21.82 | - | 2.65 | 0.52 | 0.479 | 2.0'' |
| NVSS J104105-004337 | 10 41 05.2 | -00 43 37.5 | 27.0 | 18.71 | 0.82 | 1.41 | 0.91 | 0.153 | 3.1'' |
| NVSS J104105-004324 | 10 41 05.5 | -00 43 24.7 | 27.0 | 18.86 | 0.82 | 1.46 | 0.79 | 0.169 | 10.6'' |
| NVSS J104106+011904 | 10 41 06.3 | +01 19 04.4 | 11.0 | 22.05 | - | 2.56 | 1.20 | 0.528 | 0.2'' |
| NVSS J104118+001047 | 10 41 18.2 | +00 10 47.9 | 6.3 | 21.59 | - | 2.44 | 0.85 | 0.455 | 4.7'' |
| NVSS J104121-022301 | 10 41 21.5 | -02 23 01.9 | 7.9 | 18.92 | 0.70 | 1.87 | 0.66 | 0.216 | 2.1'' |
| NVSS J104122+020902 | 10 41 22.9 | +02 09 02.4 | 250.4 | 21.49 | - | 2.35 | 1.06 | 0.449 | 2.5'' |
| NVSS J104129-003800 | 10 41 29.1 | -00 38 00.6 | 47.5 | 17.67 | 0.63 | 1.65 | 0.82 | 0.105 | 1.2'' |
| NVSS J104131-002733 | 10 41 31.9 | -00 27 33.2 | 13.7 | 17.66 | 0.71 | 1.67 | 0.90 | 0.105 | 4.7'' |
| NVSS J104139-005416 | 10 41 39.0 | -00 54 16.2 | 20.6 | 22.27 | - | 2.80 | 1.31 | 0.583 | 4.3'' |
| NVSS J104159-020144 | 10 41 59.6 | -02 01 45.0 | 48.6 | 19.79 | - | 2.19 | 0.87 | 0.301 | 3.5'' |
| NVSS J104212+015212 | 10 42 12.5 | +01 52 12.2 | 28.5 | 19.50 | 1.45 | 1.94 | 0.80 | 0.257 | 1.5'' |
| NVSS J104216+012003 | 10 42 16.2 | +01 20 03.1 | 23.5 | 21.62 | - | 1.89 | 1.56 | 0.438 | 1.3'' |
| NVSS J104231+003906 | 10 42 31.5 | +00 39 06.9 | 9.8 | 21.46 | - | 2.37 | 0.57 | 0.426 | 5.2'' |
| NVSS J104241-000946 | 10 42 41.7 | -00 09 46.1 | 12.5 | 22.91 | - | 2.68 | 1.03 | 0.611 | 1.4'' |
| NVSS J104246-022757 | 10 42 46.9 | -02 27 57.6 | 7.8 | 22.57 | - | 2.11 | 1.54 | 0.552 | 1.0'' |
| NVSS J104250+003354 | 10 42 51.0 | +00 33 54.7 | 5.8 | 21.49 | - | 2.13 | 0.71 | 0.409 | 3.4'' |
| NVSS J104301+010654 | 10 43 01.6 | +01 06 54.7 | 10.9 | 19.54 | 1.02 | 2.00 | 0.85 | 0.266 | 6.6'' |
| NVSS J104302+005047 | 10 43 02.3 | +00 50 47.9 | 56.9 | 19.71 | 1.01 | 2.14 | 0.66 | 0.286 | 7.3'' |
| NVSS J104335+011629 | 10 43 35.8 | +01 16 29.2 | 99.2 | 19.61 | 0.44 | 1.72 | 0.59 | 0.239 | 5.5'' |
| NVSS J104335-000733 | 10 43 35.9 | -00 07 34.0 | 20.8 | 21.02 | - | 2.33 | 0.68 | 0.393 | 4.8'' |
| NVSS J104339-000013 | 10 43 39.8 | -00 00 13.9 | 5.7 | 19.11 | 0.34 | 1.35 | - | 0.168 | 5.7'' |
| NVSS J104346+010042 | 10 43 46.0 | +01 00 42.5 | 13.0 | 23.08 | - | 2.39 | 1.31 | 0.617 | 3.9'' |
| NVSS J104348-012400 | 10 43 48.0 | -01 24 00.3 | 8.7 | 20.70 | - | 2.15 | 0.67 | 0.351 | 4.1'' |
| NVSS J104352+000603 | 10 43 52.4 | +00 06 03.5 | 7.5 | 22.24 | - | 3.01 | 0.82 | 0.570 | 3.4'' |
| NVSS J104412-023831 | 10 44 12.6 | -02 38 31.6 | 5.8 | 19.75 | - | 1.83 | 0.60 | 0.257 | 1.9'' |
| NVSS J104414-015147 | 10 44 14.3 | -01 51 48.0 | 6.8 | 19.65 | 0.99 | 1.79 | 0.70 | 0.249 | 5.7'' |
| NVSS J104415-010946 | 10 44 15.8 | -01 09 46.9 | 15.6 | 21.24 | - | 1.91 | - | 0.358 | 1.5'' |
| NVSS J104455+005655 | 10 44 55.1 | +00 56 55.7 | 16.6 | 17.88 | 0.52 | 1.52 | 0.83 | 0.113 | 2.4'' |
| NVSS J104509-015843 | 10 45 09.4 | -01 58 43.3 | 9.7 | 22.06 | - | 2.49 | 0.98 | 0.507 | 1.3'' |

Table C.6: Radio Galaxy Catalogue

| NVSS Source | RA (J2000) | Declination (J2000) | $S_{1.4\text{mJy}}$ | B_J | $U - B_J$ | $B_J - R$ | $R - I$ | z | Optical-Radio Offset |
|---------------------|---------------|------------------------|---------------------|-------|-----------|-----------|---------|-------|-------------------------|
| NVSS J104513-004929 | 10 45 13.4 | -00 49 29.9 | 7.4 | 21.34 | - | 2.72 | 0.63 | 0.454 | 3.5'' |
| NVSS J104513+014557 | 10 45 13.8 | +01 45 57.4 | 10.1 | 21.09 | - | 2.72 | 0.83 | 0.444 | 2.1'' |
| NVSS J104516-010607 | 10 45 16.5 | -01 06 07.3 | 12.5 | 20.53 | - | 2.07 | 0.72 | 0.332 | 2.2'' |
| NVSS J104525+001241 | 10 45 25.0 | +00 12 41.5 | 10.6 | 22.35 | - | 2.29 | 0.61 | 0.492 | 1.2'' |
| NVSS J104537+000116 | 10 45 37.3 | +00 01 16.6 | 14.7 | 20.53 | - | 2.36 | 0.93 | 0.369 | 3.1'' |
| NVSS J104603-023015 | 10 46 03.8 | -02 30 15.2 | 10.6 | 22.55 | - | 2.95 | 0.74 | 0.585 | 0.6'' |
| NVSS J104603+014907 | 10 46 03.8 | +01 49 07.4 | 18.3 | 21.47 | - | 2.47 | 0.81 | 0.446 | 1.5'' |
| NVSS J104626-005030 | 10 46 26.1 | -00 50 31.0 | 6.8 | 21.67 | - | 2.36 | 0.57 | 0.441 | 5.7'' |
| NVSS J104630-001212 | 10 46 30.7 | -00 12 12.7 | 6.5 | 21.34 | - | 2.19 | 0.84 | 0.409 | 3.4'' |
| NVSS J104632-011338 | 10 46 32.4 | -01 13 38.5 | 133.7 | 19.23 | 0.84 | 1.53 | 0.61 | 0.203 | 2.4'' |
| NVSS J104633-021713 | 10 46 33.1 | -02 17 13.2 | 38.1 | 18.49 | 0.79 | 1.66 | 0.72 | 0.176 | 2.1'' |
| NVSS J104650-000109 | 10 46 50.8 | -00 01 09.6 | 35.6 | 22.22 | - | 2.02 | 0.56 | 0.453 | 5.5'' |
| NVSS J104650-000115 | 10 46 51.0 | -00 01 15.1 | 35.6 | 20.90 | - | 2.46 | 0.89 | 0.405 | 0.4'' |
| NVSS J104658-014727 | 10 46 58.4 | -01 47 27.2 | 11.5 | 21.94 | - | 2.03 | 1.83 | 0.503 | 2.5'' |
| NVSS J104723-021849 | 10 47 23.7 | -02 18 49.7 | 30.3 | 20.51 | - | 1.96 | 0.64 | 0.319 | 4.0'' |
| NVSS J104733+001526 | 10 47 33.5 | +00 15 26.5 | 49.7 | 23.27 | - | 2.47 | 1.47 | 0.660 | 0.6'' |
| NVSS J104738-022259 | 10 47 38.6 | -02 22 59.5 | 214.4 | 19.79 | 0.42 | 1.71 | 0.61 | 0.249 | 4.4'' |
| NVSS J104744+013637 | 10 47 44.3 | +01 36 37.9 | 28.9 | 23.49 | - | 2.16 | - | 0.574 | 5.2'' |
| NVSS J104754+012900 | 10 47 54.8 | +01 29 00.4 | 9.6 | 18.87 | 1.09 | 1.96 | 0.79 | 0.224 | 6.3'' |
| NVSS J104801-013014 | 10 48 01.9 | -01 30 14.4 | 5.4 | 17.70 | - | 1.27 | 0.80 | 0.105 | 3.0'' |
| NVSS J104805+000858 | 10 48 05.9 | +00 08 58.2 | 47.8 | 22.69 | - | 2.80 | 0.87 | 0.591 | 0.8'' |
| NVSS J104828+003938 | 10 48 28.7 | +00 39 38.4 | 5.2 | 18.06 | 0.24 | 1.31 | 0.87 | 0.117 | 12.3'' |
| NVSS J104829-020008 | 10 48 29.5 | -02 00 08.9 | 22.1 | 18.71 | 1.04 | 1.78 | 0.78 | 0.198 | 2.2'' |
| NVSS J104850-011227 | 10 48 50.0 | -01 12 27.6 | 5.9 | 21.06 | - | 2.31 | 0.77 | 0.396 | 2.5'' |
| NVSS J104905-015747 | 10 49 05.4 | -01 57 47.7 | 9.0 | 21.84 | - | 1.92 | 0.87 | 0.424 | 1.6'' |
| NVSS J104910-003640 | 10 49 10.6 | -00 36 40.3 | 18.2 | 23.14 | - | 2.81 | 1.59 | 0.697 | 3.4'' |
| NVSS J104923+000027 | 10 49 23.2 | +00 00 27.6 | 23.2 | 22.12 | - | 2.64 | 0.71 | 0.513 | 0.2'' |
| NVSS J104926-000347 | 10 49 26.5 | -00 03 47.7 | 6.7 | 20.30 | - | 2.17 | 0.76 | 0.328 | 4.5'' |
| NVSS J104926+005609 | 10 49 26.5 | +00 56 09.5 | 33.9 | 18.26 | 0.50 | 1.60 | 0.71 | 0.148 | 1.1'' |
| NVSS J104928-022730 | 10 49 28.6 | -02 27 30.0 | 8.2 | 18.72 | 0.83 | 1.75 | 0.83 | 0.195 | 1.9'' |
| NVSS J104933-002741 | 10 49 33.9 | -00 27 41.9 | 15.3 | 23.40 | - | 2.19 | 1.25 | 0.625 | 1.6'' |
| NVSS J104935-011408 | 10 49 36.0 | -01 14 08.3 | 5.2 | 22.29 | - | 1.90 | - | 0.438 | 3.9'' |
| NVSS J104958-022624 | 10 49 58.3 | -02 26 24.1 | 14.7 | 22.65 | - | 2.55 | 0.93 | 0.564 | 2.2'' |
| NVSS J105026-020426 | 10 50 26.9 | -02 04 26.0 | 14.4 | 21.68 | - | 1.93 | 1.28 | 0.431 | 3.1'' |
| NVSS J105036-023616 | 10 50 36.5 | -02 36 16.3 | 14.5 | 17.61 | 0.73 | 1.77 | 0.59 | 0.108 | 2.3'' |

| NVSS Source | RA (J2000) | Declination (J2000) | $S_{1.4\text{mJy}}$ | B_J | $U - B_J$ | $B_J - R$ | $R - I$ | z | Optical-Radio Offset |
|---------------------|---------------|------------------------|---------------------|-------|-----------|-----------|---------|-------|-------------------------|
| NVSS J105037-004724 | 10 50 37.5 | -00 47 24.7 | 125.7 | 22.86 | - | 2.34 | - | 0.541 | 4.5'' |
| NVSS J105045+004542 | 10 50 45.6 | +00 45 42.2 | 6.4 | 19.82 | 1.17 | 1.88 | 0.73 | 0.268 | 4.4'' |
| NVSS J105047+010739 | 10 50 47.4 | +01 07 39.4 | 30.4 | 23.25 | - | 2.25 | 1.39 | 0.627 | 0.8'' |
| NVSS J105101-001738 | 10 51 01.2 | -00 17 39.0 | 16.5 | 20.27 | - | 1.98 | 0.90 | 0.311 | 2.4'' |
| NVSS J105103-021259 | 10 51 03.6 | -02 12 59.8 | 6.6 | 22.77 | - | 2.02 | 0.67 | 0.509 | 2.7'' |
| NVSS J105112-011510 | 10 51 12.4 | -01 15 10.5 | 23.7 | 20.50 | - | 2.29 | 0.74 | 0.353 | 1.4'' |
| NVSS J105120-014259 | 10 51 20.6 | -01 42 59.1 | 6.3 | 20.08 | 1.66 | 2.04 | 0.78 | 0.302 | 3.4'' |
| NVSS J105126-014403 | 10 51 26.2 | -01 44 03.1 | 17.2 | 22.83 | - | 2.87 | 0.79 | 0.607 | 2.5'' |
| NVSS J105138-011921 | 10 51 38.5 | -01 19 21.1 | 5.2 | 17.94 | 0.81 | 1.53 | 0.70 | 0.126 | 1.9'' |
| NVSS J105150+011351 | 10 51 50.7 | +01 13 51.0 | 10.1 | 23.19 | - | 2.43 | 0.76 | 0.594 | 1.8'' |
| NVSS J105158+005045 | 10 51 59.0 | +00 50 45.4 | 13.8 | 20.67 | - | 2.58 | 0.63 | 0.391 | 1.4'' |
| NVSS J105159+005047 | 10 51 59.5 | +00 50 47.8 | 13.8 | 18.66 | 0.86 | 1.59 | 1.27 | 0.154 | 9.5'' |
| NVSS J105227-014108 | 10 52 27.1 | -01 41 08.4 | 23.3 | 21.71 | - | 2.20 | 0.55 | 0.427 | 3.7'' |

Table C.7: Radio Galaxy Catalogue